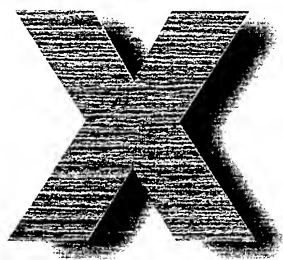




Proceedings Part I

NOVOSIBIRSK-TOMSK, RUSSIA



9 - 16 July, 2000

DISTRIBUTION STATEMENT A
Approved for Public Release
Distribution Unlimited

International Conference on the Methods of Aerophysical Research

THIS COPY NOT INTEGRATED 4

20000913 066

REPORT DOCUMENTATION PAGE

Form Approved OMB No. 0704-0188

Public reporting burden for this collection of information is estimated to average 1 hour per response, including the time for reviewing instructions, searching existing data sources, gathering and maintaining the data needed, and completing and reviewing the collection of information. Send comments regarding this burden estimate or any other aspect of this collection of information, including suggestions for reducing this burden to Washington Headquarters Services, Directorate for Information Operations and Reports, 1215 Jefferson Davis Highway, Suite 1204, Arlington, VA 22202-4302, and to the Office of Management and Budget, Paperwork Reduction Project (0704-0188), Washington, DC 20503.

1. AGENCY USE ONLY (Leave blank)		2. REPORT DATE 28 August 2000	3. REPORT TYPE AND DATES COVERED Conference Proceedings	
4. TITLE AND SUBTITLE International Conferences on Methods of Aerophysical Research (ICMAR'2000), <i>Part 1</i>			5. FUNDING NUMBERS F61775-00-WF022	
6. AUTHOR(S) Conference Committee				
7. PERFORMING ORGANIZATION NAME(S) AND ADDRESS(ES) Institute of Theoretical and Applied Mechanics Institutskaya 4/1 Novosibirsk 630090 Russia			8. PERFORMING ORGANIZATION REPORT NUMBER N/A	
9. SPONSORING/MONITORING AGENCY NAME(S) AND ADDRESS(ES) EOARD PSC 802 BOX 14 FPO 09499-0200			10. SPONSORING/MONITORING AGENCY REPORT NUMBER CSP 00-5022	
11. SUPPLEMENTARY NOTES Two volumes. <i>Part 11</i>				
12a. DISTRIBUTION/AVAILABILITY STATEMENT Approved for public release; distribution is unlimited.			12b. DISTRIBUTION CODE A	
13. ABSTRACT (Maximum 200 words) The Final Proceedings for International Conferences on Methods of Aerophysical Research (ICMAR'2000), 9 July 2000 - 15 July 2000 This is an interdisciplinary conference. Topics include 'Problems of Modeling at Sub/Trans/Super/Hypersonic Velocities'; 'Methods of Flow Diagnostics'; 'Instrumentation in Aerophysical Experiments'; 'Verification of Computational Fluid Dynamics (CFD) Models and Methods'.				
14. SUBJECT TERMS EOARD, Hypersonic Flow, Diagnostics, Computational Fluid Dynamics (CFD)			15. NUMBER OF PAGES 244, 228	
			16. PRICE CODE N/A	
17. SECURITY CLASSIFICATION OF REPORT UNCLASSIFIED	18. SECURITY CLASSIFICATION OF THIS PAGE UNCLASSIFIED	19. SECURITY CLASSIFICATION OF ABSTRACT UNCLASSIFIED	20. LIMITATION OF ABSTRACT UL	

NSN 7540-01-280-5500

Standard Form 298 (Rev. 2-89)
Prescribed by ANSI Std. Z39-18
298-102

SIBERIAN BRANCH OF RUSSIAN ACADEMY OF SCIENCES
RUSSIAN NATIONAL COMMITTEE ON THEORETICAL AND
APPLIED MECHANICS
INSTITUTE OF THEORETICAL AND APPLIED MECHANICS
INTERNATIONAL CENTER OF AEROPHYSICAL RESEARCH

***INTERNATIONAL CONFERENCE ON THE METHODS
OF AEROPHYSICAL RESEARCH***

*9 – 16 July, 2000
Novosibirsk – Tomsk, Russia*

**Proceedings
Part I**

**Novosibirsk
Publishing House of Siberian Branch
of Russian Academy of Sciences
2000**

AQ F00-12-3863

ICMAR-2000 PROGRAM COMMITTEE

V.M. Fomin, Russia, Co-Chairman
A.M. Kharitonov, Russia, Co-Chairman
V.A. Lebiga, Russia, Scientific Secretary
N.A. Anfimov, Russia
S. Bogdonoff, USA
Ph.E. Cassady, USA
A.M. Grishin, Russia
V.N. Gusev, Russia
M.S. Ivanov, Russia
D. Knight, USA
W. Koschel, Germany
V.V. Kozlov, Russia
E. Krause, Germany
A.A. Maslov, Russia
G.E.A. Meier, Germany
J. Muylaert, The Netherlands
A.S. Rudakov, Russia
J.-P. Taran, France
E.P. Volchkov, Russia
A.V. Zabrodin, Russia

**The papers are printed by direct reproduction from the authors' originals.
The authors are responsible for possible misprints and the quality of
translations.**

ISBN 5-7692-0305-6

**© Composing, Institute of Theoretical and Applied
Mechanics SB RAS, 2000**



The conference is dedicated to the centenary of
Academician M.A. Lavrent'ev

ICMAR'2000 is sponsored with:

- Russian Foundation for Basic Research (RFBR)
- American Institute of Aeronautics and Astronautics (AIAA)

We wish to thank

**the United States Air Force European Office of Aerospace
Research and Development (EOARD)**

for its contribution to the success of the Conference

EXPERIMENTAL INVESTIGATION OF LOCALIZED DISTURBANCES IN A SEPARATION BUBBLE

A.R. Ablaev, A.V. Dovgal, G.R. Grek,
M.M. Katasonov, V.V. Kozlov

Institute of Theoretical and Applied Mechanics SB RAS,
630090 Novosibirsk, Russia

1. Introduction

The present topic is instability and transition to turbulence at laminar boundary-layer separation. Flow instability turns much higher as the boundary layer separates from the wall so that even at low Reynolds numbers rapid transition to turbulence takes place behind the point of separation. Occurring in separation regions it is fairly well understood under the low-turbulence conditions through experimental modeling and numerical simulation, see in [1, 2]. However, one expects much effect of the free-stream turbulence upon the transition process.

Research data available for attached boundary layers indicate large differences between laminar flow breakdown, occurring at low ($Tu \leq 1$ per cent) and high ($Tu \geq 1$ per cent) free stream turbulence levels. Their origin is the spanwise base-flow modulation induced by the so-called streaky structures typical for the second case. The transition process in highly disturbed flows was made clear by the results of wind tunnel experiments in which the streaky structures observed under natural conditions were reproduced by controlled boundary-layer excitation. After examination of these artificially generated 3D perturbations, called "puff structures", their streamwise evolution, and interactions with other instabilities a particular scenario of the boundary-layer transition affected by the free-stream turbulence has been developed, outlined as follows [3, 4]. At first, the 2D base flow is modulated in the spanwise direction with the streaks generated by external perturbations. Then, high frequency secondary oscillations amplify which are initiated by transverse velocity gradients of the modulated boundary layer or by interactions of the streaks with other instabilities. As a result, incipient spots and, finally, turbulent spots are generated, interacting with each other.

Approaching mechanisms of the transition in separation regions at a high turbulence level, influence of a stationary 3D perturbation upon instability of the separated layer was investigated in [5]. In the present work we proceed with experimental modeling of the transition process, focusing a nonstationary localized disturbance in the region of laminar boundary-layer separation.

2. Experimental arrangement

Results of the study were obtained in a subsonic wind tunnel of the Institute of Theoretical and Applied Mechanics. The closed test section of facility is $200 \times 200 \times 800$ mm, the free-stream turbulence level is about 0.1 per cent.

The experimental model was a polished flat plate of 725 mm length, 200 mm span, and 10 mm thickness mounted horizontally in the centreplane of the test section, Fig. 1. Pressure distribution close to the nose of the model was adjusted by a trailing-edge flap. Laminar boundary layer separated at a 2D bump of the height $h = 2$ mm at 224 mm from the nose of the model. The puff-structures were generated in the boundary layer before the bump by periodic excitation through a transverse slot of 3 mm length and 0.4 mm width at the surface of the plate connected by a flexible tube with a loudspeaker outside of the test section.

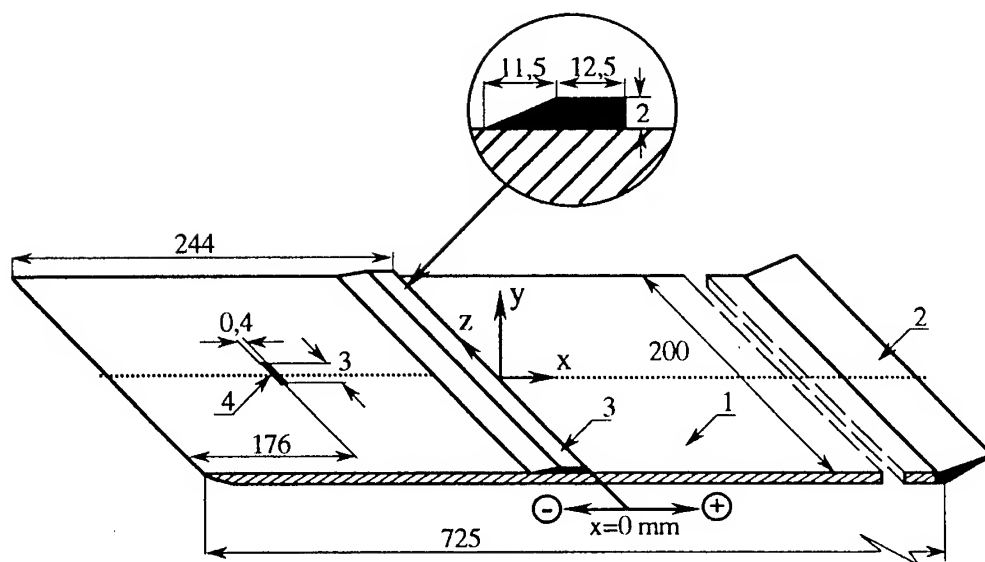


Fig. 1. Experimental sketch. 1 - flat plate, 2 - trailing-edge flap, 3 - 2D bump, 4 - slot

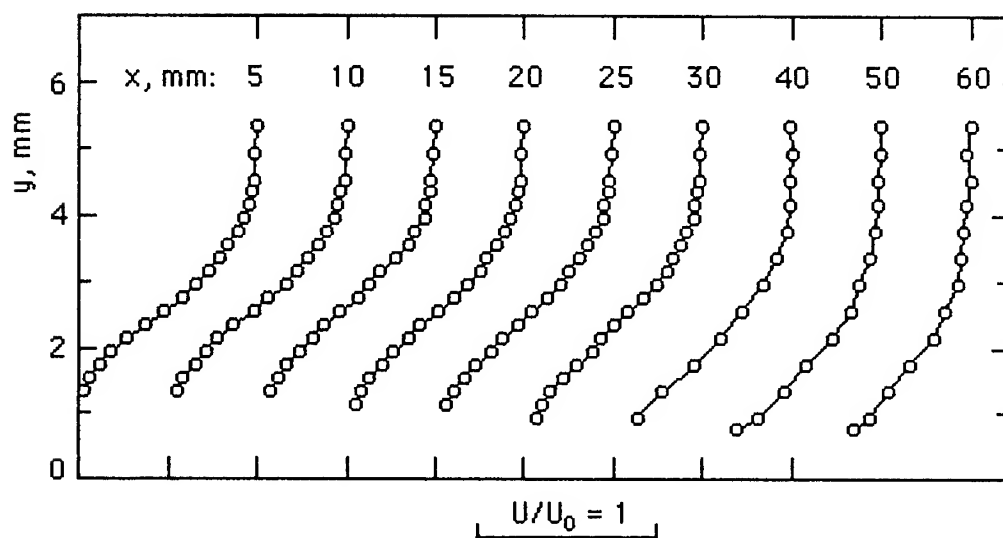


Fig. 2. Mean velocity profiles behind the bump

The streamwise component of flow velocity was measured by a hot-wire system (DISA 55 M01) with single-wire probes. To carry out phase correlated measurements the hot-wire signal was synchronized with output of the disturbances generator. Data processing included ensemble averaging technique to reduce background components. Spectral data on velocity perturbations were taken through Fourier transform. The coordinates used in what follows are: x — streamwise distance with $x = 0$ at the rear side of the bump, y is normal to the wall, and z is the spanwise coordinate measured from the central section of the plate.

3. Results and discussion

3.1. Base flow

The following results were obtained at the external flow velocity above the bump $U_\infty = 6.8$ m/s, making the Reynolds number $Re_h = 870$. At separation the displacement (δ_1) and momentum (θ) thickness of the boundary layer were related as $\delta_1/h = 0.42$ and $\delta_1/\theta = 2.30$. Under these conditions a local region of separation occurred. The mean flow distributions are shown in Fig. 2 where the profiles are normalized by local values of the external flow velocity U_0 . The reattachment length is estimated from these data as $x_r = 40$ to 50 mm, thus, the separation bubble was large enough to get characteristics of flow disturbances with reasonable spatial resolution. Natural instability of the separated layer resulted in streamwise growth of small-amplitude oscillations with frequencies centered around 200 Hz. At rather low Reynolds number taken in the present work the transition point was in the reattached flow behind the separation region.

3.2. Evolution of the localized disturbance

For the following we distinguish two regimes which differ one from the other by the initial amplitude of generated disturbances. In both cases they were periodically injected into the boundary layer by 2-Hz pulses of the loudspeaker.

The results for "small" amplitude excitation are given in Fig. 3. The disturbance at $x = -3$ mm, that is just before the separation point, at the maximum of perturbations across the boundary layer is shown in Fig. 3, *a*. Velocity contours plotted by dotted and solid lines are its negative and positive deviations from the mean value, respectively. Those are in the range of -4.2 to 1.14 as percentage of the external flow velocity. The map of disturbance in $z - t$ plane and its spectrum indicate the puff-structure dominated by the streamwise streaks with oblique waves on both sides [4].

Transformation of this disturbance, passing over the separation bubble, is illustrated in Fig. 3, *b*. Two points are to be emphasized in this case. The first one is that amplitude of the streaks decays with the streamwise coordinate. The second observation is that the 3D waves induced by the puff-structure turn into almost 2D oscillations. Propagating velocity of the latter is nearly 0.4 of the external flow velocity and the dominant frequency is about 160 Hz, being characteristics of the instability waves, amplifying in the separated shear layer.

The results obtained at the amplitude of disturbance about three times larger than it was in the previous case are given in Fig. 4. Initially, Fig. 4, *a*, there is the puff-structure which is quite similar to that in the small-amplitude regime, but in the separation region, Fig. 4, *b*, its behaviour is much different. The perturbation amplify in the streamwise direction with high-frequency secondary oscillations, sitting on the streaks, which transform, finally, into turbulence. This scenario was observed before in the boundary layer [3, 4]. The peripheral disturbances are dominated by the oblique waves. This also correlates with the previous data

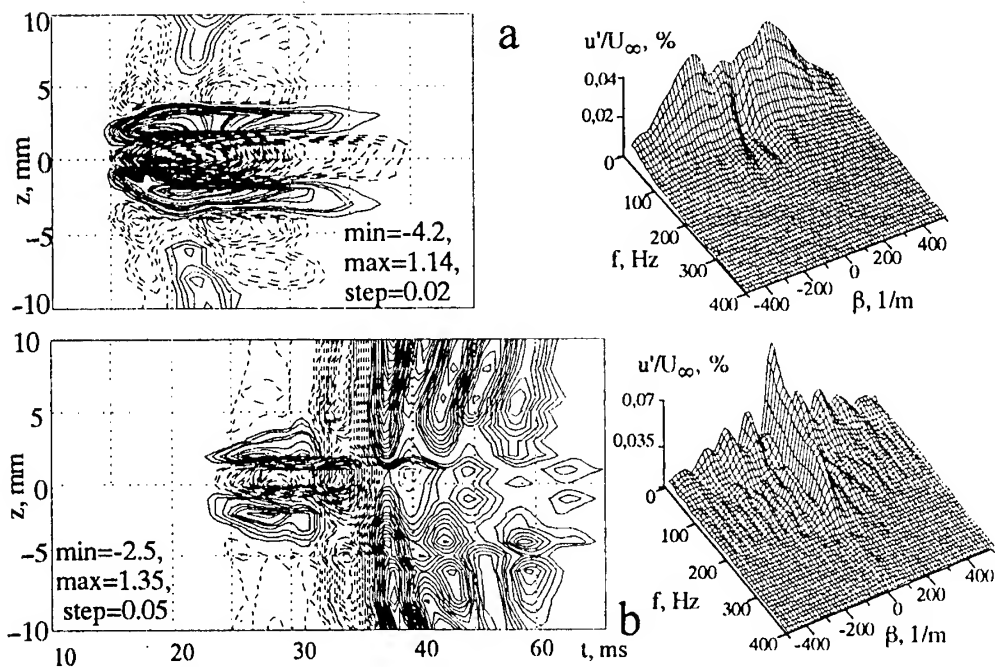


Fig.3. Small-amplitude disturbance, contours of velocity perturbations (left) and frequency - wave number spectra (right). a - $x = -3$ mm, b - $x = 40$ mm

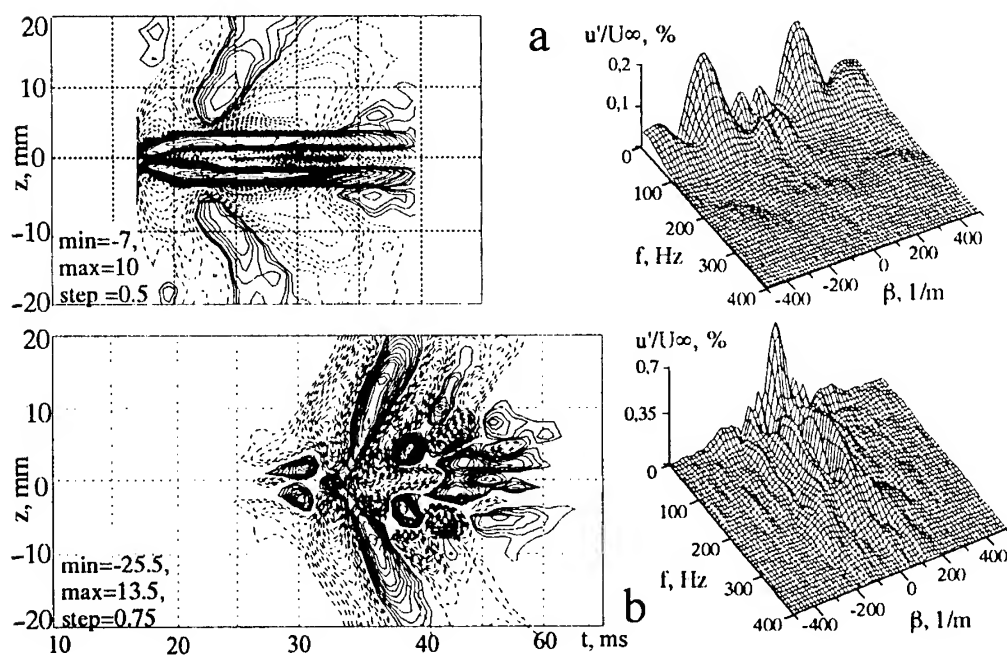


Fig.4. Large-amplitude disturbance, contours of velocity perturbations (left) and frequency - wave number spectra (right). a - $x = -3$ mm, b - $x = 40$ mm

for attached flow; the only difference to be noticed is that the 3D waves grow behind the separation point while in the attached flow they decay.

The above experimental findings are in accordance with numerical data of [6] where the localized disturbances were examined in the boundary layer with inflexional base flow induced by an adverse pressure gradient. The calculations have shown the same trends for amplification of the 2D waves under the small-amplitude conditions and prevalence of the streaks with secondary instabilities in the other case.

4. Conclusion

In this work we dealt with the separated-layer transition initiated by controlled excitation of localized laminar-flow perturbations. In this way, different features of the transition process were modelled which are expected in a high-turbulent flow. It is found that, depending on the amplitude of disturbance, the 2D instability waves or the generated 3D structures prevail at breakdown to turbulence. The transition process dominated by the localized disturbance with its secondary instability is similar to that observed before in the attached boundary layer. Also, the results correlate with numerical data on localized perturbations with different initial amplitudes, evolving in the adverse-pressure gradient flow.

Acknowledgements

The study was supported by the Russian Basic for Sciences Foundation (grant No. 99-01-00591) and INTAS (grant No. 96-2225).

References

1. Dovgal A.V., Kozlov V.V., Michalke A. Laminar boundary-layer separation: instability and associated phenomena // *Progr. Aerospace Sci.* – 1994. – Vol. 30. – P. 61-94.
2. Rist U. Zur Instabilität und Transition in laminaren Abloseblasen. Habilitationsschrift, Universität Stuttgart. Shaker Verlag, Aachen, 1999.
3. Boiko A.V., Grek G.R., Dovgal A.V., Kozlov V.V. Origin of turbulence in wall shear layers. Novosibirsk: Nauka, 1999 (in Russian).
4. Bakchinov A.A., Grek G.R., Katasonov M.M., Kozlov V.V. Experimental investigation of the interaction of longitudinal streaky structures with a high-frequency disturbance // *Fluid Dynamics.* – 1998. – Vol. 33, No. 5. – P. 667-675.
5. Dovgal A.V., Kozlov V.V., Sorokin A.M. Effect of a local stationary disturbance on the separated boundary-layer instability // *Mekhanika Zhidkosti i Gaza.* – 2000. – No. 1. – P. 174-178 (in Russian).
6. Bech K.H., Henningson D.S., Henkes R.A.W.M. Linear and nonlinear development of localized disturbances in zero and adverse pressure gradient boundary layers // *Phys. Fluids.* – 1998. – Vol. 10, No. 6. – P. 1405-1418.

SHAREABLE DATABASE OF AERODYNAMIC EXPERIMENTS AND COMPUTATIONS *

N.P. Adamov, M.D. Brodetsky, V.M. Gilyov, M.S. Ivanov, A.E. Medvedev, and
O.N. Mosseichuk

Institute of Theoretical and Applied Mechanics SB RAS, 630090 Novosibirsk, Russia

1. Introduction

At present, in various research centers of Russia and other countries, a great body of information is accumulated, both experimental, obtained on aerodynamic setups, and computational, obtained in the course of various numerical studies in the research field of aerodynamics. Very often, such data are stored in the form of protocols or files available only for data supplier. The latter makes using the accumulated data by other researchers extremely difficult. Only advanced data storage and exchange technologies can ensure more effective use of this wealth of data. In various institutions, development of special software facilities and databases for this purpose is under way. For example, in 80ths, in the Institute of Theoretical and Applied Mechanics a system SNAOD for collecting aerodynamic data was created, which enables also performing their easy analysis and processing [1]. This system ensured automated entry of data of various experimental aerodynamic studies into a BESM-6 computer and their processing. In early 90ths, in collaboration with S. A. Chaplygin SibNIA, a unified system for automated entry of experimental data into computer was developed [2]. This system offered the possibility to load into its database not only experimental results, but also additional data about the experimental conditions adopted, including description of experimental facilities employed in the experiment, characteristics of the model under study, various technological parameters, etc. All these made possible easy real-time adjustment to specific purposes of various data accumulating and processing software facilities.

To model aerodynamics of rarefied gases, an integrated packet RAMSES [3] was designed in the Institute, which contained a specialized database. Also, a database ExtFlow2 was created intended for studying external flows of viscous heat-conducting gas around bodies of finite dimensions [4]. A number of other programs were developed as well.

However, all the above databases had rather a narrow scope of application. They were intended for solving some specific problems. Another their feature was that they were oriented on individual work, without any access to them possible through the computer network. Hence, only work on the same computer that was used for loading data into the database was possible, and also under that operating system for which the program was initially intended. For this reason, multi-user access to this database and interaction of users with one another were greatly hindered.

In this connection, beginning from 1997–1998, the development of a new shareable general-purpose database was started in ITAM [5]. This database was intended for storing experimental data and computational results on a server working under the multi-user operating

* This work was supported by the Russian Foundation for Basic Research (grant No. 99-07-90217).

system Linux. Being intended for a work in the network variant, this database is available, through the computer network, simultaneously for many users 24 hours a day. A typical regime includes writing data by one user (for instance, an experimenter) and their reading, secondary processing and comparison with computational results by another researcher (for example, a theorist). Doing so, both users can work under either of the operation systems used in the Institute, Linux or Windows 95/98.

2. Structure of software and hardware facilities

Figure 1 shows the structure of software and hardware facilities offered by the system to its users.

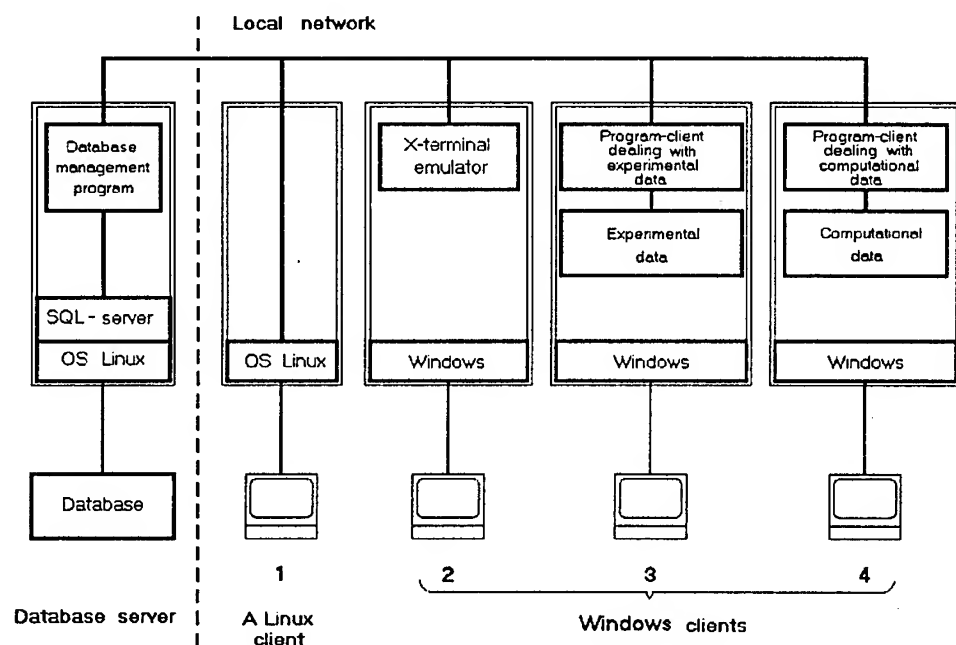


Fig. 1. Structure of software and hardware facilities of the system.

The system under consideration is based on the client-server technology. It consists of a database as it is and means of remote access to it. The core of the system is an SQL server. All users can work with the database using special programs. These programs offer users a friendly graphic interface and highly developed visualization means.

As the server, a personal computer working under the operating system Linux and an SQL server PostgreSQL are used, intended for work in a multi-user regime. This configuration has proved its high efficiency, reliability and acceptable speed of operation.

A client can work either under the operating system Linux or under Windows. Under Linux, the client is provided with an immediate connection with the database server through a local network (client 1).

The work under Windows can be exercised in the X-terminal regime, with all software facilities, provided by the server, being available to the user (client 2). Also, the work with special-purpose software products is possible (clients 3 and 4). These products ensure work both with experimental and computational results.

3. System architecture

In designing any database, it is extremely important to clearly realize the main principles to be laid to the database basis and the ideology of users' work. As mentioned above, the modern aerodynamic experiment is characterized by a wealth of data, which are closely interrelated with one another. When a rigidly specified data structure is used, the flexibility of the whole system worsens. On the other hand, flexibility is obviously a beneficial property of the system. It enables the researcher to collect various data and establish complex interrelations between them. However, experience shows that only those people can work with the database that loaded it, i.e., administrators. The loss of some links, as well as partial loss of data, being highly probable, the maintenance of the database is in fact a hard job that requires high labor cost. In a database with a fixed structure, these difficulties can be avoided, its functional scope being however strongly restricted from the very beginning, since it is often a difficult task to add data of new types into such a database. In many cases, this problem cannot be successively solved at all.

The solution of this problem consists in devising a special storage format for each individual data set. For instance, a series of runs performed on one wind tunnel yields one set of data, and a certain data structure is required for allocating these data. We call such a structure a data class. In fact, under this term we mean a certain format of database fields, tables, and functional relations. The data of each full-scale experiment are stored in a special data class intended for them. Computational studies in which conditions of full-scale experiments are modeled contain data of another type. These data include parameters that characterize the calculation procedure adopted, and, for their storage, another data class must be introduced. All classes are specified according to their own prescribed data format compatible with the ideology of the system, and they contain some compulsory reserved fields that ensure the integrity of data and their close integration into the whole system. It is quite reasonable that the descriptions of admissible classes, as a rule, are also stored in the database, in special tables.

The logic of work with the database is fixed. It is prescribed by admissible data formats. The whole work can be subdivided into parts executable at three levels. At the first level, the user deals with names introduced in the course of the experiment, with names of geometric models, data classes and catalogs. It should be noted that the database under consideration supports a system of catalogs of any level of nesting, created by the user rather arbitrarily. Choosing required data, the user proceeds to work at the next level.

At the second level, only data of primary significance, which are met most frequently, are available. Normally, these are initial data or integral characteristics of results chosen at the first level. These data can be viewed on the screen, edited, plotted in graphs, represented in a tabular form, and compared with available reference data. At the second level, the widest possible data sets are available for viewing and editing. Usually, these data sets are made up by values of vastly distributed physical quantities, flow-pattern elements, etc. The user interface at this level is similar to the one available at the second level, plus some extra-options.

Much attention in using the database is paid to visualization means. Apparently, data sets that include tens or, sometimes, even hundreds of thousands of individual elements are of little use when being represented in the form of tables. It is why representation in the form of tables, although possible, is normally used less frequently than the flexible instrumentation intended for graphic representation of information and 2D and 3D flow-field visualization means. The elaborated data-storage structure permits, alongside with storage of visualization results, storage of a description of the imaging methods employed. The visualization itself is ensured by external facilities. In developing the database, we tried to achieve the closest possible integrity of various visualization programs with the database. At present, packets Kagr and Kapić

developed in ITAM, SD RAS, have gained wide utility, with a provision made for using standard systems Gnuplot, Tecplot, and Vigie.

4. Some examples of using the system

Below, two examples are described of using the database under consideration.

4.1. Database of aerodynamic studies

Figure 2 shows the general appearance of a computer screen during the work of a user with physical characteristics spatially distributed over vast surface of an aerodynamic model. The upper left window is the main data window. It shows available data. Here, the user can mark those data that he would like to get in the tabulated form. The tabulated data are available in the left bottom window. Choosing an argument, parameters, and intervals in the right bottom window, the user can have all functions of interest plotted. In addition, another window can be brought up in which the 3D model under study can be depicted, with visualization of those points which have been used in plotting data.

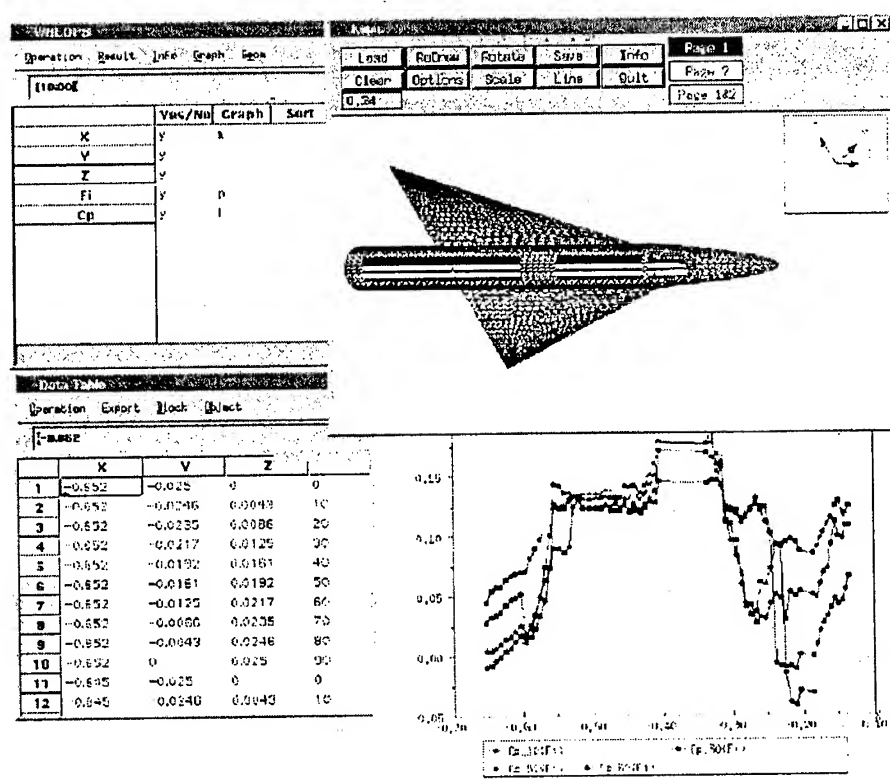


Fig. 2. Using the database for the work with aerodynamic characteristics.

The potentialities of the database can be also illustrated by the example of using it for verifying results of simulation of the interaction of two bodies of revolution moving at

supersonic velocities. These aerodynamic data were introduced into a special section of the database [6].

Figure 3 shows the diagram of isolines of pressure coefficients measured for one of bodies of revolution in the T-313 wind tunnel (Fig. 3b) in comparison with simulation data obtained by solving Euler equations at M.V. Keldysh Institute of Applied Mechanics (Fig. 3a). As is seen, database utilities permit easy comparison of results in any longitudinal or transverse cross sections, as well as comparison of integral values of parameters.

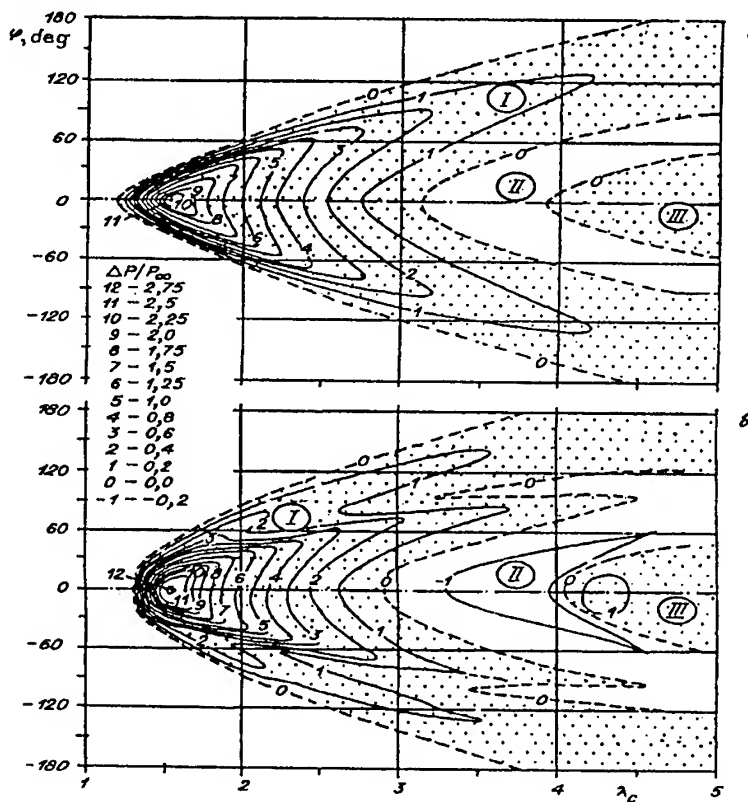


Fig. 3. Isolines of pressure coefficients (a – calculation, b – experiment).

4.2 Database of problems on high-speed interaction of projectiles with obstacles

Within the program on the development of the all-Institute general-purpose database, a section "High-speed interaction between bodies and properties of solid material" was created. This section was compiled on the basis of a local database EAAI (Engineering Analytical Approximation of Impact) and some reference and experimental data collected in the Institute.

Into the database, analytical formulas are included which permit calculation of penetration depths of projectiles for different parameters of the process. Also, various graphs, illustrations and a bibliographic list are available. Figure 4 presents, as an example of using the data, a crater depth vs impact velocity plot for projectiles made from various materials [7].

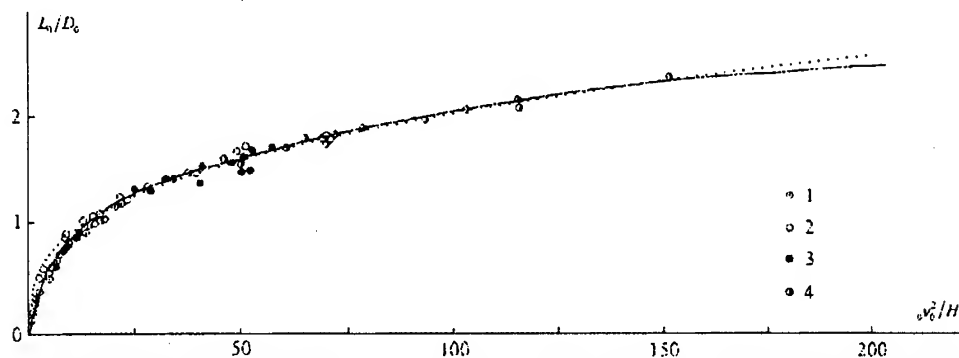


Fig. 4. Crater depth vs impact velocity plot for different projectile materials – experimental data (symbols) and analytical curve [7].

Conclusion

Thus, the developed database software and hardware facilities offer the researchers that work in the field of mechanics wide opportunities in conducting highly efficient studies. The users working in the network regime can load data into the database, search for required data, and scroll them. Also, data editing and visualization utilities are provided. The joint storage of experimental and computational data permits easy comparison between them, as well as their combined processing with the help of a variety of software products.

References

1. Vyshenkov Yu.I., Glinskii A.N., and Ivanov M.S. Software facilities used in ASNI ITAM: System for data accumulation, analysis and processing // Automation of Aerodynamic Studies. –Novosibirsk: ITAM, SD of the USSR Acad. Sci., 1985. – P. 13–22 [in Russian].
2. Vyshenkov Yu.I., Gilyov V.M., Myezhakova E.S., and Usoltsev E.G. Informational aspect of organization and quality control of mass aerophysical experiment // Intern. Conf. on the Methods of Aerophys. Research: Proc. Pt. 1. –Novosibirsk, 1994. – P. 204–208.
3. Zhukova G.A., Kashkovskii A.V., and Mosseichuk O.N. RAMSES: a system for modeling aerodynamics of rarefied gases for Earth satellites. –Novosibirsk, 1995. –32 p. –(Preprint / Acad. Sci. of the USSR, Sib. Div., ITAM; No. 4–95).
4. Lebedeva M.K., Medvedev A.E., Tamavsky G.A. ExtFlow2 database for informational support of numerical simulation of external aerodynamic problems // Optoelectronics, Instrumentation and Data Processing (Avtometriya) –1994. –No. 5. –P. 70–77.
5. Mosseichuk O.N. The development of a database of aerodynamic experiments and computations performed at ITAM // Intern. Conf. on the Methods of Aerophys. Research: Proc., Pt. III. –Novosibirsk, 1998. P. 193–199.
6. Zabrodin A.V., Lutsky A.E., Brodetsky M.D., and Derunov E.K. Comparison of numerical and experimental results of supersonic flow around a combination of two bodies of revolution // Thermophysics and Aeromechanics. –1995. –Vol. 2. – No. 2, –P. 89–94.
7. Medvedev A.E. and Shabalin I.I. Analytical representation of A.N. Zlatin modeling curve // Fiz. Mezomekh., –1999. – Vol. 2, –No. 5. –P. 105–107.

NUMERICAL AND PHYSICAL MODELING OF SUPERSONIC FLOW AROUND SEPARATING WINGED BODIES

N.P. Adamov, M.D. Brodetsky, A.M. Kharitonov,

A.V. Zabrodin, A.E. Lutsky

Institute of Theoretical and Applied Mechanics SB RAS, Novosibirsk

Keldysh Institute of Applied Mathematics RAS, Moscow

The process of separation of the stages of aerospace vehicles is accompanied by complex interactions of incident and reflected shock waves and expansion waves with each other and with boundary layers. Therefore, the development of methods for numerical simulation of such flows is impossible without careful verification and validation. Schematized winged models of the first and second stage were chosen for experimental investigation of the most probable concepts of TSTO systems [1]. In this formulation, the experimental results obtained ensure the best fitting to the requirements of testing the models and methods of numerical simulation of flows typical of the flow around flying vehicles with separation. A detailed study of distributed characteristics combined with visualization of interacting shock waves allows one to understand better the formation conditions of the interference components of aerodynamic forces and moments. Similar information obtained in a wide range of flow parameters and relative positions of the first-stage and second-stage models is used for verification of the Euler model and the method of numerical simulation of the characteristics of a two-stage system upon separation.

The first-stage and second-stage models are combinations of an axisymmetric conic-cylindrical body with a flat tapered wing that has sharp leading and trailing edges (Fig. 1). The sweep angle of the leading edge is $\chi=53^\circ$. The wing has a hexagonal profile with a constant thickness along the wing span corresponding to 4% of the airborne chord. The wing is mounted

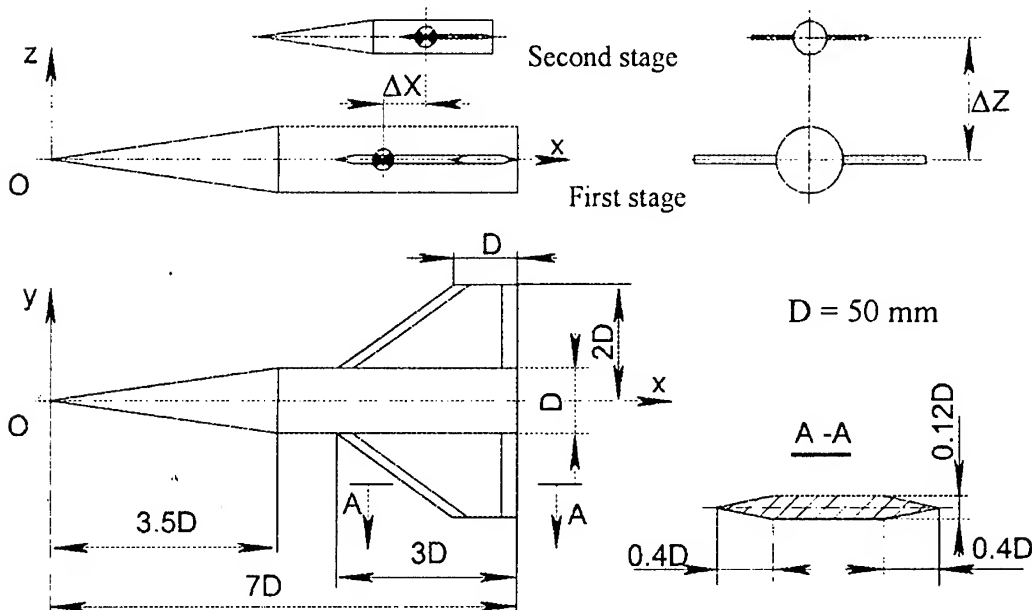


Fig. 1.

in the mid-wing monoplane position so that its trailing edge is located in the rear plane of the body.

The first-stage model allowed pressure measurements at 20 points of the generatrix of the cylindrical part of the body located in the vertical plane of symmetry on the side of the second stage.

The second-stage model is a half-scaled copy of the first-stage model and has 17 pressure taps on the surface, five of them being located on the conical nose. All pressure taps are located in the vertical plane of symmetry of the model on the side of the first stage.

By means of a tail sting with a shield, the first-stage model was mounted in an arc-shaped suspension of the standard mechanical balance whose α -mechanism ensured the range of the angle of attack $\alpha = -4 \div 22^\circ$. The second-stage model was mounted on a strut of a specially developed testbench [2], which ensured variation of the angle of attack of the second-stage model simultaneously with the first-stage model within the range $\alpha = 0 \div 10^\circ$. At the same time, the testbench allows simulation of the process of separation of the second-stage model from the first one within the following ranges of linear and angular parameters:

- discrete displacement of the second-stage model in the transverse direction $\Delta Z = D \div 3D$ ($50 \div 150$ mm);

- longitudinal displacement of the second-stage model relative to the first one $\Delta X = -0.5D \div 1.5D$ ($0 \div 100$ mm). The relative positions (the distances ΔZ and ΔX) of the first- and second-stage models were determined from conventional centers of mass located at the longitudinal axis at a distance of two diameters of the corresponding model from the end cross section.

The experiments were conducted in the supersonic wind tunnel T-313 based at ITAM SB RAS for Mach numbers $Ma_\infty = 3.01$, Reynolds numbers $Re_1 = 35 \cdot 10^6 \text{ m}^{-1}$; $\Delta Z = \infty$, D , and $1.5D$; $\Delta X = D/2$ for angles of attack within $\alpha = 0 \div 6^\circ$.

The aerodynamic forces and moments of the first-stage model were measured by the mechanical balance AB-313M of the wind tunnel, and these parameters for the second-stage model were measured by a strain-gage balance designed for the following limiting loads: longitudinal force $R_x = 15$ kg, normal force $R_y = 15$ kg, and pitching moment $M = \pm 0.5$ kg·m.

The pressure distributions on the models of both stages were measured by a multichannel meter MID-100 with the class of accuracy 0.3.

In the course of processing the results, the coefficients of the longitudinal force $C_A = -R_x/qS$, normal force $C_N = -R_y/qS$, and pitching moment $m_z = M/qSL$ were calculated for each stage in a fixed coordinate system whose origin coincides with the model tip of the corresponding stage (see Fig. 1). The mid-section area was used as the reference area S and the length of the corresponding stage was used as the reference length L . The pressure coefficients $C_{p_i} = (P_i - P_\infty)/q$ were determined from the tests with pressure measurements.

The results of metrological tests confirmed rather low values of random errors and good agreement of the characteristics.

The calculations were conducted by the pseudotransient method using a code for numerical simulation of the system of unsteady equations of gas dynamics, which depend on three spatial variables and time. The code of numerical integration of unsteady gas-dynamic equations was written in accordance with the principle of adaptability of the algorithm to particular features of the problem. This adaptation is ensured by a number of functional capabilities. The overall flow field is divided into computational domains, hexahedrons with curved boundaries. The positions of the boundaries can change in time taking into account the main discontinuities of the flow or the relative motion of the bodies. This multiblock

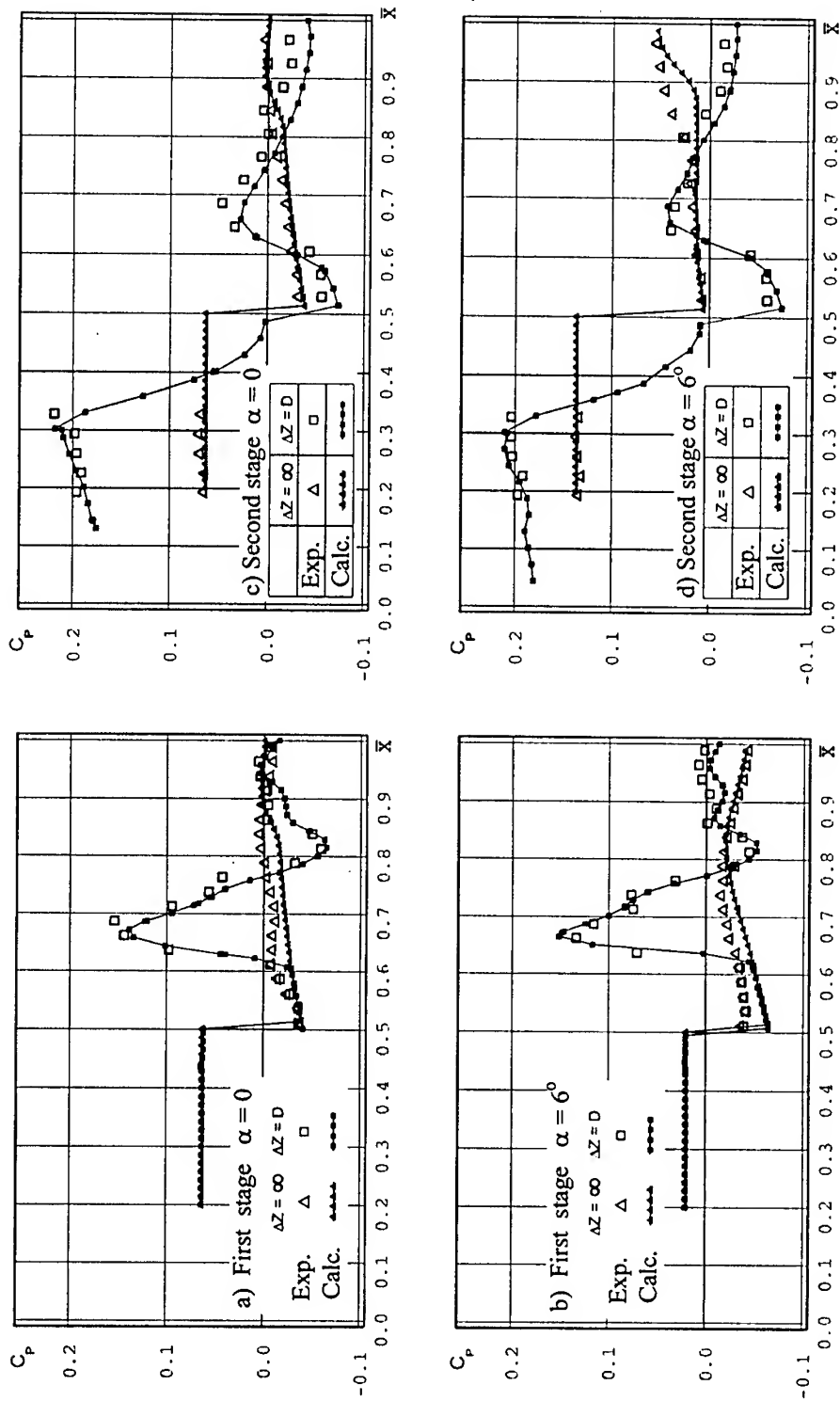


Fig. 2.

representation of the flow field facilitates the implementation of the algorithm on computers with parallel architecture. The difference scheme is constructed by discretization of unsteady gas-dynamic equations written in the integral form. The values of gas-dynamic quantities at the cell boundaries are determined by solving the Riemann problem. Thus, the difference scheme used is an extension of S.K. Godunov's scheme to a multi-dimensional case. The variant of the algorithm presented employs the classical version of the scheme with a piecewise-constant representation of the fields of gas-dynamic functions. The use of the model of three-dimensional unsteady gas-dynamic equations imposes rather high requirements to computer performance and memory. Thus, the results presented were obtained on a grid containing 367630 cells, and about 2000 time steps are needed to reach a steady flow. Therefore, the computations were conducted using a multiprocessor computer of the MVS family. The time needed to compute one variant is roughly 2 hours. The MVS-100 system is implemented at the Keldysh Institute of Applied Mathematics; it is a family of supercomputers of parallel architecture with a possibility of increasing the performance up to 100 billion operations with a floating point per second (100 GFLOPs).

As an illustration, Fig. 2 shows the experimental and calculated dependences $C_p(x)$ in the vertical plane of symmetry for the upper surface of the first stage for angles of attack $\alpha=0$ (Fig. 2a) and $\alpha=6^\circ$ (Fig. 2b) for $\Delta Z=\infty$ (i.e., in the absence of the second stage) and for $\Delta Z=D$. The same dependences are plotted for the lower surface of the second stage (Fig. 2c, d). Figure 3 shows the calculated gas-dynamic schemes of interference of the models for $\Delta Z=D$, $\alpha=0$ and $\alpha=6^\circ$, which were obtained without account of the wings. These results are in good agreement with the Schlieren pictures.

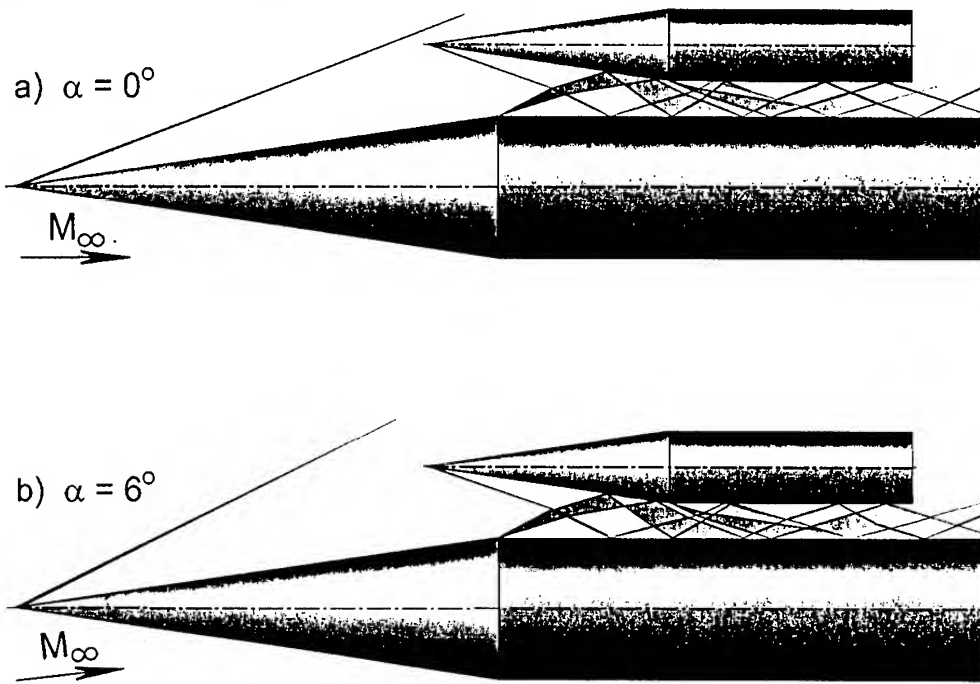


Fig. 3. $M = 3$, $\Delta Z = D$.

As follows from Fig. 2a, for $\Delta Z = \infty$ and $\alpha = 0$, noticeable disagreement with the numerical data is observed within the range $x \approx 0.6 \div 0.85$. Nevertheless, it is practically within the measurement error and is most likely caused by a small local non-uniformity of the velocity field in the rear part of the wind tunnel. At the rear part of the body ($x > 0.85$), where the calculation yields a moderate increase in pressure due to arrival of the shock wave (SW) from the leading edge of the wing to the upper part of the body, the calculated and experimental results almost coincide.

A discrepancy of the same order is observed for $\alpha = 6^\circ$, $\Delta Z = \infty$ (Fig. 2b) within the range $x \approx 0.5 \div 0.75$. The results are almost identical further downstream on the body where the pressure decreases due to arrival of the expansion fan (EF) from the upper surface of the wing.

A noticeable discrepancy between the experiments and computations on the lower surface of the second stage for $\Delta Z = \infty$ (Fig. 2c, d) is observed only for $\alpha = 6^\circ$ and $x > 0.8$, where the pressure increases due to arrival of the SW from the lower surface of the wing. The computation yields a more rear position of the beginning of pressure increase as compared to the experiment though the maximum values are identical.

For $\Delta Z = D$ and $\alpha = 0$, as follows from Fig. 3a, the effect of the second-stage model on the first-stage model is as follows. The conical bow shock wave (BSW) from the second stage falls onto the body of the first stage, which leads to a dramatic increase in pressure (Fig. 2a). Then, due to the EF from the first stage reflected on the second stage, the pressure on the body significantly decreases, which is additionally favored by the incident EF from the forebody/cylinder joining of the second stage. Then the pressure increases again due to arrival of the twice reflected BSW from the second stage, and an additional moderate increase in pressure is observed on the rear part of the body owing to the incidence of the SW from the leading edge of the second-stage wing.

As the angle of attack increases to $\alpha = 6^\circ$ (Figs. 2b and 3b), the qualitative pattern of interaction remains almost unchanged, and only due to the increase in intensity of the BSW from the second stage and the SW from its wing, the pressure diagram on the first stage moves slightly upwards, i.e., the positive phase of pressure increases and the negative one decreases. The integral relationship between these phases, both for $\alpha = 0$ and $\alpha = 6^\circ$, indicates the negative interference, i.e., a decrease in the lifting properties of the first stage. As follows from the graphs presented, the disagreement between the experimental and calculated results in both cases is within the measurement error, except for a small section $x \approx 0.85 \div 0.92$, where the calculated data lie slightly lower. This is apparently explained by the fact that the twice reflected BSW from the second stage and the SW from the leading edge of its wing arrive at the same place on the first-stage body in experiments, whereas in computations the point of incidence of the latter shock wave is shifted slightly to the rear part of the body. This shift was already observed on the second stage for $\alpha = 6^\circ$ and $\Delta Z = \infty$ (Fig. 2d).

The effect of the first stage on the lower surface of the second stage for $\Delta Z = D$ can be also considered in detail using Fig. 3. In this case, the forebody of the second stage is located behind the BSW of the first stage in the conical flow field, which generates something like an additional angle of attack in this region. As a result, the pressure on the forebody of the second stage increases significantly even for $\alpha = 0$ (Fig. 2c). Then, due to the effect of the EF from the first stage, the pressure on the lower surface of the second stage dramatically decreases, which is additionally favored by its own EF from the forebody/cylinder joining. After that, the body of the second stage is hit by its own BSW reflected from the first stage, which leads to the corresponding increase in pressure. Then, due to the effect of the twice reflected EF from the first stage, the reflected EF from the second stage, and also the EF from the first-stage wing, the pressure decreases monotonically toward the end of the body.

As the angle of attack increases to $\alpha=6^\circ$ (Fig. 2d), the interaction pattern between the model remains principally unchanged. However, since the strength of the BSW from the first stage on the upper surface of the cone decreases and, as a consequence, so do the angles of flow inclination in the conical flow field relative to the second stage, the interference pressure diagram is shifted slightly downwards, i.e., the positive phases of the excess pressure decrease and the negative phases increase. The integral relationship between these phases indicates a rather favorable interference (i.e., an increase in the lift force of the second stage) for $\alpha=0$ and its decrease with increasing angle of attack.

The numerical data, as confirmed by the graphs considered, are in good qualitative and quantitative agreement with the experiment in both cases. The same good agreement is observed for the total aerodynamic characteristics of the first stage. For the second stage, the agreement between the computations and experiments is slightly worse. The reason seems to be a lower density of the computational grid for the second stage because of its smaller dimensions. Thus, the present study for given parameters allowed us to study the formation of the interference loads of a schematized TSTO system during separation of the stages. It is shown that the inviscid Euler computations conducted within the examined range of parameters yield an identical qualitative pattern and a good quantitative pattern of interaction of the stages.

This work was supported by the Russian Foundation for Basic Research (Grant No. 98-01-00701).

References

1. Bonnefond T., Adamov N.P., Brodetsky M.D., Vassenev L.G., Derunov E.K., and Kharitonov A.M. Spatial supersonic flows upon separation of TSTO aerospace system // *J. Appl. Mech. Tech. Phys.*, 1997. No.1.
2. Adamov N.P., Bonnefond T., Brodetsky M.D., Vassenev L.G., Derunov E.K., and Kharitonov A.M. An experimental investigation of aerodynamic interference of TSTO winged systems during separation. 1. Experimental technique. Distributed aerodynamic characteristics // *Thermophysics and Aeromechanics*. 1996. Vol. 3, No. 3.

THE STUDY OF INFLUENCE OF AIRFOILS CONTOUR APPROXIMATION ON ITS RATING CHARACTERISTICS

S.M.Aulchenko, A.F.Latypov, and Yu.V.Nikulichev

Institute of Theoretical and Applied Mechanics SB RAS,
Novosibirsk, Russia

Comparisons of the results of numerical calculations of flow around airfoils with experimental data or with the results of other researches often omit the question about the method of airfoil contour approximation given as a rule in a tabular form. This may be the basis for incorrect interpretation of the results obtained, especially if the results differ widely from each other and the reason of that is often in different methods of contours approximation.

The problem of analytical description and numerical representation of various curvilinear boundaries, which is closely related to the representation of tabulated functions, often arises in applications. Depending on specific requirements, the reference points can either lie on the curve itself or belong to the characteristic frame that defines its form. The main problems associated with the existing methods are the tendency of polynomial representations to oscillate, a rather low degree of conjugation smoothness of piecewise polynomial representations, and the requirement for derivatives to be prescribed at the nodes in Hermitian interpolation. One shortcoming of the Fergusson - Bernstein - Besieux methods [1] is their weak correlation with the characteristic polygon for polynomials of high degrees which makes it impossible to ensure both the required degree of conjugation and sufficient proximity to the frame nodes when necessary.

To describe the boundary geometry the authors of the present paper established the methods of the parametric polynomial approximations with the different degree of smoothness (LL-approximation) which are free from oscillations on variation of the determining parameters. Theorems which assure the absence of inflections, monotonicity and accuracy estimations [2, 3] are proved.

The first variant of the approximation presented has a fixed degree of interpolating polynomials on intervals which are equal to four and a degree of smoothness equal to one. This polynomial has a following form:

$$P = (\xi - 1)^2 \Phi + \xi^2 \Psi, \quad (1)$$

where

$$\Phi = a_0 + a_1 \xi + 0.5 a_2 \xi^2, \quad \Psi = b_0 + b_1 (\xi - 1) + 0.5 b_2 (\xi - 1)^2, \quad \xi \in [0, 1]$$

While studying the problem of interpolation of the function on the interval $[0, 1]$ with given values of the function and its derivatives on the both ends of the interval and requiring of fulfillment of two additional conditions

$$\Phi(1) = f_1, \quad \Psi(0) = 0.$$

we obtain (1) in the following form:

$$P = \xi^2 [b_0 + \xi(\xi - 1)b_1]$$

where $b_0 = g_1$, $b_1 = G_1' - 2g_1$. This representation is valid in the local coordinate system chosen so that the boundary conditions have the form:

$$g(0) = G'(0) = 0, \quad g(1) = g_1, \quad G'(1) = G'_1.$$

The values of functions g and its derivatives G' are taken from the polygon constructed on the nodes of the table.

It is shown [1] that, with a proper choice of conjunctive nodes of interpolating polynomials (1), whose values at nodes are not equal to the corresponding points of the table, oscillation on interpolation intervals are absent.

The second variant of the approximation presented is more universal and it allows one to choose the degree of interpolating polynomials and to vary it from interval to interval. In addition, this approximation is infinitely smooth because of the requirement of all derivatives except the first one to be equal to zero at the nodes of conjunctions of the intervals.

This polynomial at the interval $[z_i, z_{i+1}]$ has the form:

$$\begin{aligned} P(\xi) &= (1 - \xi)^{L+1} F_0(\xi) + \xi^{L+1} F_1(\xi), \\ F_0(\xi) &= \sum_{k=0}^L a_k \xi^k, \quad F_1 = \sum_{k=0}^L b_k (1 - \xi)^k, \\ \xi &= \frac{x - z_i}{\Delta z}, \quad x \in [z_i, z_{i+1}], \quad \xi \in [0, 1] \end{aligned} \quad (2)$$

The conditions for determining the coefficients are:

$$\begin{aligned} P(0) &= g_i, \quad P^{(1)}(0) = G'_i \Delta z, \quad P^{(k)}(0) = 0, \\ P(1) &= g_{i+1}, \quad P^{(1)}(1) = G'_{i+1} \Delta z, \quad P^{(k)}(1) = 0, \quad P^{(k)} = \frac{d^k P}{d\xi^k}, \quad k = 2, 3, \dots, L \end{aligned}$$

where the values of the functions g_i, g_{i+1} and their derivatives G'_i, G'_{i+1} also taken from the linear carcass built on given abutment points (x_i, f_i) .

The formulas for determining the coefficients a_k, b_k are:

$$\begin{aligned} a_k &= C_{L+k}^L \left[f_{i+1} + G'_i \frac{k\Delta z - (L+k)\Delta x}{L+k} \right], \\ b_k &= C_{L+k}^L \left[f_{i+1} + G'_{i+1} \left(\frac{L\Delta z - (L+k)\Delta x}{L+k} \right) \right], \quad k = 0, 1, \dots, L, \quad C_i^j = \frac{i!}{j!(i-j)!}. \end{aligned} \quad (3)$$

For this approximation the following are proven

THEOREM 1:

For $\Delta z \in \left[\left(2 - \frac{1}{L+1} \right) \Delta x, \left(2 + \frac{1}{L} \right) \Delta x \right]$ polynomial (2) with coefficients (3) has no points of inflections on the interval $(0, 1)$.

THEOREM 2:

If $\Delta z = 2 \Delta x$ and $G'_i \cdot G'_{i+1} > 0$, then the function $P(\xi)$ is monotonous on $[0, 1]$.

THEOREM 3:

If $\Delta z = 2 \Delta x$, then polynomial (2) with coefficients (3) is such that

$$\lim_{L \rightarrow \infty} P(\xi(x_{i+1})) = f(x_{i+1}).$$

For the first variant of approximation of an airfoil given by the table of points it is necessary to determine the coordinates of the abutment points of the carcass from the condition of deviation values of the curve built on the carcass from the points of the table with a required accuracy. A number of nodes of the carcass and, respectively, a number of variables to be determined by means of solving the problem of minimizing a function of several variables – the problem to which our problem reduces – a much less than the number of tabular points. In the realized variant, it is, respectively, 7 and 36 with a given accuracy of 10^{-4} .

The second variant gives an opportunity directly to build the curve which passes through given points with a prescribed accuracy ε , including $\varepsilon = 0$, by means of a single-valued chose of the corresponding dummy nodes of the carcass. Here the number of the carcass nodes has to be equal to the number of the function values given by the table. It is clear that in this case the variation approach to determining of abutment points can be realized. We realized the direct method with $\varepsilon = 0$.

Further, in the framework of the given paper, by means of the boundary element method [4], a subsonic flow around an airfoil given by the table [5] by an ideal gas with free stream Max number $M_\infty = 0.1$ was calculated. Attack angle was $\alpha = 0^\circ$. The number of boundary elements, their distribution around the contour and other parameters of the algorithm are identical at all presented results. It is necessary to note that the number of boundary elements to which the contour of an airfoil is divided for solving the problem of the flow is not equal to the number of abutment points and is not equal to a number of the table nodes and their distribution on the contour is determined from a certain optimal criterion. Besides that the particular feature of the boundary element methods is a tendency to worsening of the matrix conditioning, as the matrix dimensionality increases. The coefficients of the influent matrix are completely determined by the contour geometry and are rather sensitive to the behavior of its derivatives, which allows one to reject unsuitable variants of approximation.

For comparative analysis of the influence of different methods of boundary geometry representation, four variant of approximation were used:

1. Parametric approximation of the first - order smoothness with the degree of polynomials on intervals $S=4$.
2. LL -approximation of the second order ($L=2$), with the degree of polynomials on intervals $S=5$ with an infinite order of smoothness.
3. Cubic spline.
4. LL -approximation of the first order ($L=1$), with the degree of polynomials on intervals $S=3$ with an infinite order of smoothness.

The geometry of the contour and the pressure coefficient distributions are presented in Figs. 1, 2, 5, 6, correspondingly to approximation variants. In Figs. 3, 4, 7, 8 the first and the second derivatives of the functions describing upper contour on the chord interval $[0.6, 1]$ correspondingly to approximation variants are presented. Note that the results of computations presented in Fig. 1 are close to the results in Fig. 2 and also, the results presented in Fig. 5 are close to the results presented in Fig. 6; nevertheless, both groups differ greatly from each other. As far as comparisons with the experimental data from [5] are concerned, we can say that the results for the lift coefficient C_Y lie in the interval 10 %, but variants 1, 2 are better than variants 3, 4. The moment coefficient M_Z for variants 5, 6 differs significantly from

experimental data and from variants 1, 2. This difference can be explained by the behavior of the first and second derivatives presented in Figs 7, 8 and 3, 4. Oscillations in the pressure coefficient distributions are generated by oscillations of the second derivative of the contour in spite of smoothness of the contour itself on intervals and even closeness to linear. These oscillations depend on the amplitudes of second derivatives of the contour. We can not prefer the first variant of approximation because of the existence of discontinuities in the contour curvature, which can lead to appearance of singularities in the boundary value problem. Thus the preferred variant is *LL*-approximation with a high degree of polynomials on intervals with a small amount of intervals, which significantly decreases the amplitude of oscillations of the derivatives at the nodes of conjunctions (for *LL*-approximation, the second derivative on interval retains its sign [3]). The number of intervals at the second variant was chosen equal to the number of the contour coordinates given by the table, which is redundant in terms of accuracy of approximation.

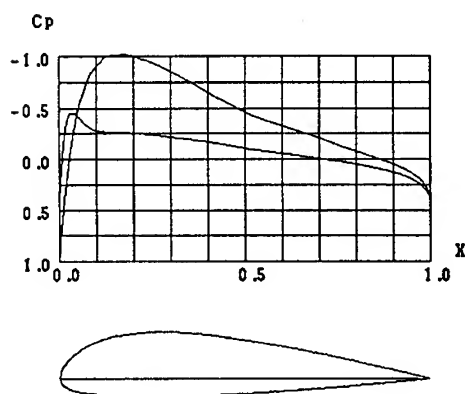


Fig. 1.

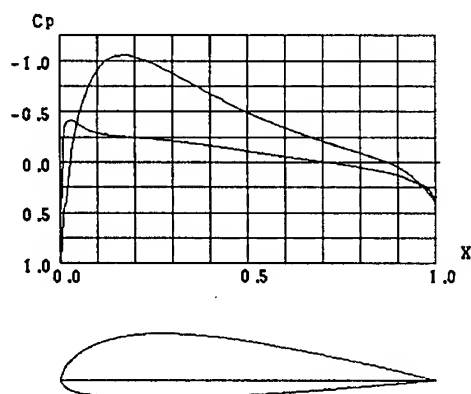


Fig. 2.

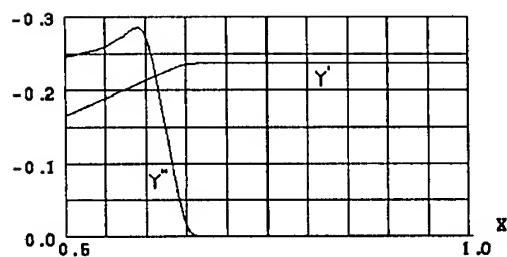


Fig. 3.

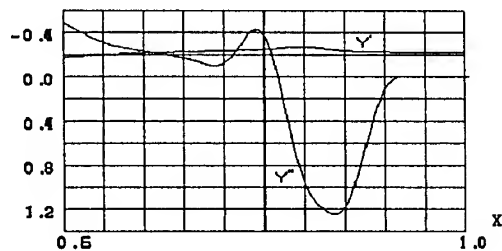


Fig. 4.

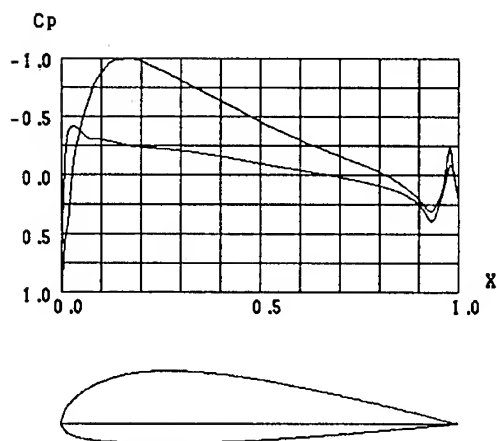


Fig. 5.

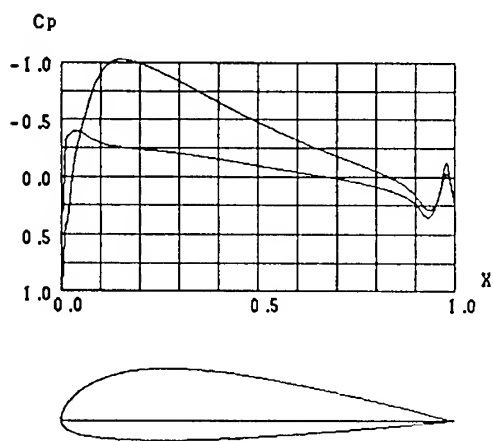


Fig. 6.

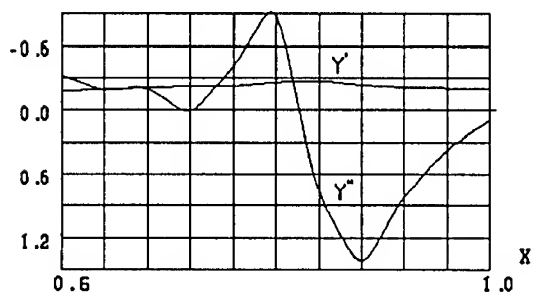


Fig. 7.

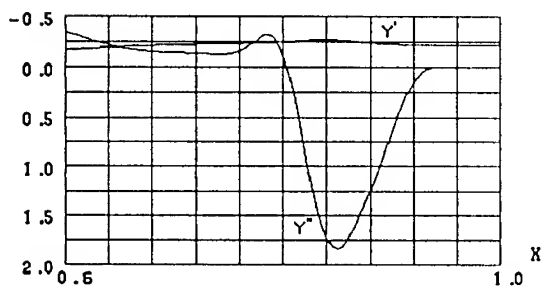


Fig. 8.

REFERENCES

1. Faux I., and Pratt M., Computational geometry for design and manufacture. Chichester : Ellis Horwood, 1979. Translated under the title "Vychislitel'naya geometriya, Moscow: Mir, 1982.
2. Aul'chenko S.M. and Latypov A.F., Construction of Planar Curves by Means of Parametric Polynomials of the Fourth Degree// Zh. Vychisl. Mat. Mat. Fiz. 1995, Vol. 35, No. 7. P. 1139-1142.
3. Aul'chenko S.M. and Latypov A.F., Nikulichev Yu.V. Construction of Curves by Means of Parametric Polynomials// Zh. Vychisl. Mat. Mat. Fiz. 1998, Vol. 38, No. 12. P. 1888-1893.
4. Aul'chenko S.M. and Latypov A.F. Subsonic Airfoils Design Using Numerical Optimization Techniques// Mehanika Jidkosti i Gaza 1997, Vol. 32, No. 2. P. 296-302.
5. Kashafutdinov S.T. and Moiseyeva R.V. Atlas of aerodynamic characteristic of airfoils. Moscow: Mashinosroenie, 1966.

EFFECT OF FUEL TYPE ON THE THRUST CHARACTERISTICS OF RAMJET ENGINES

V.K. Baev and V.V. Shumskii

Institute of Applied and Theoretical Mechanics SB RAS
630090, Novosibirsk, Russia

Gaseous, fluid and solid fuels can be used in hypersonic air-jet engines depending on their use. However in experimental investigations, gaseous hydrogen is preferred to be used even for those ramjets which should use liquid fuels under full-scale conditions. High hydrogen reactivity allows one to make heat inflow to a working body easier and study the cycle characteristics using a convenient model fuel.

There is a problem if the results of the working process and thrust-economic characteristics of hypersonic gaseous hydrogen ramjets obtained can be used for the analysis of the liquid fuel engine duct.

A comparison of the main mechanisms of the working process and the thrust-economic characteristics obtained in the study of small dimensional ramjet models in gas and liquid fuel tests was performed. The experiments were performed in high-enthalpy short-duration facilities using smallscale models consisting of an air intake, a combustion chamber, and a nozzle with the air jet coming into the air intake; the air jet diameter was 23 – 73.5 mm. Hydrogen with the equivalence ratio $\alpha = 1.7 - 0.2$ was used as a gas fuel and a boron-organic composition [1] with $\alpha \sim 1$ as a liquid fuel. Full-scale drag parameters for the flight Mach number $M_{\infty} = 5$ and the altitudes $H = 0 - 25$ km were reproduced.

A detailed description of the models and tests conditions are in [2-4]. The results of the analysis performed are presented below.

Combustion completeness efficiency. The combustion efficiency was determined by the results of the weights measurements and gas-dynamic method.

The hydrogen combustion efficiency determined by the weight and gas-dynamic methods was 0.9 – 0.95 for the whole static temperature range of 320 – 180 K of the air coming onto the model. These experiments were performed at constant parameters of the incoming air as well as in the pulsed regime, i.e. when the air parameters drop during the regime time.

The experiments with injection of a liquid boron-organic fuel in the front belt (at constant parameters of the air coming onto the model during a regime) performed on the model whose outer diameter was $d_m = 30$ mm showed that the liquid fuel combustion efficiency determined by the weight measurements was 0.85 – 0.95. High liquid fuel combustion efficiency values ξ were for the whole examined range of the combustion chamber expansion degrees $F_{ch} = 2.85 - 1.96$ and the incoming flow static temperature $t_{in} = \pm 50^\circ\text{C}$.

The equally high combustion efficiency in gas hydrogen and liquid fuel tests for the models $d_m = 30$ mm and the large-dimension model $d_m = 84$ mm was the consequence of:

1. Reproducing in the facility of the full-scale parameters of the coming onto the model air for the flight conditions with $M_{\infty} = 5$ at low altitudes which provided self-ignition and high velocities of the considered fuel combustion at small combustion chamber lengths 130 – 180 mm.
2. The efficiency of fuel mixing with air realized in the models.

Transition regime duration. Three regimes are possible in the two-regime combustion chamber due to the working body relative heat $\theta = T_{05} / T_{0in}$; T_{05} , T_{0in} are the stagnation temperatures of the combustion products at the chamber outlet and the air incoming onto the model.

1. $\theta < \theta_{switch}$ – heat inflow is performed to a supersonic flow on the average. θ_{switch} is a working body relative heat at which the heat inflow regime changes: from the heat inflow to a supersonic flow to the heat inflow to a subsonic flow.

2. $\theta_{switch} < \theta \leq \theta_{max}$ – heat inflow is realized to a subsonic flow on the average. θ_{max} is the working body maximum relative heat possible in the given combustion chamber geometry without break-down of the incoming flow into the model.

3. $\theta > \theta_{max}$ – the break-down of the incoming flow into the model. The normal air incoming into the model can not be provided at the given regime.

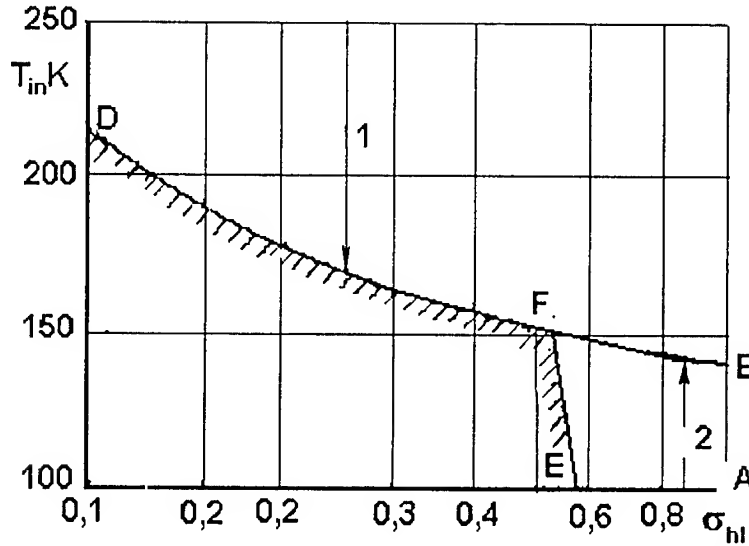


Fig. 1. Static temperature of the incoming flow at which the flow in the combustion chamber changeover. 1 – heat inflow to a supersonic stream in the combustion chamber; 2 – heat inflow to a subsonic stream in the combustion chamber; $M = 4.52$; $F_{ch} = 1.884$.

The static temperature T_{in} of the air coming onto the model at which the flow in the combustion chamber (CC) is transformed depending on the hydraulic losses in the CC (in the model duct section from the air intake throat, the subscript 2 to the chamber outlet, subscript 5) is given in Fig. 1; σ_{hl} is the total pressure recovery coefficient owing to hydraulic losses in the CC (local losses and friction losses). The point B is the temperature of switching T_{switch} at $\sigma_{hl} = 1$; at T_{in} which are below the point B, the heat will be supplied to a subsonic flow, at T_{in} which are above the point B, the heat will be supplied to a supersonic flow. If $\sigma_{hl} < 1$ and is to the right of the DE line the heat in the CC will be supplied to a subsonic flow when T_{in} is lower than the line BE and to a supersonic flow when T_{in} is above the line BE. The line BE at $\sigma_{hl} < 1$ and the point B at $\sigma_{hl} = 1$ correspond to the switching temperature at which the heat inflow regimes in the CC change.

If σ_{il} values are to the left of the line DE and below GE, heat inflow in the CC to a subsonic flow is impossible, which follows from the flow rate equation for cross-sections 2a and 5 where 2a cross-section is behind the normal shock wave located in the air intake throat.

The curvature of the lines $C_R = f(T_{in})$ is observed in the thrust coefficient experimental dependences C_R on $f(T_{in})$. The reason is that some time is necessary to change over the flow: during the regime time the working body flow in the CC has to change from the supersonic one set during the first 2 ms of the facility operation when there was no fuel supply to a subsonic one. The experiments showed that the time for this transition determined by the thrust measurements is 20-28 ms. The time of the transition process determined by the pressure measurements in the CC is 20-25 ms and agrees well with the time of the transition process determined by the force measurements.

A thermodynamic analysis of the change of the heat inflow regime was performed irrespective of the fuel type: the working body relative heating in the model duct was the main argument. The experiments with the models confirmed this fact: the duration of the transition regime from the supersonic heat inflow process set in the first milliseconds of the facility operation to the subsonic one is the same for the hydrogen fuel model as well as the liquid fuel model.

Break-down of the air inflow into the model. In model testing in the pulsed regime, a the break-down of the air inflow into the model took place. The complex $\beta \sqrt{T_{05} / T_{0in}}$ was constant at the moment of the inflow break-down for all experiments with different fuels, β is the growth of the working body mass due to the fuel supply. Immediately before the break-down of the air inflow into the model the value of $\beta \sqrt{T_{05} / T_{0in}}$ was considerably smaller than a possible limit at the thermal choking for the tested CC configurations. The reason for the break-down was the fact that the zone in which the flow transits from a supersonic to a subsonic one due to heat inflow was too close to the cross-section 2. When the CC initial section length was increased, the break-down of the inflow into the region of significant heating of the working body was "delayed".

The relative heat remained constant during the regime in the experiments with the constant parameters of the air incoming into the model during the regime time during the regime time. That is why if the relation of the chamber initial section length F_{ch} and the relative heating was such that the onset of the pseudo-shock wave came out into the surfaces of external compression of the air intake, the break-down of the inflow into the model took place at the regime onset.

Thus, in the hydrogen model and liquid fuel model tests, one and the same mechanism of break-down of the air inflow into the model took place. The measures to eliminate the inflow break-down were also identical. They were connected with the increase of the number of gauges of the initial CC section length.

The effect of the combustion chamber on the air intake operation. The effect of the CC on the air intake operation is understood as follow. If disturbances of the chamber caused by the pressure growth in it are transmitted upstream behind cross-section 2 to the compression surface, the CC influences the air intake as disturbance transmission to the compression surface leads, as a rule, to the break-down of the inflow into the air intake. If the chamber disturbances are not transmitted through cross-section 2 to the compression surfaces, the CC work does not effect the air intake operation.

The flow transition in the duct from supersonic to subsonic at $M > 2$ occurs in a pseudo-shock wave. The pseudo-shock wave has some length and can be located in this or that place of the combustion chamber depending on the relative heating of the working medium in

the model duct. The pressure growth typical of the pseudo-shock wave is shown by the curves of pressure distribution along the chamber.

Comparison of the filming at the initial zone with the pressure measured along the initial zone shows that the pressure growth is not caused by the combustion in the initial zone. When there is a step, the flame is not spread forward to the initial zone but is located beginning from the step or the place where injectors are placed. That is why the pressure growth in the initial zone is caused by the transition of the supersonic flow into the subsonic one through a pseudo-shock wave.

Gas-dynamics of the flow in the duct depends only on the total heat supply and temperature distribution along the chamber length. The relative heat supply is determined by the heat effect of the fuel H_u and combustion efficiency, i.e. the heat input to 1 kg of air which passes through the model. Fuels used had approximately the same value of $H_u / (1 + \alpha L_0)$, i.e. the same heat input to 1 kg of air; L_0 is stoichiometric coefficient. Since, as it was shown above, the parameters of the air incoming onto the model provided the effective combustion of gaseous hydrogen and liquid fuel, the combustion chamber did not affect the operation of the air intake depending on the type of the fuel, the effect was the same in the hydrogen and liquid fuel test.

An analysis of data on pressure and force characteristics, cinegrams and a numerical model makes it possible to explain the effect of the combustion chamber on the air intake operation which in many cases leads to break-down of the inflow into the model upon fuel combustion with increasing heating of the working medium. This effect is connected with the location of the pseudo-shock wave in the initial section of the combustion chamber [3 - 5].

Thrust-economic characteristics. The calculated values of C_R for various fuels used in the models in the tests are presented in Fig. 2. It is seen that $C_R = f(T_{in})$ are close for H_2 and liquid boro-organic fuels.

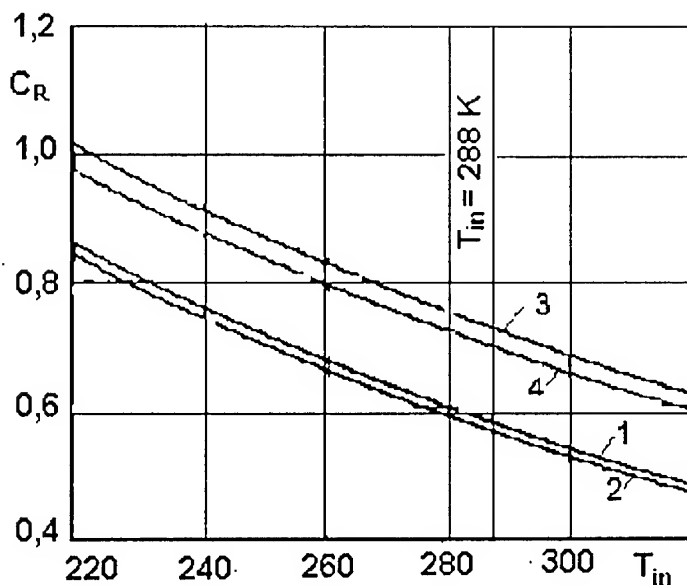


Fig. 2. Thrust coefficient depending on the static temperature of the incoming air for various fuels.

1, 2 - $F_{ch} = 2.85$; 3, 4 - 1.96; 1, 3 - liquid fuel; 2, 4 - H_2 .

A comparison of the experimental data on these fuels shows the same. Thrust-economic characteristics shortage for both fuels in comparison to their values at $F_{ch, min}$ is $\sim 30\%$, see Fig. 3. Figure 3 shows for $T_{in} = 288\text{ K}$ (basic temperature in relation to which the results of ground-based tests are given) a decrease in the main characteristics of the model at F_{ch} increase from $F_{ch, min}$: for $T_{in} = 220\text{ K}$, $\sigma_{bl} = 0.9$, $\xi = 0.8$ value $F_{ch, min} = 1.538$ for H_2 and $F_{ch, min} = 1.55$ for a liquid boro-organic fuel.

Here the y-coordinate is A/A^0 , where A is any of the thrust characteristics: thrust coefficient, specific thrust, specific impulse, frontal thrust; A^0 is the value of the corresponding characteristic at $F_{ch, min}$.

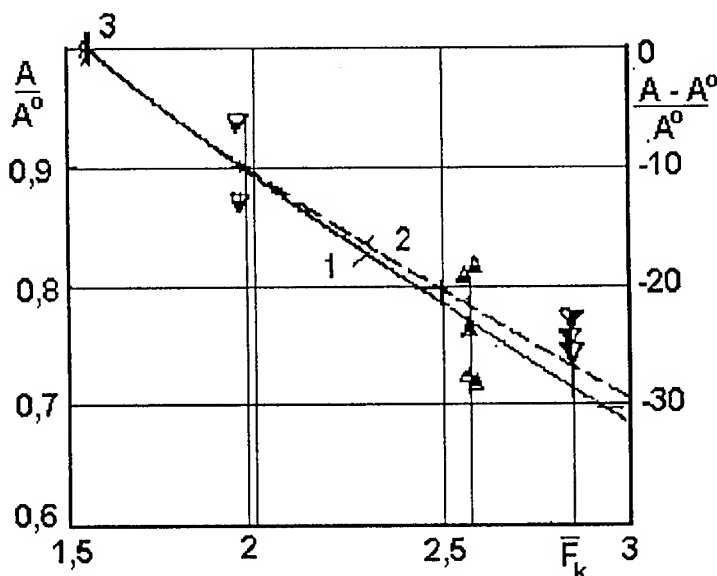


Fig. 3. Dependence of the thrust-economic characteristics on the degree of the combustion chamber expansion at $T_{in} = 288\text{ K}$. 1, 2 - calculation; 3 - $F_{ch} = 1.55$ (minimum expansion of the combustion chamber for liquid fuel at $T_{in} = 220\text{ K}$, $\sigma_{bl} = 0.9$, $\xi = 0.8$); 1, symbols - liquid fuel; 2 - H_2 .

The calculated and experimental data in Fig. 3 show that after the decrease in F_{ch} from 2.85 to 1.96 the value of A are by 7 - 9 % smaller than the respective $F_{ch} = F_{k, min}$. The degree of CC expansion $F_{ch} = 1.96$ was minimum for fuel supply in the first belt for the model with $d_m = 30\text{ mm}$. At $F_{ch} < 1.96$, special measures were needed to avoid the break-down of the air inflow into the model.

The experiments conducted showed that at the combustion chamber regime of heat inflow into a subsonic flow it is possible to decrease F_{ch} to a minimum value determined by the gas-dynamics of the flow. The thrust-economic characteristics which are the highest possible for both fuels: specific impulse $\sim 25\text{ km/s}$ for hydrogen, $\sim 9\text{ km/s}$ for a liquid boro-organic fuel were obtained. The specific thrust was the same for both fuels $\sim 700\text{ m/s}$.

Conclusions. Thus, the analysis of the working process shows that at reproduction in the setup of parameters of the air incoming onto the model for flight at low altitudes at the Mach number 5 the main characteristics of the working process of the models using gaseous

hydrogen and a liquid boro-organic fuel are identical. This conclusion is grounded by the coincidence of the main characteristics of the working process for all mentioned types of fuels.

The investigations conducted show that under the given conditions the results of the working process and thrust-economic characteristics obtained in the hydrogen tests can be used in developing engines of hypersonic ramjets using liquid boro-organic fuels.

REFERENCES

1. Michajlov B.M. *Chemistry of hydroborous*. Moscow: Nauka 1967. 520 p.
2. Baev V.K., Shumskii V.V., Yaroslavtsev M.I. Pressure distribution and heat exchange in gasdynamic model with combustion, over which a high-enthalpy air stream flows // *J. Appl. Mech. Thech. Phys.*, 1985. No. 5. P. 56 – 65.
3. Baev V.K., Shumskii V.V., Yaroslavtsev M.I. Some methodological aspects of the study of gasdynamic models with heat and mass inflow in a pulsed wind tunnel // *Combustion, Explosion and Shock Waves*, 1987. Vol. 23, No. 5. P. 548-557.
4. Baev V.K., Shumskii V.V. Effect of model dimensions on the thrust characteristics of ramjet engines in tests in a short-duration facility // *Ibid.*, 1999. Vol. 35, No. 1. P. 1 – 7.
5. Tretyakov P.K. Determination of heat inflow in a duct with a pseudo-shock wave // *Ibid.* 1993. Vol. 29, No. 3. P. 71 – 77.

A METHOD FOR CALCULATION OF HYDRAULIC AND THERMAL CHARACTERISTICS OF THE DISK ROTOR MACHINES WITH TANGENTIAL INPUT AND OUTPUT OF THE WORKING BODY

V.K. Baev, G.V. Klimchik, A.D. Frolov, and D.V. Chusov
Institute of Theoretical and Applied Mechanics SB RAS,
630090, Novosibirsk, Russia

INTRODUCTION

The idea of using the disk rotors for simultaneous transport of the working body and its cooling (heating) was born for the first time at the Institute of Theoretical and Applied Mechanics about 20 years ago. It was realised for the first time in the design of the electric discharge CO₂ laser with a closed contour [1].

During the subsequent years, the main attention was paid to the development of low-noise disk fans that combined in a number of cases the functions of the separation of solid and liquid particles as well as the heat transfer via the rotating shaft for the purpose of the water condensation from air [2,3,4].

In recent years, the scientific research was conducted that was directed towards the development of computational techniques applicable for their use in the design works in connection with the development of the ideas on a rational use of the multiple purpose disk rotor machines in various branches of technology and know-how's. It turned out that the external surfaces protecting the rotor, which give rise to the main hydraulic losses in the machine, may be used effectively for the heat exchange [5,6].

An elevated friction and heat exchange intensity on the cowl revealed experimentally was served a basis for obtaining a patent for the technique of the heat transfer intensification [7]. One of the practical realisations of this technique was patented in [8].

Another practical realisation was carried out at the fabrication of a sample of an autonomous source for power supply to order of the Krasnoyarsk State Foundation «The Conversion Technopark». The design of the external protection (the cowl) with internal ribbing for an additional significant heat transfer intensification was applied for the first time in this development. This has enabled one to use the relatively low-temperature modules for the thermal generation of electric current.

The experience accumulated during the recent years enables us to suppose that the disk rotor machines may become the basis for a new direction in the power-plant engineering. In this connection, the problem of the development of the methods for their calculation applicable for a wide use in the practice of the design works and certainly in the research works of applied character becomes topical.

It is obvious that the calculation technique proposed in the present paper should be improved and augmented as the experimental material and the experience of the manufacturing an operation of the samples of new machines are accumulated. This is especially true for some recommendations based on purely experimental results.

CALCULATION METHOD

The method presented below for the computation of the basic integral characteristics of the disk rotor machines may be applied for any working bodies in the domain of the parameters, where the gas (fluid) may be assumed to be incompressible.

In connection with the fact that the use of such machines as fans is the most typical case, the terminology refers in our technique right to this variant. The basic calculation relations are presented in [5]. More general relations taking into account the working body compressibility have also been obtained. But the experimental research to elucidate the compressibility effect was not carried out, therefore, the more general dependencies are not used here. The method refers to the fan diagram shown in Fig. 1. This Figure also indicates the reference cross-sections and the notation of geometric parameters.

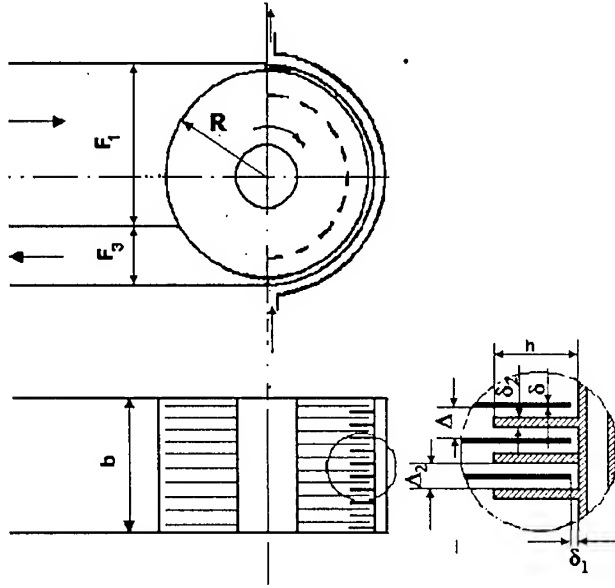


Fig.1.

The following dependencies for the pressure head and flow rate are used in calculation:

$$\Delta \bar{p} = \frac{\Delta p}{\Delta p_0} = \frac{1}{2\phi} \frac{1 + \frac{\phi}{2}}{1 + \frac{\xi}{1 + \phi}} \frac{\phi_1^2}{(1 + k)^2}; \quad \bar{G} = \frac{G}{G_0} = \frac{\phi}{\sqrt{1 + \frac{\phi}{2}}} \sqrt{\Delta \bar{p}}.$$

Here $\Delta p_0 = \rho u_d^2 / 2 = \rho (2\pi R n)^2 / 2$; $\phi = F_3 / F_1$; $G = \rho u_3 F_3$ is the flow rate, F_3 is the outlet cross-section area, u_3 is the mean velocity in outlet cross-section; $F_1 = 2Rb / (1 + \phi)$ is the inlet cross-section area; $G_0 = \rho u_d F_1 = \rho (2\pi R n) 2Rb / (1 + \phi)$, $u_d = 2\pi R n$ is the maximum velocity of the disk surface; b is the fan length along its axis; n is the number of the disk revolutions, ρ is the air density, R is the disk radius.

The fan aerodynamic efficiency η_1 is determined by the internal drag ξ and the non-dimensional geometric parameter ϕ :

$$\eta_1 = \left(1 + \frac{\xi}{1 + \phi} \right)^{-3/2}.$$

Here $\xi = \xi_{il} + \xi_c$; ξ_{il} are the inner losses; ξ_c are the additional losses of the fan duct;

$$\xi_{il} = \left\{ 1,5(1-\phi_1) + 1,5(1-\phi_2) + \frac{3,34\bar{\Delta}}{k^2} \frac{\lambda_c}{\lambda} \frac{1}{1-6,67\delta_1} \left[\frac{1-\phi_1}{\phi_1} (1+k)^2 + \frac{F_r}{F} \right] \right\} \frac{\phi_1^2}{2\phi};$$

$$\frac{F_r}{F} - 1 = \frac{\bar{h}}{(1+\delta_1)(b/N)} \left\{ 2 \left[2(1+\delta_1) - \bar{h} \right] - \delta_2 \frac{\delta}{R} \right\};$$

F is the smooth cowl area; F_r is the area of the ribbed cowl surface; h is the rib height, $\bar{h} = h/R$, δ is the disk thickness, δ_1 is the size of the gap between the disks and cowl, δ_2 is rib thickness, $\bar{\delta}_2 = \delta_2/\delta$; $\bar{\Delta} = \Delta/R$; $\phi_1 = \Delta/(\Delta + \delta)$; $\phi_2 = (R + \delta_1)\Delta_2 / ((R + \delta_1)\Delta_2 + h\delta_2)$, λ is the friction coefficient of air and disks; λ_c is the friction coefficient of air and cowl, Ω is the part of disks covered by housing; $k = \sqrt{2\bar{\Delta}/(\lambda\Omega)}$.

At the calculation of power $W = G\Delta p/(\rho\eta_1)$, the fan aerodynamic efficiency η_1 is taken into account. Another technique to calculate the power is based on the friction moment M_r of the rotating disks

$$W = M_r(2\pi n), \quad (1)$$

where $M_r = C_M(\rho(2\pi n)^2 R^5/2)N$. Here N is the number of disks. The friction coefficient C_M enters the expression for the moment. Its relation to the local friction follows from the obvious relation (the friction on two sides):

$$M_r = 2NC_f \int_0^R 2\pi r \frac{\rho(2\pi n)^2}{2} r^2 dr = \frac{4\pi}{5} C_f \frac{\rho(2\pi n)^2}{2} R^5 N.$$

Here C_f is the local friction coefficient of disk. Then $C_M = (4\pi/5)C_f$. According to the Reynolds analogy between friction and heat exchange, $C_f = 2St$. The expression

$$St = 0.0311 Re^{-0.2}, \quad (2)$$

corresponds to experiment at large Re numbers, where $Re = \rho u_d R / \mu$, $\rho u_d R / \mu$, μ is the air viscosity. Hence, $C_M = 0.156 Re^{-0.2}$. This expression agrees satisfactorily with the expression obtained by T. Karman numerically for the freely rotating disks $C_M = 0.146 Re^{-0.2}$. Thus, the moment $M_r = 0.156 Re^{-0.2} (\rho(2\pi n)^2 R^5/2)N$. The power is expressed by formula

$$W = 0.156 Re^{-0.2} \frac{\rho(2\pi n)^3 R^5}{2} N$$

respectively.

It is to be expected that the computation by (1) will yield the maximum power values, since the drag coefficient reduces in the presence of protective surfaces. For the prediction of the electric drive power it is necessary to take into account the electric η_e and the mechanical η_m efficiencies, that is $W_e = W/(\eta_e \eta_m)$.

The fan dynamic characteristics depend on the drive torque M_t , the rotor inertia moment I , and the resistance moment M_r resulting from the disk friction with respect to air:

$$\frac{dn}{d\tau} = \frac{M_t}{2\pi l} - \frac{M_r}{2\pi l}.$$

At M_t , which does not depend on n , the time τ for the acceleration up to the number of revolution n will be

$$\tau = \frac{1}{2} \frac{2\pi l}{\sqrt{M_t A_M}} \ln \left(\left(1 + \sqrt{\frac{A_M}{M_t}} n \right) / \left(1 - \sqrt{\frac{A_M}{M_t}} n \right) \right),$$

where $A_M = 0,156 \text{ Re}^{-0,2} (\rho(2\pi)^3 R^5 / 2) N$.

The heat exchange in fan is calculated with regard for the effect of the density gradient in the field of centrifugal forces. For this purpose, a theoretical formula for the heat transfer coefficient $\alpha = \alpha'(1 + 2\Delta T/T)$ was used, where ΔT is the mean temperature jump between air and wall, and T is the mean air temperature; or the experimental dependency

$$\alpha = \alpha' \Delta T^{0.09} \quad (3)$$

which is close to it was used, where $\alpha' = Nu \lambda_a / R$ and λ_a is the air heat conduction coefficient. The criterial dependence following from the Reynolds analogy [9] for the rotating disks at large Re numbers is $Nu = 0.0311 \text{ Re}^{0.8}$. The further calculation is performed by using the conventional formulas of heat transfer with regard for the ribbing efficiency.

EXPERIMENTAL DATA AND THE RESULTS OF THE VALIDATION OF CALCULATION METHOD

We present below the experimental data obtained on several samples of disk fans in terms of the pressure head, power, and heat transfer.

A significant part of the experimental material is presented for the first time. In particular, the investigation of the characteristics of the fans with the ribs on protective surfaces was carried out specifically in connection with the fabrication of experimental samples and the need in the development of a calculation method for their modelling.

It should altogether be noted that the amount of the available experimental information is still insufficient, which does not eliminate a subsequent correction of the computational relations.

The pressure head characteristics are presented in Fig. 2. The geometric parameters are given in the same Figure. The computational re-

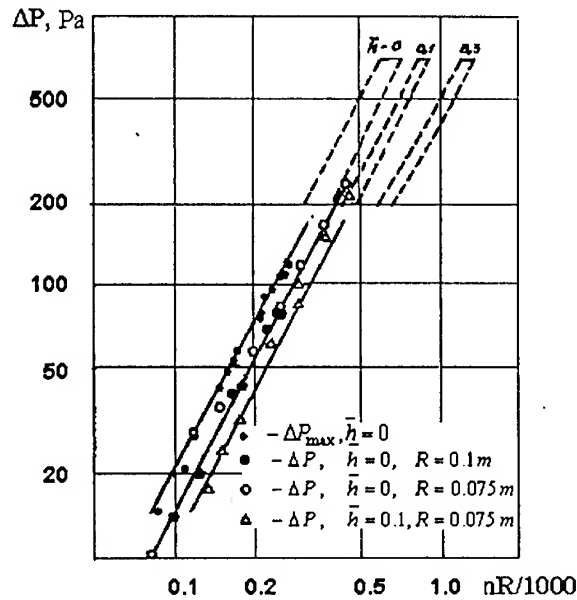


Fig. 2.

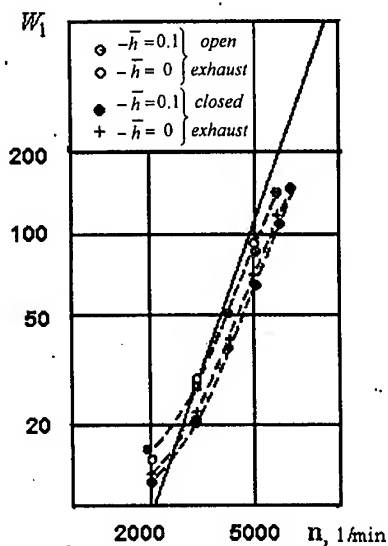


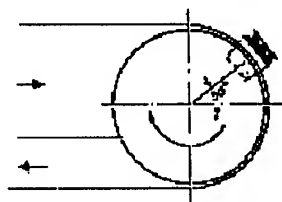
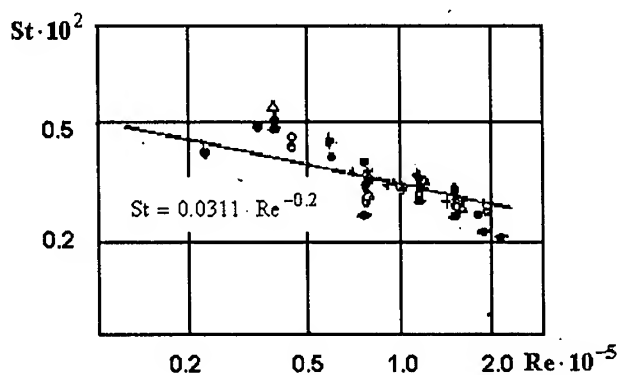
Fig. 3.

power. This seems to be related partially to inaccurate values of η_e and η_m . But the main discrepancy is related apparently to the protection effect on the friction on disks. An increase in power at an open exit in comparison with the case of a closed exit points to this fact.

It is also interesting to note a weak effect of the ribbing on the power consumed at a fixed number of revolutions. Thus, the power computation by the proposed technique may be considered to be acceptable, because the discrepancy with experiment is not very large, and the drive power should be chosen with an excess with respect to the one needed to ensure the starting characteristics. All the data available on the heat transfer are presented in Fig. 4 in co-ordinates $St(Re\delta)$. The experimentally measured values of the heat transfer coefficients have been corrected to take into account the effect of the temperature jump in accordance with (3) and the rib efficiency in accordance with experimental data. It may be seen

gion boundaries are limited by the values of φ from 0.2 to 0.5 and are not shown for the values below $\Delta p = 200$ Pa to avoid the overloading of the Figure. The upper experimental curve corresponds to the measured maximum value of the pressure head (Δp_{max}) in the exit fan section. The remaining measurements have been conducted at a completely closed exit, which has enabled us to obtain in a methodically simple manner the pressure head characteristics, although it introduces a certain error by decreasing the values of the maximally attainable pressure head. It is seen from Fig. 2 that the computation agrees quite satisfactorily with the experimental data both in a qualitative behaviour of curves and in terms of the quantitative agreement.

We compare in Fig. 3 the measured power of the electric drive with the computation by the above technique. The efficiency values have been assumed on the basis of the experimental estimates to be $\eta_e = 0.8 - 0.85$; $\eta_m = 0.9$. It can be seen that the computation yields the elevated values of



	h, mm	δ, mm	R, mm
Δ	4	1.5	75
\diamond	8	1.0	75
\bullet	8	1.5	75
\blacklozenge	8	2.0	75
\circ	16	1.5	75
+	0	0	100

Fig. 4.

that the recommended dependence (2) correlates satisfactorily with experimental data.

The experiments were conducted on the ribbed inserts that were positioned in accordance with the diagram presented in Fig. 4. This position approximately corresponds to the mean value of α over the total length of a semicircle enclosing the rotor.

Fig. 5 shows the measurements in another position, where the heat transfer is less efficient. Fig. 5 illustrates the reduction of the heat transfer efficiency at the disposition of ribs outside the rotor. In this case, the heat transfer coefficients were measured by the method of the resistance thermometers that operated simultaneously as the heaters. There were four strips over the rib height, which served as the resistance thermometers, and a number of measurements have been conducted on each of them to estimate the distribution of α over the rib height. Fig. 6 shows the obtained dependence for the variation of the relative heat transfer coefficient along the rib height; the location of points corresponds to a distance from the corresponding strip middle to the edge for the revolution numbers indicated by their numerical values.

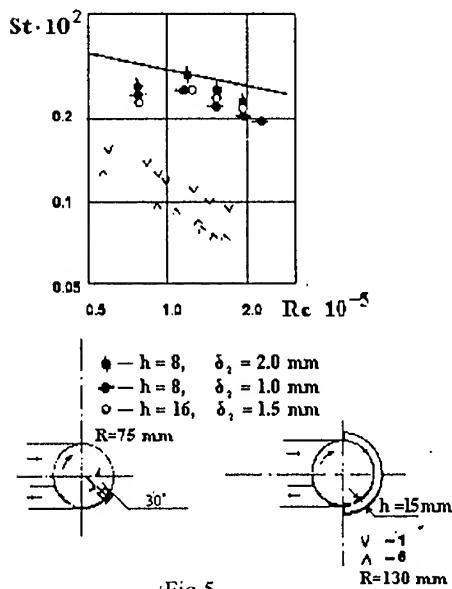


Fig. 5.

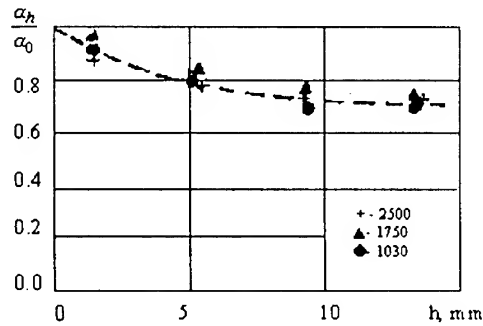


Fig. 6.

The experimental results give reason, on the whole, to believe that the proposed calculation method may be used for a preliminary estimation of the characteristics of rotor disk machines with the combination of the functions of fan and heat exchanger in the same aggregate.

CONCLUSION

The proposed calculation method is oriented mainly towards the execution of engineering computations at the stage of the design of the disk rotor machines with the combination of the functions of fan and heat exchanger.

Taking into account the approximate character of the models for the construction of analytic dependencies at a very complex local flow pattern in the flow duct and the limited amount of the accumulated experimental material, it is reasonable to use in computations the air parameters under normal conditions for a preliminary estimation of the characteristics and the choice of geometric parameters.

The test computation of a chosen design scheme should be carried out more carefully with regard for the effect of temperature variation on the thermophysical properties of the working body (air) and the used materials.

In addition, the specifics of the disk machines are to be taken into account, for which the pressure head, power, and heat transfer characteristics at an invariable rotor geometry depend mainly on the number of revolutions, and the flow rate also depends on the diaphragm position (φ). This is especially true for the machines with a large internal resistance caused by the ribs.

The effect of heat conduction of disks on the heat transfer on the protective surfaces and the uniformity of the temperature field is practically not investigated. The separate experimental observations altogether show that this can sometimes be a significant circumstance. The calculation method has been derived under the assumption that the diameter of the shaft on which the disks are located is negligibly small. This assumption is valid at least up to the aspect ratio of the shaft diameter to the disk diameter ~ 0.3 . At the use of larger aspect ratios, the corrections should be introduced in the calculation method.

At the organization of the heat transfer via the shaft its computation can altogether be based on the same formulas, and with an even greater reason, because it has been assumed in our technique that the heat transfer on the cowl is described by the laws related to the disks. But in this case the efficiency of ribbing should be taken into account by using the conventional relations for circular ribs.

REFERENCES

1. Baev V.K., Belomestnov P.I., Vyazovich E.I., and Yakobi Yu.A. The gas flow laser, the author certificate No. 1718314, 1981: The Russian Federation Patent No. 1718314, Moscow: Izobreteniya, 1992, No. 9, p. 215.
2. Belomestnov P.I. The disk pump: the Russian Federation Patent No. 1681057, Moscow: Izobreteniya, 1991, No. 36, p. 162.
3. Belomestnov P.I. The device for drying and cleaning the air: the Russian Federation Patent No. 1679142, Moscow: Izobreteniya, 1991, No. 35, p. 137.
4. Belomestnov P.I. The disk pump, the Russian Federation Patent No. 1768801, Moscow: Izobreteniya, 1992, No. 39, p. 109.
5. Baev V.K., Nikulinskih A.V., Potapkin A.V., Frolov A.D., and Yakovlev V.N. Aerodynamics and heat transfer in a disk rotor machine with tangential input and output of the working body // Int. Conference on the Methods of Aerophysical Research: Proc. Pt. III, - Novosibirsk, 1998, p. 47-51.
6. Baev V.K., Potapkin A.V., and Yakovlev V.N. The heat transfer processes on the disk fan cowl // The 1st Internat. Congress "Resource and Power Saving Technologies for Reconstruction and New Civil Engineering", Novosibirsk, 1999, p. 16-22. (in Russian)
7. Baev V.K., Potapkin A.V., and Yakovlev V.N. The technique for heat transfer intensification // The Russian Federation Patent No. 2122167, Moscow: Izobreteniya, 1998, No. 32, p. 432.
8. Baev V.K., Potapkin A.V., Yakovlev V.N., Dolmatov V.A., Trubitsyn A.I., Frolov A.D., and Chusov D.V. The heat exchanger // The Russian Federation Patent No. 2133935, Moscow: Izobreteniya, 1999, No. 21, p. 442.
9. Schlichting H. Boundary Layer Theory. New York: McGraw-Hill, 1979.

AEROTHERMODYNAMICS AT THE DLR GÖTTINGEN. EXPERIMENTAL AND NUMERICAL TOOLS

Walter H. Beck

Institute of Fluid Mechanics,
German Aerospace Center DLR,
37073 Göttingen, Germany

1. Introduction

The aim of this paper is to give an overview and an update of the tools (facilities, measurement techniques, numerical codes) used to carry out aerothermodynamic work in the Aerothermodynamics Section of the DLR Institute of Fluid Mechanics in Göttingen. A more comprehensive overview of the results cannot be given here: neither work prior to about 1990, nor activities at other research sites will be covered. Only the present activities will be exemplified by referring briefly to a few selected topics.

The aerothermodynamic activities in the Institute involve studies of hypersonic flows and can be divided into two mainstreams, each with its own emphasis and specialised tools – satellite aerothermodynamics (rarefied flows – outside the earth's atmosphere) and space transporter aerothermodynamics (high enthalpy flows – altitudes of 40 – 90 km):

1.1 Satellite aerothermodynamics. These activities span 40 years of research effort on thruster plumes, with particular attention being paid to plume simulations, rarefied effects (large distances from thruster and/or large angles to the thruster axis), plume/plume interactions, plume contamination effects and gas/surface interactions. (These thrusters are used in positioning and orbital trajectory control of satellites, and for propulsion of space transporters in space.) The vacuum tunnels built here in the 1960's and 70's to study these rarefied flows are not able to simulate a true space environment; the pumping systems are not able to maintain a sufficiently low background gas pressure ($< 10^{-3}$ Pa) under gas load, so that the plume spreading is strongly influenced by the background gas. To overcome this, the new cryogenically-pumped High Vacuum Plume Test Facility STG was built here in Göttingen and has been in operation for plume simulation studies for about 3 years – it is world-wide unique in that it uses liquid helium as coolant to attain the low background pressures, and as such forms the centre-piece of the European Thruster Plume Center which has been established also here in Göttingen. Measurements in this facility are supported by modern measurement techniques such as REMPI to obtain (internal) temperatures, densities and velocities of the plume gases. Furthermore, theoretical and numerical modelling of plume flows, interactions and impingement with the help of the DLR semi-empirical plume model and the DSMC code MONACO are used to augment hand-in-hand the experimental measurements.

1.2 Space transporter aerothermodynamics. These activities received a strong impetus in the 1980's during the ESA-supported development of the European space shuttle HERMES, and also in subsequent ESA work in technology maintenance and manned-space programs. The atmospheric reentry of a space shuttle at speeds of 4 – 6 km/s and at altitudes where the air density is already quite high is accompanied by strong shocks, leading to high temperatures and ensuing chemical (dissociation) reactions. The influence of these high temperature effects on the external aerodynamics – pressure distribution, flap efficiencies, shock/shock

interactions, boundary layer growth, etc. – and on the heating loads – surface catalysis – comprise the other major effort in this Institute. Here also specialised tools had to be manufactured or further developed. The High Enthalpy Shock Tunnel HEG was built and commissioned in the early 1990's to simulate these high temperature effects – the two key simulation parameters hereto are the flow velocity (specific enthalpy) and the binary scaling parameter ρL (ρ = density; L = characteristic length), where this latter parameter scales appropriately the (dissociation) reaction lengths behind a strong shock. Apart from the classical surface pressure and temperature (heat transfer) measurements, much effort has been put into the use of optical diagnostic techniques to probe the flow field: Schlieren (shock shapes), holographic interferometry (density changes), LIF (shock positions, internal temperatures), diode laser absorption (flow velocity, translational temperature, species concentration). Techniques being further developed for implementation here are time-resolved Schlieren and force measurements. Extensive effort has been (and is being) put into the development of non-equilibrium versions of the DLR in-house codes CEVCATS-N and TAU-N (further developments of the DLR pilot code NSHYP). These codes can (or will) treat chemical non-equilibrium and imperfect gas behaviour. They are used in every phase of high enthalpy testing, from determining a suitable nozzle contour, calibrating the free stream conditions, looking at flows around models (including complex flow interactions), to calculating test model surface properties such as pressure and heat transfer.

2. Facilities

2.1 The High Vacuum Plume Test Facility STG

The STG, as shown schematically in Fig. 1, is described in greater detail elsewhere (Dettleff and Plähn 1997, Plähn 1999). It consists of a liquid helium driven cryopump made of ribbed copper of area 30 m^2 and enclosing a cylindrical volume of length 5.25 m and diameter 1.6 m . The cryopump is encased in a liquid N_2 cooled mantle. The cryopump operating temperature can be low enough to maintain a H_2 background pressure of less than 10^{-3} Pa during load ($< 4.67 \text{ K}$), thereby permitting all relevant flow types – continuum, free molecular, isentropic core, boundary layer expansion region including backflow – to be obtained. Thrusters up to 10 N can be tested in continuous or pulsed mode operation mode.

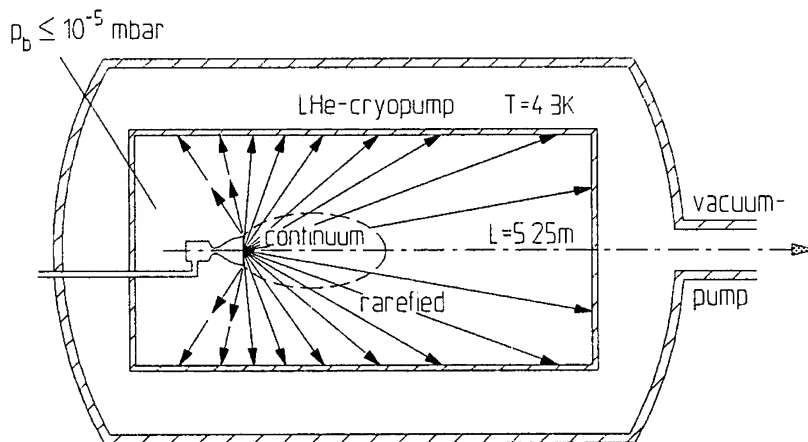


Fig. 1 Schematic overview of STG

2.2 The High Enthalpy Shock Tunnel HEG

The HEG, a free piston-driven shock tunnel operating in the reflected shock mode (Stalker tube), is more fully described elsewhere (Schnieder 1998 and references therein). It consists of a 33 m driver tube separated from a 17 m shock tube by a metal diaphragm, a 3.75 m long by 0.88 m exit diameter nozzle and a 1.2 m diameter test section. The freely moving piston in the driver tube compresses the helium gas until the burst pressure of the diaphragm is reached, whereupon a strong shock propagates down the shock tube to be reflected off the end-wall, thereby forming the nozzle reservoir – see Fig. 2. Pressures up to about 100 MPa are routinely used (200 MPa are attainable).

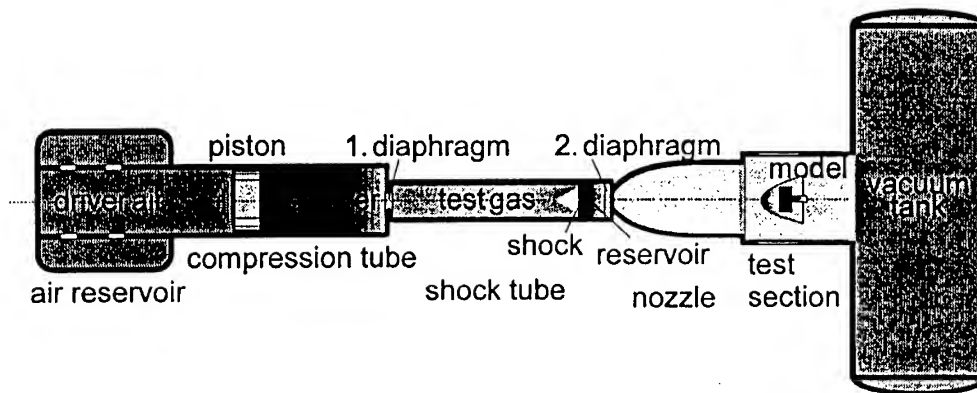


Fig. 2 Schematic overview of HEG

3. Numerical codes

3.1 MONACO

This is a DSMC particle method used to calculate rarefied flows (Dietrich and Boyd 1996). It uses the natural sample size method of Baganoff and McDonald for collision sampling. Particle elastic collisions are modelled with the variable hard sphere model, whereas inelastic collisions are accounted for using the Larsen-Borgnakke model with extensions to allow for discrete vibrational energy levels. A simple diffuse reflection model with full thermal accommodation handles gas/surface interactions. The code runs on different computers with parallel architecture (e.g. IBM SP2 or Sun Sparc MP). The transition from continuum (e.g. in the nozzle) to rarefied flow solvers can involve different degrees of coupling, depending on the flow properties. Here a de-coupled scheme is adequate as long as the interface is located in the supersonic part of the flowfield (viz. no upstream influences). Continuum breakdown parameters defined either by Boyd or Bird can be used to locate the interface between continuum and rarefied flow solvers.

3.2 CEVCATS-N

The full Navier-Stokes equations in integral form for mixtures of perfect and reacting gases in thermochemical equilibrium and non-equilibrium are solved with a numerical scheme consisting of hybrid upwind flux vector splitting and using a five-stage Runge-Kutta scheme for time integration (Brück et al 1997). Local time stepping, implicit residual averaging and full multigrid are used to accelerate the convergence process. Viscosity is computed with Sutherland's formula for perfect gases and with Blottner curve fits for reacting gases. The chemical model contains (but is not restricted to) five species. Boundary conditions on the wall

allow different temperatures (adiabatic, prescribed, equilibrium). The influence of catalytic effects can also be included. Several tools are used for generation of the structured grids. The computational performance on a NEC SX4/4 (single processor) is about 1.1 GFLOPS.

3.3 TAU-N

The DLR TAU-Code is a finite-volume Euler/Navier – Stokes solver working with hybrid, unstructured or structured grids (Gerhold et al 1997). The flow solver is a three-dimensional parallel hybrid multigrid code. It uses a finite volume scheme for solving the full Navier-Stokes equations. The temporal gradients are discretized using a multistep Runge – Kutta scheme. For accelerating the convergence to steady state a local time-stepping concept is employed. The calculation of the inviscid fluxes is performed using an AUSM or a Roe type 2nd-order upwind scheme. The gradients of the flow variables are determined by employing a Green-Gauß formula. Alternatively, a central method with either scalar or matrix dissipation is employed. The viscous fluxes are discretized using central differences. The turbulence model implemented in the solver is the one-equation transport model according to Spalart and Allmaras. This model uses only local quantities for calculating turbulent transport which makes it suitable for unstructured methods. For time-accurate solutions global time stepping as well as a dual time-stepping multigrid scheme is implemented. The time discretization can be chosen to be first, second or third order (where a higher order implies increased overhead). The primary grid can be adapted to the flow solution by cell division if a better resolution of the flow field is required in certain regions of the computational domain. The TAU code is being further extended to (TAU-N) to cover high Mach number flows and to include real gas, high temperature (non-equilibrium) effects.

4. Measurement techniques

These can be broadly (and somewhat arbitrarily) divided into two categories – surface (or bulk) and optical measurement techniques.

4.1 Surface(bulk) techniques

The following techniques (technique; measured property; application) have been implemented in rarefied flows:

Pitot probe	Pressure	Plume characterisation
Thermoelements	Temperature (\Rightarrow heat transfer)	Surface heating
Patterson probe	Gas mass flux	Plume characterisation
Microbalances	Forces; surface shear stresses	Plume impingement
QCM	Deposit thickness	Surface contamination

and in high enthalpy flows:

Pitot probe	Total pressure	Free stream flow
Static pressure probe	Static pressure	Free stream flow
Thermoelement on sphere	Stagnation point heat transfer	Free stream flow
Pressure taps	Surface pressures	Model surface
Thermoelements	Temperature (\Rightarrow heat transfer)	Model surface
*Stress wave force balance	Forces, moments	Aerodynamic coefficients
(* still under development for HEG)		

A literature survey covering work carried out on plume testing from 1980 – 1996, wherein references to test techniques can be found, is to be found in a DLR report (Boettcher and Dettleff 1997). The Patterson probe is described in Plähn 1999. An overview of the established techniques for high enthalpy work is given in Schnieder 1998.

4.2 Optical techniques

These techniques have been implemented to measure the gas properties themselves, and thereby give insight into various fluid mechanical phenomena (plume expansion, interactions and impingement; free stream flow; shock shapes and stand-off distance; shock/shock and shock/boundary layer interactions;...). Measurements have been carried out in the rarefied regime:

LIF	$T_{\text{rot}}, T_{\text{vib}}$ (1)	Plume; visualisation; surface interactions
REMPI	$[N_2]; [H_2]; T_{\text{rot}}, T_{\text{vib}}, u$ (2)	Plume gas properties up to large distances/angles
electron beam	$T_{\text{rot}}, T_{\text{vib}}, [N_2]$ (3)	Plume properties; plume interactions/impingement
gas discharge	Density gradients (4)	Shock shapes; plume interactions/impingement
and in high enthalpy flows:		
LIF	$T_{\text{rot}}, T_{\text{vib}}, [NO]$ region; wakes (5)	Free stream flow; visualisation (shock shape);shocked
DILAB	$T_{\text{trans}}, [NO]; u$ (6)	Free stream properties
Schlieren	Density jumps (7)	Shock shapes/interactions
HI	Density gradients (7)	Shocked gas regions; wakes; interactions

(LIF – laser induced fluorescence; REMPI – resonant enhanced multiphoton ionisation; DILAB – diode laser absorption; HI – holographic interferometry; u – flow velocity). References: (1) – Gundlach 1995; (2) – Nazari 1999; (3) – Dankert et al 1994; (4) – Pot et al 2000; (5) – Wollenhaupt 1997; (6) – Trinks 1998; (7) – Kastell 1997.

5. Current work

5.1 Plume simulation

Experiments are being carried out in STG on simulated plumes with various test gases and with the help of different measurement techniques to measure plume characteristics in the highly rarefied regions far from the nozzle exit. Fig. 3 shows a plot of normalised density n/n_0 (n_0 = reservoir density) as a function of normalised distance r/d from an orifice of diameter d ($d = 0.6$ mm) for a measurement in STG with N_2 as test gas ($p_0 = 50$ kPa; $T_0 = 300$ K) – see Nazari 1999 and Plähn 1999. Three curves are shown: a. Measurements with REMPI; b. A calculation using the standard DLR plume model (Boettcher and Legge 1980); c. Measurements with the Patterson probe. Results were obtained as far out as 5000 (!) orifice diameters, where the gas is highly rarefied. One can see that although all three plots follow the expected $1/r^2$ dependence over a large range of r/d values (except for REMPI at large r/d), there is still an unresolved difference in the absolute values of n/n_0 .

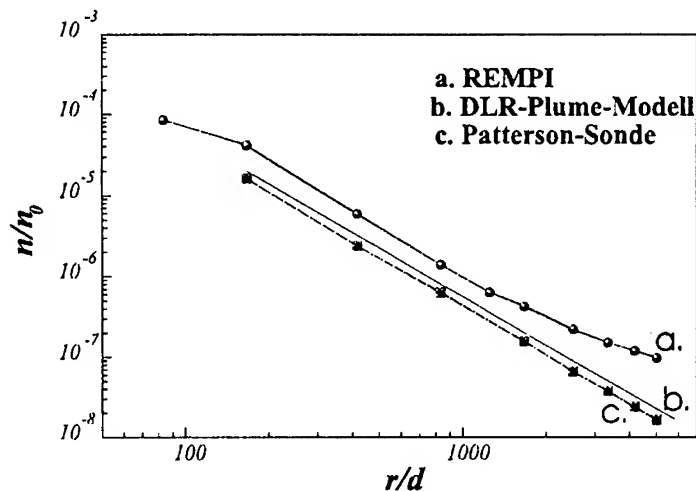


Fig. 3 Normalised mass fluxes in STG – measured and calculated.

5.2 X38/Crew Rescue Vehicle

In a national program TETRA (including industry participation) and together with NASA and ESA a data base for the flap region of the test vehicle X38 for the future CRV (crew rescue vehicle) of the ISS (International Space Station) is being developed. Extensive numerical effort using CEVCATS-N has been put into modelling the flow around X-38, including surface pressure and thermal load distributions for both flight and tunnel tests (Brück 1999). Figure 4 shows calculated results for flight at 73 km and 4.8 km/s (right half of CFD plot) and for HEG tests at condition III – 44 MPa, 12.5 MJ/kg (left half). Sensor locations are shown by small squares. The plot at right shows calculated and measured pressures for two HEG runs along the line of sensors (small squares) shown in the figure at left.

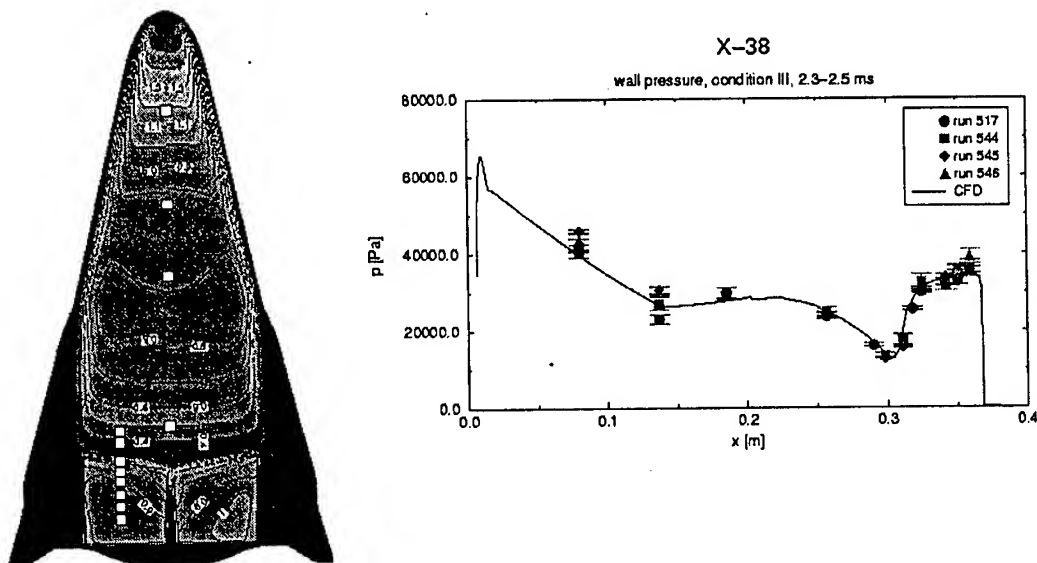


Fig. 4 Measured and calculated pressure distributions on an X38 model in HEG

References

- Boettcher R-D and Legge H 1980 A study of rocket exhaust plumes and impingement effects on space craft surfaces, DFVLR Internal Report, 1980-81.
- Boettcher R-D and Dettleff G 1997 Plume Testing Technology Transfer. WP 1.2: Documentation of DLR work 1980 – 1996 relevant for plume impingement, DLR-IB 223-97 A 16.
- Brück S, Radespiel R and Longo JMA 1997 Comparison of nonequilibrium flows past a simplified Space shuttle configuration, AIAA Paper 97-0275, presented at 35th Aerospace Sciences Meeting, Reno, NV, USA.
- Brück S 1999 TETRA Technologie für zukünftige RaumTRANSPORTsysteme Investigation of the heating uncertainties at the body flap of the X-38 configuration, DLR-IB 223-99 A 01, 1999.
- Dankert C, Boettcher R-D and Gundlach G 1994 Electron beam technique: a review for wind tunnel application, DLR IB 223-94 A 12.
- Dettleff G and Plähn K 1997 Initial experimental results from the new DLR high vacuum Plume test facility STG, AIAA Paper 97-3297, presented at 33rd AIAA Joint Propulsion Conference, Seattle, 1997.
- Dietrich S and Boyd ID 1996 Scalar and parallel optimized implementation of the Direct Simulation Monte Carlo method, J. Comp. Phys. 126(2) 328-42.
- Gerhold T, Friedrich O, Evans J and Galle M 1997 Calculation of Complex Three-Dimensional Configurations Employing the DLR-TAU-Code, AIAA-paper 97-0167, 1997.
- Gundlach G 1995 Untersuchung der Rotationsenergie-Wechselwirkung von NO an technischen Oberflächen in verdünnter Hyperschallströmung mit laserinduzierter Fluoreszenz, Dissertation, DLR FB 95-38, 1995.
- Kastell D 1997 Aerodynamik eines stumpfen Kegels in reagierender Überschallströmungen, Dissertation, DLR FB 97-06, 1997.
- Nazari BK 1999 Untersuchung von Abgasstrahlen aus Kleintriebwerken mit der Lasermesstechnik REMPI, Dissertation, DLR FB 99-27, 1999.
- Plähn K 1999 Experimentelle Untersuchung und Modellierung von Abgasstrahlen aus Kleintriebwerken in der Kryo-Vakuum-Anlage STG, Dissertation DLR FB 99-39, 1999.
- Pot T, Dankert C and von Roden G 2000 Hypersonic flow visualisations in the R5Ch wind tunnel by glow discharge technique. ONERA-DLR co-operative action, ONERA Technical Report. RT 52/4362 DAFE/N.
- Schnieder M 1998 Wechselwirkung einer starken und einer schwachen Stoßwelle in reagierender Hochenthalpieströmung, Dissertation, DLR FB 98-31, 1999.
- Trinks 1998 Application of a diode laser absorption technique with the D2 transition of atomic Rb for hypersonic flow field measurements, Applied Optics 37:30, 7070-75, 1998.
- Wollenhaupt M 1997 Einzelpuls Zwei-Linien-Thermometrie mit planarer laserinduzierter Fluoreszenz an NO-Molekülen in Hochenthalpieströmungen, Dissertation, DLR FB 97-23, 1997.

STUDY OF RESONANT INSTABILITY WAVE INTERACTION IN SELF-SIMILAR BOUNDARY LAYER WITH ADVERSE PRESSURE GRADIENT

V.I. Borodulin, Y.S. Kachanov, D.B. Koptsev

Institute of Theoretical and Applied Mechanics, 630090, Novosibirsk, Russia

1. Introduction

The first strict experimental evidence of the enhancement of the instability wave growth in presence of an adverse pressure gradient (APG) has been obtained in the classical experiments by Schubauer and Skramstad [1]. At the same time, the nonlinear mechanisms of transition in the APG boundary layers were not investigated for a long time. A significant role of the resonant wave interactions at initial nonlinear stages of the Blasius boundary-layer transition was shown both experimentally and theoretically many years ago (see for review [2]). The subharmonic-type resonances were of the most importance. Probably first strong evidence of an important role of the subharmonic resonance in the process of the laminar-turbulent transition in the APG boundary layer was obtained experimentally in [3]. Approximately at the same time, a powerful resonant amplification of 3D subharmonics in presence of the 2D fundamental wave was observed by means of DNS in [4] during simulation of the laminar-turbulent transition in the APG boundary layer. Somewhat later, an inviscid nonlinear asymptotic theory of the resonant triplets was developed in [5] for Rayleigh modes propagated in the APG boundary layer. The theory predicted a strong (double-exponential) growth of the subharmonics under the influence of the exponentially growing primary instability wave. For later (essentially nonlinear) stages of the disturbance development an "explosive" joint amplification of both fundamental and subharmonic modes was predicted. Further downstream, a saturation of the all waves participating in the resonant interaction was predicted and observed in the DNS. The only available at present direct experimental study of the subharmonic resonant interactions in the APG boundary layer was performed in [6] for rather small values of Hartree parameter ($\beta_H = -0.06$ and -0.09). In agreement with the theoretical prediction the rapid growth and subsequent saturation of the subharmonic amplitudes was found at controlled disturbance conditions. However, the double-exponential growth and the explosive amplification have not been found. Moreover, some important properties of the resonant interactions were not investigated. In particular, an influence of the initial phase shift between the fundamental and subharmonic modes on the resonant amplification remained unclear and the role of detunings in the values of the disturbance frequency and spanwise wavenumbers from the resonant values was not studied. There was also a complete lack of information about a possible interaction of the primary wave (with the frequency f) with continuous-spectrum background perturbations, as well as about a possible amplification of the high-frequency harmonics of the subharmonic wave (such as $3f/2$, $5f/2$, etc.). The subsequent, essentially non-linear stages of the transition were also not studied in previous experiments.

The goal of the present experiments was to fill the gaps mentioned above and to investigate in more detail both the properties of the tuned and detuned subharmonic resonances in the APG boundary layer and to clear up the subsequent destiny of the transition process including its essentially nonlinear stages.

2. Experimental Setup and Basic Flow

Experiments were conducted in the low-turbulence subsonic wind tunnel T-324 of the ITAM at the free-stream velocity $U_\infty \approx 9$ m/s and turbulence level less than 0.02 %. The wind-tunnel

has a 4 m long test section with a 1 m × 1 m cross-section. The APG was induced over a flat plate (equipped with a flap and installed horizontally) with the help of an adjustable wall-bump. In general, the experimental setup was similar to that used in [7] and in a receptivity study presented in this book by Kachanov and Koptsev. The difference is that in the present experiments a flat plate was somewhat shorter (1300 mm) and a special disturbance source was used for excitation of the 2D and 3D instability modes in a controlled way. The source was mounted at a distance $x_s = 300$ mm from the leading edge of the plate and consisted of a set of "point-like sources" aligned with the model span. Main features of such generator are described in [8].

The basic flow under investigation was a boundary layer with Hartree parameter $\beta_{H1} = -0.115$. All measurements were carried out by means of a hot-wire anemometer. The mean flow structure was measured carefully both in the potential flow and inside the boundary layer. Main characteristics of the mean flow obtained were compared with the theoretical ones calculated for the experimental conditions by Smorodsky in [7]. An investigation of the streamwise dependence of the boundary-layer shape factor $H = \delta_1/\delta_2$ (where δ_1 is the displacement thickness and δ_2 is the momentum thickness), as well as its comparison with the corresponding theoretical values, have shown that in the range $x \approx 420$ to 620 mm ($Re = U_0\delta_1/\nu \approx 901$ to 1148) the flow is self-similar (see also [7]).

The following coordinate system was used in the experiment: y -axis is normal to the model surface; x -axis corresponds to the streamwise direction ($x = 0$ at the plate leading edge); z is parallel to the leading edge of the model.

3. Generation of Disturbances

As was mentioned above, the TS-waves were excited in the boundary layer by means of the "linear" disturbance source (see [8] for more details) that represented a spanwise slot in the model surface with 82 outlets of tubes positioned under the slot and connected by flexible pipes with eight loudspeakers. The specially designed eight-channel electronic unit gave a possibility to generate in the boundary layer the disturbances in a wide range of frequencies and spanwise wavenumbers β . In the present work the source was used in a number of regimes. In main regimes the following modes were excited: (i) a large-amplitude 2D fundamental wave ($f_1 = 109.1$ Hz, $\beta = 0$) and a pair of small-amplitude 3D subharmonics ($f = f_{1/2} = f_1/2 = 54.6$ Hz, $\beta = \pm \beta_{1/2}$) simultaneously, (ii) the 2D fundamental mode only (regime F), (iii) the pair of subharmonics only (regime S), (iv) the fundamental mode introduced simultaneously with a small-amplitude continuous-spectrum ('noise-like') disturbance that simulated some background boundary-layer perturbations (regime NR), and (v) the 'noise-like' disturbance only (regime N). In regime (i) three sub-regimes were investigated, namely: regime MR (Main Resonant regime)

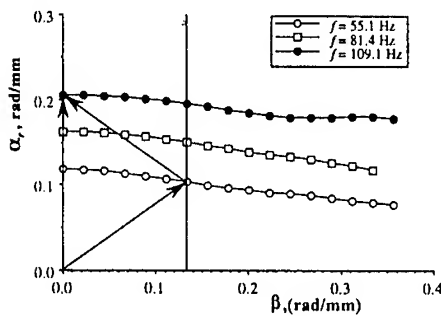


Fig. 1. Dispersion curves for different frequencies

– with an initial fundamental (Fun) amplitude $A_{01} = A_{m01}$ and an initial subharmonic (Sub) amplitude $A_{01/2} = A_{m01/2}$ and with a 'resonant' phase relationship between the Sub and Fun modes; regime 2FR – with two times greater initial Fun amplitude $A_{01} = 2A_{m01}$ and Sub amplitude $A_{01/2} = A_{m01/2}$; regime 4SR – with Fun amplitude $A_{01} = A_{m01}$ and four times greater Sub amplitude $A_{01/2} = 4A_{m01/2}$; and regime AR (Anti-Resonant regime) – with initial Fun and Sub amplitudes the same as in regime MR but with a phase shift between the Fun and Sub modes orthogonal to the resonant one (ϕ_{01} was shifted by π). In addition a dependence of the disturbance

behavior on initial phase relationship was studied for various initial phases. An influence of Sub frequency detuning on the resonant interaction was also studied at conditions of regime MR but at excitation of quasi-subharmonic wave at frequencies $f = f_{1/2} + \Delta f$, where Δf varied from $-0.9f_{1/2}$ to $+0.9f_{1/2}$ (regimes MRD)

In regime NR the 'random' (noise-like) component of the signal was repeated periodically from one sample to another (every 20 fundamental periods) that gave possibility to produce phased locked ensemble averaging of such disturbances and, thus, to separate the controlled 'random' perturbations from uncontrolled "natural" noise. At these conditions it was possible also to measure the phases of the continuous-spectrum modes and to investigate the phase relationships between these components and the fundamental instability wave.

A previously obtained information about the boundary layer under investigation (namely, the dispersion curves) was used to chose the Sub spanwise wavenumbers $\pm\beta_{1/2}$ in order to satisfy the resonance phase synchronism conditions (see Fig. 1). For the 2D Fun wave of a given frequency the streamwise wavenumber $\alpha_1 = 0.205$ rad/mm. The dispersion curve shows that a Sub wave with $\beta_{1/2} = 0.134$ rad/mm has a value of the streamwise wavenumber $\alpha_{1/2} = 0.103$ rad/mm that is two times lower than the fundamental one. Thus, the pair of sub waves with a spanwise wavelength of $\lambda_{z1/2} = 48$ mm $\approx 2\pi/\beta_{1/2}$ and with the spanwise wavenumbers $\beta_{1/2} = \pm 0.134$ rad/mm has been chosen in all studied regimes (when the Sub or quasi-Sub waves were excited) except for regimes NR and N.

4. Subharmonic Resonance and Its Properties

4.1. Spanwise distributions and normal-to-wall profiles. The examples of spanwise distributions of the Sub and Fun amplitudes and phases are shown in Fig.2 for regime MR. At this x -position (approximately in the center of a region of resonant amplification) the Fun amplitude and phase (open symbols) are almost constant and their z -behavior corresponds to a plain wave. The Sub amplitude and phase distributions correspond to a superposition of two oblique modes that gives a picture of a standing wave in spanwise direction. Such distributions were taken in several positions downstream. It was found that at $x > 510$ a spanwise modulation of the Fun amplitude and phase is observed which indicates an essentially nonlinear (non-parametric) interaction of the Sub and Fun waves at late stages.

To determine the location of disturbance-amplitude maxima in every regime measurements, y -profiles of disturbance amplitudes and phases were studied. Series of y -profiles were obtained in several streamwise locations in the spanwise position of the Sub amplitude maximum. It was found that the eigenfunctions of the Fun and Sub modes, observed in resonant regimes at stages of a rapid resonant amplification of Sub waves, coincide practically with the corresponding eigenfunctions measured in regimes F and S. The y -profiles were very typical for the linear eigenfunctions of 2D and 3D TS-waves. These observations indicate that at initial

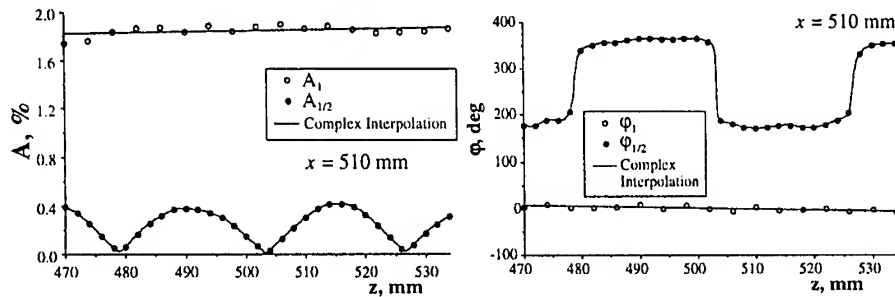


Fig. 2. Spanwise distributions of Fun and Sub amplitudes (a) and phases (b) in MR regime.

stages the resonant amplification of the Sub waves is a parametric one (i.e. without any back influence of the 3D Sub modes to the 2D Fun wave and with a resonant amplification of linear, eigen modes at Sub frequency).

4.2. Amplification curves. An exponential growth of the Fun wave is observed both in regime MR and F (Fig. 3). In regime F the Sub waves grow also exponentially. However, during the resonant interaction (regime MR in Fig. 3) the Sub-waves growth increases. It is seen from Fig. 4 that this growth is double exponential. This fact is in consistence with weakly-nonlinear theory [9] by Zelman & Maslennikova. The phase behavior observed in regime MR has shown a satisfaction of the phase synchronism conditions (see [10]) that is necessary for the resonant amplification of subharmonics.

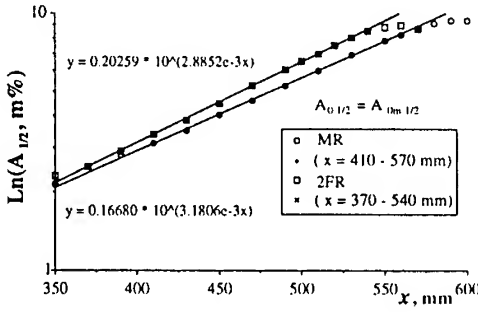
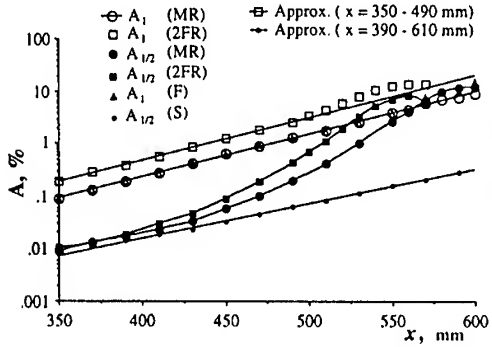


Fig. 3. Amplification curves for Fun and Sub waves.

Fig. 4. Double-exponential growth of subharmonics.

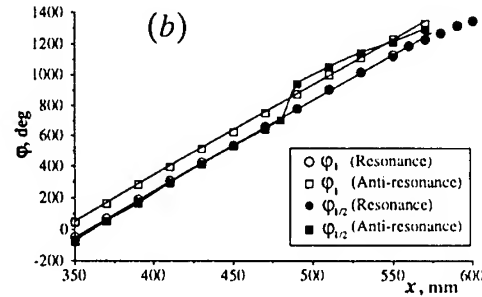
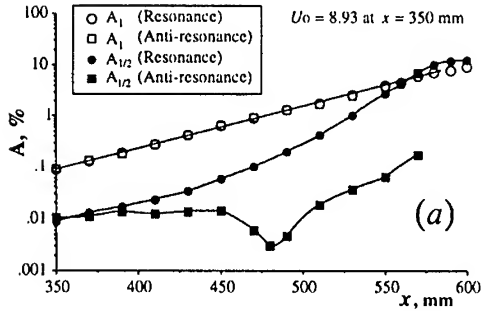


Fig. 5. Amplification curves for Fun and Sub modes in MR and AR regimes.

4.3. Influence of phase and frequency detunings. The resonance is very sensitive to the initial phase shift between the Fun wave and the two superimposed Sub waves. This is seen from Fig. 5 where regime AR is presented. The only difference from regime MR is in a phase shift of Fun wave by 180 degrees. The Sub wave attenuates initially because the phase relationship is orthogonal to the resonant one (see Fig. 5b). In the end (beyond the $x \approx 470$ mm) the subharmonics starts to amplify because a very small component of the Sub wave with the resonant phase shift survives, while the component with the orthogonal phase is disappeared (see phase change at $x \approx 470$ mm). The dependence of the subharmonics amplitude at $x = 510$ mm (far from the source) on initial phase shift is shown in Fig. 6. It is seen both a very strong amplification of the subharmonic when the resonant component is present and even its suppression when the phase shift is orthogonal ($\Delta\phi \sim 240^\circ$).

Variation of the initial frequency of quasi-subharmonic waves (regimes MRD) has shown that the subharmonic resonance has a great width in the frequency spectrum and can amplify even waves with frequencies $0.1f_{1/2}$ and $1.9f_{1/2}$!

4.4. Influence of initial amplitudes of fundamental and subharmonic modes. In regime 2FR the increment of the double-exponential growth of subharmonic increases (see Fig. 3). In regime 4SR the Sub-wave growth is weaker. In the former regime an additional growth of the Fun wave is observed at late stages due to an essentially non-linear interaction with the subharmonics. This growth is called in weakly nonlinear theory (see c.f. [9]) an 'explosive growth'.

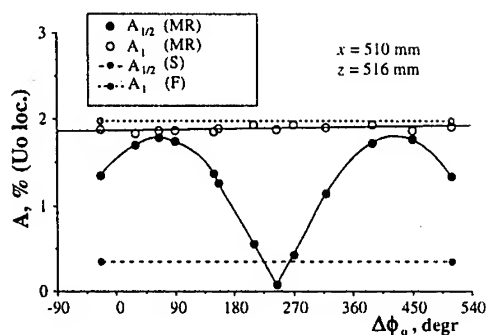


Fig. 6. Subharmonic amplitude vs. initial phase shift.

5. Resonant Amplification of Random Perturbations

The downstream development of the amplitude spectra of instability waves obtained in regime NR is presented in Fig. 7. It is seen that the resonance amplifies a wide continuous spectrum of perturbations, which are shown to be 3D ones with a dominant spanwise wavenumber close to that studied in resonant regimes with deterministic Sub waves. It was found that the eigenfunctions of perturbations observed in the boundary layer in regime NR at the subharmonic frequency are exactly the same as in deterministic regimes MR and S.

The amplification curves measured in regime NR are shown in Fig. 8. It is seen that starting from $x \approx 450$ mm the random quasi-subharmonic perturbations start to be amplified with the same double-exponential growth rate as in regime MR. In case "noise only" (regime N)

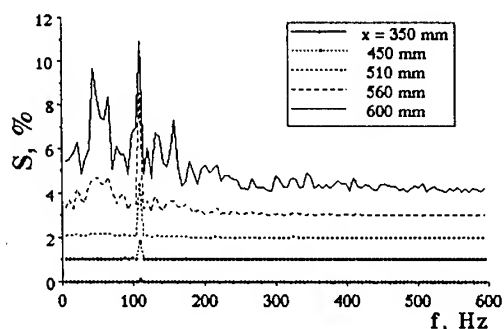


Fig. 7. Downstream evolution of amplitude spectra in NR regime.

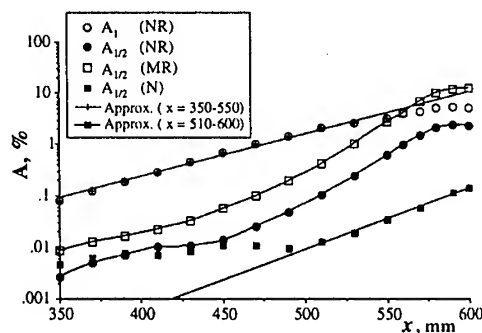


Fig. 8. Streamwise distributions of amplitudes of Fun and Sub waves.

the random quasi-subharmonic perturbations do not amplify initially, then they grow exponentially in consistence with the linear stability mechanism (with much weaker growth rate than in the resonant case). The resonant phase synchronism condition was found to be also satisfied in regime NR in the range of the resonant amplification of continuous-spectrum perturbations (i.e. starting from $x \approx 450$ mm).

6. Conclusions

1. The subharmonic resonance is studied using an advanced methods of measurements and data processing. Similar to the Blasius case the resonance is found to be very strong.
2. The resonance is shown to be very wide in the frequency spectrum and very sensitive to the phase shift between the subharmonic and fundamental waves.
3. The resonance is found to lead to a very rapid amplification of background continuous-spectrum perturbations.
4. The double-exponential resonant growth of the subharmonic (tuned and detuned) waves, predicted by weakly-nonlinear theory, is found experimentally.
5. An experimental evidence of the "explosive" (at least "additional") amplification of the fundamental wave under the influence of the subharmonic waves is found at late stages of the resonant interaction (following after the stage of parametric resonance).

The work was supported by Russian Foundation for Basic Research (grant 0001-00835).

References

1. Schubauer, G.B., Skramstad, H.K. 1948. Laminar boundary layer oscillation and stability of laminar flow. NACA Rep. No 909.
2. Kachanov Y.S. 1994. Physical mechanisms of laminar-boundary-layer transition. *Annu. Rev. Fluid Mech.* 26: 411-482.
3. Wubben, F.J.M., Passchier, D.M., Van Ingen, J.L. 1990. Experimental investigation of Tollmien-Schlichting instability and transition in similar boundary layer flow in an adverse pressure gradient. In: *Laminar-Turbulent Transition* (D. Arnal, R. Michel, eds), pp. 31-42. Berlin: Springer-Verlag.
4. Kloker M., Fasel H. 1990. Numerical simulation of two- and three-dimensional instability waves in two-dimensional boundary layers with streamwise pressure gradient. In: *Laminar-Turbulent Transition* (D. Arnal, R. Michel, eds), p. 681. Springer-Verlag.
5. Goldstein M.E., Lee S.S. 1992. Fully coupled resonant triad interaction in an adverse-pressure-gradient boundary layer. *J. Fluid Mech.* 245: 523.
6. Corke T., Gruber S. 1996. Resonant growth of three-dimensional modes in Falkner-Skan boundary layers with adverse pressure gradients. *J. Fluid Mech.* 320: 211-233.
7. Kachanov Y.S., Koptsev D.B. Three-dimensional stability of self-similar boundary layer with negative Hartree parameter. 1. Wave trains // *Thermophysics and Aeromechanics*. - 1997. - V. 6, No 4. P. 463-477.
8. Borodulin V. I., Gaponenko V. R., Kachanov Y. S. Investigation of normal instability modes in a three-dimensional boundary layer // *Thermophysics and Aeromechanics*. - 1998. - V. 5, No 1. P. 21-31.
9. Zelman, M. B., Maslennikova, I. I. 1993. Tollmien-Schlichting-wave resonant mechanism for subharmonic-type transition. *J. Fluid Mech.* 252: 499-78
10. Kachanov, Y. S., Levchenko, V. Ya. 1984. The resonant interaction of disturbances at laminar-turbulent transition in a boundary layer. *J. Fluid Mech.* 138, 209

EXPERIMENTAL INVESTIGATION OF THE SUPERSONIC FLOW ON THE LEE SIDE OF A DELTA WING: EXPERIMENTAL TECHNIQUES AND RESULTS

M. D. Brodetsky¹, A. M. Kharitonov¹, E. Krause², A. A. Pavlov¹,
S. B. Nikiforov¹, and A. M. Shevchenko¹

¹Institute of Theoretical and Applied Mechanics SB RAS, Novosibirsk, Russia

²Aerodynamisches Institut, RWTH Aachen, Germany

1. Introduction

As is well known, the supersonic flow around a delta wing can be classified into several flow regimes characterized by streamwise vortices on the leeward side of the wing, by internal shocks, and other features of the flow. Caused by the vortex system, the flow on the upper surface of the wing separates and reattaches, yielding convergence and divergence lines for the limiting streamlines on the surface. With increasing flight velocity, the surface heat transfer attains maxima in regions of flow reattachment. For certain conditions, flow separation causes a shift of the center of pressure and a change in the moment characteristics of the wing. In addition, dangerous influence on other aircraft may result from the primary vortices and internal shocks in the wake downstream from a delta wing.

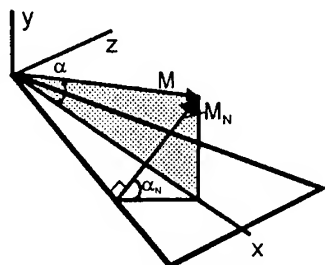


Fig. 1. Normal Mach number M_N and normal angle of attack α_N according to Stanbrook & Squire [1].

Numerous attempts were made to classify the flow regimes around delta wings in order to be able to predict critical flow situations or even only specific features of the flow as a function of the free stream conditions and the wing geometry. Stanbrook and Squire [1, 2] suggested that the normal angle of attack α_N and the normal Mach number M_N should be used as correlation parameters for the flow topology. These two quantities are obtained from the projection of the velocity vector onto the plane normal to the leading edge of the wing (Fig. 1). Stanbrook and Squire [1, 2] identified three main flow regimes: a) flows with leading edge separation, b) flows without leading edge separation but with a detached shock wave, and c) flows without leading edge separation and with an attached shock wave. They were also able to determine the boundaries between these regimes.

Later Maikapar [3] identified 13 flow regimes with the aid of the laser light-sheet visualization technique. Wood and Miller [4], however, found only seven flow regimes. The regimes differ from each other by the number and the location of vortices and shock waves. Szodruch and Peake [5] suggested a similar classification for thick wings. Finally, Seshadri and Narajan [6] proposed another classification, which seemed to complement the classification of [4], although some of the regimes, identified by the latter authors, were not confirmed.

In 1983 Vorropoulos and Wendt [7] found a new flow regime exhibiting cross-flow shocks under the primary vortices. In 1990 Brodetsky and Shevchenko [8] confirmed the existence of the cross-flow shocks with pressure probe measurements and laser sheet visualizations. They also found new flow regimes in which the cross-flow shocks are observed together with inboard cross-flow shocks above and between the primary vortices.

It is noted that the cross-flow shocks were observed for values of normal angles of attack and normal Mach numbers equal to those of the experiments of [4]. The difference between the two experiments consisted in the initial values of the angles of attack, sweep angles, and Mach numbers. Until now, it was not possible to derive a flow correlation from experiments, which offers a unique prediction of flow topology.

In order to clarify the controversial issues in conjunction with the flow regimes observed so far, an experimental study of the flow around three wings with sweep angles $\chi = 68^\circ$, 73° and 78° was initiated at the Institute of Theoretical and Applied Mechanics of the Russian Academy of Sciences, Novosibirsk. The test conditions mentioned guaranteed a smooth transition from subsonic to supersonic leading edge flow, and clearly revealed the formation of the primary, secondary, and tertiary vortices, and also of internal shocks.

Application of advanced conventional and improved laser light-sheet techniques provided reliable surface pressure distributions, limiting surface streamlines, and visualizations of the flow structure near the surface. From the analysis of these data, the extent of different flow regimes could be determined, confirming already known and adding new flow regimes to the topological map proposed in [4]. The results of this analysis are described in the present paper.

2. Experimental techniques and set-up

The experiments were performed with three models of a delta wing with sharp leading and trailing edges. The wings had leading edge sweep angles $\chi = 68^\circ$, 73° and 78° . All three wings had 3 percent symmetric parabolic profiles.

All experiments were carried in the supersonic blow-down wind tunnel T-313 of the Institute of Theoretical and Applied Mechanics of the Russian Academy of Sciences with the test section dimensions $0.6 \times 0.6 \times 2$ m. The test conditions were varied in a range of Mach number $M = 2 - 4$, corresponding unit Reynolds numbers $Re_1 = (26 - 56) \cdot 10^6 \text{ m}^{-1}$, and angles of attack $\alpha = 0 - 22^\circ$.

The test conditions were chosen so as to guarantee the largest possible range for the normal angle of attack α_N and also for the normal Mach number M_N , for which primary and secondary vortices, internal and external shock waves above and below the primary vortex were to be expected. Another reason for the choice of the test conditions was that the experimental data should be obtained with different wings, different free-stream Mach numbers and angles of attack, but, whenever possible, for the same values of α_N and M_N in order to test the quality of the correlation with these parameters.

The experimental techniques used included flow diagnostics on the model surface by visualizing the limiting streamlines with the method of soot-oil coating, the laser light-sheet technique for visualizing vortex structures, and surface pressure measurements.

The pressure on the model surface was measured using hanging pipelines as proposed in [9]. The pressure orifices were made in five cross-sections normal to the model axis with the step of 3 mm on the 68° and 73° wings and in six cross-sections on the 78° wing. The pressure measurements were performed with the multi-channel pressure meter MID-100 [10] with a measurement range of 10^5 Pa, and an instrumental error of 0.3 percent of the upper limit of measurement. The pressure coefficients $C_p = (p - p_\infty)/q_\infty$ were directly computed from the results of static pressure measurements.

The flow patterns in the various cross-sections over the model were visualized with the laser light-sheet technique described in [11]. The image registration system was adapted specifically for the experiments reported here, and software was developed for enabling real-

time variation of the parameters of the registration system. Thereby it was possible to obtain the best-quality image, decrease the cost of the experiments, and increase the information that can be obtained during a single test run.

3. Results and discussion

Figure 2 shows typical experimental results obtained with various techniques: flow pattern obtained with the laser light-sheet technique (a), the limiting streamlines obtained with the oil-flow technique (b), the surface pressure distributions for six streamwise cross sections (d), and

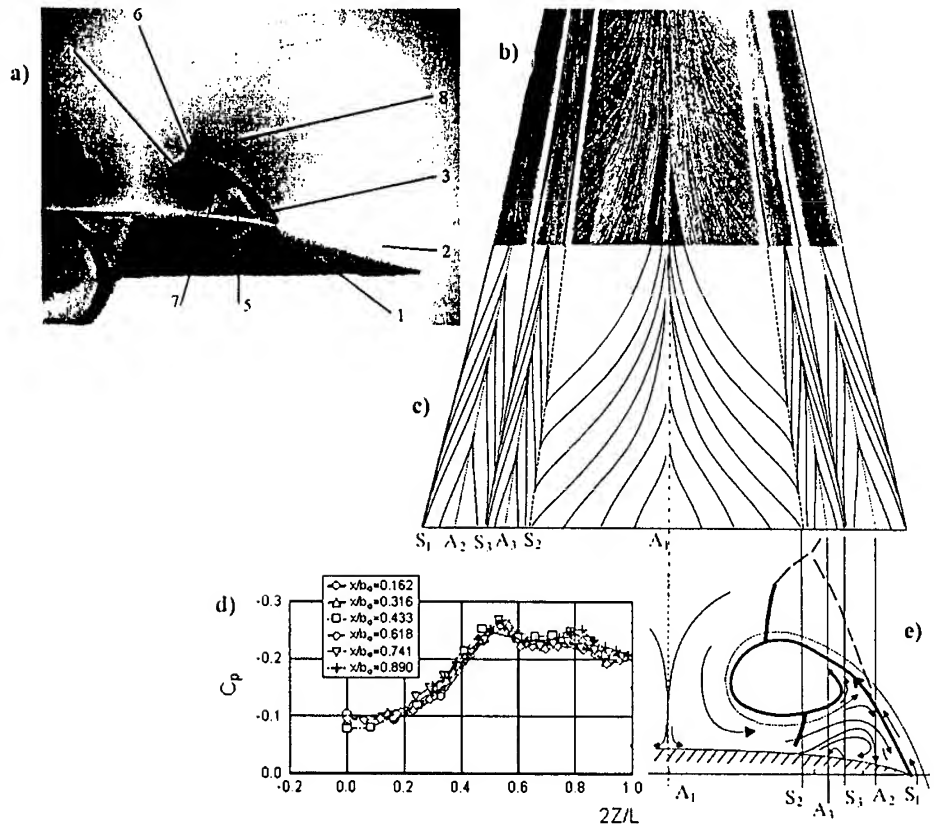


Fig. 2. Flow patterns, $X = 78^\circ$. a) laser sheet image at $M=2.75$, $\alpha=16^\circ$; b) oil-flow patterns at $M=2$, $\alpha=14^\circ$; c) surface flow topology; d) surface pressure distributions; e) crossflow topology.

The flow separates along the leading edge S_1 (Fig. 2c), and after the roll-up of the vortex sheet 3 (Fig. 2a) reattaches along the divergence line A_1 . The flow reattachment causes the local pressure to increase along the reattachment line, but the surface pressure under the primary vortex decreases over a large region. The minimum value of the pressure is determined by the spanwise position of the core of the primary vortex 4 (Fig. 2a). With increasing angle of attack, the strength of the primary vortex also increases causing a further decrease in pressure. The slight increase in pressure between its minimum and the leading edge can be large enough to

force the cross-flow boundary layer to separate along the convergence line S_2 and form a secondary vortex 5 (Fig. 2a). The cross-flow has to reattach again along the divergence line A_2 . For sufficiently high angles of attack, tertiary separation along the convergence line S_3 with reattachment along the divergence line A_3 will set in inside the region of secondary separation, however with a significantly smaller influence on the surface pressure distribution than that of the primary vortex. The decrease in pressure to a second minimum caused by the secondary vortex and the subsequent increase to another local maximum caused by repeated reattachment of the flow along the line A_2 are usually small. The tertiary separation does not exhibit any noticeable influence on the surface pressure distribution at all. It can, however, be visualized with the oil-flow technique in the pattern of the limiting streamlines on the model surface (Fig. 2b).

At sufficiently high angles of attack crossflow shock waves above the primary vortex 6 and under one 7 could be observed (Fig. 2a). The shock wave under the primary vortex is apparently caused by the fact that supersonic cross-flow under the primary vortex is decelerated toward the secondary separation and becomes subsonic flow through passing a locally normal shock. The necessity of turning two supersonic crossflows, which are directed from the leading edge of the wing to the plane of central symmetry toward each other, in the axial direction, causes the onset of crossflow shocks above the pair of the primary vortices. At high normal angles of attack ($\alpha_N > 57^\circ$) the crossflow shock between the pair of primary vortices was observed too.

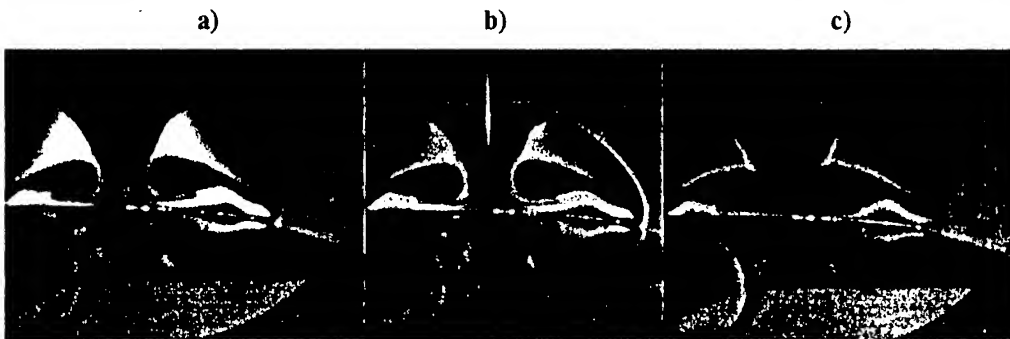


Fig. 3. Laser sheet images. $M = 3.5$, $\alpha = 16^\circ$.

a) $Re_1 = 45 \cdot 10^6 \text{ m}^{-1}$; b) transition from $Re_1 = 45 \cdot 10^6 \text{ m}^{-1}$ to $Re_1 = 29 \cdot 10^6 \text{ m}^{-1}$; c) $Re_1 = 29 \cdot 10^6 \text{ m}^{-1}$.

The registration of the laser sheet image in a continuous mode has allowed us to observe the phenomenon appearing at laser sheet visualization of a unsteady flows. So laser sheet images obtained at $M = 3.5$, $\alpha = 16^\circ$ and various unit Reynolds numbers are shown in Fig. 3. As it is shown, the laser sheet images corresponding to steady flow close each other (see Fig. 3a and c). At the continuous transition from high Re_1 to lower one (i.e. decreasing the stagnation pressure) the structure 1 is observed (Fig. 3b). There are no reasonable explanations of its appearance. Probably, the shock of condensation is visible in Fig. 3b. For detailed analysis of this phenomenon additional researches are required.

The analysis of the results allows detecting the influence of the angle of attack, of the sweep angle, and of the free-stream Mach number on the topology of the cross-flow. The flow regimes chart is shown in Fig. 4 with the normal Mach number M_N and the normal angle of attack α_N as the coordinates. The experimental data (test matrix) are indicated by the symbols. The gray shaded curves marked by the Roman numerals represent the boundaries of various flow regimes defined by Wood and Miller [4].

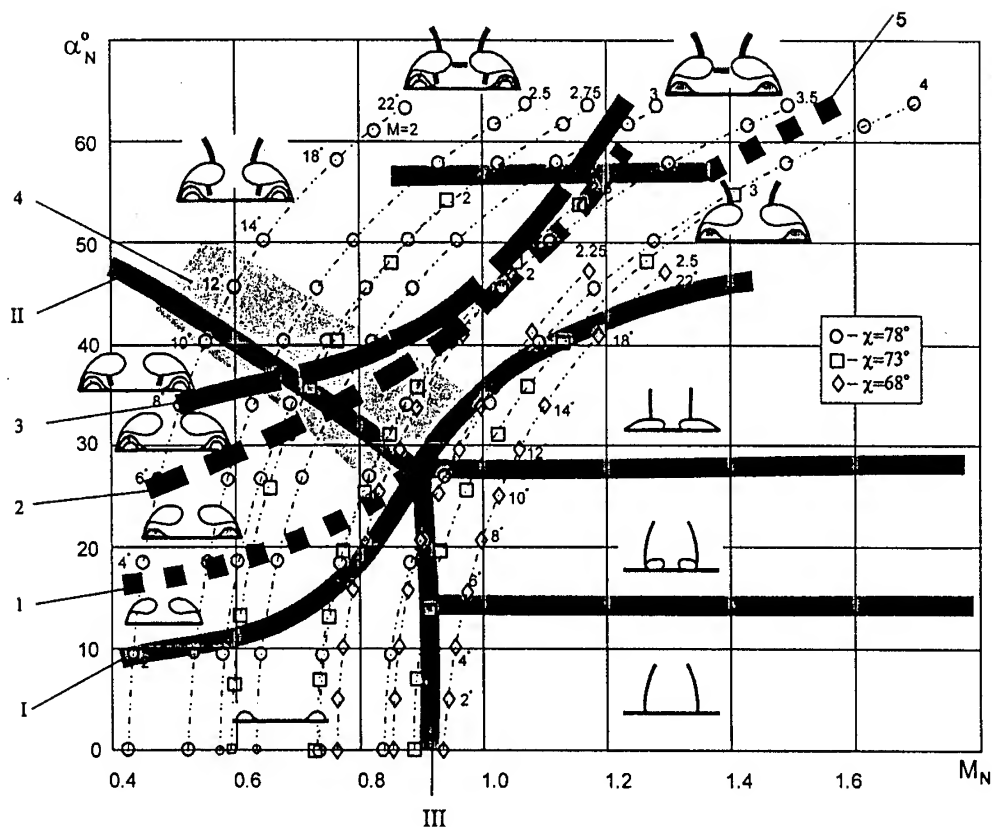


Fig. 4. Flow regimes topology map.

The analysis of the results allowed us to plot the boundary for the onset of secondary separation. In Fig. 4, this is boundary 1, which lies slightly above boundary I dividing the regimes with flow separation from the leading edges and without it. Line 2 in Fig. 4 is the boundary of flow regimes with tertiary separation. It should be noted that it lies higher than a similar boundary obtained in [6]. According to the data of [6], the tertiary separation should appear at $\alpha_N = 16^\circ$. The boundary line 3 shown in Fig. 4 indicates the region in which a shock wave appears under the primary vortex. For flows above the boundary line 3, a shock wave is formed, and flows below the line 3 are shock-free. It is seen in Fig. 4 that the boundary line 3 is close to the boundary line 2 for the onset of tertiary separation. This result seems to indicate that the emergence of the tertiary vortex is related to the shock wave under the primary vortex. Region 4 of flow regimes corresponds to the transition from the flow regime without the shock wave above the primary vortex to the regimes with this shock wave. It was obtained that the shock between the primary vortices disappears for free-stream Mach numbers $M > 3.5$. This transition is indicated by the boundary line 5 in Fig. 4, which divided flow regions with formation of a shock wave between the pair of the primary vortices and without it.

4. Conclusions

The flow around delta wings with sharp leading edges was investigated experimentally with the laser light-sheet technique, the surface oil-flow technique and with surface pressure measurements for supersonic speeds. The leeside vortex structures were recovered from the experimental data up to tertiary vortex formation. As a result the knowledge about the local flow conditions on delta wings could substantially be extended.

The well-known Wood-Miller chart of flow regimes around delta wings can be substantially supplemented by the following features:

- the boundary of emergence of the secondary separation,
- the boundary of emergence of the tertiary separation,
- the boundary of regimes characterized by a shock wave under the primary vortex,
- the right boundary of regimes with formation of a shock wave lying in between the primary vortices,
- the region of smooth transition from the regime without the shock wave above the primary vortex to regimes with formation of this shock wave.

Acknowledgement

The work was supported by International Association for the promotion of cooperation with scientist from New Independent States of the former Soviet Union (INTAS), grant No. 96-2358.

References

1. Stanbrook A., Squire L.C. Possible types of flow at swept leading edges // *Aeronaut. Quart.* 1964. Vol. 15, № 2. P. 72-82.
2. Squire L.C. Flow regimes over delta wings of supersonic and hypersonic speeds // *Ibid.* 1976. Vol. 27, № 1. P. 1-14.
3. Maikapar G.I. Separated flows at the leeward side of a triangular wing and a body of revolution in supersonic flow // *Uch. Zapiski TsAGI.* 1982. Vol. 13, No. 4. P. 22-33.
4. Wood R.M., Miller D.C. Lee side flow over delta wings at supersonic speeds // *J. Aircraft.* 1984. Vol. 21. P. 680-686.
5. Szodruch J.G., Peake D.J. Leeward flow over delta wings at supersonic speeds // *NASA TM.* - №81187, April, 1980.
6. Seshadri S.N., Narayan K.Y. Possible types of flow on lee-surface of delta wing at supersonic speeds. // *Aeronautical J.* 1988. № 5. P. 185-199.
7. Vorropoulos G., Wendt J.F. Laser velocimetry study of compressibility effects on the flow field of a delta wing // *AGARD CP 342*, 1983.
8. Brodetsky M.D., Shevchenko A.M. Some features of a separated flow and supersonic vortex structure at the leeside of a delta wing // *Separated Flows and Jets: Proc. IUTAM Symp. Novosibirsk, 1990.* Berlin et al.: Springer-Verlag, 1991. P. 341-344.
9. Brodetsky M.D., Bruk S.N., Makhnin A.M. The study of the errors in pressure coefficients at supersonic speeds // *A collection of scientific papers / Inst. Theor. Appl. Mech. SB USSR Acad. Sci., 1977, P. 94-113 (in Russian).*
10. Brodetsky M.D., et al. Multichannel pressure transducer MID-100 // *A collection of scientific papers / Inst. Theor. Appl. Mech. SB USSR Acad. Sci., 1978. P. 99-113 (in Russian).*
11. Vasenev L.G., Nikiforov S.B., Pavlov A.A., Shevchenko A.M. Development of the laser sheet imaging method for supersonic wind tunnels // *Intern. Conf. on the Methods of Aerophys. Research: Proc. Pt II. Novosibirsk, 1998. P. 206-211.*

THE DEVELOPMENT OF NATURAL DISTURBANCES IN HYPERSONIC BOUNDARY LAYER ON A SHARP CONE

D.A. Buntin, A.A. Sidorenko, A.N. Shiplyuk

Institute of Theoretical and Applied Mechanics SB RAS, 63009, Novosibirsk, Russia

The work deals with investigation of hypersonic boundary layer stability. Here there are results of experimental research of unit Reynolds number effect on laminar-turbulent transition and of natural disturbances development in laminar boundary layer of a sharp heat-insulated cone with half angle of 7° .

Disturbance spectra are obtained as well as their spatial distributions and wave amplification rates. The presence of second mode of disturbances is supported. Good agreement with calculation data is achieved.

To develop space technology and aviation, it is necessary to know the processes occurring in hypersonic boundary layer which are responsible for laminar-turbulent transition. By now transition mechanisms for hypersonic velocities are studied poor. It is connected with more complicated experiments and theoretical analysis. Physical processes of laminar-turbulent transition at hypersonic velocities differ in kind from the processes which are typical for subsonic and supersonic flows. The main reason of this distinction is occurrence of theoretically supposed by Mack modes of acoustic type instability (the second, third, etc. modes). According to calculations [1], the second mode of disturbances must play the dominating role in transition beginning with $M \approx 4$.

At the moment quite a few works are realized in the area of stability of hypersonic boundary layer (for example, [2-7]), but the obtained facts are in slight contradiction to each other and they are not enough to make laminar-turbulent transition clear. Hence it follows that this problem is necessary to be confirmed and further studied.

1. Experimental equipment

The experiments were carried out in hypersonic wind tunnel T-326, Institute of Theoretical and Applied Mechanics, SB RAS, at Mach number of incident flow $M_\infty = 5.92$ and at unit Reynolds number $Re_1 = 12.5 \cdot 10^6$ 1/m. Pulsations were measured with the help of hot-wire anemometer of constant resistance, with frequency range up to 500 kHz. Single-wire probes of 1.3 mm length made from tungsten wire of 5 μ m were used.

To obtain pulsation spectra, alternate signal was digitized with frequency of 1.25 MHz. It allowed to carry out spectrum analysis up to frequency of 612 kHz.

A model was a sharp cone with half angle of 7° and of 0.5 m length. Nosetip radius of model was less than 0.1 mm. The model was installed at nil angle of attack and nil yaw angle. In view of model massiveness, it can not be heated up at the experiment start, then, to meet with adiabatic condition, an electric heater was set into it. Wall temperature $T_w \approx 320$ K was controlled with thermocouple which was set into the model and situated near its surface.

2. A location of laminar-turbulent transition

The position of laminar-turbulent transition was determined by maximum in pressure distribution P'_0 , which corresponded to the end of laminar-turbulent transition. P'_0 was measured by a pitot probe. The pitot tube thickness was 0.7 mm.

Figure 1 shows the transition Reynolds numbers Re_{tr} (calculated by parameters on the boundary layer edge) versus Mach number M_e on a graph with data of other researchers, where subscript e means boundary layer edge conditions. It can be seen that data obtained in these experiments are situated much above the correlation curve. But first of all one should remember that nevertheless it is averaging curve, and there are many data above and below this curve. The next possible reason of such behavior is following. As will be shown later, initial amplitudes of the second mode disturbances are much smaller than ones of first mode due to free stream noise. But amplification rates of high frequency waves (which corresponds to the second mode) is bigger than ones of low frequency waves (corresponding to the first mode). And such situation when the slowly growing low frequency fluctuations play a dominant role in a transition (that will be shown below) can result in downstream shifting of transition location.

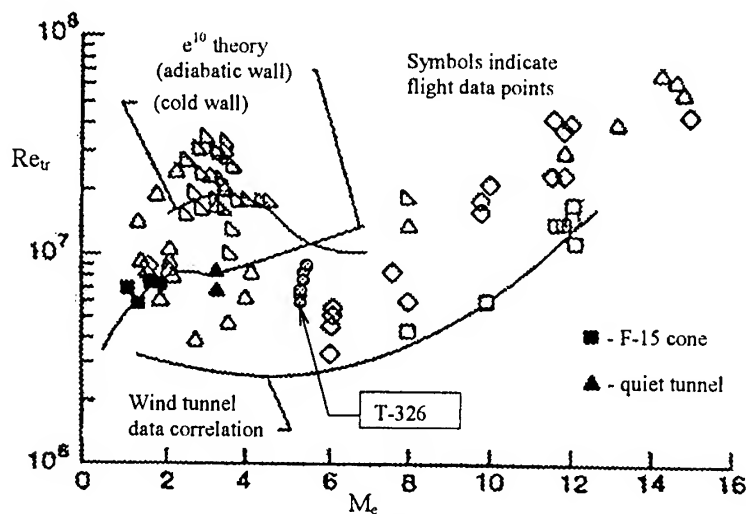


Fig. 1

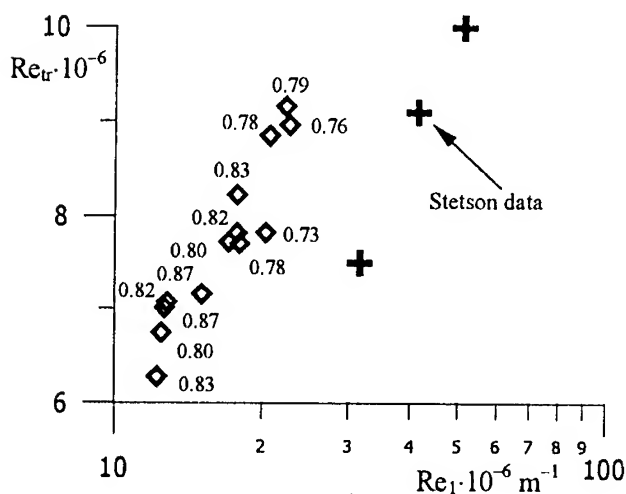


Fig. 2

Figure 2 is a dependency graph of transition Reynolds numbers on unit Reynolds number Re_1 . For comparison purposes Stetson data [8] obtained for the sharp cone with half angle of 8° at $M = 6$, are given. The ratio of wall temperature to stagnation temperature is shown near every point. The good qualitative agreement is seen.

3. Pulsation spectra in boundary layer

The measurements of distributions of disturbance spectra in boundary layer were carried out in 17 sections. For six of them in Fig. 3 there are distributions of average velocities U and mean-square amplitudes of integral pulsations of mass flow $\langle \rho u \rangle$. $\langle \rho u \rangle$ are normed by the average values of mass flow. Coordinate y was counted out from model surface perpendicularly to its axis. In the Figure y is normed by the thickness of boundary layer δ . R means root of Reynolds number: $R = \sqrt{Re_{1e} \cdot x}$, where Re_{1e} is unit Reynolds number, which is calculated by parameters on boundary layer edge, x is the distance along generatrix of the cone. Curves 1 and 2 – calculation of velocity profile for laminar and turbulent boundary layers correspondingly. It is evident from the Figure that at Reynolds numbers less than 2300 flow is laminar: measured velocity profiles coincide with laminar profile (curve 1), pulsations are small and concentrated in quite narrow region at $y \approx 0.8\delta$. At large Reynolds numbers $R > 2300$ average velocity profile and pulsation profile are filled, pulsation level increases, which is to say that boundary layer turbulization begins. Besides, sharp increasing of boundary layer thickness was observed.

To determine amplification rates of instability waves, measurements in the layer of maximum pulsations were done. The obtained spectrum distributions are shown in Fig. 4. A peak on high frequencies corresponding to the second disturbance mode is obvious. The estimation of wave length of these fluctuations with phase velocity used (calculated by linear local-parallel theory of stability ($C_x = 0.92$)) illustrates that it is approximately equal to two boundary layer thicknesses. This value corresponds to the wave length of the second disturbance mode obtained by some researchers ([6, 9]).

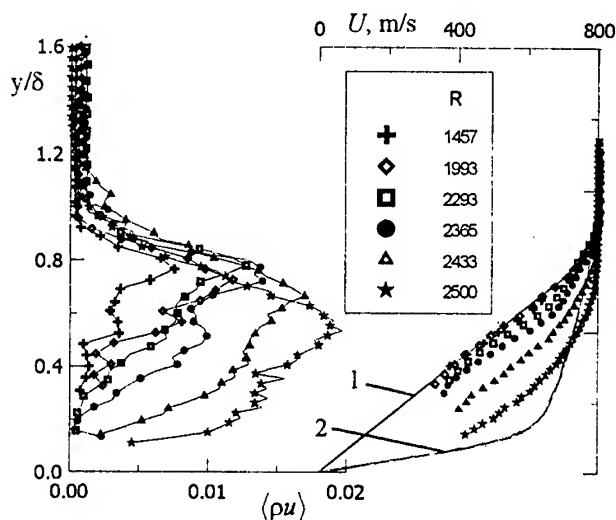


Fig. 3

Dimensionless frequency $\left(F = \frac{2\pi f}{\text{Re}_{1e} U_e} = 1 \div 1.5 \cdot 10^{-4} \right)$ corresponds to this type of instability

too. In the Figure one also may follow the evolution of this peak: amplitude increase is seen clear as well as pulsation maximum shift towards low frequencies area. Such a behavior is typical for the second mode: wave length of this mode is approximately 2δ , therefore as δ rises downstream wave length increases, then, frequency decreases. As can be seen from the figure the low frequency first mode pulsation amplitudes are higher then second mode pulsation amplitudes so the first mode plays dominant role in the laminar-turbulent transition.

4. Disturbance amplification rate

To obtain amplification rates of disturbance waves, distributions of pulsation amplitudes (measured in pulsation maximum) on R (Fig. 4), were smoothed and approximated by polynomial. Then amplification rates were calculated by formula: $-\alpha_i = \frac{1}{2A} \frac{\partial A}{\partial R}$.

The results of processing are presented in Figs. 5, 6. A peak is seen clearly in the area of frequencies which correspond to the second mode. Though the main energy of pulsations is located at low-frequency fluctuations, which correspond to the first mode, the waves of Mack mode turned out to be the most unstable, as it is predicted by theory. In Fig. 5 one may observe frequency shift with maximum amplification rate towards lower frequencies and it also agrees with theoretical prognosis. In Fig. 6 quite good qualitative and quantitative coincidence of calculated and experimental data for α_i is observed. The calculation of α_i was carried out by linear local-parallel theory of stability for waves with two different inclination angles: 0 and 50 degree.

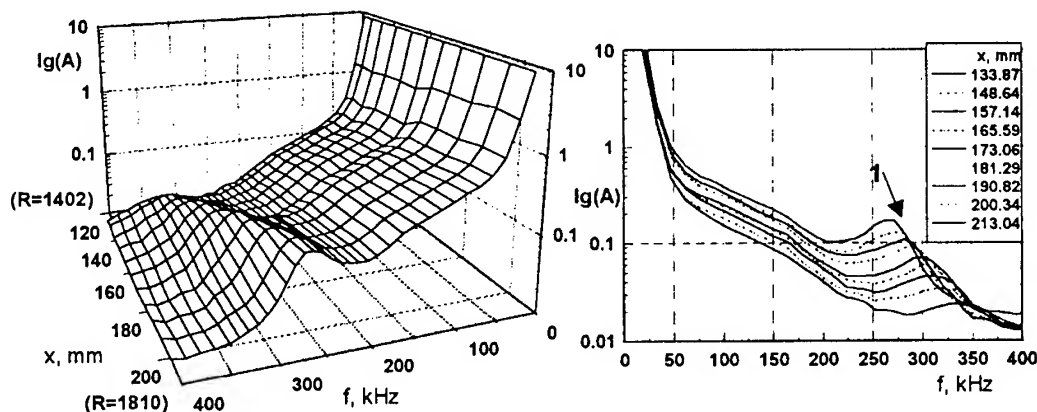


Fig. 4. Natural disturbances spectra distribution in the maximum pulsation layer.
1 – second mode.

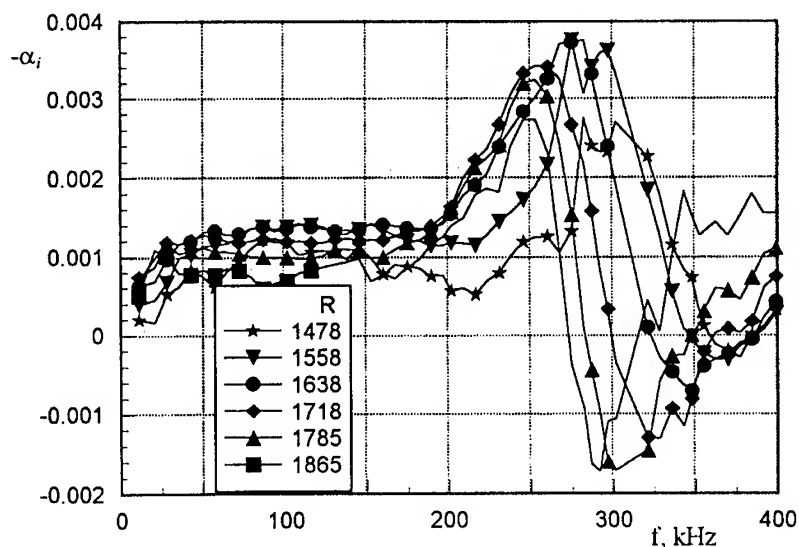


Fig. 5. Amplification rate versus frequency

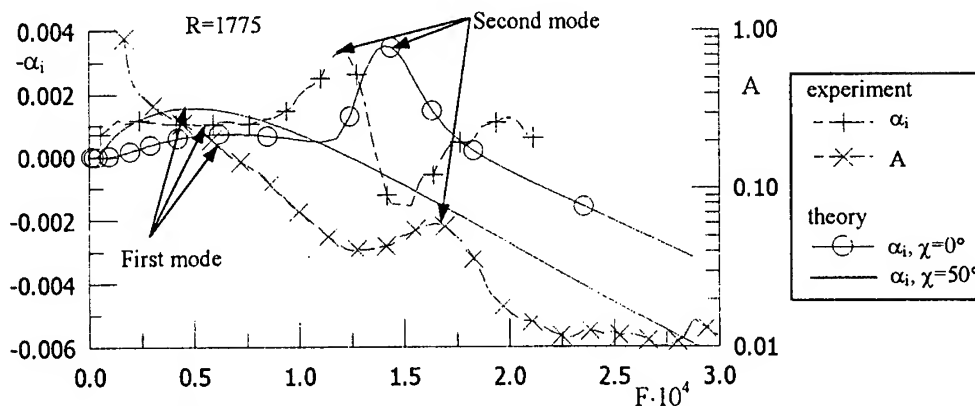


Fig. 6. Wave amplitude, theory and experimental amplification rates versus dimensionless frequency

Conclusion

In the work there are data about Reynolds number influence on laminar-turbulent transition on the model of sharp 7° cone when $M_\infty = 5.92$.

The stability of hypersonic boundary layer is studied. The average flow in boundary layer is researched and spatial distributions of pulsation spectra are measured.

The presence of the second disturbance mode is confirmed experimentally. Wave amplification rates for the first and second modes of instability are obtained. It is shown that disturbances of second mode have bigger amplification rates.

Good coincidence of experimental and calculated data is reached.

The work was supported by the Russian Foundation for Basic Research (grant No. 98-01-00735) and ISTC (grant No. 128).

References

1. **Mack L.M.** Boundary layer stability theory: Document 900-277, Rev. A. Pasadena, California, JPL, 1969. P. 388.
2. **Kendall J.M.** Supersonic boundary layer stability experiments // Proc. of Boundary Layer Transition Study Group Meeting. Vol. 2 / Aerospace Corporation, August 1967.
3. **Kendall J.M.** Wind tunnel experiments relating to supersonic and hypersonic boundary layer transition // AIAA J. 1975. Vol. 13. P. 290-299.
4. **Demetriades A.** Boundary layer instability observations at mach number 7 // J. of Appl. Mech., ASME. 1977. Vol. 99, No. 1.
5. **Demetriades A.** New experiments on hypersonic boundary layer stability including wall temperature effects // Proc. of the Heat Transfer and Fluid Mechanics Institute, 1978. P. 39-54.
6. **Stetson K., Kimmel R.** On hypersonic boundary-layer stability. AIAA 92-0737, 1992.
7. **Wikinson S.** A review of hypersonic boundary layer stability experiments in a Quiet Mach 6 Wind Tunnel. AIAA 97-1819, 1997.
8. **Stetson K.** Effect of bluntness and angle of attack on boundary layer transition on cones and biconic configurations. AIAA 79-0269, 1979.
9. **Demetriades A.** Laminar boundary layer stability measurements at Mach 7 – including wall temperature effects. AFOSR-TR-77-1311, 1977.

EXPERIMENTAL STUDY OF K-REGIME OF BREAKDOWN IN STRAIGHT AND SWEEP WING BOUNDARY LAYERS

V.G. Chernoray¹, A.A. Bakchinov², V.V. Kozlov¹ and L. Lofdahl²

¹ Institute of Theoretical and Applied Mechanics, Novosibirsk, Russia

² Chalmers University of Technology, Gothenburg, Sweden

Understanding and controlling laminar-turbulent transition in Three-Dimensional (3D) boundary layers remain so far unsolved problem in fluid dynamics and its applied applications. There still exist various unknown transition scenarios because of complexity of phenomenon underling the breakdown of laminar flow to turbulent stage [1]. In the case of not very high levels of external perturbations a 'normal' transition scenario is realized (in opposite conditions the 'bypass' transition scenario takes place). In this case two main regimes of the 2D boundary layer breakdown have been identified and investigated experimentally: first the K-regime (after Klebanoff et al. [2]) and second the N-regime found by Kachanov et al. [3]. In study [4] the conditions were found for realizing both K- and N-regimes of transition. After the pioneer complex investigation of K-breakdown by Klebanoff [2], many experiments and theoretical studies were conducted to adequately describe this phenomenon (see for instance Hama and Nutant [5], Kachanov et al. [6], Herbert [7], Rist and Fasel [8]). The N-regime of transition has been investigated in detail too (see for instance Kachanov et al. [3], Saric, Kozlov and Levchenko [4], Kozlov et al. [9], Bake et al. [10], Fasel [11]). The comparison of both types of transition was conducted in Saric, Kozlov and Levchenko [4], Bake et al. [10], Laurien and Kleiser [12]. Nevertheless, no experimental works or computations are known on K-type of breakdown on real wings. In order to study the generation and evolution of the viscous eigenwaves in 3D swept wing boundary layers experiments have been performed in a low turbulence level wind tunnel L2 at the department of Thermo and Fluid Dynamics in Chalmers University of Technology, Gothenburg, Sweden.

The wind tunnel L2 is a closed-circuit tunnel with a test section of 1.8 m wide, 1.2 m height and about 3 m length. The free-stream velocity U_o was fixed at 12.8 m/s. Under this velocity the free-stream turbulence level in the test section was below 0.1 % in a frequency range between 0.1 and 10000 Hz. The investigation was conducted on a C-16 wing profile, 500 mm chord, 1500 mm long and 80 mm thick. The profile was mounted horizontally in the test section. The adjustable supporting mechanism was designed to adjust attack angle and angle of sweep in wide range. The existing traverse system has been improved in order to study flow in transversal direction (a spanwise coordinate was added to streamwise and vertical axes). This traverse system carried a probe with precision of $1\mu\text{m}$ in both Y and Z directions, and $5\mu\text{m}$ in X direction. Experimental set-up and the coordinate system used are shown in Fig. 1. Preliminary experiments were conducted with the airfoil model at several sweep angles (0, 30 and 45 degrees). The main series of experiments were conducted with model set at two different sweep angles, namely, at zero sweep angle (straight wing configuration) and 30 degrees (swept wing configuration). The attack angle of wing was chosen to produce weak adverse pressure gradient distribution in the measurement region on the test surface (see Fig. 2). On this figure and in other presentations the downstream coordinate X is undimensionalized by wing cord c which was 500 mm for plane wing and 580 mm for swept wing configuration. At this angle of attack no local separation of the flow was observed and transition was occurred on the wing when sound of frequency $F_o = 300$ Hz with intensity of about 13.5 Db as the "artificial" disturbance

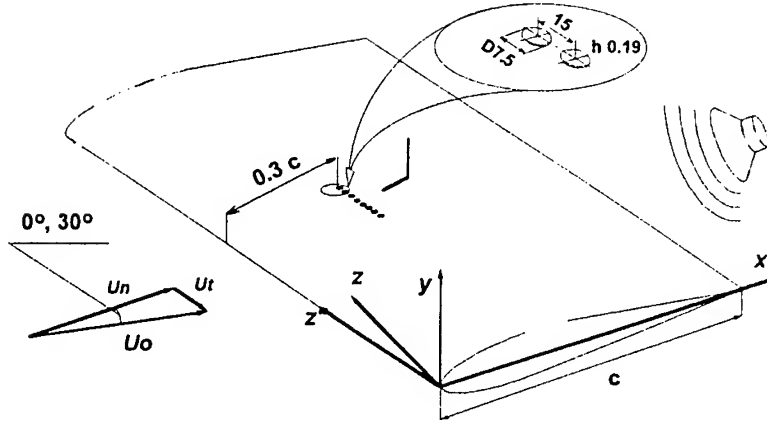


Figure 1. Scheme of the experimental set-up and coordinate system used.

source was implemented. To map the flow patterns in the disturbed boundary layer the measurements were triggered with this sound by microphone. To control the spanwise variation in wave amplitude in order that the structure of the three-dimensionality of transitional processes could be reliably studied in detail, the roughness array was created on the wing surface. The roughness array consisted of 10 cylindrical humps (7.5 mm diameter and 0.19 mm height) along the leading edge with spacing of $\Delta Z_o = 15$ mm. Position of humps at the chord region $X/c = 0.30$, where the pressure gradient changed its sign from negative to positive, was chosen for best receptivity to acoustic field. The local Reynolds number based upon the displacement thickness Re_{δ^*} at position of humps was about 600 and 640 for straight and swept wing configuration respectively, which corresponded to boundary layer thickness δ of 1.94 and 2.33 mm. Detailed mapping of flow were made by a single, constant temperature hot-wire. For mean crossflow field measurements V-shape two-wire probe have been used, rather than X-type, in order to avoid difficulty from the steep gradients across the layer. The separation between centres of the wires in the V-wire arrangement was 1.2 mm. Signal from hot-wire anemometer have been triggered with external sound, ensemble averaged (more than 300 averaging series have been applied) and stored in a PC for a subsequent analysis.

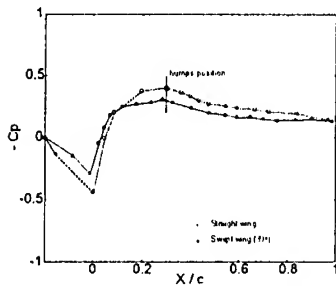


Figure 2. Chordwise pressure coefficients distribution for straight and swept wing configurations.

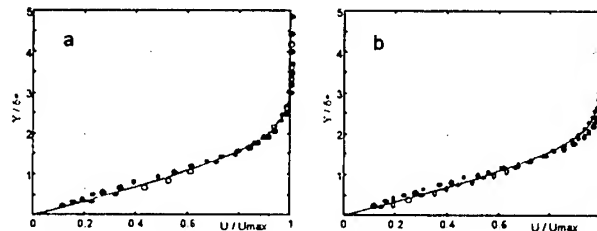


Figure 3. Mean streamwise velocity profiles on straight (a) and swept (b) wings compared with Blasius profiles. $X/c = 0.32$ — open circle symbols, $X/c = 0.48$ — filled circle symbols.

As noted above, a weak adverse pressure gradient was established on the wing surface in the measurement region. (see Fig. 2). Magnitude of pressure gradient parameter $dC_p / d(X/c)$ was less than 0.9 in both cases. In the range of $X/c = 0.5-0.7$ the low of the pressure grow was almost equal. Distribution of C_p does not demonstrate any local separation of the flow. Figure 3 shows profiles of undisturbed mean streamwise velocity measured at $X/c = 0.32$ and 0.48 compared with Blasius. At first streamwise position the profiles are full, but later they demonstrate inflectional point for both straight and swept wing configuration. In both cases the external sound field have been transformed by roughness elements to eigen waves of frequency F_0 in boundary layer. Disturbances have grown downstream with formation of full turbulence at $X/c = 0.9$. Spectra of time traces on Fig. 4 demonstrates disturbance of frequency F_0 at $X/c = 0.6$, growth of high-frequency spectral modes at $X/c = 0.7$ and complete randomization of the flow at $X/c = 0.9$ for both straight and swept wing configurations. It can be concluded from this figure that transition on straight wing arises little bit earlier than on swept wing due to higher pressure gradient. The time traces have been measured in boundary layer at constant distance Y from the wing. Position on Z coordinate corresponded to centre of a roughness element.

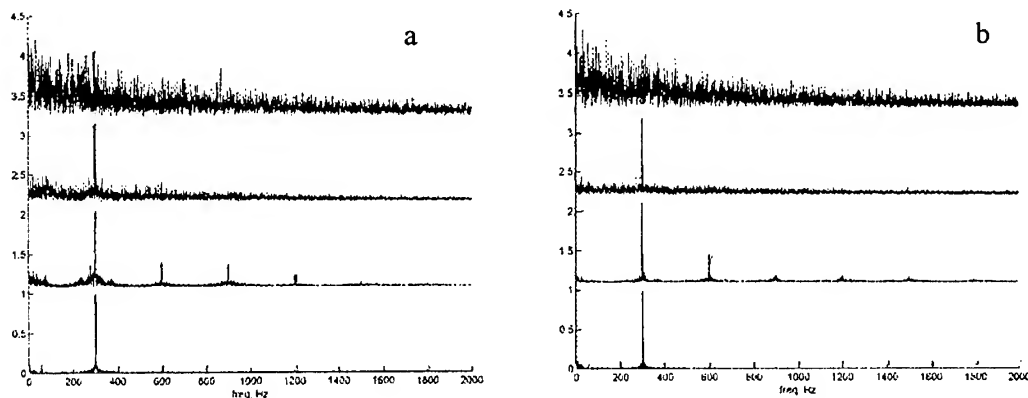


Figure 4. Amplitude-frequency spectra of hot-wire anemometer signal time traces measured in straight (a) and swept (b) wing flows for different positions from noise $X/c = 0.6, 0.7, 0.8, 0.9$. $Y = \text{const}$. All spectra are undimensionalised by their maximum value.

More detail investigation showed that in boundary layer modulated wave grows (see Fig. 5, b). The amplitude maxima of this wave have been located at position of spacers ($Z\beta_0 = 1, 2, \dots, \beta_0 = 1 / \Delta Z_0$). At downstream position $X/c = 0.48$ amplitude of wave was detectable and corresponds to $0.39\% U_\infty$ and $0.27\% U_\infty$ for straight and swept wing respectively, there U_∞ — streamwise velocity of inviscid flow. Phase velocity of wave was measured of $0.41U_0$ with the wave front along wing's leading edge. In the case of straight wing configuration the spanwise modulation of wave was symmetrical and corresponded to combination of plane spectral mode $(F_0, 0)$ and two oblique modes $(F_0, \pm \beta_0)$ in Fourier space. In the case of swept wing the modulation was non-symmetrical and corresponded to combination of plane spectral mode $(F_0, 0)$ with only one oblique mode (F_0, β_0) . Disturbances grew downstream with formation of 'peaks' and 'valleys' in transversal direction with high amplitudes of perturbations in peak positions. At $X/c = 0.66$ (Fig. 5, a) nonlinear stage of disturbance development are shown. Amplitude of disturbances is more than 15% of U_∞ . In straight wing boundary layer

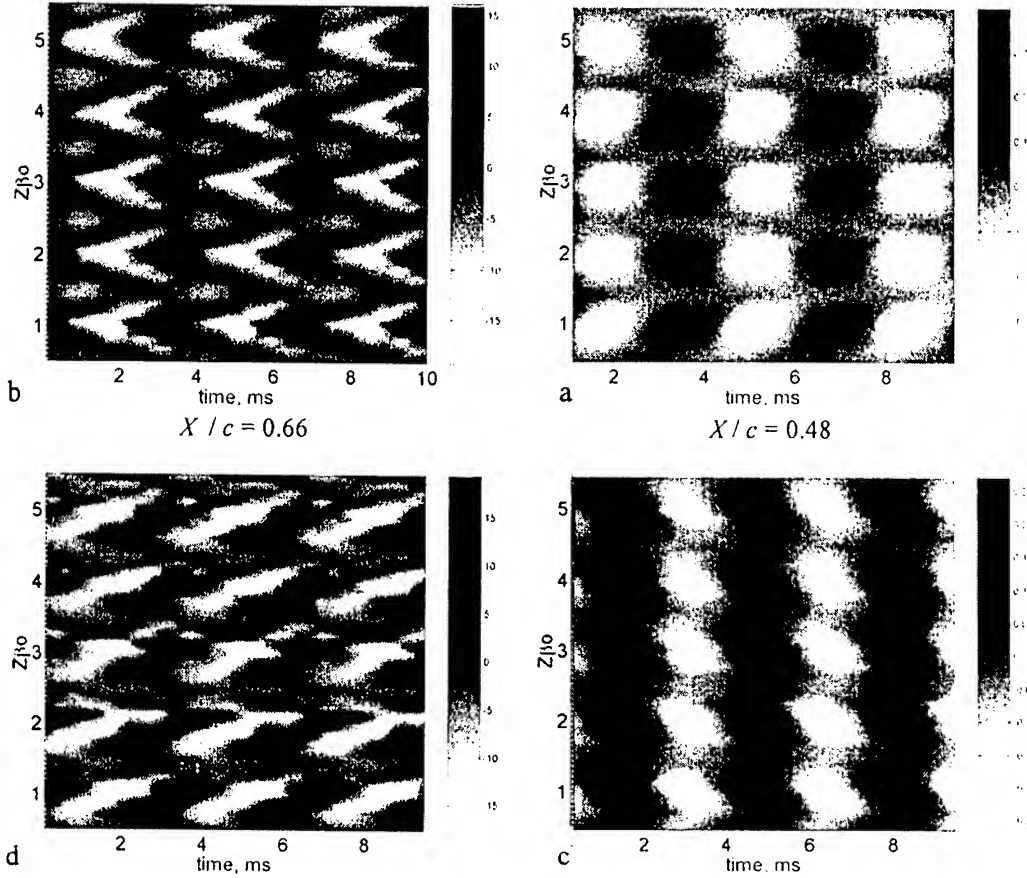


Figure 5. Patterns of instantaneous streamwise velocity disturbance in (t, z) -planes which shows the scenario of transition in straight (a, b) and swept (c, d) wing flows. $X/c = 0.48$ (a, c), $X/c = 0.66$ (b, d).

well-defined Λ -structures are forming as in experiments of Klebanoff [2]. In swept wing case non-symmetrical structures is observed. It should be noted that non-symmetry was changed its sign if compared with $X/c = 0.48$. Fourier decomposition shows that modes $(F_o, \pm 2\beta_o)$ growth in the case of straight wing (formation of 'legs' of Λ -structures) and more complicated development in swept wing case. In this case process of disturbance development included damping of initial (F_o, β_o) mode with process of amplification of anti-symmetrical mode $(F_o, -\beta_o)$. Later, when mode (F_o, β_o) was damped, the grow of mode $(F_o, -2\beta_o)$ with $(F_o, 0)$ damping was observed. Disturbance shown on (Fig. 5, d) composed mainly from modes $(F_o, 0)$, $(F_o, -\beta_o)$ and $(F_o, -2\beta_o)$. Non-symmetry of disturbances in the case of swept wing configuration can be explained by presence of crossflow. Earlier it have been shown in study of Grek et al. [13] that crossflow cause of formation of non-symmetry in streaky-structures, which was generated by injection trough transversal slot on the surface of swept wing. To support this idea the detailed measurements of crossflow have been made (Fig. 6). This

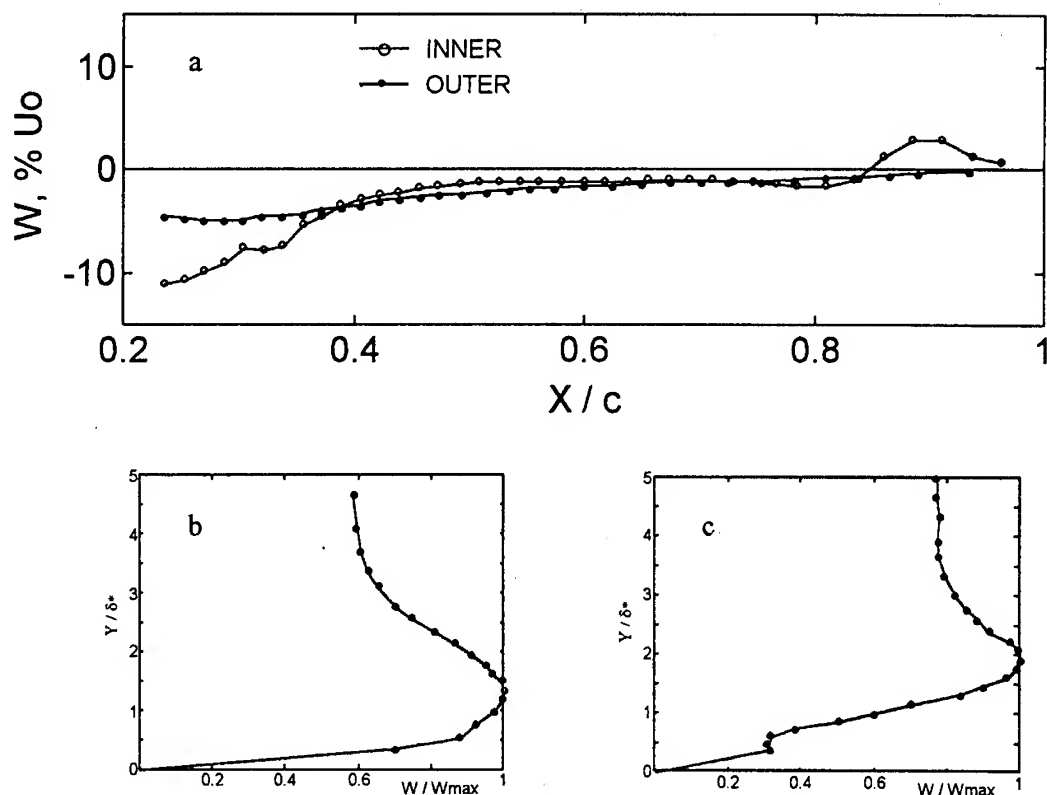


Figure 6. Results of crossflow measurements on swept wing. Chordwise mean crossflow distribution (a) for inviscid flow (OUTER) and inside boundary layer (INNER) for Y position corresponds to $W = W_{max}$. Distribution of mean crossflow velocity across boundary layer: $X/c = 0.32$ (b) and $X/c = 0.48$ (c).

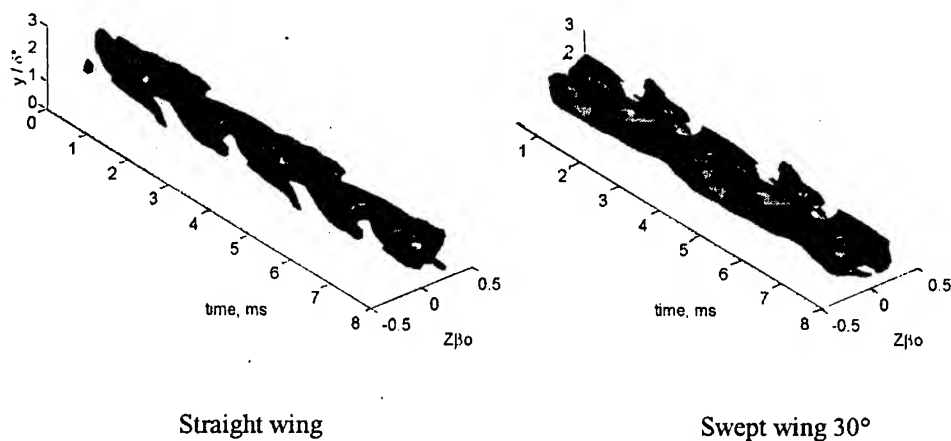


Figure 7. Isosurfaces of instantaneous streamwise velocity disturbance of $u = 8 \% U_\infty$ — dark shading, $u = -8 \% U_\infty$ — light shading. $X/c = 0.66$. Λ -structures in straight wing flow (a), non-symmetrical structures in swept wing flow (b).

measurements showed that crossflow component of velocity have taken place all over in boundary layer of swept wing. At $X/c = 0.3$ where the roughness elements have been placed magnitude of this component of velocity was about 10 % of U_o inside boundary layer and about 6 % of U_o at outer edge of boundary layer. Downstream the crossflow component was about constant from $X/c = 0.5$ to $X/c = 0.8$ with magnitude of 3 % of U_o . The step on INNER curve at $X/c = 0.3$ because of streamlines displacement by roughness elements. After $X/c = 0.85$ the crossflow component of velocity change sign from negative to positive. Maximum of this component across boundary layer is lifted up downstream.

A detailed measurements of the streamwise velocity field in (Y, Z) plane help for understanding of complicated nature of K-type of breakdown on real wings. Figure 7 shows Λ -structures in (Y, Z, t) coordinates for straight wing and non-symmetrical structures for swept wing flow. It is clear that structures in both cases are different not only for one special Y -position but across the boundary layer. Due to the crossflow, the temporal-spatial structures of the disturbed flow field over swept wing have revealed significant differences in K-type transition to turbulence.

References

1. Reed H.L., Saric W.S. Stability of three-dimensional boundary layers// *Annu. Rev. Fluid. Mech.* 1989. Vol. 21. P. 235–284.
2. Klebanoff P.S., Tidstrom K.D., Sargent L.M. The three-dimensional nature of boundary layer instability // *J. Fluid Mech.* 1962. Vol. 12. P. 1–34.
3. Kachanov Y.S., Kozlov V.V., Levchenko V.Y. Nonlinear development of a wave in a boundary layer // *Izv. Akad. Nauk SSSR, Mekh. Zhidk. Gaza.* 1977. Vol. 5. P. 85-94 (in Russian). Transl. in: *Fluid Dyn.* 1978. Vol. 12. P. 383–390.
4. Saric W., Kozlov V., Levchenko V. Forced and unforced subharmonic resonance in boundary layer transition. *ALAA Paper No. 84-0007*, 1984.
5. Hama F., Nutant J. Detailed flow-field observations in the transition process in a thick boundary layer // *Proc. Heat Transfer and Fluid Mech. Inst. Stanford Univ. Press, CA.* 1963. P. 77–93.
6. Kachanov Y.S., Kozlov V.V., Levchenko V.Y., Ramazanov M., Experimental study of the K-regime breakdown of a laminar boundary layer: Preprint No. 9-84 / *Inst. Theoret. Appl. Mech., USSR Acad. Sci., Sib. Branch. Novosibirsk*, 1984 (in Russian).
7. Herbert T. Secondary instability of boundary layers // *Annu. Rev. Fluid Mech.* 1988. Vol. 20. P. 487–526.
8. Rist U., Fasel H., Direct numerical simulation of controlled transition in a flat-plate boundary layer // *J. Fluid Mech.* 1995. Vol. 298. P. 211–248.
9. Kozlov V.V., Levchenko V.Y., Saric W. S. Formation of three-dimensional structures in a boundary layer at transition: Preprint No. 10-83 / *Inst. Theoret. Appl. Mech., USSR Acad. Sci., Sib. Branch. Novosibirsk*, 1983 (in Russian).
10. Bake S., Fernholz H.H., Kachanov Y.S. Resemblance of K- and N-regimes of boundary layer transition at late stages // *Eur. J. Mech. B – Fluids*. 2000. Vol 19. P. 1–22.
11. Fasel H. Numerical simulation of instability and transition in boundary layer flows // *Laminar Turbulent Transition / Eds D. Arnal, R. Michel. Heidelberg et al.: Springer-Verlag*, 1990. P. 587–598.
12. Laurien E., Kleiser L. Numerical simulation of boundary layer transition and transition control // *J. Fluid Mech.* 1989. Vol. 199. P. 403–440.
13. Grek G.R., Katasonov M.M., Kozlov V.V., Chernoray V.G. Modelling of streaky-structures in two- and three-dimensional boundary layers: Preprint No. 2-99 / *Inst. Theoret. Appl. Mech., Russian Acad. Sci., Sib. Branch. Novosibirsk*, 1999 (in Russian).

IMPINGING SHOCK WAVE / FLAT PLATE TURBULENT BOUNDARY LAYER INTERACTION AT $M = 5$ (EXPERIMENTS AND COMPUTATIONS)

N.N. Fedorova and I.A. Fedorchenko

Institute of Theoretical & Applied Mechanics,
SD of Russian Academy of Science, Novosibirsk, 630090, Russia

E. Schüle

German Aerospace Center DLR,
Institute of Fluid Mechanics, 37073 Göttingen, Germany

1. Introduction

The mathematical modeling of the shock wave / turbulent boundary layer interactions is an actual and difficult task of the computational fluid dynamics. The most complicated cases are those where the separation zone appears as a result of the interaction. The choice of the computational method and the way of turbulence modeling is important for good prediction of the physical particularities of the flows in question. So the program code and turbulence model validation is the necessary stage of the mathematical modeling of these complex aerodynamical problems. For this reason, the detailed experimental information is required that includes not only the surface pressure but also skin friction and heat transfer distributions, as well as the fields of mean gasdynamical parameters and turbulent characteristics.

The results of joint experimental and numerical investigations are presented in the paper on the two-dimensional Incident Shock Wave / Turbulent Flat Plate Boundary Interaction at $M = 5$. The problem was chosen for investigation because of the following reasons:

- the configuration is simple but still closely related to the problem of the hypersonic transport systems;
- there are no data in sufficient detail available for this configuration and Mach numbers;
- the investigated Mach number provides for compressibility effects which must be accounted for in the turbulence model utilized.

In spite of the fact that the same problem was considered experimentally and theoretically in numerous papers (see the survey in ref. [1]), it should be noted here that the authors of [1] had considered at least 18 known to the moment experimental works on this problem and rejected to include any of these data in the Hypersonic Shock / Boundary – Layer Interaction Database being created to give the necessary material for the turbulence model and computational code verification. This fact was the reason to start the new experimental investigation, that could provide the CFD community with a full set of reliable experimental data. The first part of the detailed validation experiments [1] contains the surface pressure distributions together with the mean boundary layer parameters and the flow shadowgraphs for turbulent boundary layer/shock wave interaction on a flat plate with different degree of flow separation. The experiments [1] were used as the basic test case for the numerical result validation in the scope of the ESA/ESTEC-project [2]. The comparison of results using the different codes at FFA (Sweden), München Technical University (Germany) and Dassault Aviation (France) with different levels of turbulence modeling has revealed the problems in the high speed separated flows prediction. New complete Explicit Algebraic Turbulence Model (EARSIM) based on the $k - \omega$ two-equation model was recommended as that given the best overall prediction of the validation test cases. But some deficiencies of the numerical results were also demonstrated, for example, the lag in the pressure rise prediction or poor agreement in the strongly non-equilibrium turbulent situations. It was concluded in [3], that the results of

[1] is a very valuable contribution to the database of high speed validation test cases and it should be complemented with new quantitative measurements, such as the optical skin friction measurements in the separation zone.

The present paper is the next stage in this series that includes the new experimental data on the skin friction and heat transfer measurements

2. Experimental conditions and techniques

Experiments were conducted in the supersonic/hypersonic Ludwig – Tube (RWG) of DLR at Göttingen under following conditions: Mach number $M = 5$, total temperature $T_0 = 410$ K, total pressure $P_0 = 21.2$ bar, unit Reynolds number $Re = 40 \cdot 10^6 \text{ m}^{-1}$. The wall temperature of test model was 300 ± 5 K during the run.

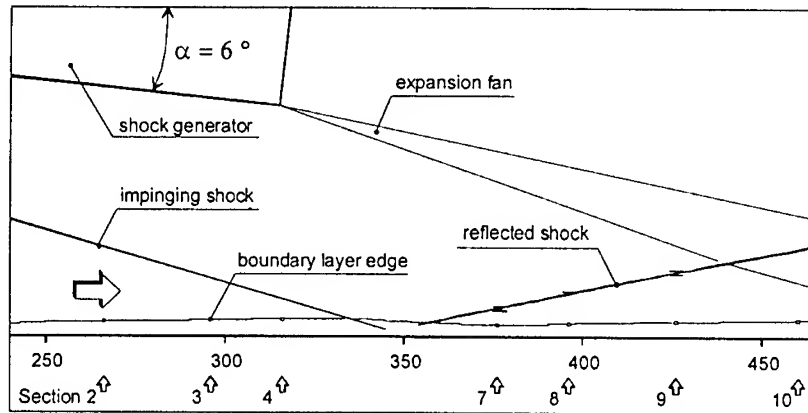


Fig. 1. The flowfield scheme at $\alpha = 6^\circ$

The cases $\alpha = 0^\circ$ (without shock generator), 6° , 10° and 14° were considered. Flow patterns in the interaction region depend on the generator angle and include both attached (6°) and separated (10° , 14°) flows. The quantitative flowfield scheme of the flow investigated is presented in the Fig. 1 for the case without separation (6°), obtained from the shadowgraphs as well as by the analysis of pitot, static pressure and velocity profiles surveys in the specific sections 2 – 10. The distance from the leading edge of the plate (in mm) is shown at the bottom of Fig. 1. The experimental data include the flow shadowgraphs, the surface pressure, skin friction and heat transfer distributions as well as the temperature, velocity and density profiles in the sections 2 – 4 before the interaction and in sections 7 – 10 downstream the interaction, that makes good basis for the computational result validation.

For the wall pressure measurements 67 static pressure taps were located in the different intervals from 2 to 20 mm along the lines in the streamwise as well as in spanwise directions. The taps were connected to a 32-port PSI ('PRESSURE SYSTEMS INC.') pressure transducer module with a measurements range of ± 15 psi (± 103400 Pa). The rated accuracy is quoted by the manufacturer to be of the order of ± 0.1 % full scale output (± 100 Pa) or ever better.

Pitot and static pressures in the boundary layer and freestream were measured by the corresponding probes. The survey mechanism and special optical equipment were used for a precise positioning of the pressure probes. That achieved the precision of probe position during the test run to be within ± 0.05 mm in y-direction or better. The pressure probes were attached to an ENDEVCO Model 8514–10, ENDEVCO Model 8514–20 or KULITE Model XTC-190M-x3.5bar VG pressure transducer, located directly at the back of the probe (ENDEVCO

transducers) or underneath the plate, connected with a 120 mm length of tubing (KULITE transducer). The rated accuracy is quoted by the manufacturer to be of the order of $\pm 0.2\%$ FSO (ENDEVCO 8514-10), $\pm 0.3\%$ FSO (ENDEVCO 8514-20) and $\pm 0.5\%$ FSO (KULITE transducer). The measured pitot and static pressures were used to determine the Mach number flowfield distributions and further to obtain the velocity, temperature and density profiles in the boundary layer.

For skin friction measurements the oil-film interferometer technique [3] was used, which was modified and adapted for the RWG [4]. This method is based on the relationship between the thinning of an oil film, placed on the test surface exposed to the flow, and the local surface shear τ_w . The rate of thinning of the oil film was determined using the optical interference by measuring the spacing between the fringes in time. The interference pattern were captured by a progressive-scan video camera ADIMEC12P and stored on a PC's hard disk at up to 30 (1024×1024×8 bit) frames per second. For camera control and data reduction the DLR original software was used. Further information on this method may be obtained from [4].

For heat flux measurements the «thin-skin technique» [5] is used. The thin skin of an appropriate model equipped with thermocouples is locally used as a calorimeter. The local heat flux rate q is determined by the transient local temperature rise with time during tunnel run. The heat flux rates thus obtained are non-dimensionalized to Stanton numbers.

3. Mathematical model, boundary condition and method of computations

The computation were performed in ITAM, Novosibirsk, on a base of the full unsteady 2-D Favre-averaged Navier – Stokes equations in strong conservation form closed by the Wilcox $k - \omega$ turbulence model [6]. The full set of the governing equations and turbulence model can be found, for example, in [7].

The steady-state solutions of the problem in question were obtained with the help of four-step implicit finite-difference scheme of splitting according to the space directions for the time discretization, which is realized by scalar sweeps. The third order TVD-type schemes based on Flux Vector Splitting were used to approximate the inviscid fluxes space derivatives. Viscous terms were differenced to the second order accuracy in a centered manner. The details of scheme used in the computations are described in [8].

The mean quantities were made dimensionless with the help of undisturbed flow parameters: $\bar{u} = u/U_\infty$, $\bar{\rho} = \rho/\rho_\infty$, $\bar{T} = T/(c_v U_\infty^2)$, $\bar{p} = p/(\rho_\infty U_\infty^2)$, where, c_v is specific heat at

constant volume, $c_v = 715$ J/kg·K, $U_\infty = 825$ m/s, $\rho_\infty = 0.215$ kg/m³. The computation domain does not include the generator, and was restricted by the plate surface and the upper, inlet and outlet sections chosen far enough from the interaction zone (see Fig. 2). The mean velocity, density and temperature profiles at the inlet 1 section were generated with boundary layer code to match the experimental boundary layer integral

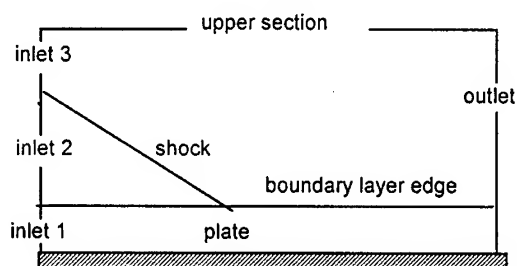


Fig. 2. The sketch of computation domain

parameters and skin friction prior the interaction. At the inlet 2 section the free-stream boundary condition was specified: $\bar{u} = 1$, $\bar{\rho} = 1$, $\bar{T} = 0.072$. The special conditions obtained from the exact solution of the inviscid problem were specified at the inlet 2 section to model the generator effect. For $\alpha = 6^\circ$ it is $\bar{u} = 0.983$, $\bar{v} = -0.1$, $\bar{\rho} = 1.66$, $\bar{T} = 0.09$, for $\alpha = 10^\circ$ it is

$\bar{u} = 0.95, \bar{v} = -0.17, \bar{\rho} = 2.1, \bar{T} = 0.105$ and for $\alpha = 14^\circ$ it is $\bar{u} = 0.91, \bar{v} = -0.23, \bar{\rho} = 2.63, \bar{T} = 0.12$. The “simple wave” boundary conditions were set at the upper section. At the outlet section so called “soft” boundary condition (zero second derivatives of all the calculated parameters) were specified. On the plate surface, the no-slip boundary condition for velocities were used. To match the experimental condition, the constant temperature $T = 300$ K was set: The density at the plate surface was calculated using zero pressure gradient condition.

A fixed regular grid was constructed in the computation domain with exponential stretching near the plate surface. The stretching parameter was chosen to satisfy the condition $y^+ < 1$, where y^+ is the wall law variable. In the most of the computations the grid consists of 200 points in the streamwise direction and 150 points in the normal to the surface direction. Special case of more fine grid was used to shows the convergence o computational results.

4. Experimental and computational results

Figure 3 present the experimental and computed surface pressure distributions for all three cases of generator angle: $\alpha = 6^\circ, 10^\circ, 14^\circ$. Figure 3 shows rather good coincidence of experimental (symbols) and computed (lines) distributions in the region of shock wave/boundary layer interaction. In the Fig. 4 the computed and experimental skin frictions distribution are compared. Note, that the open markers are for the velocity profile data and closed markers are for data obtained using oil-film interferometer technique. Figure 4 demonstrates that the computations predict the skin friction distributions well except the strongest interaction case, where the level of skin friction after the interaction is underpredicted.

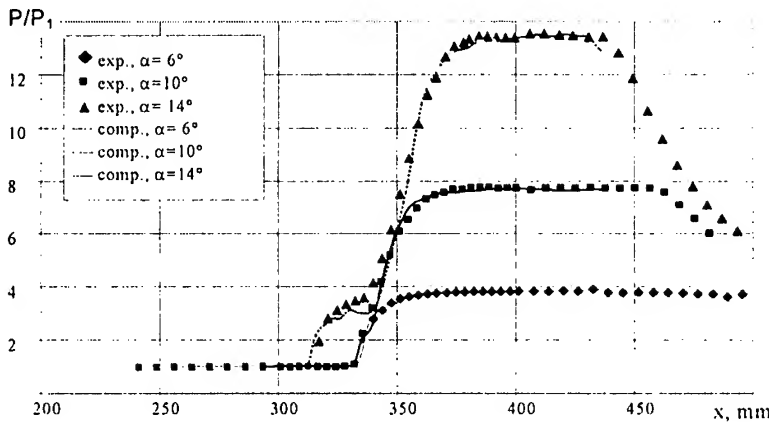


Fig. 3. Experimental and computed surface pressure distributions for $\alpha = 6^\circ, 10^\circ, 14^\circ$

The next series of the figures shows the velocity, temperature and density profiles at various cross-sections. The sections No. 2 ($x = 266$ mm) and No. 3 ($x = 296$ mm) are before the interaction while the sections No. 7 ($x = 376$ mm), No. 8 (396 mm) and No. 9 (426 mm) lie after the interaction. Figs. 5 and 6 present the temperature and mean velocity profiles for the unseparated flow case $\alpha = 6^\circ$.

Figures 7, 8 show the experimental and computed density and velocity profiles for the case $\alpha = 10^\circ$ at various cross-section and exhibit the slight disagreement on the boundary layer thickness at the section 9. The significant experimental and computed velocity profiles discrepancy at the section 8 can be caused by the turbulence model by the turbulence model and computational algorithm drawbacks and errors of the experimental measurements.

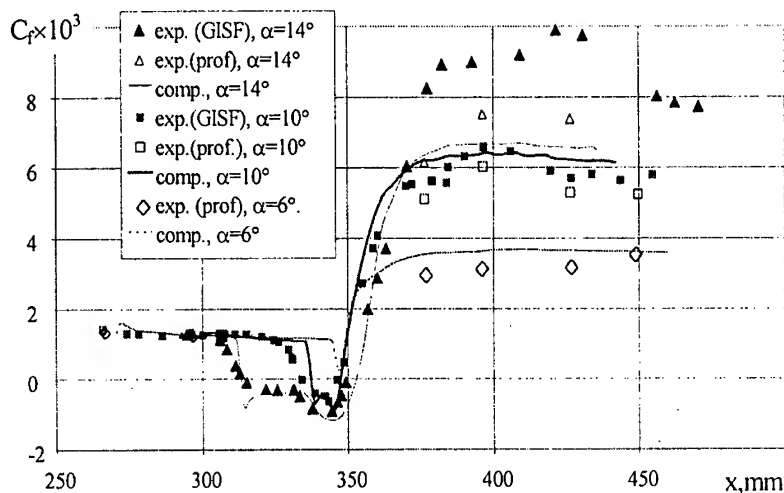


Fig. 4. Experimental and computed skin friction distributions for $\alpha = 6^\circ, 10^\circ, 14^\circ$

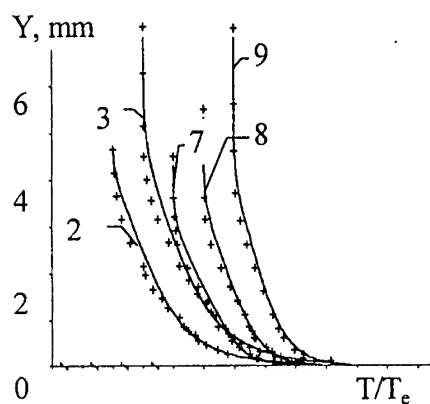


Fig. 5. Experimental and computed temperature profiles at various cross-sections for $\alpha = 6^\circ$

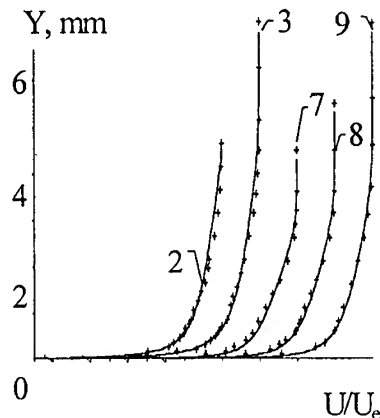


Fig. 6. Experimental and computed velocity profiles at various cross-sections for $\alpha = 6^\circ$

The strengthening of the interaction leads to a stronger computation and experimental data disagreement, that confirm the Figs. 9, 10, in which the velocity and temperature profiles for the case $\alpha = 14^\circ$ are presented.

Fig. 11 presents the comparison of the experimental and computed Stanton numbers for all three cases investigated. It should be mentioned that for $\alpha = 6^\circ$ the computed results are in good agreement with the experiments. For the $\alpha = 10^\circ$ case the computation overpredicts the heat transfer level just after the reattachment point, that is caused by the high turbulent viscosity values. Further downstream the level of heat transfer drops to the slightly underpredicted value comparing to the experiments. For the case of the strongest interaction, a smaller upstream shock influence is observed in calculation despite of the fact that size of separated zone is

predicted rather good. The effect of overpredicted Stanton number after the reattachment with the further too strong drop described for previous case also takes place here.

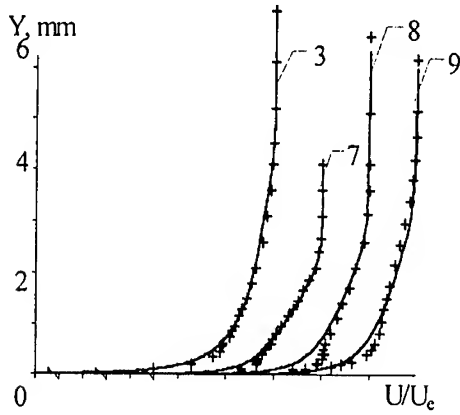


Fig. 7. Experimental and computed velocity profiles at various cross-sections for $\alpha = 10^\circ$

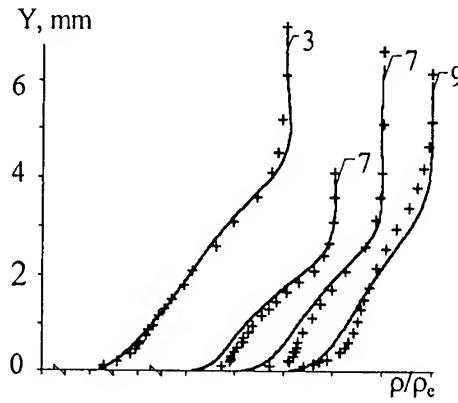


Fig. 8. Experimental and computed density profiles at various cross-sections for $\alpha = 10^\circ$

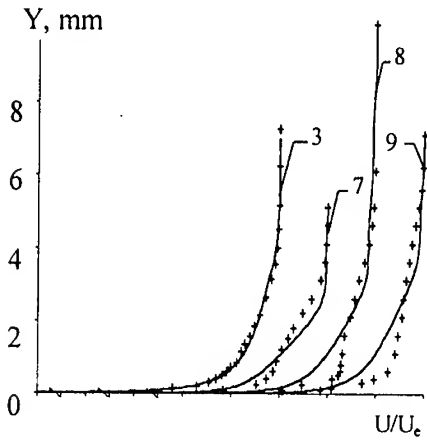


Fig. 9. Experimental and computed velocity profiles at various cross-sections for $\alpha = 14^\circ$

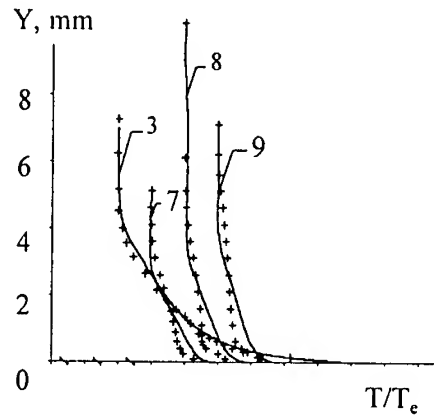


Fig. 10. Experimental and computed temperature profiles at various cross-sections for $\alpha = 14^\circ$

6. Conclusions and future work

The comparison of experimental and theoretical (computed) results having done in the paper shows the ability of the $k-\omega$ turbulence model and computation algorithm to predict the flowfield picture, pressure distribution and skin friction for all three interaction cases of oblique Shock Wave/Turbulent Boundary Layer Interaction. In the case of slight and moderate interaction the close agreement was demonstrated for the Stanton number distribution as well as the velocity, density and temperature profiles after the interaction. The main disagreement in the 14° case is the underpredicted skin friction and heat transfer level after reattachment and the underpredicted boundary layer thickness. The possible reason of this disagreement is the turbulence model inability to describe properly the turbulence intensity growth after interaction

with the strong shock wave. Another possible reason of this disagreements may be the fact that the computational model does not take into account all the factors of the real physical problem such as the acoustic perturbations coming to the region of interests from the boundary layer developing on the generator surface.

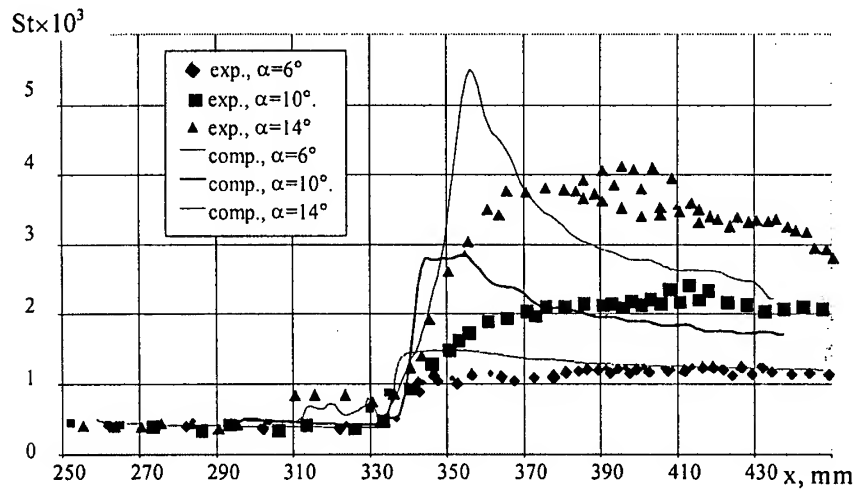


Fig. 11. Experimental and computed Stanton number distributions for $\alpha = 6^\circ, 10^\circ, 14^\circ$

The future work plan consists of the another turbulence model utilization to properly modeling of the effect of turbulence intensity rise in the region of Shock Wave / Boundary Layer Interaction. Some investigation is also designed on taking the external disturbances into account.

7. Acknowledgements

The investigations were supported by the Russian Foundation for Basic Research in a frame of the projects No. 99-01-00565 and by the ESA Contract No. 11018/94/NL/FG/(SC).

References

1. Schüle E., Krogmann P., Stanewsky E. Documentation of two-dimensional impinging shock/turbulent boundary layer interaction flow. – DLR Forschungsbericht. IB 223 - 96 A 49. October, 1996. 69 p.
2. Settles G.S., Dodson L.J. Hypersonic shock / boundary – layer interaction database // AIAA J. 1994. Vol. 32., No.7. P. 1377 - 1383.
3. Lindblad I.A.A., Wallin S., Johansson A.V., Friedrich R., Lechner R., Krogmann P., Schüle E., Courty J.-C., Ravachol M., Giordano D. A prediction method for high speed turbulent separated flows with experimental verification. AIAA-98-2547, 1998. 12 p.
4. Tanner L., Blows L. A study of the motion of oil films on surfaces in an air flow, with application to the measurement of skin friction // J. Phys. E.: Sci. Instrum. 1976. Vol. 9. P. 194–202.
5. Schüle E., Koch S., Rosemann H. Skin friction measurement and transition detection techniques for the Ludwig – Tubes at DLR // AGARD CP-601, AGARD FDP Symp. "Advanced Aerodynamic Measurement Technology", Seattle, USA, September 22–25, 1997. P. 23-1 – 23-9, AGARD, 1998.
6. Krogmann P. An experimental study of boundary layer transition on a slender cone at Mach 5 // AGARD FDP Symp. «Laminar-Turbulent Transition», Lyngby, Denmark, 2 – 4 May, 1977, AGARD, 1977. P 26-1 – 26-8, CP – 224.

-
7. Wilcox D.C. Reassessment of the scale-determining equation for advanced turbulence models // AIAA J. 1988. Vol. 26, No. 11. P. 1299– 1310.
 8. Knight D.D. Numerical solution of compressible turbulent flows using the Reynolds-averaged Navier — Stokes equations: Turbulence in compressible flows. AGARD Rep. No. 819, 1997. P. 5-1– 5-52.
 9. A.V. Borisov, N.N. Fedorova, Numerical simulation of turbulent flows near the forward-facing steps // Thermophysics and Aeromechanics. 1996. Vol. 3, No. 1. P. 69– 83.

GASDYNAMIC AND ELECTRIC PHENOMENA ON GLOW DISCHARGE IN SUPERSONIC AIR FLOW

V. M. Fomin¹, Th. Alziary de Roquefort², A. V. Lebedev¹, and A. I. Ivanchenko¹

¹ Institute of theoretical and applied mechanics, 630090 Novosibirsk, Russia

² Laboratoire d'études aérodynamiques - UMR CNRS № 6609, 86036 Poitiers, France

The self-maintained glow discharge has long been in use in aerodynamic studies [1]. It can be employed for visualizing rarefied supersonic flows for which the effectiveness of conventional shadow methods becomes low. As a rule, the discharge normally used in such experiments is a low-current one since its intensity should not induce substantial disturbances into the flow under study. Recently, special interest has been expressed to studies in which a strong-current glow discharge was used to exert an active influence on a supersonic gas flow [2 – 5]. However, the total number of works devoted to this research area still remains low. Nevertheless, it is well established that a glow discharge with a high density of current can profoundly reconstruct supersonic streams. In particular, an appreciable change in the wave pattern of the flow around blunt axisymmetrical bodies was observed. At present, there is no definite model furnishing adequate explanation to all experimentally observed phenomena arising from the interaction of the non-equilibrium plasma with a supersonic flow and a streamlined body. For such a model to be developed, data as to the gas-dynamic and electrical parameters of the flow of ionized medium around body are required. The present work was aimed at finding such parameters.

A streamwise self-maintained glow discharge was examined. The experiments were conducted in two wind tunnels with a free jet in their working part. The first wind tunnel provided a Mach number of the flow $M_\infty=3.2$, and the other $M_\infty=7.1$. The static pressure was 10.2 mbar in the first case and varied between 6 and 12.8 mbar in the second. The model consisted of two main parts (Fig. 1): an anode and a streamlined body located downstream of it, in the form of a

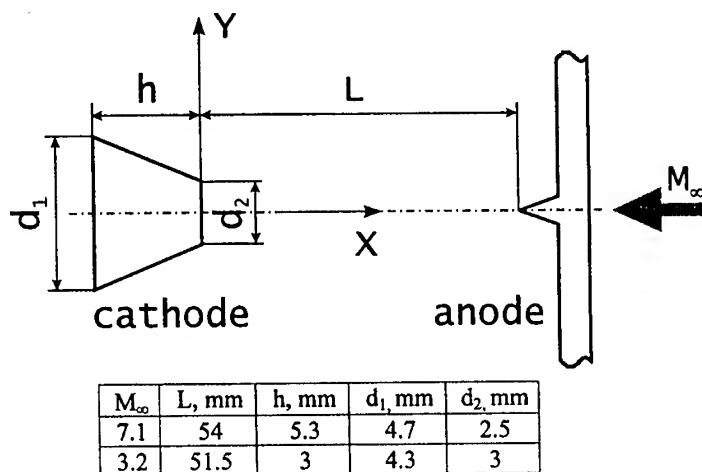


Fig. 1.

cylinder with a forebody serving as a cathode. The anode was made from a metal 0.2 mm-thick plate with a triangle bulge at its rear edge for exact positioning the electric discharge. The forebody-cathode had the shape of a truncated cone. The surface area of the cathode was chosen such that to ensure a glow over the entire surface of the cathode. In all cases, the model was installed at zero incidence. After initiating the discharge, it was glowing steadily throughout the whole experiment. The duration of each experiment was 20 and 10 sec for $M_\infty=3.2$ and 7.1, respectively. Measurements of the discharge current, the voltage drop across the spark gap, the total pressure at the upstream stagnation point on the cathode surface (at the symmetry axis of the model), and the distribution of the stagnation temperature in the discharge were carried out. In addition, shadow visualization and photographing of the visual appearance of the discharge was employed. By measurement of the total pressure behind the normal compression shock, it was shown that the anode disposed in the symmetry plane of the model distorts the pressure compared to the case with removed anode. To eliminate this effect, the anode was offset from the symmetry plane of the model by an adjustable distance, whose average value was 1.5 mm. The stagnation temperature was measured with the help of a Chromel-Alumel thermocouple 0.1 mm in diameter stretched across the flow. To visualize the wave flow pattern, we used the traditional shadow method. In the visualization studies, the knife was installed normally to the flow. Either pulse or uninterrupted sources of light were used. In photographing with uninterrupted and pulse sources, the exposure time was about 10^{-3} s and 4×10^{-6} s, respectively. The color photographing of the outward appearance of the discharged was performed with an exposure time 1/60 s.

The visual appearance of the discharge is shown in Figs. 2a and 2b (for $M_\infty=3.2$ and 7.1,

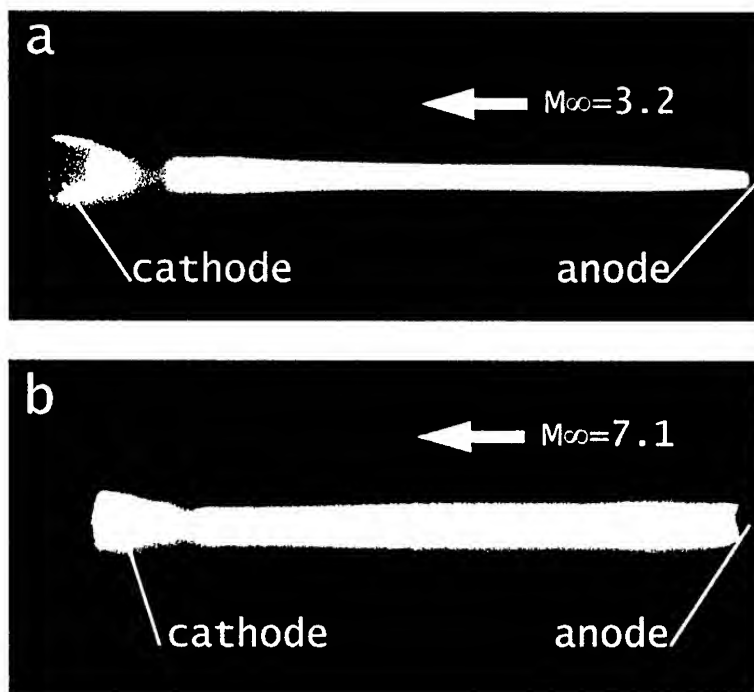


Fig. 2.

respectively). Visually, the discharge structures are similar to each other. In each case, a distinct cathode layer and a main, more extended part situated between the cathode layer and the anode can be distinguished. The cathode layer looks as a blue-violet glow covering the cathode. Its main part in the form of either a cone of large aspect ratio or a cylinder (at $M_\infty=3.2$ and 7.1, respectively) exhibits an orange-rose glowing. The main difference is the following. In the hypersonic flow, the cathode layer is forced against the electrode surface more tightly. At $M_\infty=3.2$, there is a developed transition zone stretching from the cathode layer to the main part of the discharge. It displays a characteristic orange glow and a shape of a truncated cone. In the case of $M_\infty=7.1$, this zone practically vanishes. The mean density of the electric current at the cathode surface, depending on the contributed energy, was $0.08 - 0.35 \text{ A/cm}^2$ or $0.06 - 0.18 \text{ A/cm}^2$, at the main part of discharge was $0.5 - 1.67 \text{ A/cm}^2$ or $1.1 - 3.5 \text{ A/cm}^2$ in the experiments with $M_\infty=7.1$ and 3.2, respectively.

The shadow visualization results are similar to those reported in [5]. The wave pattern for the conditions with a discharge (Fig. 3b) is drastically changed compared to the flow without discharge (Fig. 3a). The stalled bow shock almost completely vanishes. Incident shock waves arising at the periphery of the cathode region have a diffuse front. The high-speed visualization has shown that this behavior is not caused by the unsteady nature of these waves but rather by peculiarities of their interaction with the non-equilibrium discharge plasma. It should be also noted that the region where no shock waves were observed practically coincided with the region occupied by the discharge. The wave pattern was somewhat asymmetric. This asymmetry can be attributed to a displacement of the anode from the model's symmetry plane.

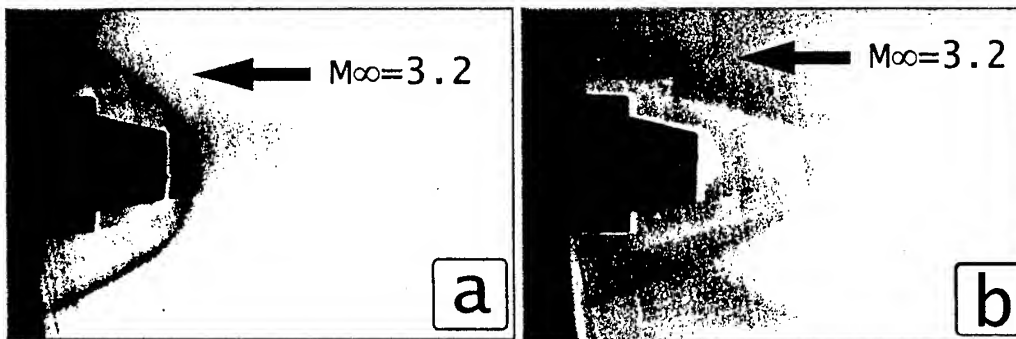


Fig. 3.

The pressure at the symmetry point at the cathode face was measured for different contributed energies, Mach numbers and static pressures in the approaching flow (only for $M_\infty=7.1$). For the hypersonic flow with a discharge, such measurements have been performed for the first time. In the absence of the discharge, the measured pressures were in line with the stagnation pressures behind the normal shock. On initiation of the discharge, a substantial fall in pressure was observed. For instance, for $M_\infty=3.2$ and a discharge power of 120 Wt, the pressure appeared to be diminished by more than eight times. These measurement results are shown in Fig. 4a. It is seen that, for all Mach numbers, the total pressure at the cathode face decreases with increasing the discharge power. On the basis of the curves obtained, a generalizing dependence was deduced which relates the changes in the total pressure at the cathode surface and the free-flow and discharge parameters. For this purpose, two dimensionless parameters were introduced. The

first parameter has the form $(P_{02}/P_{01})/M_\infty$ where P_{02} and P_{01} are the pressures at the cathode surface for the conditions with and without the discharge. The second parameter is the ratio of the total power of the discharge and the flux of the kinetic energy of the outside flow through a certain cross-sectional area. This area was taken equal to the area of the midship section enclosed by the external boundary of the cathode layer. The second parameter has the form $Q_d/Q_f = Q_d/(0.5\rho_\infty u^3 S)$, where Q_d/Q_f is the ratio of the electric power of the discharge to the flux of the kinetic energy, ρ_∞ is the density of the outside flow, u is its velocity and S is the area of the midship section. The experimental results generalized with the help of the above parameters are shown in Fig. 4b. The generalized dependences can be fairly well fitted with a third-order polynomial:

$$(P_{02}/P_{01})/M_\infty = -0.215(Q_d/Q_f)^3 + 0.554(Q_d/Q_f)^2 - 0.458(Q_d/Q_f) + 0.159$$

From the results obtained, a conclusion can be drawn that, given the relative contributed

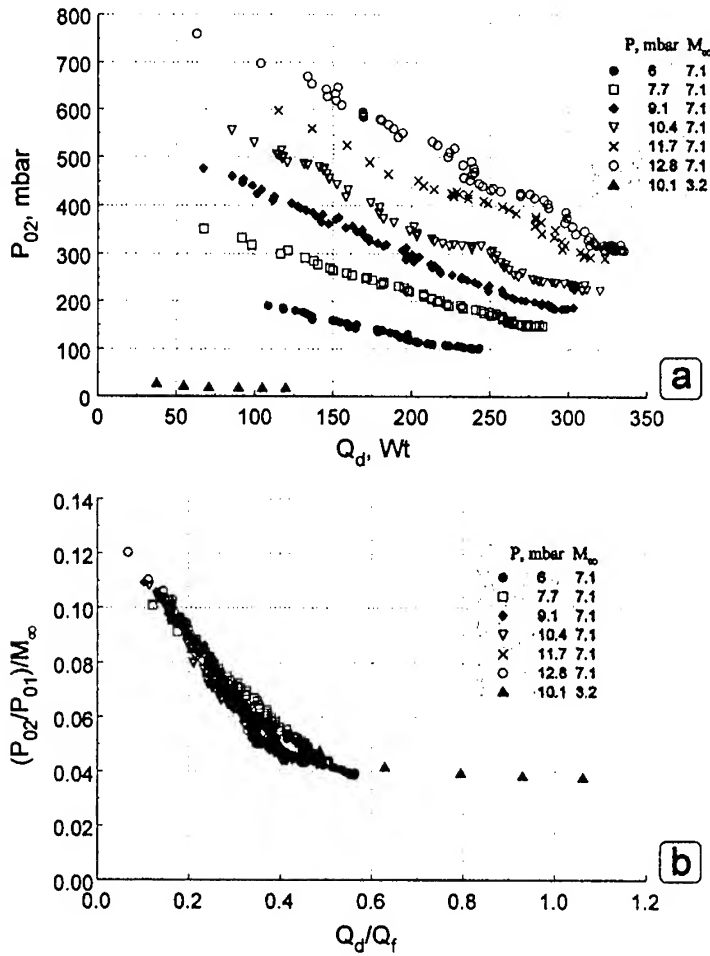


Fig. 4.

energies are identical, the stagnation pressure falls down more rapidly for smaller Mach numbers.

The stagnation temperature in the discharge region is a parameter of primary importance from the viewpoint of gaining better insight into discharge physics. Figures 5a and 5b show the stagnation temperatures measured at the symmetry axis of the discharge as a function of the contributed energy. Here ΔT_0 is the difference between stagnation temperatures in the discharge plasma and in the gas flow without a discharge. As expected, the temperature rises with increasing discharge power. For the case of $M_\infty=3.2$ and $Q_d=115$ Wt, stagnation-temperature

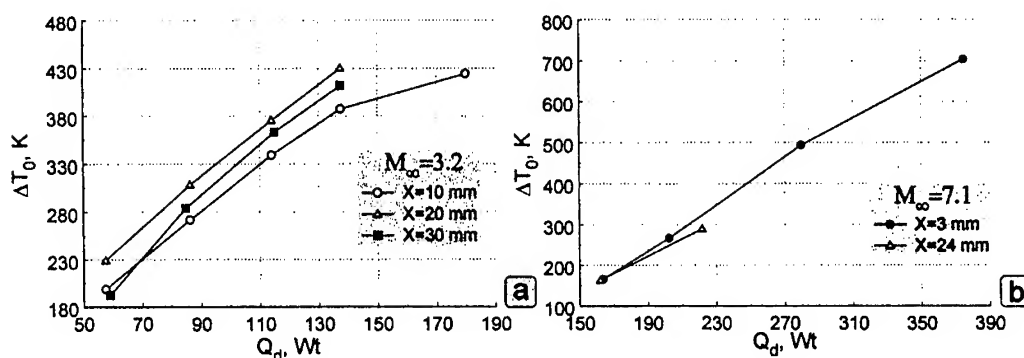


Fig. 5.

profiles over two cross sections located in the cathode region and in the main part of the discharge were measured. These profiles are shown in Fig. 6. Comparison between them and the visual appearances of the discharge shows that the stagnation temperature approaches the

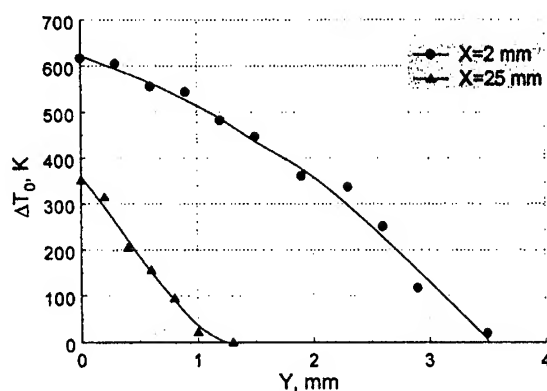


Fig. 6.

free-flow temperature just behind the boundary of the glowing region of the discharge. This observation proves that the region where the thermal energy is released is located inside the glow region of the discharge plasma that emits radiation in the visual spectral region. Figure 7 illustrates variation of stagnation temperature at the discharge axis for the case $M_\infty=3.2$ and $Q_d=115$ Wt. The temperature varies only weakly in the main part of the discharge and it

abruptly rises in the cathode region. This result is correlates well with the previously measured longitudinal distribution of the electric potential (see Fig. 8). The clearly observed voltage drop in the cathode region correlates well with the appreciable rise in temperature in this region. The stagnation temperature measured at the distance 3 mm upstream of the cathode face at $M_\infty=7.1$ is nearly identical to that measured at the middle point between electrodes. At the same time,

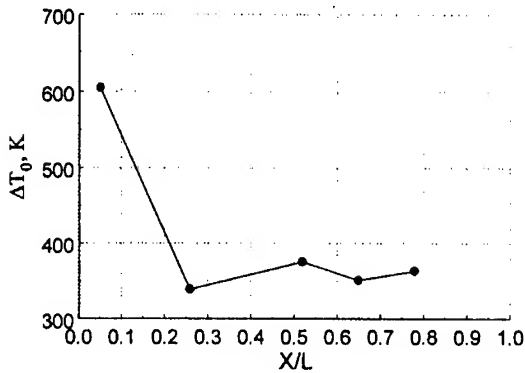


Fig. 7.

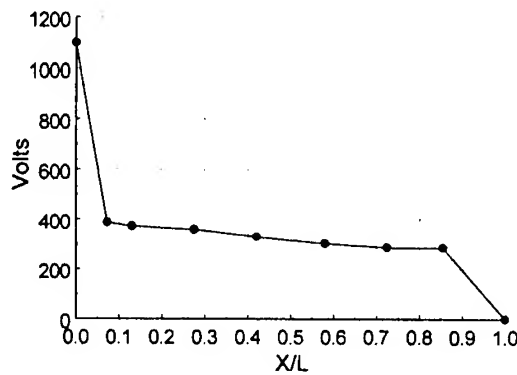


Fig. 8.

the stagnation temperature measured 2 mm away from the cathode at $M_\infty=3.2$, as stated previously, far exceeds the temperature measured in the main part of the discharge. This lends support to the observation, made previously, that at $M_\infty=7.1$ the cathode layer, i.e., the zone of predominant energy release, is pressed against the electrode surface, whereas at $M_\infty=3.2$ it is appreciably displaced upstream.

From the present study, the following conclusions can be drawn. A glow discharge with high current density initiated near a body immersed into an air stream appreciably distorts both the supersonic and hypersonic flow. The latter is manifested in a drastic change of the wave flow pattern resulting from dissipation of the bow shock wave, and also in a notable fall in pressure on the surface of the body. The temperature data cannot provide an adequate explanation of the effects observed solely on the basis of the thermal model.

This work was supported by the Russian Foundation for Basic Research (grant No. 98-02-17936).

References

1. Alferov V.I., Kalachev B.V. Visualization of supersonic flows with the help of prebreakdown discharge. // Zhurnal Prikladnoi Mekhaniki i Tekhnicheskoi Fiziki. 1968. No 4. P. 117-119. (in Russian)
2. Mishin G. I., Serov Yu. L., Yavor I. P. Flow around of sphere at supersonic movement in discharge plasma. // Pisma v ZhTF. 1991. V. 17. No 11. P. 65-71. (in Russian)
3. Mishin G. I., Klimov A. I., Gridin A. Yu. A longitudinal electric discharge in a supersonic gas flow. // Pisma v ZhTF. 1992. V. 18. No 15. P. 86-92. (in Russian)
4. Ganguly B. N., Bletzinger P., Garscadden A. Shock wave damping and dispersion in nonequilibrium low pressure argon plasmas. // Physics letters A. 1997. V. 230. P. 218-222.
5. Fomin V. M., Lebedev A. V., Ivanchenko A. I. Spatial-energetic characteristics of electric discharge in a supersonic gas flow. // Dokladi akademii nauk. 1998. V. 361. No 1. P. 58-60. (in Russian)

INFLUENCE OF A HYPERSONIC AIR FLOW ON ELECTRIC CHARACTERISTICS OF THE SELF-SUSTAINING GLOW DISCHARGE

V. M. Fomin¹, Th. Alziary de Roquefort², A. V. Lebedev¹, and A. I. Ivanchenko¹

¹ Institute of theoretical and applied mechanics, 630090 Novosibirsk, Russia

² Laboratoire d'études aérodynamiques - UMR CNRS № 6609, 86036 Poitiers, France

At present, phenomena being observed during interaction of a self-maintained glow discharge with shock waves in a supersonic gas flows have attracted considerable scientific interest [1-5]. It is established that the glow electric discharge can decrease the amplitude of a shock wave and widen the width of its front [3, 4]. It reconstructs the gas supersonic flow around bodies, the reconstruction being manifested, in particular, in dissipation of the front compression shock [5]. At present, it can be concluded that these phenomena cannot be explained solely within the model of distribution of the neutral-gas temperature [3, 4]. In this connection, a question arises as to the energy characteristics of the supersonic gas flow with a discharge. This question is of great importance from the viewpoint of distinguishing between "non-thermal" effects (related to plasma properties) and "thermal" phenomena.

Previously, we established [5] that, in a streamwise electric discharge with the approach-stream Mach number $M=3.2$, practically all the applied voltage drops across the near-electrode regions. In this case, the distribution of the electric potential over the discharge gap, except for its near-electrode parts, can be described within the non-self-maintained discharge model.

However, it remained absolutely unclear how the energy characteristics of the discharge change with the inter-electrode separation L , static pressure P (density ρ) and approach-stream Mach number M . In the present work, for the first time, data on the effect of the above parameters on the volt-ampere characteristic of the streamwise glow discharge in a hypersonic air flow are reported.

In our experiments, a discharge scheme was used similar to that previously employed in [5]. Into a hypersonic flow with $M=7.1$ or 8.15 and $\rho=2.8 \times 10^{-2} - 5.4 \times 10^{-2} \text{ kg/m}^3$, a streamlined body was immersed. It had the shape of a cylinder, 8 mm in diameter, with a spherical head part, being simultaneously the cathode. The anode, made of a 0.2-mm plate, was disposed upstream, at the distance $L = 21 - 52 \text{ mm}$ from the cathode in the symmetry plane of the model. It had a bulge of a triangular shape at its rear edge for exact positioning of the discharge. Both the plate-anode and the streamlined body-cathode were installed at zero incidence. The high-voltage power supply unit had a full-wave rectifier and no ripple filters. Usually, it took 10^{-2} s for one volt-ampere characteristic to be measured. Since the typical time of gas replacement in the discharge was $2 \times 10^{-5} - 5 \times 10^{-5} \text{ s}$, the volt-ampere characteristics could be considered as steady-state ones. Each experiment was lasted for 10 s, and, usually, about 10^3 volt-ampere characteristics could be taken and automatically recorded for this time.

The discharge in a hypersonic air flow with $M=8.5$ (Fig. 1) practically did not differ in its visual appearance from the $M=7.1$ discharge and was quite analogous to the discharge in the flow with $M=3.2$ described in [5]. The volume part of the discharge (the whole discharge minus its

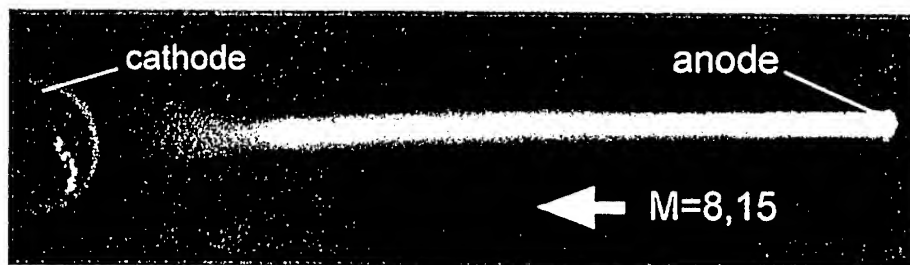


Fig. 1. Visual appearance of the discharge for $M=8.15$.

near-electrode regions) had the shape of a cylinder 3 mm in diameter which gradually transformed into a cone near the nose part-cathode of the model. On the cathode, a cathode layer was formed typical of all kinds of glow discharge. Its thickness, as determined by photographing, amounted to about 0.6 mm. The typical maximum current density at the cathode surface was 0.38 A/cm^2 , and that in the volume part of the discharge was 4.7 A/cm^2 . The geometry of the near-cathode region of the discharge was found to be independent of the inter-electrode separation, while the length of the volume part of the discharge was found to change with it. To visualize the wave flow pattern around the model, we used the shadow method. The results turned out to be similar to those obtained in [5]: under the conditions with the discharge, dissipation of the shock in front of the blunted part of the model was observed.

The volt-ampere characteristics are shown in Figs. 2-4. Each curve was obtained by averaging

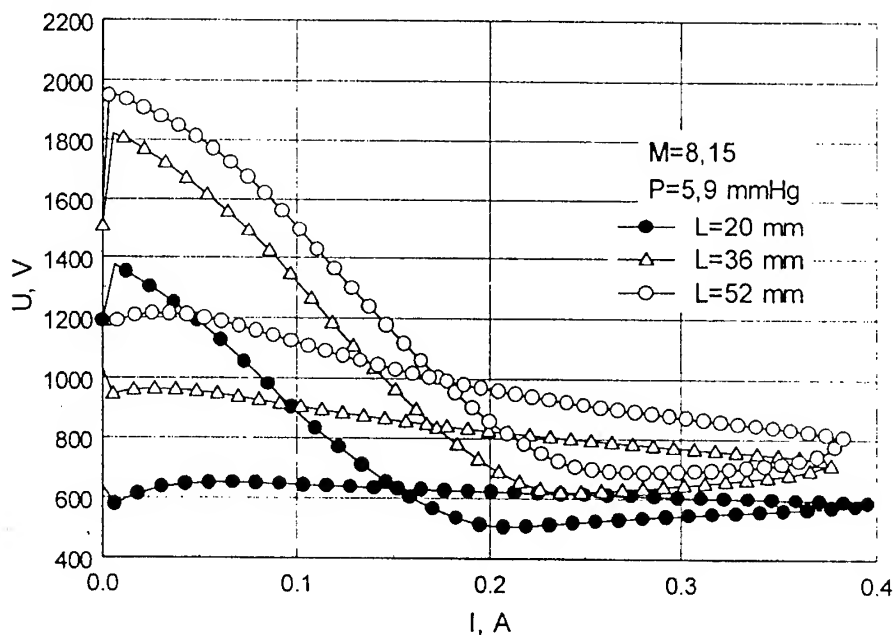


Fig. 2. Effect of inter-electrode separation on the volt-ampere characteristics.

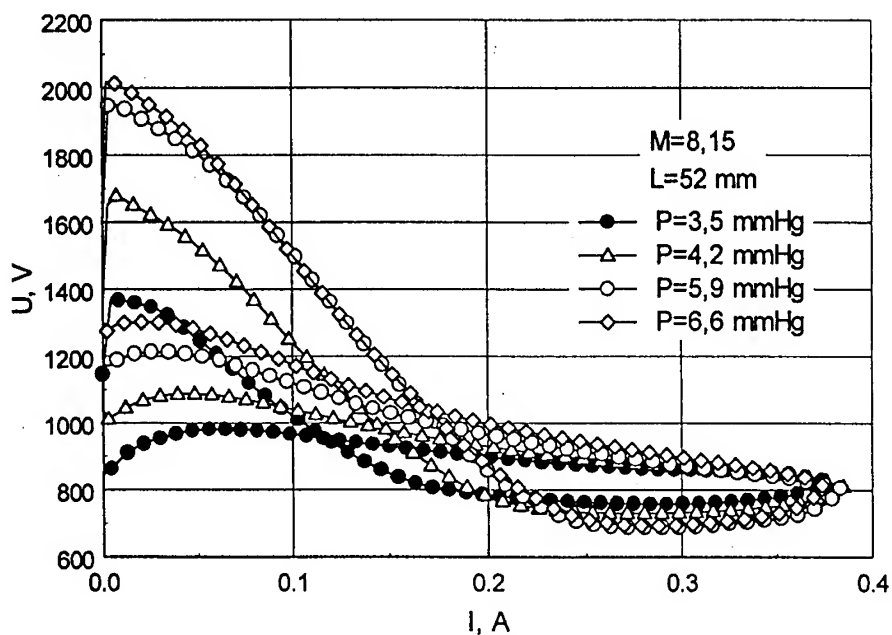


Fig. 3. Effect of static pressure on the volt-ampere characteristics.

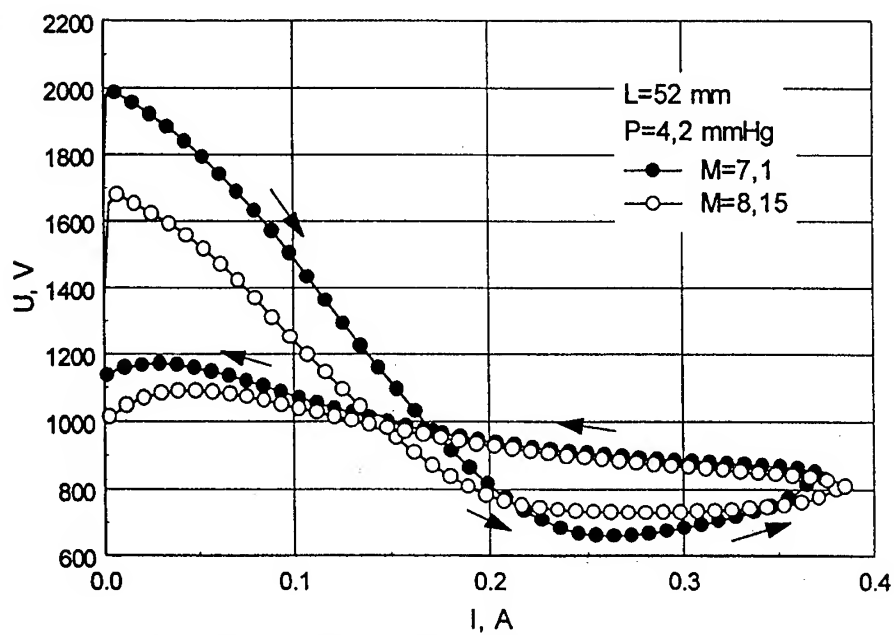


Fig. 4. Effect of Mach number on the volt-ampere characteristics.

several thousands of experimental points. In the voltage-current characteristics, a hysteresis is distinctly observed: to one and the same discharge current, two values of the applied voltage can correspond. The direction of going around the hysteresis loop, shown in Fig. 4 by arrows, is identical for all curves. Each volt-ampere characteristic can be divided into two parts. Following the direction of going around the hysteresis loop, the first part extends from the maximum applied voltage to the point of the hysteresis minimum. This part corresponds to the initiation of the discharge and is characterized by short duration, as well as by considerable spread of the experimental points. Moving along the volt-ampere characteristics, we pass its second, or main, part. This part of the hysteresis curve corresponds to the main duration of the discharge glow and is characterized by good reproducibility of experimental points. As to this section of the hysteresis curve, the following conclusions are possible. In the range of parameters studied, the greatest effect on this part of the volt-ampere characteristics of the discharge is exerted by the inter-electrode separation. As the discharge gap widens, the voltage across this gap increases, and the hysteresis appears to be more significant. An increase in the static pressure also results in a rise of the voltage drop, and a more pronounced hysteresis, but here both effects are less expressed compared to the case in which the discharge gap increases. The increase in the Mach number from 7.1 to 8.15 does not affect noticeably the volt-ampere characteristics.

Let us dwell now in more detail on the hysteresis phenomenon. According to [6], this phenomenon can be attributed to processes which occur at the cathode surface, at the interface between the zone of non-zero current and the current-free region, when only some part of the cathode surface is covered by the glow (in classical glow discharges, this regime is usually referred to as the normal one). However, the hysteresis phenomenon observed in this study cannot be explained solely by the processes which take place in the near-cathode regions. This is evidenced by the fact that the direction of going around the hysteresis loop in this study is opposite that in [6], and the hysteresis area depends on the inter-electrode separation, i.e., on the processes in the discharge volume. It seems that the decrease in the discharge volume caused by a decrease in the discharge current develops more slowly compared to the case of its growth with increasing current. The normal current density at the cathode surface may vary according as whether the discharge current grows or diminishes, which determines the emergence of the hysteresis.

This work was supported by the Russian Foundation for Fundamental Research (grant No. 98-02-17936).

References

1. Mishin G. I., Serov Yu. L., Yavor I. P. Flow around of sphere at supersonic movement in discharge plasma. // *Pisma v ZhTF*. 1991. V. 17. No 11. P. 65-71. (in Russian)
2. Mishin G. I., Klimov A. I., Gridin A. Yu A longitudinal electric discharge in a supersonic gas flow. // *Pisma v ZhTF*. 1992. V. 18. No 15. P. 86-92. (in Russian)
3. Ganguly B. N., Bletzinger P., Garscadden A. Shock wave damping and dispersion in nonequilibrium low pressure argon plasmas. // *Physics letters A*. 1997. V. 230. P. 218-222.
4. Bletzinger P., Ganguly B. N. Acoustic shock wave propagation in nitrogen and argon glow discharge. // *Proc. AIAA 8-th Intern. Space Planes & Hypersonic Systems and Technologies Conf. Norfolk (Virginia)* 1998.
5. Fomin V. M., Lebedev A. V., Ivanchenko A. I. Spatial-energetic characteristics of electric discharge in a supersonic gas flow. // *Doklady akademii nauk*. 1998. V. 361. No 1. P. 58-60. (in Russian)
6. Rothard L. Untersuchungen an Glimmentladungen mit Kathodengebieten mit und ohne Rand III: Dynamisches. // *Mber. Dt. Akad. Wiss.* 1961. Bd. 3. S. 18-23.

INFLUENCE OF NEAR-ELECTRODE REGION ON THE EFFECT OF INTERACTION OF THE GLOW DISCHARGE AND SUPERSONIC AIR FLOW

V. M. Fomin¹, Th. Alziary de Roquefort², A. V. Lebedev¹, and A. I. Ivanchenko¹

¹ Institute of theoretical and applied mechanics, 630090 Novosibirsk, Russia

² Laboratoire d'études aérodynamiques - UMR CNRS N° 6609, 86036 Poitiers, France

At present, much attention is being devoted to the self-maintained glow discharge in a supersonic gas flow [1 - 4]. This research area is of considerable importance both from the viewpoint of gaining better insight into the interaction of supersonic flows and shock waves with non-equilibrium plasma and from the viewpoint of using glow discharge for controlling external and internal flows. Yet, as a fundamental physical phenomenon, the self-maintained glow discharge remains studied poorly. For instance, there is no reported data on the role of near-electrode regions in the interaction of glow discharge with supersonic gas flows. In the present work, the effect of the near-electrode region of a self-maintained glow discharge on the supersonic air flow is studied experimentally.

Experiments were carried out in a wind tunnel with a free jet available in the working part of the tunnel. The Mach number of the approaching flow and its velocity were $M_\infty=3.2$ and $u_\infty=629$ m/s. The static pressure and static temperature were $P_\infty=7.67$ mmHg and $T_\infty=96$ K. Into the free flow, electrodes were immersed located as shown in Fig. 1. The cathode had the

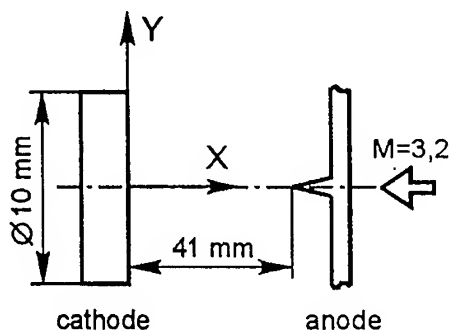


Fig. 1.

shape of a ring with 10-mm diameter, 2.5-mm height and 0.5-mm wall thickness. The anode was made from a 0.3-mm metal plate; with a bulge at its rear edge for exact positioning of the discharge. The electrodes were disposed on the symmetry axis of the jet, installed at zero incidence. The separation between the electrodes was 41 mm. In each experiment, the discharge was being maintained over the period of about 20 seconds. The discharge was visualized with the help of color photographing. The shadow visualization of the wave pattern of the flow, measurements of stagnation pressure and stagnation temperature profiles in the discharge region, and measurements of discharge current and voltage across the discharge were performed.

Three regions can be distinguished in the glow discharge under study (Fig. 2). The first one is

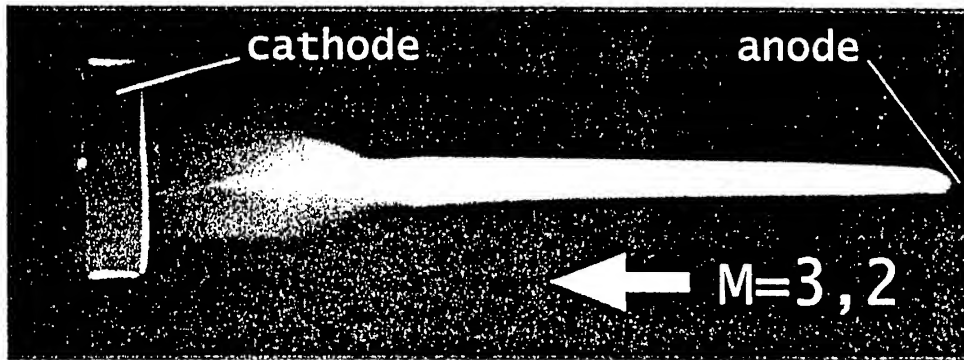


Fig. 2.

the cathode layer, a region with a blue-violet glow over the annular cathode. The width of this layer, as estimated from photographs of the discharge, amounted to 0.2 mm. In this region, the law of normal current density was observed: with increasing discharge current, the surface area of the cathode occupied by the glow was seen to increase until being totally covered by the cathode layer. Further increase in the current density resulted in higher current density at the cathode. In our experiments, the value of the minimum density of current was chosen such that practically all the cathode surface was occupied by the discharge, which had made the discharge nearly axisymmetrical. The second discharge region is the near-cathode region, which was the object of the present study. This plasma formation had the shape of a cylinder with a conical nose part. In its visible spectrum, a pink-orange color prevails. The third, and most extended part of the discharge (from here on, this part will be referred to as the anode region) had the shape of a truncated cone of large aspect ratio. This part is a kind of a "plasma conductor", the "plasma conductor" shunting the near-cathode region and the anode. Here, a pink-orange glow was also observed, but of a higher intensity compared to the near-cathode part of the discharge. The higher intensity of the glow corresponds to higher density of the discharge current in its given section. For instance, in the case of the total discharge current equal to 0.125 A, the mean current density in the near-cathode region was 0.4 A/cm² and that at the cathode surface was 0.08 A/cm². The higher the discharge current, the larger the diameter and longer the length of the plasma formation situated in the near-cathode region.

The shadow visualization of the flow was performed in the traditional manner. The knife was normal to the flow. A permanent source of light was used. At photographing, the exposure time was 10⁻³ sec. In the presence of the discharge, weak disturbances were observed introduced into the flow by both the plane anode and annular cathode. With the discharge, the wave pattern changes drastically (Fig. 3). On the conical part of the plasma near-cathode region, oblique shock waves originate. The semi-vertex angle of the head part of the near-cathode plasma and the inclination angle of the oblique shock arising here equaled 22° and 29.5°, respectively. The theoretically predicted inclination angle of an oblique shock arising in the flow around a circular cone with the same semi-vertex angle (22°) at $M_\infty = 3.2$ is 29.6°. This shows that, from the geometrical point of view, the wave patterns arising in the flow around a plasma cone and in

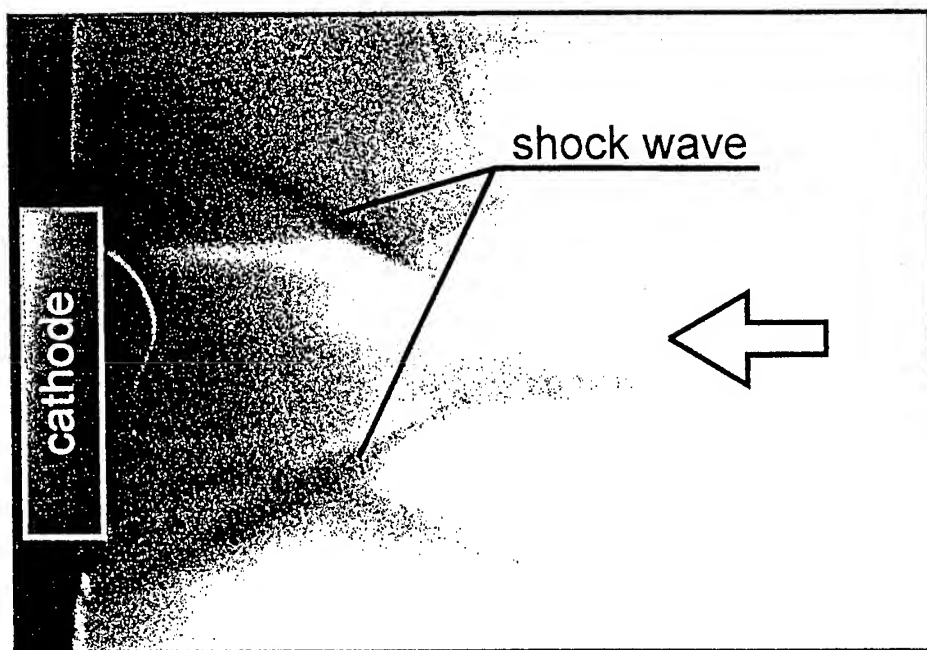


Fig. 3.

the flow around a rigid cone are nearly identical, i.e., the plasma in the near-cathode region resembles a "virtual body".

The stagnation pressure distributions in the discharge region were measured with a Pitot tube having the outside diameter 1 mm. The measurements were carried out in the symmetry plane of the discharge, 2 mm away from the front plane of the annular cathode. The results are shown

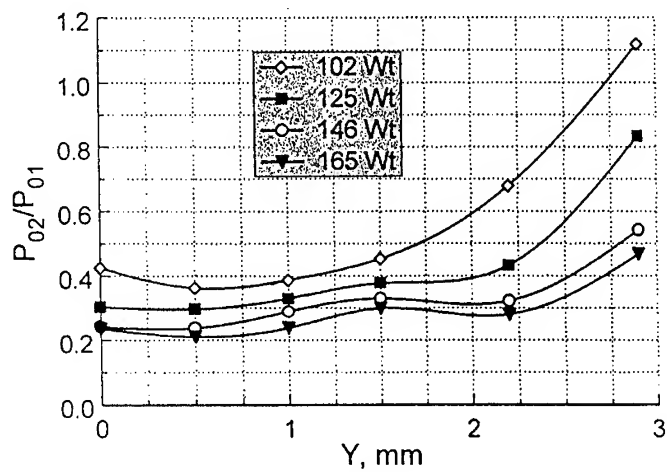


Fig. 4.

in Fig. 4. Here P_{02} is the stagnation pressure measured in the presence of the discharge and P_{01} is the stagnation pressure behind the normal shock wave measured under the conditions without discharge, the approach-stream parameters in both cases being identical. Different curves correspond to different electric power consumed by the discharge. From the shown graphs, it is seen that, as the discharge power increases, the pressure falls in value. In addition, the pressure rises in the direction from the near-axial part to the periphery, the rise being especially pronounced near the boundary of the region emitting radiation.

In stagnation-temperature measurements, a thermocouple 0.1 mm in diameter was used. In the experiments, the thermocouple was stretching to cross the flow. Measurements were conducted in the symmetry plane of the discharge, 4 mm away from the front plane of the annular cathode. The electric power consumed by the discharge was 125 W. Experimental data are shown in Fig. 5, where ΔT_0 is the difference between the stagnation temperatures at a given point under the

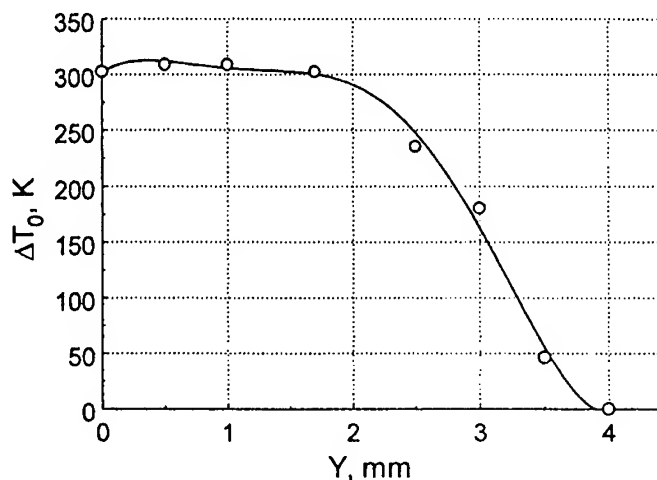


Fig. 5.

conditions with and without discharge, at identical parameters of the approaching flow. The temperature in the near-axial region varied only slightly and rapidly fell off in the peripheral region. Thus, here again, as in the case of the total pressure, the largest changes were observed near the plasma boundaries. Note also that the distance over which the stagnation temperature equalized with the approach-stream stagnation temperature was nearly identical to the radius of the radiating region.

The drop in the total pressure observed in this study can be, in principle, explained by a "thermal" model, which implies that all changes in the gas-flow parameters are caused solely by local heat supply. However, this model is not unique among other possible models, and it is not described here at length. Further experiments are required to furnish exact explanation of the observed regularities.

This work was supported by the Russian Foundation for Basic Research (grant No. 98-02-17936).

References

1. Mishin G. I. , Serov Yu. L., Yavor I. P. Flow around of sphere at supersonic movement in discharge plasma. // Pisma v ZhTF. 1991. V. 17. No 11. P. 65-71. (in Russian)
2. Mishin G. I., Klimov A. I., Gridin A. Yu. A longitudinal electric discharge in a supersonic gas flow. // Pisma v ZhTF. 1992. V. 18. No 15. P. 86-92. (in Russian)
3. Ganguly B. N., Bletzinger P., Garscadden A. Shock wave damping and dispersion in nonequilibrium low pressure argon plasmas. // Physics letters A. 1997. V. 230. P. 218-222.
4. Fomin V. M., Lebedev A. V., Ivanchenko A. I. Spatial-energetic characteristics of electric discharge in a supersonic gas flow. // Dokladi akademii nauk. 1998. V. 361. No 1. P. 58-60. (in Russian)

PRESSURE VARIATION ON THE FACE SECTION OF THE BODY OF REVOLUTION WITH A SPIKE WITH VARIATION OF ITS LENGTH, GEOMETRY AND INJECTION OF AN INERT GAS FROM THE SPIKE

A.F. Garanin

Institute of Theoretical and Applied Mechanics SB RAS, Novosibirsk, Russia

A.I. Glagolev

Institute of Mechanics, MGU, Moscow, Russia

Development of various flying vehicles sets the problem of searching for various methods to decrease aerodynamic drag.

Setting up a spike of a certain length in front of a blunted body leads to a considerable decrease in aerodynamic drag. Flows appearing in front of blunted bodies with a spike refer to separated flows.

In a flow around a blunted body with a spike there is an optimal (critical) length of the spike at which the greatest decrease of aerodynamic drag is obtained [1]. The results of the study of the structure of the flow appearing in front of blunted bodies with a spike without injection gas from it are given in [1].

The optimal value of the spike length depends on the shape of the nose section of the body, the Mach number of the incoming flow, and the shape of the spike. For a spike length equal to or less than the critical one, the flow with the separation zone at the spike end appears, which is called "end" separation.

When the spike length is increased above the critical one, the flow separation is shifted to the spike downstream. The separation of such kind is called the "delayed" separation. There is a shock-like increase in aerodynamic drag upon transition from the end separation to the delayed one.

The purpose of the present investigation is to study the effect of the blowing out of an inert gas from the spike, influence of the shape of the nose part and the spike length on the pressure variation at the front face of the body of revolution.

The research was performed in a supersonic aerodynamic wind tunnel with the test section 200×200 mm at the Mach number of the incoming air flow $M = 2.0$, stagnation pressure $P_0 = 2.0$ ata and stagnation temperature $T_0 = 290$ K. A cylindrical body of diameter 30 mm with a blunt front face and an extended spike was fixed on the tunnel wall with the help of the side pylon (Fig. 1). The spike could be constantly extended and removed with the help of a traversing mechanism

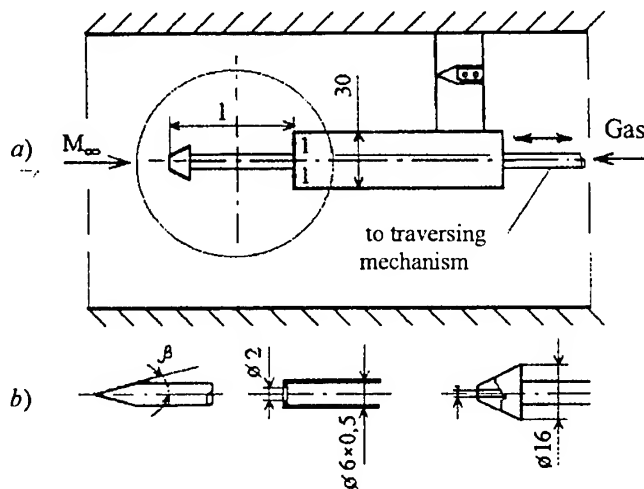


Fig. 1. Scheme of the model and its installation in the wind tunnel (a) and the shape of the nose part of the spike (b).
1 – place of pressure measurement on the face.

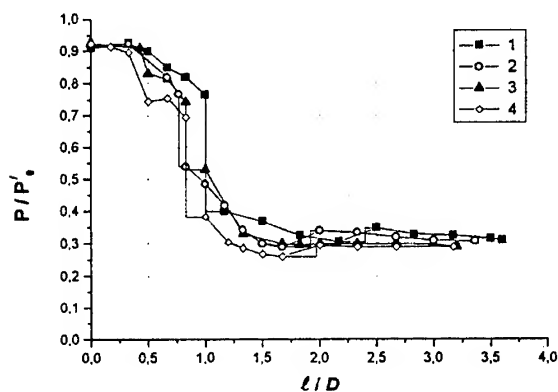


Fig. 2. Pressure on the front face of a cylinder with a spike depending on the spike length and the angle of spike sharpness.

1 - $\beta = 10^\circ$, 2 - $\beta = 20^\circ$,
3 - $\beta = 30^\circ$, 4 - $\beta = 45^\circ$.

end. The transition of the detached normal shock wave into the conical one occurred at smaller spike lengths for a spike with a larger angle of sharpness. This spike length will be called further the first critical spike length. Probably, this spike length is a boundary separating the pulsed flow from the stable flow with the end separation. The pulsed flow was studied in [1, 2, 3 etc].

A further increase in the spike length leads to a decrease in the angle of inclination of the separation zone and a pressure decrease on the body face. A jump-like pressure increase occurs at a certain spike length. This is the result of the transition of the flow separation from the end of the spike to the spike downstream to the so-called "delayed" separation. For a spike with $\beta = 10^\circ$, the transition from the tip separation to the delayed one occurred at the length $l = 2.5D$ and for spikes with the angles $\beta = 20^\circ, 30^\circ$ and 45° at $l = 2D$.

A comparison of the pressure coefficient $C_p = (P - P_\infty)/q$ (where P is pressure on the body face, P_∞ , q are static and dynamic pressures of the incoming air flow) with a spike $\beta = 10^\circ$ and the coefficient of the aerodynamic drag C_D from [1] are shown in Fig. 3. Good agreement of the data obtained on the transition length from the tip separation into the delayed one is observed.

The results of pressure distribution on the body face for spikes of various lengths and injection of an inert gas from the spike are given in Fig. 4. For this spike, the transition of the detached normal shock wave in front of the body face into the

the length range $l = (0 - 3.5) D$, where D is the diameter of the cylindrical part of the body. Various shapes of the spike nose part were investigated: pointed with a half-apex angle $\beta = 10^\circ, 20^\circ, 30^\circ, 45^\circ$, blunt ($\beta = 90^\circ$) and with a swelling in the shape of a truncated cone (Fig. 1b).

The obtained dependences of pressure variation on the front face with a pointed (sharp) spike are given in Fig. 2. It is seen from the results presented that, when the spike length is increased to the lengths $l = (0.8 - 1.0) D$, a jump-like decrease in pressure occurs on the body face. This is the result of transition of a detached shock wave in the form of a normal shock appearing on the body face at $l = 0$ into a conic shock wave with the formation of a conical separation zone coming from the spike

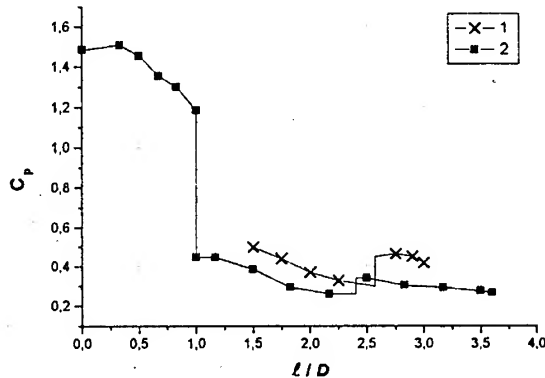


Fig. 3. Measurement of the coefficient of the wave drag of a cylinder with a spike $\beta = 10^\circ$ versus the spike length.

1 - [1]; 2 - present work.

conical one occurred at the spike length $l = 0.7 D$ without blowing out of the gas. At this spike length, the pressure coefficient decreases from $C_p = 1.0$ to $C_p = 0.45$. The transition from the tip separation into the delayed one without gas supply occurred at the length $l = 1.7 D$. Injection of air from the spike in amount $G \leq 4.5 \%$ (where $G = G \times 100 / \rho_\infty U_\infty F \%$, G is weight consumption of air, ρ_∞ and U_∞ are the density and velocity of the incoming air flow, F is the cross-sectional area of the model) leads to a decrease in

pressure on the body face at spike lengths $l < 1.2 D$. At zero spike length, the blowing out of air in amount $G = 4.5 \%$ causes a 20 % decrease in the pressure coefficient. In the range of spike lengths $l > 1.2 D$, air injection from the spike increases somewhat the value of the drag coefficient.

shlieren pictures illustrating the structure of the flow around a body with a blunt spike for the tip and delayed separation without gas injection are given in Fig. 5 ab and with gas injection in Fig. 5 cd.

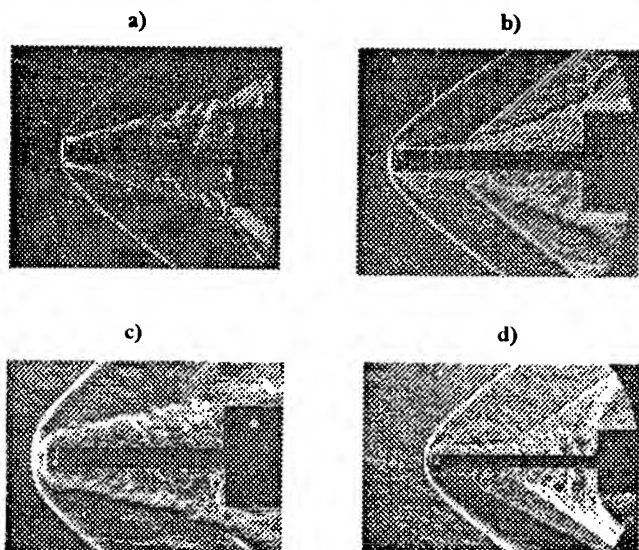


Fig. 5. Shlieren pictures of flow around a cylinder with a blunt spike.
a, b – respectively tip and delayed separation without gas injection from the spike; c, d – air injection from the spike $G = 2.4 \%$

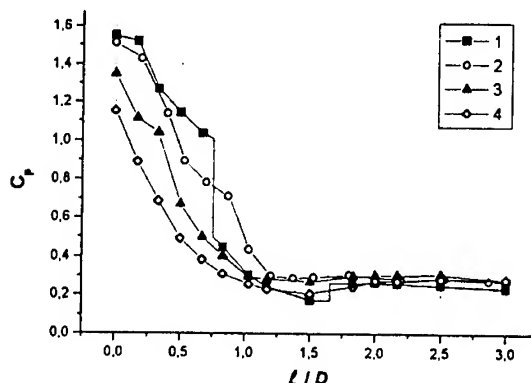


Fig. 4. Change of the pressure coefficient of a blunt body with a spike having a blunt nose. 1 – without air injection $G = 0$; 2 – injection of air $G = 1.3 \%$; 3 – $G = 2.4 \%$; 4 – $G = 4.5 \%$

The blowing out of gas from the spike in amount $G \leq 4.5 \%$ did not cause the change of the respective flow separation on the spike.

For a spike with the head in the shape of a truncated cone, the transition from the tip separation into the delayed one without air injection occurred at the spike length $l = 3.5 D$ (Fig. 6). These data agree with the dependence of the spike length at which the transition from the tip separation into the delayed one occurs on the height of the body step and the head suggested for the cavity in [1]. When the spike length is decreased, there is a hysteresis of transition from the tip separation into the delayed one with and without gas injection

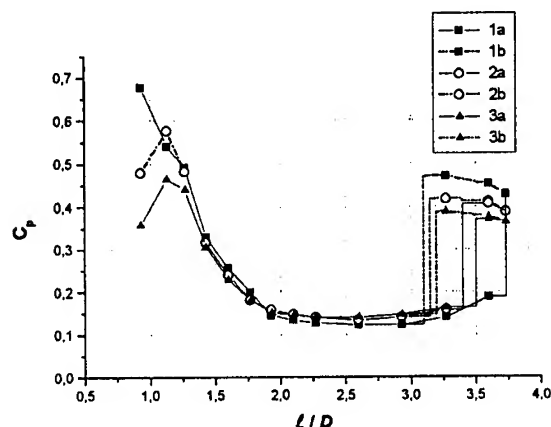


Fig. 6. Change in the pressure coefficient of a blunt body with a spike having a swelling at the end in the shape of a truncated cone

1 – without air injection $G = 0$; 2 – injection of air $G = 2.4\%$; 3 – $G = 4.5\%$; a – increase of the spike length, b – decrease.

from the spike. Blowing out of the gas from the spike decreased somewhat the value of hysteresis of transition and led to a pressure decrease on the body face at straight as well as reverse movement of the spike at $l > 3D$. The decrease in pressure on the body face in the regime with the delayed separation at air injection was caused by some increase in the separation zone in front of the body face and a decrease in the intensity of the shock wave in front of the separation zone. The decrease of pressure on the body face at air injection occurred at the spike length $l < 1.0D$. At the spike length $l = 0.95D$, the decrease in pressure on the body face was 35% at air consumption $G = 4.5\%$.

Conclusion

In the research conducted by the method of pressure measurement on the body face with a spike, dependences of the transition from the tip separation into the delayed one on the spike length and its geometry are obtained.

The dependences of pressure variation on the face with a spike at air injection from the spike on the relative air consumption and spike length variation in the range of $l = 3.5D$ are obtained.

For a cylindrical body with a blunt spike, the injection of air from the spike in amount $G < 45\%$ causes a decrease in drag at the spike length $l < 1.5D$. For a spike with the head in the shape of a truncated cone, air injection causes a decrease in drag at the spike length $l < 1.5D$ in the regime with the delayed separation at $l > 3.5D$.

REFERENCES

1. Chang P. Separation of flow. Moscow: Mir, 1972.
2. Reding I.P., Guenther R.A., Jecmen D.M. Scale effects on the fluctuating pressures in a region of spike-induced flow separation. AJAA Paper, 79-0143.
3. Khlebnikov V.S. Supersonic 3-D flow in the front separation zone // Mekhanika zhidkosti i gasa. 1995. No. 1. P. 152 – 162.

SOME HYPERSONIC INLET/AIRPLANE INTERACTIONS

Yu.P.Goonko and I.I.Mazhul

Institute of Theoretical and Applied Mechanics SB RAS
630090, Novosibirsk, Russia

A typical feature of different hypersonic flying vehicles (HFV) powered by air-breathing engines is a high degree of integration of the propulsion unit and the airplane. Numerous questions concerning their interaction arise. Some of possible aspects of such interaction for an HFV configuration with a ventral position of the engine nacelle are considered by experimental data for Mach numbers $M_\infty = 4$ and 6. First, the possibility of decreasing the adverse effect of the boundary layer developing on the forebody surface on the characteristics of the inlet and the flying vehicle as a whole is studied with the inlet positioned outside the boundary layer using bleeding wedges. Second, the efficiency of hindering the lateral spillage over the external compression wedge of the inlet using side cheeks is examined. Third, the problem of a possible effect of forebody nose bluntness is considered. In all cases, not only the characteristics of the inlet positioned under the forebody pre-compression surface are studied, but also the total aerodynamic and thrust-aerodynamic characteristics of an HFV as a whole.

MODEL. TEST CONDITIONS

A model configuration presenting a ramjet-powered HFV was experimented it is shown in Fig. 1. The relative parameters of this configuration are the following. The mid-section area of the lifting body together with the engine nacelle is $\bar{F}_m = F_m / S_{pl} = 0.0984$

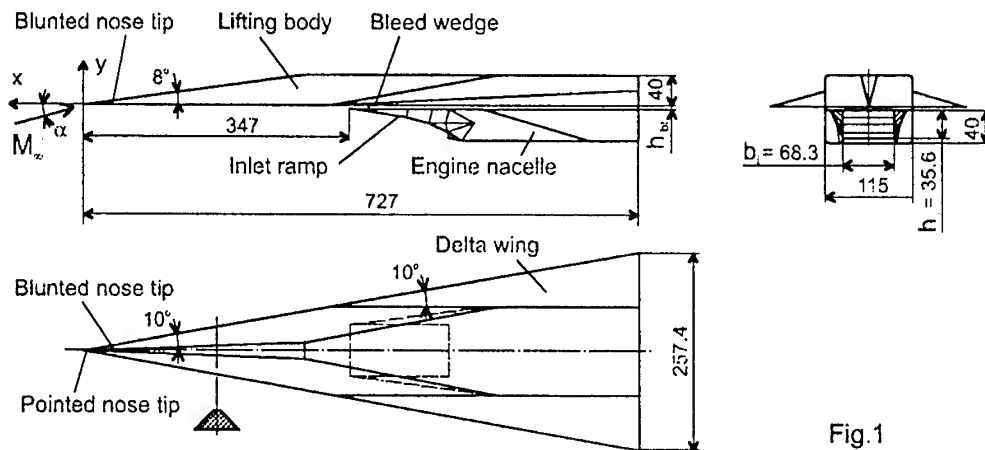


Fig.1

(where S_{pl} is the reference planform area); the relative planform area of the delta wing is $\bar{S}_w = S_w / S_{pl} = 0.305$; the thickness of the wedge-shaped profile of the wing with a flat lower

surface is $\bar{c} = 0.0524$. A nose tip of the model was replaceable: one was pointed and another had a three-dimensional bluntness (the bluntness radius in the planview was 7 mm and the bluntness radius in the vertical plane of symmetry was 2.5 mm). A two-dimensional (flat) inlet has a three-shock wedge of external compression with surface inclination angles $\theta_1 = 7.5^\circ$, $\theta_2 = 15^\circ$, and $\theta_3 = 22.5^\circ$. For the design Mach number $M_D = 6$ and the angle of attack $\alpha = 0$ the shock waves from the compression wedge focus at the inlet cowl tip. The inlet is defined by the relative frontal area of the $\bar{A}_0 = A_0 / S_{pl} = 0.026$, the relative throat area $\bar{A}_{th} = A_{th} / A_0 = 0.205$, and the relative width $b_i / h_i = 1.91$, where $A_0 = h_i b_i$, h_i and b_i are the height and width of the inlet by the leading edges, respectively. The engine nacelle of the model was replaceable, its two variants differed by the presence or absence of the side cheeks along the external compression wedge of the inlet. In tests with boundary layer bleeding, the engine nacelle was mounted on two, symmetrically located, bleeding wedges with an one-sided apex angle of 13° and bleeding height h_{bl} . The latter was $h_{bl} = 2$ and 3.7 mm for $M_\infty = 4$, and $h_{bl} = 3$ and 5 mm for $M_\infty = 6$.

The experiments were conducted in the supersonic blow-down wind tunnel T-313 of ITAM SB RAS. The free stream parameters respectively were: Mach numbers $M_\infty = 4.05$ and 6.06 ; Reynolds numbers $Re_1 = 50 \cdot 10^6$ and $17.7 \cdot 10^6$ [1/m]; and the total temperature in the plenum chamber of the wind tunnel $T_0 \approx 286$ K. Simultaneously with the balance measurement, the characteristics of the airstream captured by the inlet and passing through the model nacelle duct were also measured at the duct exit with metering nozzles (plugs) and a rake of pitot pressure probes. Based on the duct aerometry data, the flow-rate factor and the forces acting on the internal surfaces of the model nacelle duct were obtained. The latter were excluded from the balance measurement forces. The total aerodynamic characteristics of the model determined experimentally by this means include the forces over the external surfaces of the configuration and the forces over the so-called liquid surface of the stream captured by the inlet.

Along with the aerodynamic characteristics obtained experimentally, some flight properties of the HFV as a whole were estimated with consideration of all forces acting on the vehicle, including the propulsion unit. The resulting thrust-aerodynamic forces were determined with the use of the experimental values of the inlet flow-rate factor and total aerodynamic characteristics and with the calculated thrust characteristics of the engine. The flow with heat addition in the engine duct was treated as one-dimensional. The scramjet operation mode of the engine was considered, with the fuel (gaseous hydrogen) supplied into the supersonic combustion chamber.

EFFECT OF BOUNDARY LAYER BLEEDING

The effect of boundary layer bleeding was studied for the model variant with a pointed nose tip, the engine nacelle variant with the inlet without the side cheeks was mounted. According to the earlier data measured by a pitot pressure microprobe, the thickness of the boundary layer on the forebody surface a little upstream of the inlet leading edge is $\delta = 3.9$ mm for $M_\infty = 4$ and an angle of attack $\alpha = 0$. For the heights of the bleeding wedges used in the present tests, this thickness corresponds to $h_{bl} / \delta = 0.51$ and 0.95 . The calculated estimates and the schlieren pictures of the flow over the model inlet for $M_\infty = 6$ show that the said thickness is $\delta \approx 5$ mm; hence, the expected relative heights of boundary layer bleeding are $h_{bl} / \delta \approx 0.6$ and 1.0 .

The experimental data obtained have shown that the increase in the relative height of the bleeding wedges above $h_{bl} / \delta > 0.5-0.6$ affects weakly the flow-rate factor $f = A_\infty / A_0$, where

A_∞ is the cross-sectional area of the airstream captured by the inlet in the free flow. The schlieren pictures also confirmed that, for $h_{bl} = 3.7$ mm at $M_\infty = 4$ and for $h_{bl} = 5$ mm at $M_\infty = 6$, the near-wall, low-total-pressure part of the boundary layer developing on the nose surface practically does not come onto the compression wedge of the inlet. Therewith, the flow around

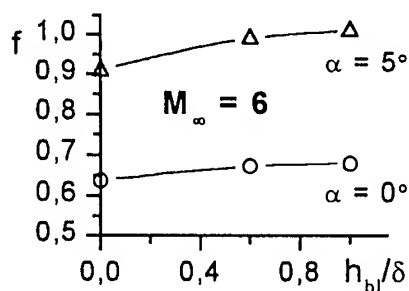


Fig. 2

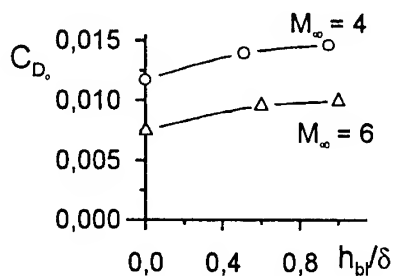


Fig. 3

the latter is affected only by the external filled part of the viscous layer. Under these conditions, a new boundary layer develops on the compression wedge. The thickness of this boundary layer in the entrance cross-section is noticeably smaller than that occurred for the engine nacelle variant without bleeding wedges. It is seen from optical visualization data that, for $M_\infty = 6$ and in the case without bleeding, the boundary layer in the inlet-entrance cross-section occupies more than 50 % of the entrance height, whereas its thickness is only about 25 % of the entrance height for $h_{bl} = 5$ mm. As a result, for angle of attack $\alpha \approx 6^\circ$ close to the angles of the maximum lift-to-drag ratios, the boundary layer bleeding leads to an increase in the flow-rate factor by ~ 5 % for $M_\infty = 4$ and by ~ 11 % for $M_\infty = 6$ (Fig. 2). Due to additional drag of the

bleeding wedges, the drag coefficient of the model $C_{D_o} = D_o / q_\infty S_{pl}$ (at zero lift force $C_L = 0$) increases by 20-26 % (Fig. 3) and, as a whole, the maximum lift-to-drag ratio $(L/D)_{max}$ decreases by 5-12 % depending on the height of the bleeding wedges.

As may be inferred from the experimental data presented above, the efficiency of the boundary layer bleeding with the use of special wedges will dependent on the compromise between the improvement of the characteristics of the inlet and the engine and the

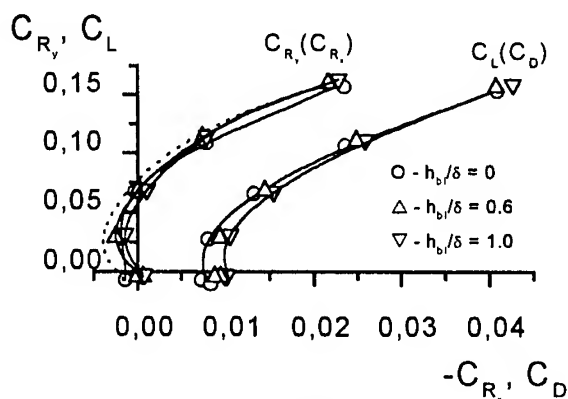


Fig. 4

increase in the external drag of the vehicle. The experimental data on the total aerodynamic characteristics and the estimates on the resulting thrust-aerodynamic characteristics of the

vehicle obtained for $M_\infty = 6$ are shown in Fig. 4. In this figure the polars of the total aerodynamic lift and drag coefficients $C_L = L/q_\infty S_{pl}$ and $C_D = D/q_\infty S_{pl}$ are presented along with the polars of the coefficients of the resulting lifting and tangential thrust-aerodynamic forces $C_{R_y} = R_y/q_\infty S_{pl}$ and $C_{R_x} = R_x/q_\infty S_{pl}$. The dashed curves show the limiting estimates corresponding to zero drag of the bleeding wedges (i.e., in a certain sense, to the case of suction of the boundary layer developed upstream of the inlet). As a whole, the accomplished analysis showed that a certain height of the bleeding wedges can lead to an increase in the resulting motive force of the vehicle.

LATERAL SPILLAGE OVER THE EXTERNAL COMPRESSION WEDGE OF THE INLET

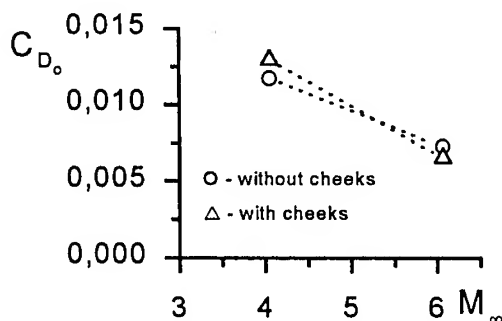


Fig.5

without nose bluntness show that the presence of the side cheeks increases the flow-rate factor at zero incidence by 1.2-2.8 %, and this value decreases as the angle of attack increases. A low efficiency of the side cheeks hindering the lateral spillage over the inlet compression wedge itself is apparently a consequence of the spatial flow around the inlet/forebody combination of the configuration.

An analysis of the aerodynamic characteristics showed that the configuration under consideration is of lower drag in the variant with the cheeked inlet for $M_\infty \approx M_D$ and in the variant with the inlet without the side cheeks for $M_\infty < M_D$. Thus, in the case of the cheeked inlet, a ~10 % increase in C_{D0} is observed for $M_\infty = 4$; for $M_\infty = 6$, vice versa, the value of C_{D0} decreases by approximately the same value as compared to the model inlet without the side cheeks (Fig. 5). Hence, for

$M_\infty \approx M_D$, the model with the cheeked inlet has better the flow-rate factor of the inlet and the

When free-stream Mach numbers are smaller than the design value for a flat inlet ($M_\infty < M_D$), side cheeks only partly bound the compression region of the inlet wedge from external flows on its outsides. Because of that, lateral spillage over the compression wedge occurs even in the presence of the cheeks. This can change the inlet characteristics, in particular, the flow-rate factor. The experimental data for $M_\infty = 4$ and 6 obtained for the considered model configuration

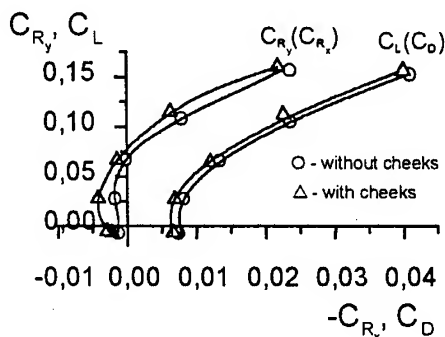


Fig.6

total aerodynamic characteristics of the configuration as compared to the model with the inlet variant without the side cheeks. The experimental polars of the total aerodynamic coefficients and the calculated polars of the resulting thrust-aerodynamic coefficients of the HFV for $M_\infty = 6$ are plotted in Fig. 6. An appreciable values of the resulting motive force ($C_{R_x} > 0$) are reached at small values of $C_{R_y} = 0-0.07$ for the configuration with the cheeked inlet, and a decrease in the total drag ($C_{R_x} < 0$) is observed for high $C_{R_y} > 0.07$.

EFFECT OF NOSE BLUNTNESS

One of the main factors determining the efficiency of inlet operation for the HFV configuration considered is the growth rate of the boundary layer on the forebody pre-compression surface and external compression wedge of the inlet itself. If the HFV forebody is blunted, the boundary layer develops under the influence of a high-entropy layer whose thickness can be comparable with the viscous layer thickness or exceed it. The nose bluntness effect also results in an increase in the flow field non-uniformity manifesting itself downstream. In accordance with experimental data obtained for $M_\infty = 4$, the nose bluntness leads to a significant increase in the thickness of the boundary layer coming onto the inlet. Thus, the values of the thickness δ , displacement thickness δ^* , and momentum thickness δ^{**} of the boundary layer increase by a factor of 2.5-2.7 within the range of the angle of attack $\alpha = 0-3^\circ$ and by a factor of 1.4-1.8 for $\alpha = 10^\circ$ as compared to the flow around a pointed configuration.

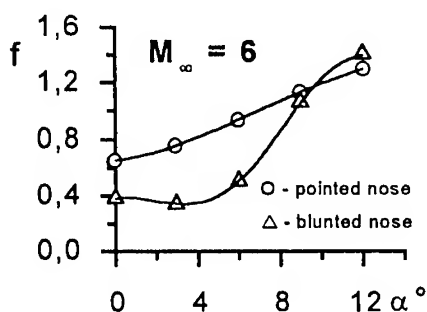


Fig. 7

An increase in the displacement thickness and flow field non-uniformity should be also accompanied by a decrease in the flow rate of the airstream captured by the inlet in the free flow. Experimental data obtained for the configuration with the inlet without the side cheeks show that the nose bluntness leads to a significant decrease in the flow-rate factor f at zero incidence by $\sim 23\%$ for $M_\infty = 4$ and by $\sim 42\%$ for $M_\infty = 6$. However, as the angle of attack increases, the effect of bluntness becomes weaker, as could be expected from the data of measuring δ^* . For $\alpha \geq 9^\circ$, the values of f for the blunted and pointed configurations are close (Fig. 7).

The character of variation of the flow-rate factor versus the angle of attack for the blunted configuration is responsible to a large extent for the behavior of the total aerodynamic characteristics including the forces over the liquid contour of the airstream captured by the inlet. Like for the flow-rate factor, the effect of the nose bluntness on the model drag increases with increasing free-stream Mach number. Thus, the increase in the drag coefficient C_{D_o} due to bluntness reaches $\sim 12\%$ and $\sim 21\%$ for $M_\infty = 4$ and 6, respectively.

It would reasonably be expected that both factors a decrease in the inlet flow-rate factor and an increase in total drag lead to a deterioration of the resulting thrust-aerodynamic characteristics. The thrust coefficient $C_P = P / q_\infty A_o$ of the power plant in the scramjet mode

calculated from experimental values of the flow-rate factor is shown in Fig. 8, with this coefficient referred to the frontal area A_0 of the inlet. For the configuration with the nose bluntness, the calculated values of C_p , in accordance with the elevated drag coefficient C_D , do not ensure positive values of the resulting tangential force, within the entire range of the angles of attack under consideration. At the same time, for the HFV configuration without the nose bluntness, positive value of C_{R_x} , i.e. a certain motive force, is obtained for the angles of attack $\alpha = 0-6^\circ$, i.e., up to flight regimes of the maximum lift-to-drag ratio (see Figs. 4 and 6).

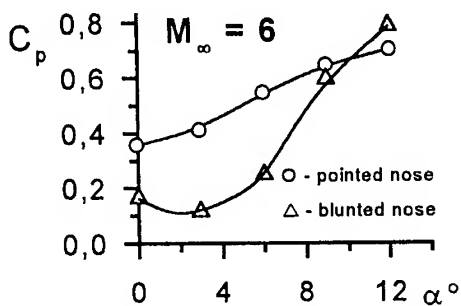


Fig. 8

CONCLUSION

The experimental studies on the fuselage/inlet interaction conducted for the model presenting an HFV configuration with a ventral position of the ramjet nacelle allow us to draw the following inferences:

1. Bleeding the boundary layer developing on the forebody pre-compression surface upstream of the inlet with use of wedges improves the flow-rate performance of the inlet and increases the internal thrust of the power plant. Despite an increase in drag, an increase in the resulting motive force of an HFV as a whole can be obtained at a certain height of the bleeding wedges.
2. The presence of the side cheeks hindering the lateral spillage over the inlet compression wedge at the examined velocities leads to a small increase of the inlet flow-rate factor both at $M_\infty \approx M_D$ and at $M_\infty < M_D$. This is apparently a consequence of the spatial flow around the inlet/forebody combination. Nevertheless, for obtaining the lower drag, a configuration is preferable with the cheeked inlet at $M_\infty \approx M_D$ and with the inlet without the side cheeks at $M_\infty < M_D$.
3. The bluntness of the aircraft forebody leads to a significant increase in the thickness of the near-wall high-entropy flow (particularly, for small angles of attack), a decrease in the inlet flow-rate factor, and an increase in the total drag coefficient. All these factors exert an adverse effect on the resulting thrust-aerodynamic characteristics of the vehicle as a whole.

SOME COMPARISON OF FLOWS AROUND HYPERSONIC AIRCRAFT WHOSE FOREBODIES ARE INTEGRATED WITH TWO-DIMENSIONAL AND THREE-DIMENSIONAL-CONVERGENT INLETS

Yu.P. Goonko, A.N. Kudryavtsev, I.I. Mazhul, and R.D. Rakhimov

Institute of Theoretical and Applied Mechanics SB RAS,
630090, Novosibirsk, Russia

For hypersonic aircraft powered by air-breathing engines, the vehicle configuration as a whole and its aerodynamic properties depend significantly on a configuration of the inlet and its integration with the airplane. From this standpoint, two types of hypersonic aircraft configurations considered should be noted. First, these are ordinary configurations with two-dimensional and quasi-two-dimensional inlets located under a plane or slightly transverse-convex lifting surface of the airplane. Second, these are configurations with three-dimensional inlets. Among the latter, convergent inlets, in particular, developed by V.V. Zatoloka, B.I. Gutov, and other should be noted, in which the compression of a supersonic inlet-captured airstream is performed along directions converging in space. Typically the characteristics of convergent inlets themselves, i.e., with no consideration of their arrangement on airplanes, were studied up to now. At the same time, of much interest are both the properties of these inlets integrated into the system of a flying vehicle and the characteristics of vehicles with these devices as a whole. Hypersonic aircraft configurations with convergent inlets are new, the flows around them and their aerodynamic characteristics have not been studied as yet. The research of these configurations in comparison with traditional configurations of hypersonic aircraft with 2D inlets is important.

Some results of computational and experimental studies of the flow around schematized configurations of hypersonic air-breathing-powered vehicles, respectively, with 2D and 3D-convergent inlets at high supersonic velocities are presented below. Both configurations are aerodynamically equivalent in the sense that they have identical or close to each other geometric parameters determining the aerodynamic properties of the configurations as a whole, including the inlet parameters. Patterns of the flow around the forebody of these configurations integrated with inlets of different types are compared.

The model configurations. Conditions of experiments and computations. The general view of the experimental models is shown in Fig. 1.

The first model configuration (Fig. 1a) has a 2D inlet located under a plane compression surface of a pyramidal-shaped forebody, which has a triangular planform with a sweep angle $\chi = 80^\circ$. The external compression ramp of the inlet is a three-stepwise wedge with inclination angles $\theta_1 = 7.5^\circ$, $\theta_2 = 15^\circ$, and $\theta_3 = 22.5^\circ$. Two versions of this inlet, respectively, with side cheeks and without these cheeks were tested.

In the other configuration (Fig. 1b), a convergent shovel-type inlet is integrated with a transverse-concave surface of the pyramid-like forebody, which also has a triangular planform and the same sweep angle. This surface is a surface of revolution with radii decreasing downstream over the length ($R_i < R_o$). It is derived by triangular carving the surface of a

truncated circular cone with the apex turned downstream and the apex half-angle $\theta_n = \theta_d = 7.5^\circ$ where θ_d is an inclination angle of the axis accepted for design of the forebody compression surface (see Fig. 1). The ramp compression surface of the convergent inlet is carved by a sector from a surface of revolution with the same design axis defined. Checks with a swept straight-line leading edge restrict an external compression region by sides of this inlet ramp. The longitudinal contour of this transverse-concave ramp includes the initial conical section with a straight-line generatrix, the subsequent section of isentropic compression, and the final conical section with a straight-line generatrix ahead of the inlet entrance. The initial angle of the ramp is $\theta_i = 7.5^\circ$, and final angle is $\theta_f = 15^\circ$, and the sector carving angle is $\psi = 75^\circ$.

The longitudinal contours of the compression ramps of the inlets for considered configurations were determined from the condition of providing an identical design level of flow compression in the entrance cross section $p_{en}/p_\infty \approx 13.6$ at the same Mach number $M_d = 6$, which is the design Mach number for the inlets proper. The relative frontal area, entrance cross-sectional area, and throat area of the 2D inlet are $A_o/S_{pl} \approx 0.026$, $A_{en}/A_o \approx A_h/A_o \approx 0.205$ and, respectively, these values are $A_o/S_{pl} \approx 0.034$, $A_{en}/A_o \approx A_{th}/A_o \approx 0.12$ for the convergent inlet (here S_{pl} is the lifting planform area of a configuration).

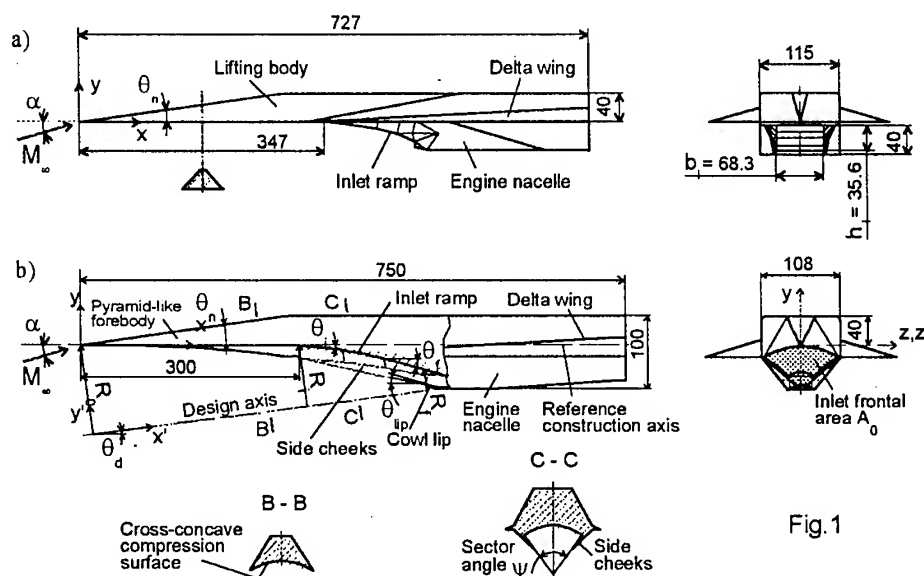


Fig. 1

The experiments were conducted in the T-313 wind tunnel (based at ITAM SB RAS) for Mach numbers $M_\infty = 2.03, 4.05$, and 6.06 . The dynamic pressure and the unit Reynolds number were $q_d \approx 7.2 \cdot 10^4, 7.6 \cdot 10^4$, and $1.2 \cdot 10^4$ [N/m²]; $Re_1 \approx 26 \cdot 10^6, 50 \cdot 10^6$, and $17.5 \cdot 10^6$ [1/m], the stagnation temperature in the plenum chamber of the wind tunnel was $T_o \approx 285-290$ K.

The computations of flows were performed using the marching method and the pseudo-transient method of solving the Euler equations, which allow shock-capturing computations of steady and unsteady supersonic flows with intensive shock waves. The methods are based on the Runge-Kutta TVD scheme up to the third order of approximation. The marching method was used to compute supersonic flows around the forebody/inlet configurations up to the entrance cross section of the inlet duct. The flow parameters obtained in these steady

computations for the entrance cross section were taken as the boundary and initial conditions for computation of the internal three-dimensional flow in the inlet ducts using the pseudo-transient method. In the latter case, it was assumed that the computed duct does not constrict behind the inlet diffuser and cannot lead to choking of a supersonic flow in the inlet duct behind the throat. The boundary conditions of supersonic exhaustion were used at the duct exit.

Patterns of the flow around the model configuration with the 2D inlet. The computations show that the flow around a pyramid-like nose part of the configuration with the 2D inlet is three-dimensional on the whole. At the same time, the flow field is rather uniform in the region where the inlet is mounted. Figure 2a-c shows a computed flow pattern for the free-stream Mach number $M_\infty = 4$ and the angle of attack $\alpha = 0$. The Mach number isolines are shown in a number of cross sections of the configuration. For the nose part proper, the cross-sectional overflow from the side surfaces to the lower surface along the swept leading edges can be noted (Fig.2a), which results from a greater flow compression over the upper and side surfaces in comparison to the lower one. Oblique shock waves forming on the cheeked wedge of the inlet are almost straight-lined in cross sections (Fig.2b and 2c), i.e., they are close to plane shocks. The fact that the flow in the airstream captured by the inlet is close to two-dimensional one was also confirmed by the pictures of oil-film visualization obtained for the model with the non-cheeked inlet version for $M_\infty = 4$ and 6, $\alpha = 3^\circ$. The streamlines were almost parallel each other on the nose compression surface ahead of the inlet. The streamlines on the inlet ramp were also close to parallel along the plane of symmetry on a significant width, and some curving these streamlines was observed only near the side edges of the ramp because of the cross-sectional overflow. It should be noted that the inlet was started within the examined range of the angles of attack both for $M_\infty = 4$ and $M_\infty = 6$. This was evidenced by Schlieren pictures of the flow in the region of external compression and by oil-film patterns of the flow immediately at the duct entrance.

Based on the data of numerical computations, the effects of flow three-dimensionality at the inlet entrance mainly manifest themselves in the corner regions of the entrance cross section where local flows have an elevated velocity, which are caused by the cross-sectional over-

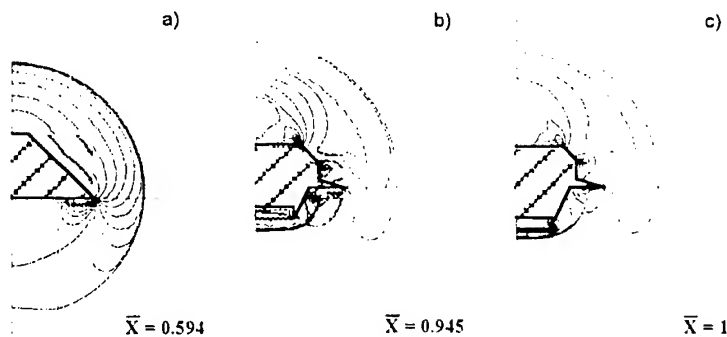


Fig.2

flow along the inlet cheeks. At the same time, the velocity in these corner zones, for example at $M_\infty = 4$ and $\alpha = 0-6^\circ$, is less than 8 % greater than that in the central part of the entrance. The central part of this cross section, where the non-uniformity of the Mach number field is less than 2 %, occupies more than 60 % of the entrance width. The results of pseudo-transient 3D computations of the internal flow in the inlet duct with a rectangular cross section showed that this flow is close to two-dimensional.

Patterns of the flow around the configuration with the 3D-convergent inlet. The structure of an inviscid flow around this forebody/inlet configuration can be exemplified by the results computed for $M_\infty = 4$, $\alpha = 0$. Pictures of isobars are shown in the plane of symmetry (Fig.3) and in a

number of cross sections (Fig.4). A special property of the transverse-concave compression surface of the considered forebody flown under an angle of attack at high super-sonic velocities is the effect of flow convergence. This convergence manifests itself, in particular, in a pressure increase downstream along the surface, even if the

latter has no change in an inclination angle in the plane of symmetry. For the angles of attack $\alpha = 5^\circ$ and 7.5° , the pressure increases by $\sim 6\%$ downstream from the nose tip of the configuration to the trailing edge of the compression surface. For angles of attack $\alpha < 5^\circ$, cross-

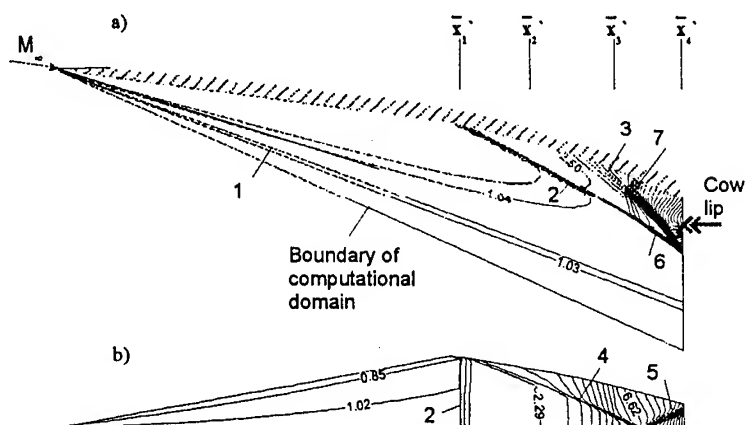


Fig.3

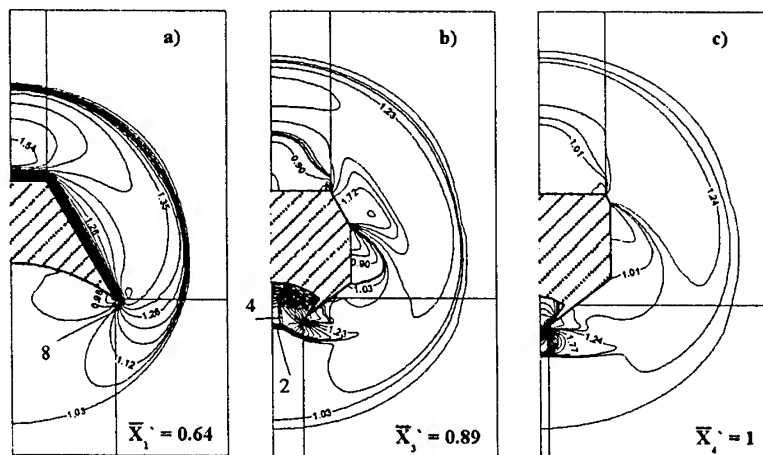


Fig.4

sectional overflow from the side surfaces to the lower surface along the swept leading edges of the forebody can also be noted. This can be seen from a isobars (8) at the side edge of the body contour in the cross section $\bar{x}_1' = x_1'/L' = 0.64$ (Fig.4a). Here $L' = 462.6$ mm is the length of the configuration from the nose tip to the inlet entrance cross section in the coordinate system $x'y'z'$ used in computations. The oil-film visualization of the limiting streamlines on the forebody compression surface also revealed flow separation along the swept leading edges and formation

of streamwise vortices at $\alpha = 0$, which is correlated with the said overflow and overexpansion of a local cross-sectional flow. The causes of the cross-sectional overflow in this instance are the same that occur for the configuration with the 2D inlet.

Another special feature of the flow over the compression ramp of the convergent inlet is “internal” side shock waves (4) induced by the side cheeks of the inlet (Fig.3b). These shocks emanate from the cheek vertices, they are not attached to the leading edges of the cheeks and are practically perpendicular to the surface of the compression ramp. They arise because the normals to internal faces of the cheeks, by the construction, are inclined at $\sim 6^\circ$ to the reference axis of the configuration. From the very beginning, side-cheek shocks (4) interact with transverse-concave shock (2) formed by the inlet ramp (Figs.3a, 4b). Shocks (4) interact also with each other in the plane of symmetry ahead of the inlet entrance, which is accompanied by appearance of side shocks (5) reflected from the plane of symmetry. Depending on the free-stream parameters, reflected shocks (5) can incident either directly onto the inlet entrance or onto the side-cheek faces somewhat upstream of the inlet entrance. In the latter case, the secondary side shock waves reflected from the cheeks are incident onto the inlet entrance. All these side shocks cause a significant pressure increase in the entrance cross section, but therewith the entrance flow field is non-uniform, in comparison to the configuration with the 2D inlet. Thus, for instance, for $M_\infty = 6$ and $\alpha = 0$, the relative pressure in the entrance cross section accounts $p_{en}/p_\infty \approx 16\text{--}27$ as compared to $p_{en}/p_\infty \approx 13.6$, which is a design value mentioned above for both the inlets considered. The complicated interaction of shock waves ahead of the inlet entrance leads to formation of resulting shock waves which, within the examined range of free-stream parameters, pass above the side cheeks (see Fig.4c) and above the leading edge of the cowl (Fig.3a). Thus, some flow spreading both in the streamwise direction above the cowl and in the lateral directions above the cheeks occurs ahead of the inlet entrance.

Based on experimental data for $M_\infty = 4$ and angles of attack $\alpha < 5^\circ$, the inlet is starting and no cross separation of the boundary layer is not observed in the flow over the inlet ramp. However, for $\alpha \geq 5^\circ$, regimes of inlet unstarting with a detached normal shock wave ahead the entrance are observed. In such cases, some complex three-dimensional flow separation occurs, with forming an initial arc-shaped cross separation line and two characteristic symmetric vortex regions.

Thus, the numerical and experimental studies of the configuration reveal a number of gas-dynamic structures, which determine the character of a three-dimensional flow over the inlet integrated with the transverse-concave compression surface of the forebody. Important features of the flow over the considered 3D-convergent inlet are those related to the appearance of the side shock waves from the cheeks and complex three-dimensional interaction of inlet shock waves with the boundary layer, including separation of the latter.

The computational results for the inviscid internal flow in the duct of a convergent inlet also revealed its significant three-dimensionality. This is related, first, with the flow non-uniformity in the entrance cross section. In particular, the vector of local flow velocity near the leading edge of the cowl is inclined relative to its internal surface; and though the angles of inclination of the cowl and compression ramp are identical ($\theta_{hp} = \theta_f = 15^\circ$), an internal shock wave arises on the cowl. The leading edge of the cowl is arc-shaped, and this shock wave is also transverse-concave. Second, in contrast to the 2D inlet, three-dimensionality of the internal flow in the duct of the convergent inlet is related to changing the cross-sectional shape along the duct length from a trapezium at the entrance to a rectangle in the throat.

Some general comparative characteristic of aerodynamic properties of the model configurations under consideration. The flow-rate characteristics of both models, respectively, with 2D and 3D-convergent inlets, are compared in Fig.5, which shows the flow-rate factor $f = A_\infty/A_0$ versus the Mach number for $\alpha = 0$. Here A_∞ is the cross-sectional area of the free airstream captured by an inlet. Note that the flow-rate characteristics obtained in tests of the models refer to the inlets integrated in the system of a flying vehicle. In comparing them, one should bear in mind two factors determining the similarity or difference of integral aerodynamic characteristics of the configurations considered: first, the aerodynamic equivalence involved when designing the configurations and, second, a significant difference in three-dimensional flow structures occurring. The configuration with the 3D-convergent inlet has some benefit in flow-rate factors about $\sim 17\%$ for $M_\infty = 4$ and $\sim 8\%$ for $M_\infty = 6$. At the same time, as it follows from the data on inlet starting, this configuration is more sensitive to changes in flow regimes depending on the angle of attack.

Our studies show that effects of the flow around the configurations considered as a whole and the compression flow in the airstream captured by the inlet can be divided into the following species. Ones are inviscid or "gas-dynamic" effects, the other are effects induced by a quasi-

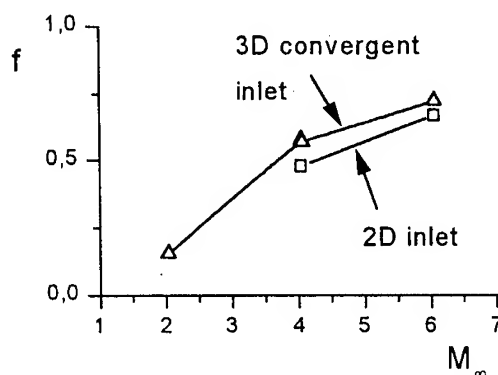


Fig.5

two-dimensional or three-dimensional interaction of the external shocked flow with the boundary layer, including separations of the latter.

In particular, the three-dimensional flows around the pyramid-like forebodies of the configurations considered forms mainly as inviscid ones. For the configuration with the plane nose compression surface and the 2D inlet, the flow over the inlet itself is close to two-dimensional with the almost plane oblique shock waves generated by the inlet ramp. Three-dimensionality of the inviscid flow over this 2D inlet is mainly related to lateral spreading above the side cheeks of the compression wedge, i.e., it manifests in the tip effects. The flow around the model with the 3D-convergent inlet is more complicated as compared to the model with 2D inlet. This is ultimately derived from the three-dimensional geometry inherent in the convergent configuration by its construction including the inlet compression ramp being double concave (in the streamwise and crossflow directions) and the side cheeks positioned three-dimensionally. Shock waves oriented spatially arise in the flow over the convergent inlet, which interact every with other and with the boundary layer. These complex interactions result in appearance flow patterns that are not typical of the model with the 2D inlet. In particular, in the flow around the side cheeks there arise oblique shock waves that are glancing relative to the compression surface of the inlet ramp.

Quasi-two-dimensionality or three-dimensionality of the external flow over an inlet determines predominately two-dimensional interaction of the shocked flow with the boundary layer for the configuration with the 2D inlet and three-dimensional interaction for the configuration with the convergent inlet, respectively. In the flow over the latter configuration, complex three-dimensional separations of the boundary layer appear in the inlet unstaring regimes.

AERODYNAMICS OF A CONVERGENT INLET INTEGRATED WITH A FOREBODY CONVERGENT-COMPRESSION SURFACE

Yu.P.Goonko, A.M.Kharitonov, A.N.Kudryavtsev, I.I.Mazhul, and R.D.Rakhimov

Institute of Theoretical and Applied Mechanics SB RAS
630090, Novosibirsk, Russia

An integrated aerodynamic configuration of a hypersonic airbreathing vehicle is studied. The configuration is noteworthy for a shovel-type convergent inlet integrated with a swept cross-concave surface of the forebody, which also forms a three-dimensional convergent compression flow at supersonic speeds. An integrated configuration of this kind allows a complete implementation of the convergence principle of compression of the stream captured by the inlet along directions converging in space. Such configurations are new, the flow around them and aerodynamic properties have been poorly studied yet. Results of experimental and numerical studies of the considered model configuration at free-stream Mach numbers $M_\infty = 4$ and 6 are described in the present paper. Some special features of formation of the flow structure over the forebody compression surface, near the inlet ramp of external compression, and in the inlet entrance duct of the examined configuration are shown.

DEFINITION OF THE MODEL CONFIGURATION

A sketch of the aerodynamic model presenting a schematized configuration of hypersonic airbreathing vehicle is shown in Fig. 1.

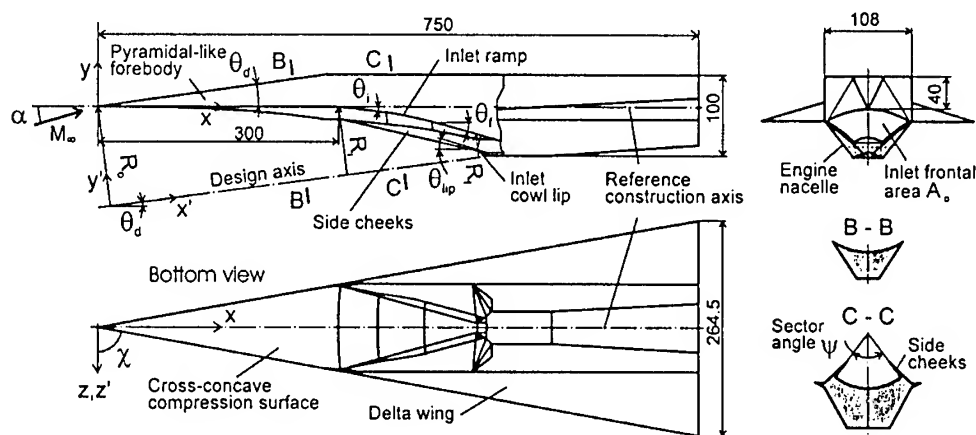


Fig.1

As a whole, the configuration constitutes a combination of a delta wing with a lifting body, it has a triangular planform with the sweep angle of the leading edges $\chi = 80^\circ$. An engine nacelle together with a convergent inlet is positioned under the lifting body. The forebody is of a pyramidal-like form, with its lower compression surface derived from triangular carving of the surface of a reverse truncated cone with a 7.5° half-angle at the apex. This compression surface is a cross-concave surface of revolution with the radii decreasing downstream ($R_i < R_o$). On

designing the shovel-type convergent inlet (Zatoloka V.V., Gutov B.I.) arranged in the system of the vehicle, the x' axis common with the axis of the forebody compression surface was chosen. It is inclined at an angle $\theta_d = 7.5^\circ$ to the reference construction axis x of the model configuration as a whole. The radii of the cross-concave surface of the inlet compression body (in particular, the initial radius R_i and the final radius R_f) were counted from this axis. The initial and final angles of the compression body surface are $\theta_i = 15^\circ$ and $\theta_f = 22.5^\circ$ relative to the x' axis ($\theta_i = 7.5^\circ$ and $\theta_f = 15^\circ$ relative to the x axis). A shovel-type inlet ramp was derived from the compression body of revolution with carving the sector in the view along the x' axis by two meridian planes with an angle $\psi = 75^\circ$ between them. Cheeks with a swept straight-line leading edge restrict an external compression region by sides of this inlet ramp.

The configuration is characterized by the following relative parameters: the mid-section area of the fuselage of lifting-body type together with the engine nacelle $\bar{F}_m = F_m / S_{ref} = 0.104$ (S_{ref} is the reference planform area of the configuration); the frontal area of the inlet $\bar{A}_o = A_o / S_{ref} = 0.034$; the cross-sectional area of the inlet entrance and throat $\bar{A}_{en} = A_{en} / A_o = 0.121$ and $\bar{A}_{th} = A_{th} / A_o = 0.123$, respectively.

NUMERICAL STUDY OF FLOW OVER THE MODEL CONFIGURATION

The calculations were performed by numerical solution of the Euler equations in partial derivatives for three-dimensional, inviscid, supersonic, steady and unsteady flows using advanced TVD schemes, which allow shock-capturing computation of flows with strong shock waves. Integration along the marching direction was conducted using explicit Runge-Kutta schemes preserving monotonicity of the solution. A multiblock approach was used to construct the computational mesh. The coordinate system $x'y'z'$ fitted with the construction axis of the forebody and inlet was used in calculations (see Fig. 1).

Forebody and inlet. An example of the computed flow around the forebody/inlet configuration for $M_\infty = 6$ and $\alpha = 0$ is shown in Figs. 2 and 3. Isomach lines are plotted in the plane of symmetry (Fig. 2a), on compression surfaces in the planform view (Fig. 2b), and in

cross-sections for the relative longitudinal coordinates $\bar{x}'_1 = x'_1 / L' = 0.64$ (Fig. 3a), $\bar{x}'_2 = 0.75$ (Fig. 3b), and $\bar{x}'_4 = 1.0$ (Fig. 3c). Here L' is the distance from the model nose tip to the inlet entrance cross-section in the coordinate system $x'y'z'$, \bar{x}'_1 corresponds to the cross-section immediately upstream of the inlet, \bar{x}'_2 to the cross-section near the beginning ($\bar{x}' = 0.77$) of the isentropic section of the external compression ramp,

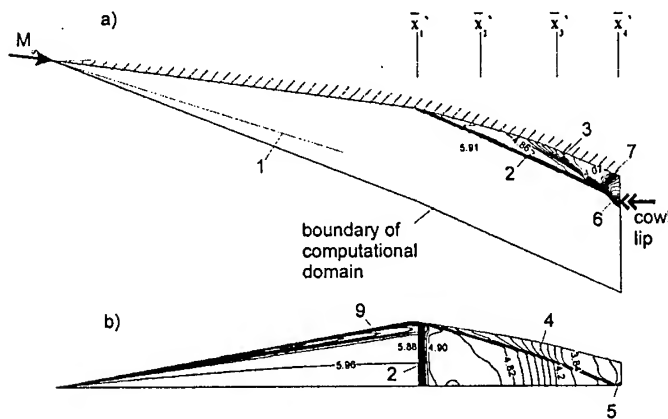


Fig.2

and \bar{x}_4' to the cross-section passing through the leading edge of the cowl lip. The cross-section $\bar{x}_3' = 0.89$ corresponding to the end of the isentropic compression section of the inlet is also marked in Fig. 2a. Note that Figs. 2 and 3 have an identical numeration of flow structures.

First of all, we consider the specific features of the flow over the cross-concave forebody surface. As earlier numerical studies show, the effect of flow convergence at high supersonic velocities is typical of such a surface inclined at an angle of attack. In particular, this effect is manifested in a pressure increase downstream along the surface. Obviously, for zero angle of attack $\alpha = 0$, when the compression surface is aligned with the free-stream flow, this effect should not be observed. Thus, the calculated data for $M_\infty = 4$ and the angles of attack $\alpha = 5^\circ$ and 7.5° show the pressure increase by $\sim 6\%$ downstream from the nose tip to the end of the surface, i.e., a weak convergence effect is observed. It should be noted that this effect for the configuration under study is attenuated by the fact that the swept leading edges are subsonic for $M_\infty = 4$ and 6, and inclination angles of the pyramid-like forebody surfaces are up to $\theta_f = 8^\circ$, i.e., they are reasonably large. For the angles of attack $\alpha < 8^\circ$, the upper and side surfaces of the forebody form a compression flow, and the cross-sectional overflow from the side surfaces to the lower surface is observed. It is evidenced by the isomach lines of the expansion fan (9) on the side edge in the cross-section \bar{x}_1' (Fig. 3a). A region of flow compression evolves behind this fan toward the plane of symmetry.

As for the flow around the forebody/inlet configuration, the following shock wave structures are evident (see Figs. 2 and 3): cross-convex shock wave (1) emanating from the nose tip of the configuration and passing under the forebody compression surface; cross-concave shock wave (2) formed by the external compression ramp of the inlet; and compression wave (3) forming at the isentropic section of the inlet ramp. The interaction of isentropic compression wave (3) with shock wave (2) from the initial part of the inlet ramp results in formation of shock wave (6), which is more intense than shock wave (2).

A typical feature of the flow is also "internal" side shock waves (4) emanating from the vertices of the side cheeks of the inlet. Note, these shocks are detached from the leading edges of the cheeks. The cause for their appearance is that, by construction, the normals to the internal faces of the side cheeks are inclined at $\sim 6^\circ$ to the longitudinal axis of the model configuration. Side cheek shocks (4) interact with each other in the plane of symmetry, their intersection line (7) manifests itself in Fig. 2a. The interaction of the said shocks is accompanied by formation of shock waves (5) reflected from the plane of symmetry. Depending on the free-stream parameters, these reflected shocks (5) can fall directly on the inlet entrance ($M_\infty = 6$ and angles of attack $\alpha = 0-7.5^\circ$) or on the surface of the side cheeks upstream of the entrance ($M_\infty = 4$ and angles of attack $\alpha = 0-7.5^\circ$). In the latter case, the inlet entrance is hit by the secondary side shocks reflected from the cheeks.

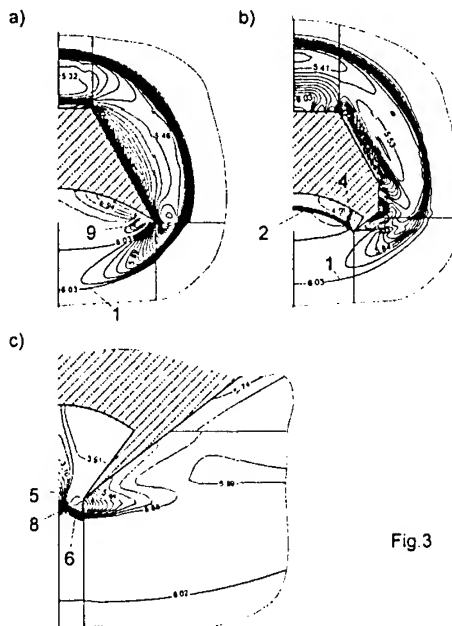


Fig 3

From the very beginning, side cheek shocks (4) interact with cross-concave ramp shock wave (2) (see Fig. 3b). In addition, both these side shocks (4) and reflected shocks (5) interact with shock wave (6) somewhat upstream of the duct entrance. This complicated interaction of shock waves upstream of the entrance results in formation of a typical "bulging" shock wave (8), which can be seen, for example, from the condensed isomach lines in the entrance cross-section near the axis of symmetry (Fig. 3c). The shocks resulting from this interaction pass above the side cheeks (Fig. 3c) and above the leading edge of the cowl lip (Fig. 2a). Thus, some spreading both in the longitudinal direction above the leading edge of the cowl lip and in the side directions above the cheeks occurs in front of the inlet entrance.

Inlet entrance duct. The calculation data of the external flow around the forebody/inlet configuration served as initial ones for computing a three-dimensional, supersonic, unsteady, internal flow in the inlet duct. In this process a steady flow inside the duct was obtained by the pseudo-transient method. For the model configuration considered, the cross-sectional shape of the inlet duct varies from a trapezium at the entrance to a rectangle in the throat. The calculated duct has no constriction at the exit and it cannot lead to flow choking in the duct behind the inlet throat. The boundary conditions for an unsteady flow in the duct entrance cross-section correspond to those flow parameters that were obtained by calculation of the external flow, and the conditions of supersonic exhaustion from the duct were used at the exit.

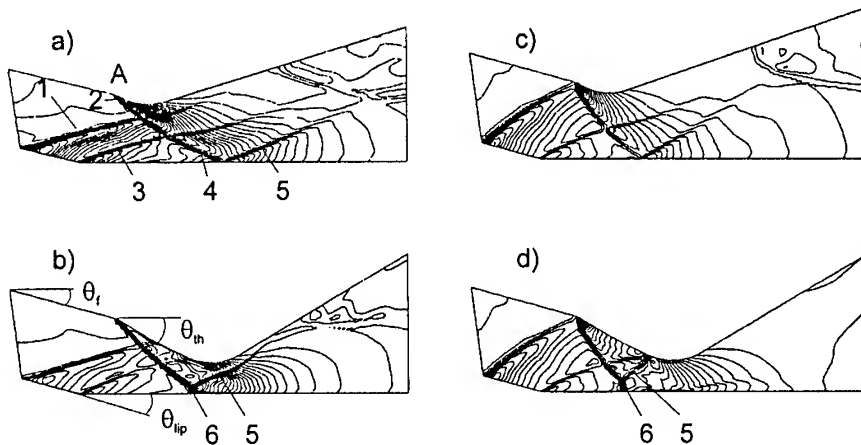


Fig.4

The numerical data on the inlet duct flow were obtained for Mach numbers $M_\infty = 4$ and 6, $\alpha = 0$ for two values of the throat height $h_{th} = 14.4$ and 7 mm (correspondingly, $\bar{A}_{th} = 0.127$ and 0.0665). The flow structure in the inlet entrance duct is shown in Fig. 4 in the form of density isolines in the plane of symmetry. In spite of the fact that the angles of inclination of the compression ramp at the entrance and the internal wall of the cowl lip are equal ($\theta_{lip} = \theta_f = 15^\circ$), shock wave (1) arises at the leading edge of the cowl lip. It is a consequence of flow non-uniformity in the entrance cross-section. At $M_\infty = 6$, this shock (1) interacts with shock wave (2) arising at the point (point A, Fig. 4a) where an internal wedge inside the inlet entrance joins the curvilinear section of a throat insert with an angle of inclination $\theta_{th} = 22.5^\circ$. For $M_\infty = 4$, the intersection of these shocks occurs practically at the point A of surface

inflection (Figs. 4c,d). The presence of shock wave (3) arising on the inflection of the internal surface of the cowl should also be noted.

As a whole, for the throat height $h_{th} = 14.4$ mm, the internal flow is supersonic everywhere both for $M_\infty = 6$ and $M_\infty = 4$ and has a complex structure of interacting shock waves. As the throat height decreases to $h_{th} = 7$ mm, the incidence of shock wave (4) onto the cowl results in its irregular reflection with formation of a rear shock wave (5) and a small Mach stem (6). In this case, the flow patterns for $M_\infty = 6$ and 4 are principally different. For $M_\infty = 6$ shock wave (5) induced by irregular reflection enters an expanding section of the duct behind the throat and does not involve any changes in the flow structure at the duct entrance (Fig. 4b). Nevertheless, for $M_\infty = 4$ this shock wave falls onto the lower surface of the inlet duct upstream of the minimal cross-sectional area of the throat (Fig. 4d). The flow is unstable in the latter case, an increase in the Mach stem height and an upstream displacement of the shock-wave system with irregular reflection are observed in computations. As a result, the supersonic inflow into the inlet duct is destroyed, and a flow regime with a bow shock wave at the entrance forms.

EXPERIMENTAL RESULTS

The model was tested in the supersonic blow-down wind tunnel T-313 of ITAM SB RAS at Mach numbers $M_\infty = 4.05$ (Reynolds number $Re_1 = 50 \cdot 10^6$ [1/m], dynamic pressure $q_\infty = 7.5 \cdot 10^4$ [N/m²]) and $M_\infty = 6.06$ ($Re_1 = 17.5 \cdot 10^6$ [1/m], $q_\infty = 1.2 \cdot 10^4$ [N/m²]). The total temperature in the plenum chamber of the wind tunnel was equal to the atmospheric temperature $T_0 \approx 290$ K.

The experimental distribution of pressure p/p_∞ on the forebody compression surface in the cross-section $\bar{x}'_1 = 0.633$ is shown in Fig. 5 for $M_\infty = 4$, $\alpha = 0$ and 5° in comparison with the calculated curves. It is pertinent to note the following feature of the real flow over this surface. The oil-film visualization of the limiting streamlines on the surface for $M_\infty = 4$, $\alpha = 0$ shows that flow separations along the swept leading edges and formation of streamwise vortices occur. The cause for the occurrence of these viscous structures is that the flow is compressed on the side surfaces of the forebody and a cross overflow to the lower surface arises, as supported by the results of numerical calculations described above. For the angle of attack $\alpha = 5^\circ$, the flow separations mentioned above are not observed yet. Despite the said change in the flow picture with the increase in the angle of attack, the character of the calculated pressure distribution over the forebody compression surface is in rather good agreement with the experimental data.

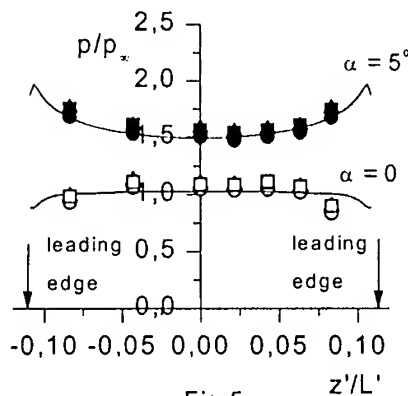


Fig.5

The streamwise pressure distribution in the plane of symmetry of the inlet compression ramp is plotted in Fig. 6 for $M_\infty = 4$, $\alpha = 0$ and 5° . Along the initial section of the inlet ramp, the calculated pressure is in good agreement with experimental data ($0.633 \leq \bar{x}'_1 \leq 0.88$ for $\alpha = 0$ and $0.633 \leq \bar{x}'_1 \leq 0.76$ for $\alpha = 5^\circ$). The pressure obtained experimentally begins to exceed the calculated values at $\bar{x}'_1 \geq 0.88$, $\alpha = 0$ and in the beginning of the isentropic compression surface

at $\bar{x}_1' \geq 0.77$, $\alpha = 5^\circ$. It follows from the numerical results for an inviscid flow that, for $M_\infty = 4$ and $\alpha = 0$, the side cheek shock waves start to interact in the plane of symmetry behind the isentropic compression section of the inlet ramp. This seems to be responsible for the stepwise growth of the calculated pressure in front of the inlet entrance at $\bar{x}_1' = 0.92-0.93$. The calculated pressure distribution at $\bar{x}_1' > 0.92-0.93$ for $\alpha = 0$ again moderately well agrees with the experimental one.

Based on the data of optical and oil-film visualization, the inlet is started for $M_\infty = 4$ at the angle of attack $\alpha = 0$. The oil-film pictures for $\alpha = 0$ show that no cross separation of the boundary layer is observed on the inlet ramp but there are three-dimensional (or oblique) separations near the

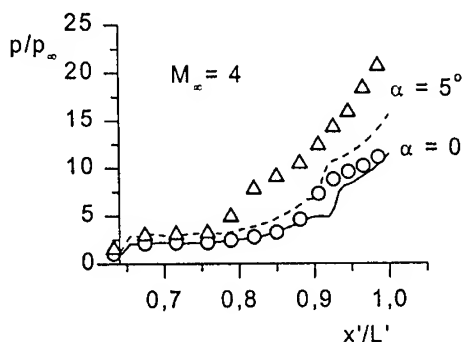


Fig. 6

cheek vertices and separation lines developing along the cheeks. Disturbances associated with these viscous structures appear not to be effect on the flow near the plane of symmetry other than a small excess of the experimental pressure values over the calculated ones at the place of intersection of the side cheek shocks near $\bar{x}_1' = 0.92-0.93$. This flow pattern flow is favorable for the said good agreement calculated and experimental pressure data. For $\alpha = 5^\circ$ the oil-film visualization reveals the presence of cross separation of the boundary layer, which arises already at the isentropic section of the inlet ramp. It might be well to note two typical symmetric vortices are formed in the separation region. These vortices can be apparently called tornado-shaped. Such a complex separation pattern is ultimately caused by the non-starting of the inlet, the appearance of the bow shock wave at the entrance and its interaction with shock waves induced by the side cheeks. From this flow pattern, it is obvious why the calculated and experimental data for $\alpha = 5^\circ$ adequately agree only at the initial section of the inlet ramp, up to the boundary layer separation region.

As follows from the schlieren pictures, the internal flow at the entrance duct section and in the inlet throat under real conditions is significantly different from the calculated patterns (for $\alpha = 0$). First, the real flow in front of the inlet duct entrance includes rather a thick boundary layer whose structure is complicated by its interaction with the glancing side shocks and viscous effects of the corner flows along the cheeks. In addition, this internal flow is apparently complicated by interaction of internal shock waves with the boundary layer on the duct walls including the boundary layer separations induced by this interaction. Note that internal shocks arising, for example, on the cowl, are glancing relative to the side walls of the duct. The shock waves arising in the entrance cross-section because of the deflection of flow by the side walls are also glancing. All these glancing shocks appear to induce three-dimensional oblique separation of the boundary layer on the duct walls.

Thus, the conducted numerical-experimental study revealed a number of gasdynamic structures, which determine the character of the flow around the model configuration considered, in particular, the flow around the forebody with a cross-concave compression surface and the flow around a convergent inlet integrated with this surface. Though viscous effects complicate the real flow around the model, a comparison of the calculated and experimental data demonstrates reasonably good agreement in the flow region without boundary layer separation.

UPGRADE OF THE AACHEN SHOCK TUNNEL WITH A DETONATION DRIVER

M. Habermann, H. Olivier

Shock Wave Laboratory, RWTH Aachen, 52056 Aachen, Germany

Introduction

For ground based simulation of hypersonic flight in general, the reentry of a body into a planetary atmosphere or the development of airbreathing rocket engines, high enthalpy wind tunnels are required. Most of the high enthalpy facilities in use for ground testing are derived from the shock tunnel principle with only minor variations. In order to extend the limited capability of conventional shock tunnels which use an electrically heated, light gas in the high pressure section, some free piston tunnels have been constructed and set up during the last decade with increasing size and investment. A cost-effective and promising alternative to gain the demanded high values of temperature and pressure for the driver section of a shock tunnel is the use of a detonation driver in which the driver state is generated by a gaseous detonation. In comparison with the sophisticated and expensive techniques of heavy piston driven shock tunnels, the practical disadvantage with a detonation driver lies in the higher precautions one has to take in preparing the reactive mixture and its handling. The goals to be achieved with the detonation driver are several, i.e. increased specific enthalpy due to the high temperature driver gas, increased test time due to the ability of different tailored interface conditions, improved repeatability of the test conditions, and relatively low costs for the facility and its operation.

Operation principle

The idea of using an upstream¹ detonation driver for a shock tunnel where the detonation is initiated at the main diaphragm was first presented by Yu et al. (1992). Lenartz et al. (1995) carried on with the theoretical deliberations and developed the detailed concept and design of an upstream detonation driver for the shock tunnel TH2 in Aachen, elaborated in the following years (Grönig et al. 1997, Habermann and Olivier 1998, Habermann et al. 1999). With an upstream detonation driver (see Fig. 1) a stable detonation is initiated at the diaphragm to the low pressure section and propagates to the backward end of the detonation section leaving behind a gas at high temperature and high pressure. After the bursting of the diaphragm this gas acts as a source from which the shock wave in the low pressure section is driven. The following processes to generate the nozzle reservoir condition behind the shock reflection are comparable to those in a conventional shock tunnel. The Taylor expansion behind the detonation wave matches the shock tube expansion wave forming a large simple wave region extending from the rear of the detonation wave to the tail characteristic of the rarefaction wave. The detonation wave is slightly reflected by the weak diaphragm to the damping section and propagates as shock wave of moderate strength through the damping section. The shock wave is finally reflected by the end wall of the damping section. The damping section has the task to avoid a severe reflection of the initial detonation wave in order to obtain a reduction of the structural load on the facility.

¹ For explanation of and comparison between the upstream and downstream detonation driver mode see Bakos and Erdos (1997).

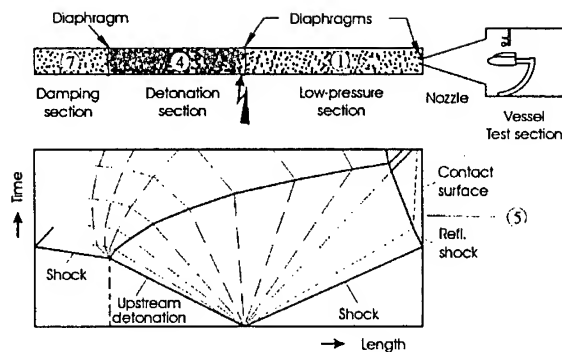


Fig. 1: Principle of an upstream detonation driven shock tunnel including set-up and wave plan. Numbers denote gas conditions at the beginning and during the run

Set-up of the facility

The detonation driven shock tunnel TH2-D consists of a dump tank with test section, a slender conical nozzle of 5.8 degree half angle and 586 mm exit diameter, a low pressure section of 15.6 m length, the detonation section of 9.4 m length and a damping section 6.4 m in length (see Fig. 2). The whole tube has an inner diameter of 140 mm and its maximum working pressure is fixed to 150 MPa. The conventional helium driver operating with a double diaphragm chamber is placed side by side to the detonation driver. If necessary the drivers can be exchanged within one day. Operating the detonation driver, only one diaphragm to the low pressure section is used. The initiation tube is located a few centimeters upstream of the main diaphragm. The detonation section is filled with an oxyhydrogen mixture diluted with argon or helium. The mixing rate of the gases is controlled by thermal mass flow controllers. The combustion process in the detonation wave produces water steam. To avoid its condensation in the test section during or shortly after the run a fast acting plug valve has been installed in front of the nozzle entrance. The closing mechanism of this valve is controlled by the incident shock (Bird et al. 1964). The valve closes the nozzle entrance a few milliseconds after the useful running period.

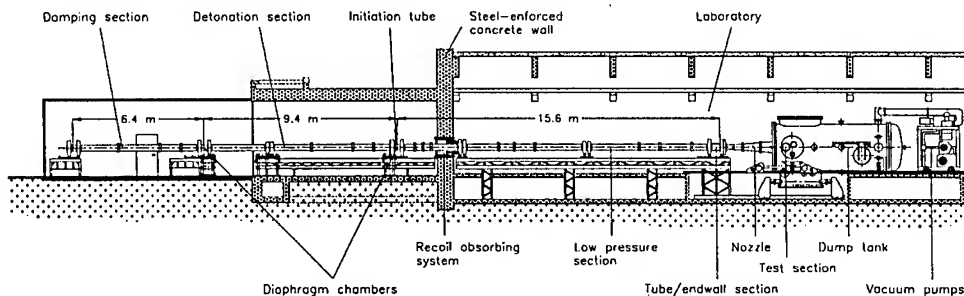


Fig. 2: The detonation driven shock tunnel TH2-D

The detonative gas mixture is ignited by an exploding wire located at the upper end of an igniter tube. The igniter energy is about 4 J. Within the initiation tube after a certain propagation length a detonation wave is formed which runs into the main tube to cause a direct

initiation there which immediately leads to a detonation wave travelling upstream in the detonation section.

Theoretical estimation of flow conditions

The adjustment of the testing conditions of a detonation driven shock tunnel is made, besides the variation of the initial pressure ratio p_4/p_1 , by the choice of the detonative gas mixture. Stoichiometric oxyhydrogen is used here with varying admixtures of helium or argon to gain a wide range of tailored interface conditions. Helium is added to achieve a high stagnation enthalpy at the expense of test time whereas argon dilution yields a quite long test time and a higher Reynolds number in the test flow.

The numerical results represented in the following are calculated for tailored interface conditions generated by an upstream detonation driven shock tunnel with the dimensions printed in Fig. 2. Figure 3 shows the dependence of the endwall stagnation enthalpy h_5 , the endwall stagnation pressure p_5 , and the required initial pressure p_1 on the helium or argon volume fraction. With an increasing amount of helium the stagnation enthalpy first rises to a maximum value of 19.5 MJ/kg before it starts decreasing. The former gain in enthalpy is due to the influence of the helium on the speed of sound of the driver gas. For larger helium concentrations the gain in speed of sound is over-compensated by the loss of chemical energy released in the detonation process. An increasing fraction of argon permits significantly higher values for the initial pressure p_1 and yields an increasing endwall stagnation pressure p_5 up to about 43 MPa as the stagnation enthalpy h_5 drops drastically to values typical for conventional shock tunnels.

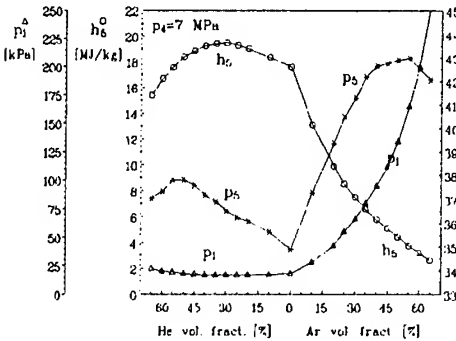


Fig. 3: Calculated properties of tailored endwall conditions versus concentration of helium or argon admixture to stoichiometric oxyhydrogen

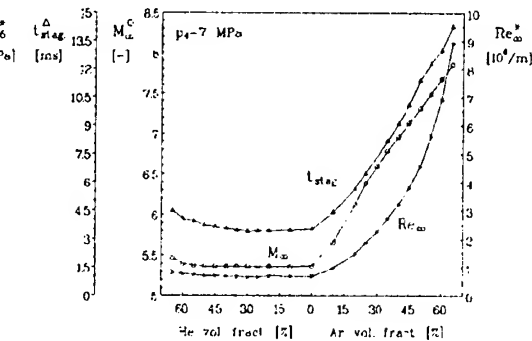


Fig. 4: Test section flow properties and ideal testing time for tailored endwall conditions according to Fig. 3

The test flow conditions in Fig. 4 have been calculated for a quasi one-dimensional thermochemical equilibrium nozzle flow. The nozzle geometry is given by the critical diameter $d^* = 37$ mm and the area ratio $A/A^* = 250$. For an increasing helium concentration the theoretical stagnation time t_{stag} rises from about 3.5 ms up to about 4 ms, whereas the Mach number of about $M_\infty \approx 5.4$ and the Reynolds number of about $Re_\infty \approx 0.7 \cdot 10^6/m$ do not change remarkably. Due to the low density of the high temperature free stream, the Reynolds number for a high helium fraction is lower than for conventional shock tunnels with comparable nozzle

dimensions. But with an increasing concentration of argon, Reynolds and Mach number rise up to $Re_\infty \approx 7 \cdot 10^6/m$ and $M_\infty \approx 7.7$. The ideal stagnation or testing time goes up to more than 14 ms which is relatively long for shock tunnel operation in the reflected mode.

Experimental results of calibration tests

First, the behaviour of the detonation wave in the detonation section has been studied. For this, pressure histories and the detonation wave velocity have been recorded for various gas mixtures and initial filling pressures of the detonation section. In comparison with a combustion driver the state in the high pressure section of the detonation driver is quite stable and well reproducible. The measured detonation velocity gained in several experiments is presented in Fig. 5 for a variety of diluent concentrations. The agreement with the values predicted by the Chapman-Jouguet theory is very good.

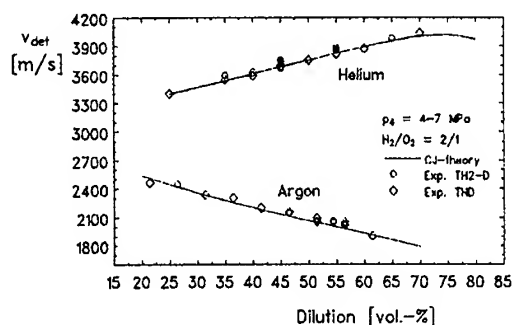
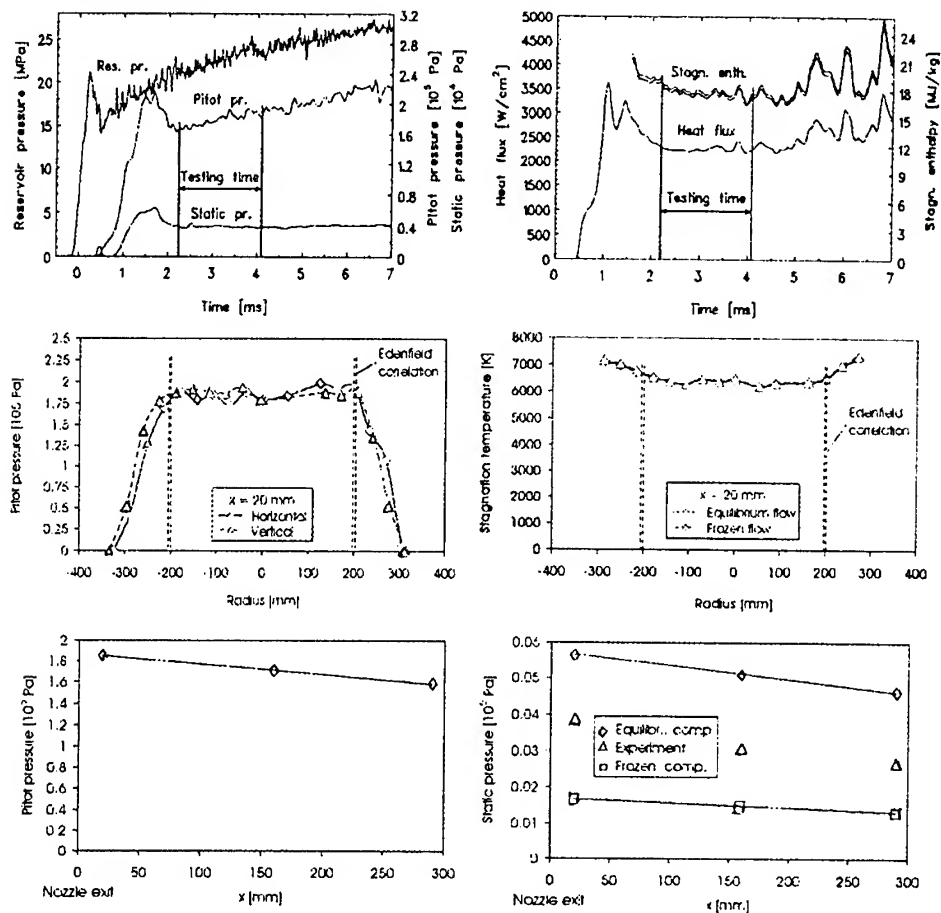


Fig. 5: Detonation wave velocity versus dilution concentration

After this, experiments have been performed in the shock tunnel mode with a calibration rake, consisting of four cross arms. Totally 36 Pitot pressure and 19 heat flux sensors have been installed. The pressure gauges as well as the coaxial thermocouples were mounted at the stagnation point of small spheres having a diameter of 20 mm. Additionally one static pressure probe has been mounted in the Pitot rake. The calibration rake was used to measure the flow field in three axial positions located 20, 160 and 290 mm behind the nozzle exit. From the measured Pitot pressures and stagnation point heat fluxes for each radial position on the calibration rake the total enthalpy of the flow as well as the free stream conditions have been determined (Olivier 1993). Figure 6 shows typical results of the calibration experiments for the highest and lowest stagnation enthalpy condition.

For the high enthalpy condition the reservoir pressure increases to its ideal value corresponding to the pressure behind the reflected shock. This theoretical value amounts to 210 MPa which fits very well with the first peak in the reservoir pressure history. But then the pressure decreases to rise again after one half millisecond. The same behaviour, delayed and smoothed by the nozzle starting process, can be recognized for the Pitot and the static pressure. This test condition is slightly overtailored, obvious from the slight increase of the reservoir pressure. The overtailoring is caused by the cooling of the driver gas on the way down from the detonation section to the shock tube endwall. Recalculating the measured reservoir pressure signal shows that the loss of driver gas temperature amounts to about 17 %. The useful testing time is defined by a period of time of more or less constant stagnation enthalpy. The Pitot pressure profile shows the expected behaviour with slight variations in the core flow region

High enthalpy condition:



Low enthalpy condition:

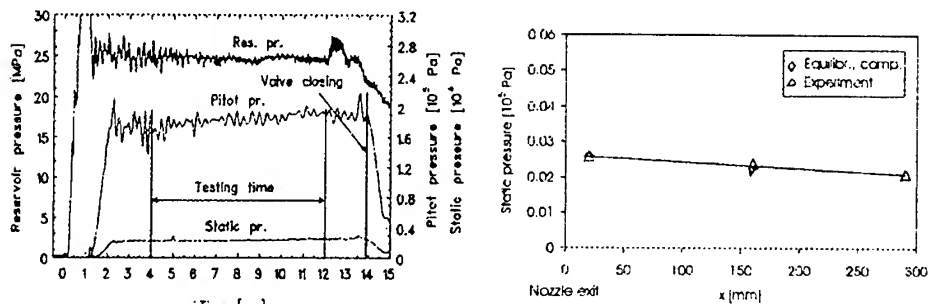


Fig. 6: Typical calibration results of the detonation driven shock tunnel TH2-D for a high and a low enthalpy condition

which extends about 400 mm in radial direction. The boundary layer thickness at the nozzle exit amounts to about 100 mm which is in agreement with the Edenfield correlation. The measured static pressure of the free stream can be used to characterize the thermochemical state of the flow. As it is obvious in this case the measured static pressures along the nozzle exit are between the computed values assuming fully equilibrium and frozen nozzle flow, respectively.

For the low enthalpy condition the pressure signals show a nicely constant behaviour during the useful testing time which amounts to 8 ms in this case. As expected, for this low enthalpy condition ($h_0 = 2.1 \text{ MJ/kg}$) the measured static pressure is in good agreement with the theoretical values for fully equilibrium flow. In this example the effect of the closing of the plug valve in front of the nozzle is seen by the Pitot pressure drop after 14 milliseconds. The valve seals the nozzle entrance so that only a negligible amount of combustion products enter the test section.

Conclusions

The calibration tests have shown that a detonation driver is suitable to generate high enthalpy flows in a shock tunnel. There is no difference in flow quality compared to a conventional driver. The performances are slightly decreased by heat losses of the driver gas on the way down to the nozzle reservoir. The same phenomenon occurs for piston drivers, too. A fast acting plug valve in front of the nozzle entrance avoids that combustion products enter the test section. The performances of the detonation driver can be increased significantly by using a driver tube of larger cross section than the driven tube. For the same tube dimensions, detonation and heavy piston drivers yield nearly the same performances.

Acknowledgements

Part of this work was supported by the Deutsche Forschungsgemeinschaft (DFG) within the Special Collaborative Research Center SFB 253 „Fundamentals of the Design of Aerospace Planes“.

References

- Bakos R.J., Erdos J.J. (1997) Optimizing pressure recovery in a detonation driven reflected shock tunnel. Proceedings of the 21st International Symposium on Shock Waves 2: 1359-1365
- Bird K.D., Martin J.F., Bell T.F. (1964) Recent Developments in the Use of the Hypersonic Shock Tunnel as a Research and Development Facility. Third Hypervelocity Techniques Symposium, Denver, CO
- Grönig H., Olivier H., Habermann M. (1997) Development of a detonation driver for a shock tunnel. Review High Pressure Science Technology 7: 879-884
- Habermann M., Olivier H. (1998) Experimental studies in a detonation driven shock tube at elevated pressures. Proceedings of the Symposium on Shock Waves, Japan, 551-554
- Habermann M., Olivier H., Grönig H. (1999) Operation of a high performance detonation driver in upstream propagation mode for a hypersonic shock tunnel. Presented at the 22nd International Symposium on Shock Waves, London
- Lenartz M., Wang B., Grönig H. (1995) Development of a detonation driver for a shock tunnel. Proceedings of the 20th International Symposium on Shock Waves 1: 153-158
- Olivier H. (1993) An improved method to determine free stream conditions in hypersonic facilities. Shock Waves 3: 129-139
- Yu H-r, Esser B, Lenartz M, Grönig H. (1992) Gaseous detonation driver for a shock tunnel. Shock Waves 2: 245-254

NUMERICAL STUDY OF 3D REGULAR AND MACH REFLECTIONS OF STEADY SHOCK WAVES

M.S.Ivanov, A.N.Kudryavtsev, D.V.Khotyanovsky, G.N.Markelov¹
Institute of Theoretical and Applied Mechanics, Novosibirsk, 630090, Russia

1. Introduction

The transition between regular and Mach shock wave reflections, having more than a century's history of research, still remains one of the last unsolved problems of classical gas dynamics. The existence of two possible solutions at the same flow conditions, and related hysteresis phenomenon make this problem be one of the most interesting and challenging research tasks. In recent experimental and numerical studies [1-4] the hysteresis in transition between regular (RR) and Mach (MR) reflections of steady shock waves has been reported. However, in the experiments the $RR \Rightarrow MR$ transition occurs at the incident shock wave angle α close to the von Neumann angle α_N (the lower theoretical bound of the existence of MR), or a few degrees higher, within the *dual solution domain*. At the same time, the computations show that transition angles correspond to the detachment criterion α_D (the upper theoretical bound of the existence of RR). The reverse $MR \Rightarrow RR$ transition occurs near α_N both in the experiments and in computations. It should be mentioned, that the difference between two theoretical criteria increases significantly at high Mach numbers, e.g. $\alpha_D - \alpha_N = 8.5^\circ$ at $M=5$, see Fig.1 where the theoretical criteria are given versus the flow Mach number. The reasons for the discrepancies between experimental and numerical transition angles and for those existing between the results obtained at different experimental facilities are supposed to be twofold. The first reason is the effect of the free stream disturbances, which must be accounted of when considering conditions of the transition in the wind tunnels. The effect of the disturbances was investigated numerically [4-5]. It was shown that the perturbations of some kind could indeed lead to a "forced" transition between the two types of reflection. It was also found that $RR \Rightarrow MR$ transition can be achieved easier than the reverse transition, and the levels of the perturbation, necessary for this transition, decrease when approaching to the upper limit of the existence of RR, α_D . Still, the amplitudes of these disturbances can hardly be relevant to the real experimental flows, and it is not clear why the $RR \Rightarrow MR$ transition in some experiments takes place at α_N .

The other reason for the discrepancies is the flow three-dimensionality, which is also present in the experiments where the wedges of finite span are used as the test models. These effects are now being extensively studied in detail, both numerically and experimentally. Detailed theoretical consideration of these was provided in [6]. Depending on the wedge relative span b/w the shock wave configuration may either have a 2D portion in the vertical plane of symmetry, or the overall configuration may be purely three-dimensional when the rarefaction waves from the wedge tips reach the inner portion of the flow. Three-dimensionality is even more crucial for the Mach reflection when a subsonic region behind the Mach stem surface exists, and the rarefaction can affect the inner flow through this region. In other words, Mach reflection is *always* three-dimensional. In previous numerical studies (see, for example [4]) it was shown that three-dimensionality might affect the transition between RR and MR: the

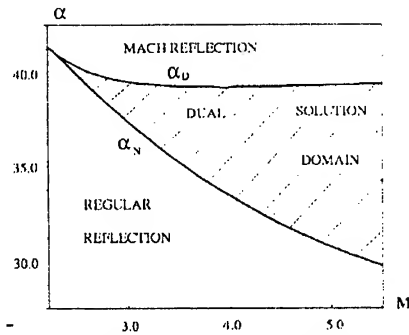


Fig. 1. Transition criteria vs. flow Mach number

angles of the transition increase when b/w decreases. The transition angles correspond to two-dimensional criteria only for sufficiently high aspect ratios b/w , say $b/w > 4$. It was also confirmed numerically [4] that a hysteresis phenomenon in $RR \Leftrightarrow MR$ transition exists in 3D case as well as in previous 2D simulations.

In the following we will present our recent numerical results on the effects of flow three-dimensionality in the problem of the $RR \Leftrightarrow MR$ transition.

2. Problem formulation and numerical techniques

The flow around two symmetrical bodies used as shock wave generators is investigated – see Fig.2, where necessary notions are also given. This double wedge configuration is exactly the same as that experimentally studied in a number of works devoted to transition between RR and MR. In our Euler computations we replace the wedges by two inclined flat plates for easier body-fitted grid generation. Owing to the symmetry of the problem, the computations are performed only in a quarter of the domain. The downstream boundary is located far enough so that the flow there was supersonic. The upper and lateral boundaries are sufficiently far from the body so that the uniform free stream conditions could be imposed on them. The angle of the wedge is changed by rotating the wedge around its trailing edge, i.e. the distance g between the horizontal symmetry plane and the trailing edge is constant during the rotation.

The three-dimensional unsteady Euler equations for a perfect gas (the specific heats ratio $\gamma = 1.4$) are solved with a high-order total variation diminishing (TVD) scheme. The HLLE

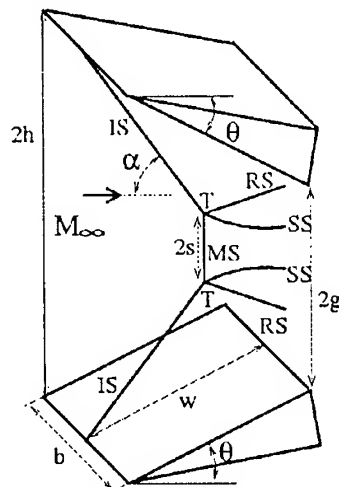


Fig. 2. Schematic of the double-wedge configuration

(Harten–Lax–van Leer–Einfeldt) solver is used for evaluation of the numerical fluxes on the inter-cell boundaries because of its robustness for flows with strong shock waves and expansions. The variables in the "left" and "right" states on the inter-cell boundaries are reconstructed from cell averaged ones using the 4-th order formula of [7]. The reconstruction is applied to the primitive variables (density, velocity components and pressure). The use of a high-order reconstruction formula allows us to decrease a large numerical diffusion inherent to the HLLE solver and provide a high resolution at smooth parts of the solution without a loss of robustness near strong shock waves. The third-order explicit Runge-Kutta scheme is used for time stepping. It should be mentioned that an accurate modelling of unsteady phenomena can prove to be important in this problem. A multi-block body-fitted grid is used in the simulations with the number of cells up to 945,000.

3. Results and discussion

Normalised Mach stem heights s/w obtained in our 3D Euler simulations of the MR are given in Fig.3 versus the incident shock wave angle α . For comparison, the Mach stem heights measured in the ITAM experiments [3] for corresponding flow conditions are also given. The flow Mach number is $M=4$, and the corresponding theoretical criteria are $\alpha_N = 33.4^\circ$ and $\alpha_D = 39.2^\circ$. The transition to MR occurred when α was being increased from 39° to 40° . When the shock wave angle was decreased, MR was preserved down to the angles close to α_N , where an RR formed. Thus, the results of simulations give clear evidence that, within the dual solution domain, the final reflection type depends on initial conditions, and the hysteresis exists as well as in 2D numerical simulations. Moreover, the transition angles are in reasonable agreement with the theoretical values. An early MR \Rightarrow RR transition, i.e. slightly above α_N , can be explained by insufficient resolution of the very small Mach stem height at the angles close to α_N . This height becomes comparable with the size of numerical cells and cannot be resolved without further grid refinement. It is also clear, that the numerical and experimental Mach stem heights for the same spanwise aspect ratios b/w are in beautiful agreement. Fig.3a also illustrates the influence of the wedge span on the numerical Mach stem heights (for comparison, their computed values at $b/w=2$ and in 2D case are also given).

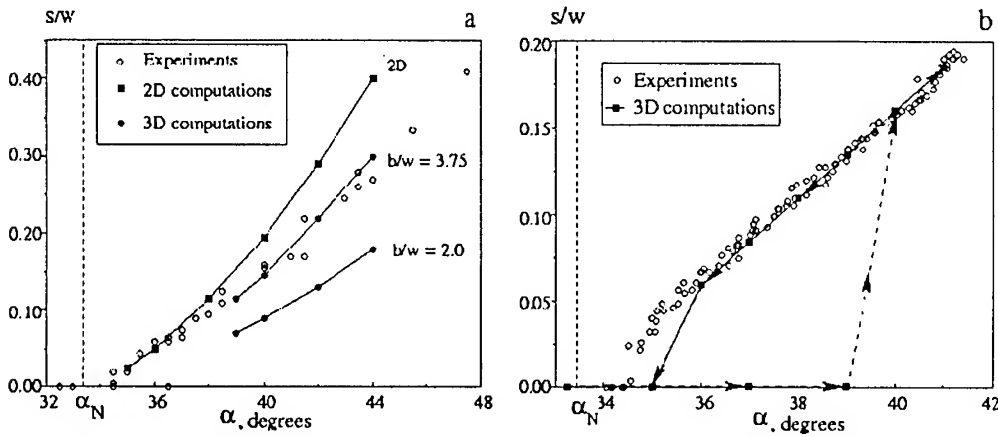


Fig. 3. Experimental and numerical Mach stem heights vs. incident shock angle for $M=4$; and (a) $g/w = 0.56$, $b/w = 3.75$; (b) $g/w = 0.3$, $b/w = 2$

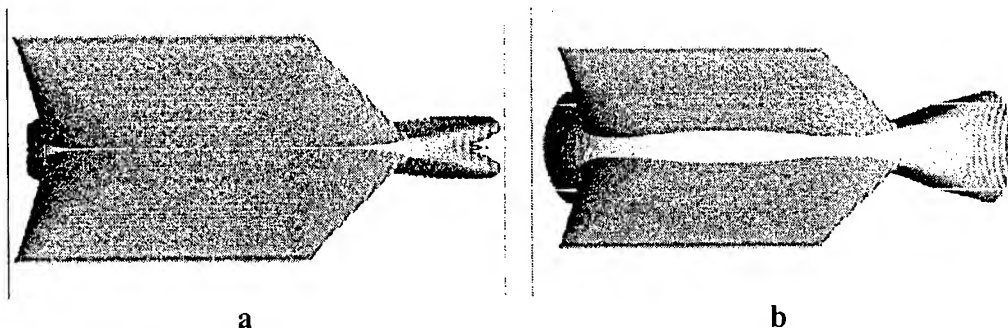


Fig. 4. Density isosurfaces $\rho/\rho_\infty = 2.2$ for RR (a) and MR (b). Euler computations, $M=4$, $\alpha = 38^\circ$, $b/w=2$, $g/w=0.3$

In order to investigate in detail the 3D structure of the shock wave reflection we have reconstructed the shock wave surfaces of RR and MR. These are shown in Fig. 4 for identical flow parameters and incident shock angle within the dual solution domain. These images clearly visualize a spatial configuration of RR and MR. As can be seen, a *peripheral Mach reflection* exists in an RR case (Fig. 4a) at far distance from the vertical symmetry plane. The flow behind the peripheral Mach stem surface is supersonic. There is a point where the RR and peripheral MR co-exist in equilibrium. It is obvious that in case of MR (Fig. 4b) the Mach stem height demonstrates a non-monotonous behaviour in a transverse direction. Its height has a maximum in the vertical plane of symmetry. Closer to periphery its height decreases, reaches a minimum, and then increases again forming a peripheral Mach reflection similar to that observed in RR case.

More detailed information can be derived from two-dimensional slices of the flowfield at different values of the spanwise co-ordinate z ($z=0$ corresponds to the vertical plane of symmetry). These slices are shown in Fig. 5 for RR and MR. It can be noted that at large z (at the periphery) the Mach stem is convex to the oncoming flow. Far from the test model, both the incident shock and Mach stem degenerate into a weak conical wave.

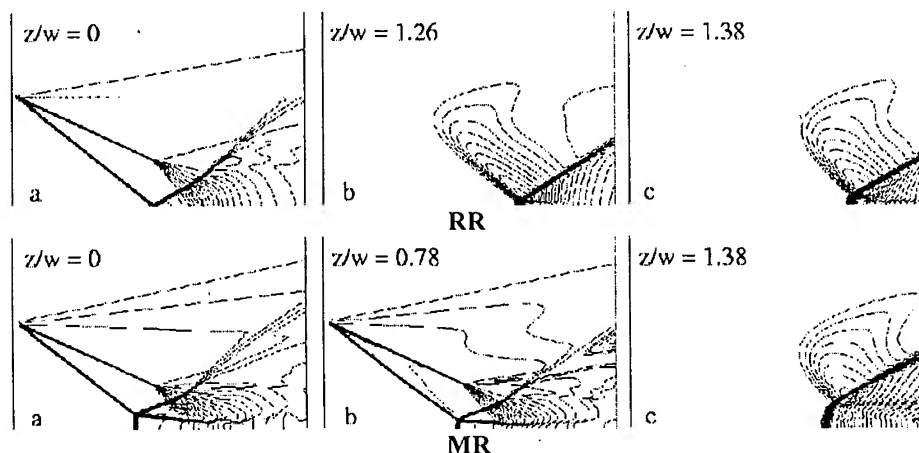


Fig. 5. Two-dimensional slices of density for RR and MR at different spanwise locations. Euler computations, $M=4$, $\alpha = 38^\circ$, $b/w=2$, $g/w=0.3$

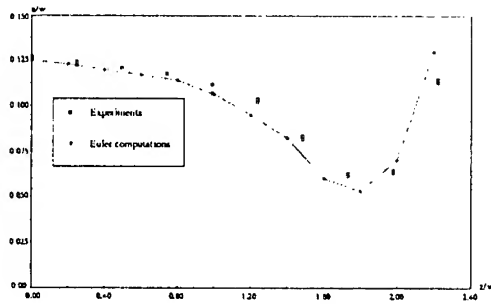


Fig. 6. Mach stem height variation in spanwise direction in comparison with ITAM experimental data.
 $M=4$, $\alpha = 37^\circ$, $b/w=3.75$, $g/w=0.3$

The Mach stem heights variation in spanwise direction is given in Fig. 6 in comparison with the ITAM experimental data [8] measured with the help of laser sheet visualizations taken at different locations along span. It is obvious that the numerical data are in close agreement with the experimental ones.

To compare our numerical flowfields with experimental schlieren visualizations, we calculated an averaged density gradient field as $\overline{\nabla \rho}(x, y) = \int \nabla \rho(x, y, z) dz$. It was then visualised as a half-tone grey-scale picture with a special non-linear scale. This “numerical schlieren” is presented in Fig.7 in comparison with an experimental flow image for an MR. A close resemblance of numerical and experimental pictures is evident. Fine features of the MR configuration are perfectly reproduced in the computations, e.g. the triple point traces along the direction of integration (curved lines between the slip surfaces and the reflected shocks).

At some flow parameters, if the Mach stem height in the central plane is small enough, a particular shock wave configuration with a combined type of reflection is possible: MR with a small stem in the central plane, RR at some spanwise distance to the periphery, and MR again – at far periphery. This configuration was first revealed with the DSMC method [9]. Now, its existence has been confirmed with Euler computations, and is shown in Fig. 8. It is important to mention that this shock reflection configuration, first observed numerically, has been recently identified in course of ITAM experiments [8,10] with the laser sheet visualisation.

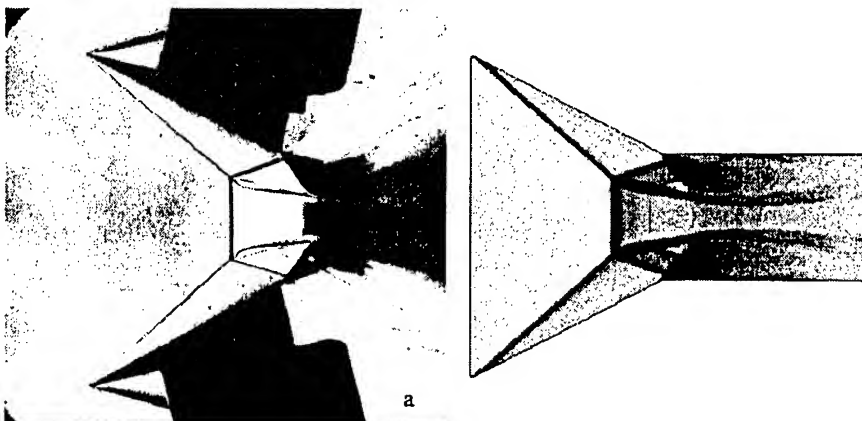


Fig. 7. Experimental (a) and numerical (b) schlieren pictures for MR at $M=4$, $\alpha = 40^\circ$, $b/w=2$, $g/w=0.3$

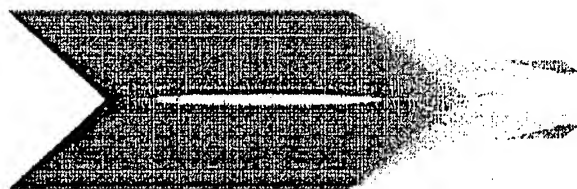


Fig. 8. Combined type of shock wave reflection. $\alpha = 35.5^\circ$, $b/w=3.75$, $g/w=0.3$. Euler computations.

Density isosurface.

4. Conclusions

3D numerical simulation of steady shock wave reflection between two bodies of finite spanwise width has been performed. The existence of the hysteresis phenomenon in the transition from regular to Mach reflection, and back, is revealed. A close agreement between the Mach stem heights in the experiments and the computations is shown, and a strong dependence of the Mach stem height on the spanwise extent of the wedges is confirmed. 3D shapes of interacting shock waves are visualised for regular and Mach reflections and demonstrate the existence of peripheral Mach reflection in regular reflection case, and non-monotonous variation of the Mach stem height in spanwise direction. Also, a close resemblance of numerical and experimental flow patterns is shown with the help of numerical schlieren pictures integrated along the spanwise co-ordinate. A particular, combined type of shock wave reflection configuration has been observed in the numerical simulations.

Acknowledgements

The authors would like to thank S.Nikiforov for his help in preparing this paper. This work was supported by Russian Foundation for Basic Research, Grant No.00-01-00824. The third author wishes to acknowledge the support of INTAS, Young Scientists Fellowship YSF 99-4061.

References

- [1] Chpoun A, Passerel D, Li H, Ben-Dor G. Reconsideration of oblique shock wave reflections in steady flows. Part I. Experimental investigation // *J. Fluid Mech.*—1995. — Vol. 301. — P. 19-35.
- [2] Ivanov M.S., Gimelshein S.F., Beylich A.E. Hysteresis effect in stationary reflection of shock waves // *Phys. Fluids.* — 1995. — Vol. 7. — P. 685-687.
- [3] Ivanov M.S., Klemenkov G.P., Kudryavtsev A.N., Nikiforov S.B., Pavlov A.A., Fomin V.M., Kharitonov A.M., Khotyanovsky D.V., Hornung H.G. Experimental and numerical study of the transition between regular and Mach reflection of shock waves in steady flows // *Proc. 21st Intern. Symp. Shock Waves.* — 1997 — Vol. 2. — P. 819-824.
- [4] Ivanov M.S., Markelov G.N., Kudryavtsev A.N., Gimelshein S.F. Numerical analysis of shock wave reflection transition in steady flows // *AIAA Journal.* — 1998. — Vol. 36. — P. 2079-2086.
- [5] Khotyanovsky D.V., Kudryavtsev A.N., Ivanov M.S. Numerical study of transition between steady regular and Mach reflections caused by free-stream perturbations // *Proc. 22nd Intern. Symp. Shock Waves.* — 1999. — Vol.2. — Paper 3700. — P. 1261-1266.
- [6] Skews B.W. Aspect ratio effects in wind tunnel studies of shock waves reflection transition // *J. Shock Waves.* — 1997. — Vol.7. — P. 373-383.
- [7] Yamamoto S., Daiguji H. Higher-order-accurate upwind schemes for solving the compressible Euler and Navier—Stokes equations // *Computers and Fluids.* —1993. — Vol.22. — P. 259-270.
- [8] Ivanov M.S., Klemenkov G.P., Kudryavtsev A.N., Nikiforov S.B., Pavlov A.A., Kharitonov A.M., Fomin V.M. Experimental investigation of 3D steady shock wave interaction // *Proc. 10th Intern. Conf. Methods Aerophysical Research.* — 2000.
- [9] Ivanov M.S., Gimelshein S.F., Kudryavtsev A.N., Markelov G.N., Khotyanovsky D.V. Numerical simulation of three-dimensional regular and Mach reflections of shock waves in steady flows // *Comput. Fluid Dynamics'98. Proc. 4th ECCOMAS Conf.* — 1998. — Vol.1. — Part 2. — P. 869-874.
- [10] Ivanov M.S., Klemenkov G.P., Kudryavtsev A.N., Nikiforov S.B., Pavlov A.A., Kharitonov A.M., Fomin V.M. Wind tunnel experiments on shock wave reflection transition and hysteresis// *Proc. 22nd Intern. Symp. Shock Waves.* — 1999. — Vol. 2. - Paper 1121. — P. 1191-1196.

EXPERIMENTAL INVESTIGATION OF 3D STEADY SHOCK WAVE INTERACTION

M.S. Ivanov, G.P. Klemenkov, A.N. Kudryavtsev, S.B. Nikiforov, A.A. Pavlov,
A.M. Kharitonov, V.M. Fomin

Institute of Theoretical and Applied Mechanics SB RAS,
630090 Novosibirsk, Russia

INTRODUCTION

It is well known that two different configurations, the regular reflection (RR) and the Mach reflection (MR), can be observed when a steady shock wave reflects from a plane surface. For strong shock waves there exists a range of angles of incidence $\alpha_N < \alpha < \alpha_D$ (*dual solution domain*) where both reflection types are theoretically possible. Here α_N and α_D are the angles deduced from so called *von Neumann* and *detachment* criteria, respectively. As a consequence, it can be assumed, see [1], that a hysteresis phenomenon should be observed when changing the angle continuously, i.e. the angles of transition from RR to MR α_{tr}^F , and of the reverse transition α_{tr}^B , should differ, namely $\alpha_{tr}^F = \alpha_D$, but $\alpha_{tr}^B = \alpha_N$. However, in the experiments of [3] it was found that $\alpha_{tr}^F \approx \alpha_{tr}^B \approx \alpha_N$. Nevertheless, the hysteresis phenomenon at shock wave reflection transition was later really observed both in the wind tunnel experiments of [2] and the DSMC (Direct Simulation Monte Carlo) computations of [4]. In some next years, considerable effort has been devoted to the further experimental and numerical investigation of the steady shock wave interaction. The experimental investigations revealed that α_{tr}^F is really close to α_N , but the value of α_{tr}^F probably depends on the wind tunnel type. It is approximately equal to α_N in wind tunnels with a closed test section [3, 9], but for open free-jet facilities, α_{tr}^F lies within the dual solution domain, it is some degrees higher than α_N [2, 8].

Thus, the experimental values of α_{tr}^F differ significantly from each other as well as from numerical ones. One possible reason for this discrepancy may be different levels of free-stream perturbations in different wind tunnels. Besides the perturbation level, the shock wave reflection investigated in experiments is strongly influenced by 3D effects, which are inevitable because of the finite width of the wedges.

An attempt to study experimentally the 3D features of the shock wave reflection was undertaken by [15] using a skewed schlieren technique. At the same time, numerical simulations of 3D shock wave configurations were started by [5, 6]. Later, more detailed numerical studies were performed by [7, 10]. These simulations give many predictions concerning the 3D structure of shock wave reflection and reveal that the 3D effects have a strong influence on some important parameters, for example, on the Mach stem height. Recently, an experimental investigation of 3D shock wave reflection was carried out by [17] with the spanwise laser sheet method.

In the present paper we use a novel modification of the laser sheet technique to visualize the 3D shock wave configurations, investigate the role of 3D effects, and check the predictions deduced from the numerical simulations.

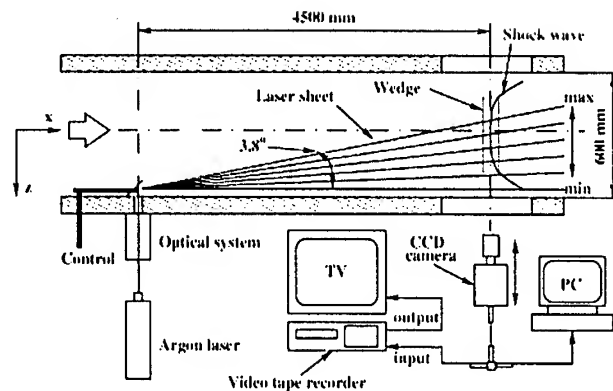


Fig. 1. Schematic of experimental set-up (top view) and optical diagnostic system.

1. EXPERIMENTAL SET-UP

The experiments were performed in the wind tunnel T-313 of the Institute of Theoretical and Applied Mechanics at the Mach number $M=4$. This wind tunnel has a rectangular closed test section of 600 x 600 mm size. The stagnation temperature of air was equal to 290°C and the pressure in the settling chamber was 10 ata. Two symmetrical wedges with the length $w=80$ mm mounted in the wind tunnel test section were used as shock wave generators.

The angle of attack θ and, consequently, the angle of generated shock wave α can be varied by simultaneous rotation of the wedges around their trailing edges. Thus, the distance between the trailing edges, $2g$, remains constant during rotation. Models with a different spanwise width b were used to consider the shock wave reflection under either greater or lesser influence of 3D effects. The streamwise laser sheet imaging technique was used for the visualization of a shock wave reflection configuration. This technique utilizes the laser light scattering on micron-sized particles of water. As a result, only the flow in the plane of the laser sheet is visualized, in contrast to the common schlieren technique, which gives an image integrated along the spanwise direction.

A schematic of experimental set-up and optical diagnostic system is shown in fig. 1. As a light source, an argon-ion laser was used. The power of the laser was adjusted at 3 W to provide clear pictures. The laser beam was expanded to the light sheet using a combination of convex and spherical lenses. The light sheet thickness was about 1 mm. In order to investigate the 3D structure of shock wave reflection configurations, the laser sheet was traversed in the spanwise direction scanning the flowfield from the central plane of the test section up to the wall. The maximum angle between the laser sheet and the wind tunnel axis did not exceed 3.8°. An appropriate amount of water (less than $1.1 \text{ g}_{\text{H}_2\text{O}} / \text{kg}_{\text{air}}$) was seeded in the wind tunnel before the settling chamber. Slices of the flow pattern were grabbed by the CCD camera mounted outside the test section. To avoid the image scale disturbances the movement of the CCD camera was synchronized with the laser sheet movement. The maximum number of flow images corresponding to different streamwise planes, which were obtained at different spanwise locations during one pass across the test section, was equal to 20. The CCD camera was connected to both the computer frame grabber and the video tape recorder (VTR). A TV set was also connected to the VTR.

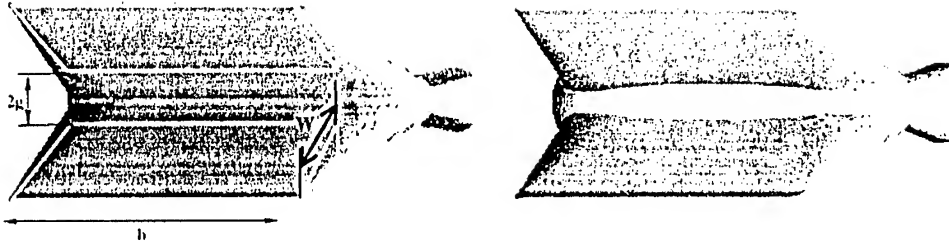


Fig. 2. Typical 3D shock wave configuration of RR (left) and MR (right) resulting from Euler

2. RESULTS AND DISCUSSION

The numerical simulations predict a rather complicated shape of the shock waves generated by two symmetrical wedges of finite width. Figure 2 shows typical 3D shock wave shapes for both RR and MR resulted from the Euler simulations of [13] (on the left picture, a schematic of the test model is superimposed).

One can see that, though we refer to the left configuration as a regular one, it is true only for its central part. On the periphery, due to side effects, RR becomes impossible, and MR is formed. However, the Mach number remains supersonic behind the peripheral Mach stem surface. In the case of MR configuration (right picture), MR exists at all spanwise locations and the flow behind the central part of the Mach stem is subsonic. The Mach stem height is nearly constant in the central part, where the influence of side effects is not significant. At larger distances from the vertical symmetry plane, the Mach stem height decreases and then, on the periphery, it considerably increases. Such behaviour can be hardly foreseen *a priori*.

The schlieren picture gives an image integrated along the spanwise direction. Therefore, such an image does not correspond to the flow pattern in any plane. The features that refer to different spanwise locations can be simultaneously seen on a schlieren picture. This statement is illustrated by the left image in fig. 3, where 3D features are distinctly visible. In addition to three shock waves and the slip surface, the curved black lines originating from triple points can be noticed. In fact, they are traces of a triple point motion on the periphery, which are seen in an image integrated along the spanwise direction. In contrast, the laser sheet image (right picture) is free from similar traces and gives a true flowfield pattern in a certain plane.

Let us compare the features of 3D shock wave interaction from the computations [7], [10] with our new experimental data obtained with the help of the laser sheet method. Figures 4, 5 show three spanwise slices of the flowfield for $M=4$, $b/w=0.66$, and $g/w=0.15$. Note that the transition to MR in this case was observed at $\theta=22.7^\circ$ ($\alpha=35.6^\circ$), and the reverse transition – at $\theta=22.3^\circ$ ($\alpha=35.1^\circ$), whereas the theoretical von Neumann angle is $\theta_N=20.8^\circ$ ($\alpha_N=33.4^\circ$).

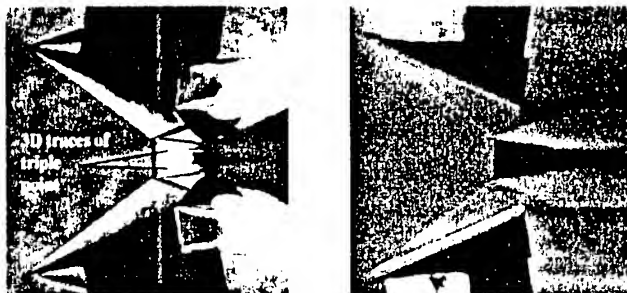


Fig. 3. Comparison of schlieren picture (left) and streamwise laser sheet image (right) at $M=4$, $b/w=3.75$, $g/w=0.3$, $\theta=23.6^\circ$, $\alpha=36.7^\circ$.

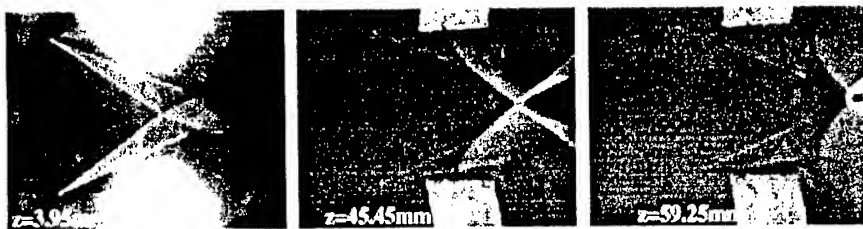


Fig. 4. Streamwise slices of flowfield at $M=4$, $b/w=0.66$, $g/w=0.15$, $\theta=22.1^\circ$.



Fig. 5. Streamwise slices of flowfield at $M=4$, $b/w=0.66$, $g/w=0.15$, $\theta=30.5^\circ$.

Figure 4 refers to the wedge angle $\theta=22.1^\circ$, which corresponds to the shock wave angle $\alpha=34.9^\circ$. The first slice is taken very close to the central plane and the shock wave reflection is regular there. The second slice is chosen soon after arising of the peripheral MR, and the third shows the peripheral MR with a quite large stem. Thus, the experimental data confirm the existence of the peripheral MR. It can be noted that the Mach stem on the periphery is considerably convex to the approaching flow, exactly as in the numerical simulations.

In figure 5, $\theta=30.5^\circ$ and $\alpha=46.0^\circ$. In this case, MR exists throughout the whole spanwise extension of the shock wave configuration. Nearer to the periphery the Mach stem grows very fast. Note, no visible decrease of its size occurs in any spanwise location for this strongly 3D case. It does not contradict with the numerical picture in fig. 2, however, because the latter was obtained for a more two-dimensional case.

Figure 6 gives the slices for another wedge width/length aspect ratio $z/w=3.75$ at $\theta=23.6^\circ$ and $\alpha=36.7^\circ$. Here for a long time the Mach stem height remains constant when moving away from the central plane. After that, it noticeably decreases – see the second slice. Eventually, it starts fast growing on the periphery – exactly as it happens in numerical simulations.

Figure 7 shows a new, surprising, shock wave configuration with intermittent reflection types. For this case $\theta=21.4^\circ$, $\alpha=34.1^\circ$, and $b/w=3.75$, as earlier. In the central plane MR with a small stem is observed (the first slice). When moving to the periphery, its height decreases, and, in some spanwise location, the reflection becomes regular (the second slice). Farther to the periphery, MR arises again and the Mach stem height starts growing (the third slice).

Such shock wave configuration with intermittent reflection types has been found earlier in the numerical simulation of [10], [12]. However, because of a small size of the Mach stem in the central part and possible influence of non-zero viscosity in the cited above DSMC computations, it was difficult to decide ultimately whether this configuration is a real essence or a numerical artifact. Nevertheless, the numerical prediction proves again to be surprisingly exact!

In conducted experiments the transition from MR to RR proceeds through the intermittent shock wave configuration. At the angles close to α_w the Mach stem height is small enough in the vicinity of the central plane and its height decreases towards the periphery, probably, due to 3D spreading of the flow behind the Mach stem. As a result, at some spanwise distance MR

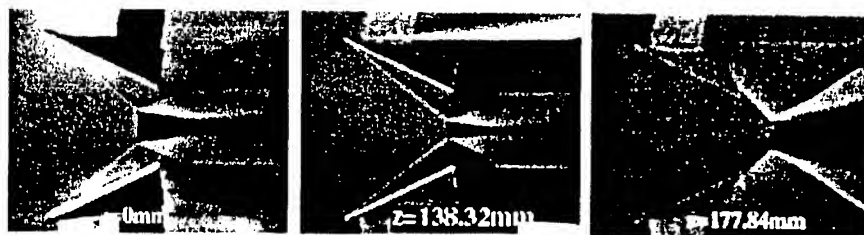


Fig. 6. Streamwise slices of flowfield at $M=4$, $b/w=3.75$, $g/w=0.3$, $\theta=23.6^\circ$.

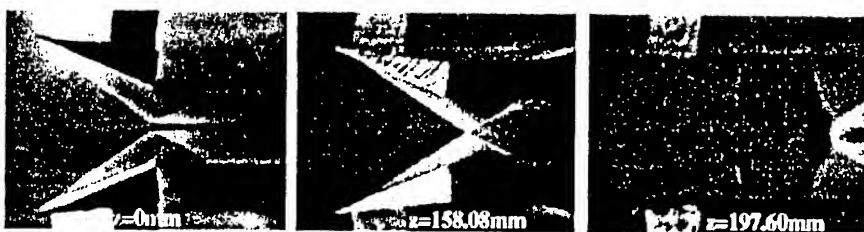


Fig. 7. Streamwise slices of flowfield at $M=4$, $b/w=3.75$, $g/w=0.3$, $\theta=21.4^\circ$.

transforms into RR. Farther to the periphery the curving of incident shock wave forces the recovery of MR. The transition from RR to MR in the wind tunnels with closed test sections occurs at α_{tr}^F , which is mainly close to α_N . In this case the transition is also realized through the intermittent configuration. If α continues to increase, the Mach stem in the central part of the flow becomes large and merges with the peripheral MR at some incident shock wave angle. As a result, the complete Mach reflection is formed. This fact can also be illustrated by figure 8, where heights of the Mach stem along the spanwise co-ordinate are shown. The heights of the Mach stem were measured from the images of streamwise slices of the flowfield taken at different spanwise coordinates starting from the vertical plane of symmetry of the model. White markers correspond to Mach reflection, black markers – to intermittent one. Also note that at the angles slightly smaller than for fig. 7 we observed the unsteadiness of the shock wave configuration. Visible oscillations of the Mach stem height with no wedge rotation were detected. Their period can be estimated as fractions of a second. For even smaller angles these oscillations turn into reiterated transitions from MR to RR and back.

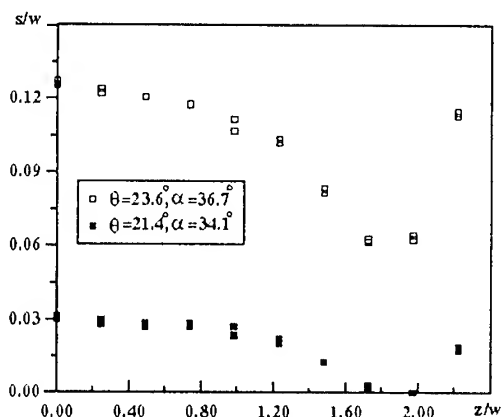


Fig. 8. Mach stem heights along spanwise co-ordinate ($M=4$, $b/w=3.75$, $g/w=0.3$).

3. CONCLUSIONS

A novel streamwise modification of the laser sheet technique has been used to visualize the 3D structure of shock wave reflection in the wind tunnel experiments with symmetrical wedges. The observed structure of the regular and Mach reflections has been found to be in close agreement with the predictions of the numerical simulation. A new shock reflection configuration also predicted numerically has been observed. In this configuration, when moving along the spanwise direction, the Mach reflection existing in the central plane is changed into the regular one, and later again the peripheral Mach reflection appears. This work was supported by the INTAS under Grant No.96-2356.

REFERENCES

- 1 Hornung HG, Oertel H, Sandeman RJ Transition to Mach reflexion of shock waves in steady and pseudosteady flow with and without relaxation // *J. Fluid Mech.* – 1979. – Vol. 90. – P. 541.
- 2 Chpoun A, Passerel D, Li H, Ben-Dor G Reconsideration of oblique shock wave reflections in steady flows. Part 1. Experimental investigation // *J. Fluid Mech.* – 1995 – Vol. 301. – P. 19.
- 3 Hornung HG, Robinson ML Transition from regular to Mach reflection of shock waves. Part 2. The steady flow criterion. // *J. Fluid Mech.* – 1982. – Vol. 123. – P. 155.
- 4 Ivanov MS, Gimelshein SF, Beylich AE Hysteresis effect in stationary reflection of shock waves // *Phys. Fluids.* – 1995 – Vol. 7 – P. 685.
- 5 Ivanov MS, Gimelshein SF, Kudryavtsev AN, Markelov GN Numerical study of the transition from regular to Mach reflection in steady supersonic flows // 15th International Conference on Numerical Methods in Fluid Dynamics: Proc. 1996, P. 394–399.
- 6 Ivanov MS, Markelov GN, Kudryavtsev AN, Gimelshein SF Transition between regular and Mach reflections of shock waves in steady flows. – AIAA Paper 97-2511, 1997.
- 7 Ivanov MS, Gimelshein SF, Kudryavtsev AN, Markelov GN Transition from regular to Mach reflection in two- and three-dimensional flows // Proceedings of the 21st International Symposium on Shock Waves: Proc. Pt. 2, P. 813–818, 1997.
- 8 Ivanov MS, Klemenkov GP, Kudryavtsev AN, Nikiforov SB, Pavlov AA, Fomin VM, Kharitonov AM, Khotyanovsky DV, Hornung HG Experimental and numerical study of the transition between regular and Mach reflection of shock waves in steady flows // Proceedings of the 21st International Symposium on Shock Waves: Proc. Pt. 2, P. 819-824, 1997.
- 9 Ivanov MS, Klemenkov GP, Kudryavtsev AN, Fomin VM, Kharitonov AM Experimental investigation of transition to Mach reflection of steady shock waves // *Doklady Akademii Nauk* – 1997 – Vol. 357. – P. 623.
- 10 Ivanov MS, Gimelshein SF, Kudryavtsev AN, Markelov GN, Khotyanovsky DV Numerical simulation of three-dimensional regular and Mach reflections of shock waves in steady flows // Computational Fluid Dynamics'98: Proceedings of the 4th European ECCOMAS Conf.: Pt. 1(2), P. 869, 1998.
- 11 Ivanov MS, Markelov GN, Kudryavtsev AN, Gimelshein SF Numerical analysis of shock wave reflection transition in steady flows // AIAA J. – 1998. – Vol. 36. – P. 2079.
- 12 Ivanov MS, Kudryavtsev AN, Markelov GN, Gimelshein SF, Khotyanovsky DV Numerical study of three-dimensional effects on transition between steady regular and Mach reflections // The 13th International Mach Reflection Symposium 3: Proc., 1998
- 13 Kudryavtsev AN, Khotyanovsky DV, Markelov GN, Ivanov MS Numerical simulation of reflection of shock waves generated by finite-width wedge // The 22nd International Symposium on Shock Waves: Proc. Paper 1120, 1999.
- 14 Passerel D Etude de la transition entre réflexion régulière et réflexion de Mach. Thèse de doctorat de l'Université Pierre et Marie Curie (Paris), – 1996.
- 15 Skews BW, Vukovic S, Draxl M Three-dimensional effects in steady flow shock wave reflection transition // 12th International Mach Reflection Symposium, P.152–162, 1996.
- 16 Skews BW Aspect ratio effects in wind tunnel studies of shock waves reflection transition. *Shock Waves* 7, P. 373–383, 1997.
- 17 Sudani N, Sato M, Watanabe M, Noda J, Tate A, Karasawa T Three-dimensional effects on shock wave reflections in steady flows. – AIAA Paper 99-0148, 1999.

SUPPRESSION OF 3D VIBRATION RECEPTIVITY OF BOUNDARY LAYER BY AN ADVERSE PRESSURE GRADIENT

Y.S. Kachanov, D.B. Koptsev, B.V. Smorodsky
Institute of Theoretical and Applied Mechanics, 630090, Novosibirsk, Russia

1. Introduction

The problem of localized vibration receptivity of the 2D boundary layers describes the mechanism of transformation of the surface vibrations, localized in the streamwise direction, into Tollmien-Schlichting (TS) waves, which are three-dimensional in the present case. The most important characteristic of this mechanism is the receptivity function (or the receptivity coefficient) that represents a quantitative measure of an effectiveness of the transformation mechanism. Being defined in Fourier space (for the linear receptivity problem), the receptivity coefficient is a function of only two disturbance parameters: the frequency and the spanwise wavenumber.

The problem of influence of the adverse pressure gradient (APG) on characteristics of the laminar-boundary-layer receptivity to three-dimensional surface vibrations has not been investigated experimentally in previous studies. First quantitative experimental results on the 3D vibration receptivity were obtained in [1, 2] for the non-gradient (Blasius) boundary layer only. In particular the values of the complex (amplitudes and phases) receptivity coefficients were determined in this experiment as functions of the disturbance frequency and the spanwise wavenumber. These results were compared in [1] with calculations carried out by A. Michalke for the experimental conditions. A rather good agreement was found for the behavior of the receptivity amplitudes and phases with the frequency and wavenumber. However the procedure of extrapolation needed to be improved.

Simultaneously with the present work the problem of 3D vibration receptivity was studied in [3, 4] for the zero and favorable pressure gradient (FPG) cases. The experimental method was improved in this study (see [3]) in order to increase the accuracy of determining the initial (i.e. at the position of the vibrator) spectra of the TS-waves. The results were compared with calculations performed by K. Neemann for the experimental conditions. A very good quantitative agreement has been observed for both the receptivity amplitudes and phases. It is found that the FPG (Hartree parameter $\beta_{H1} = 0.099$) leads to a growth of the receptivity coefficients compared to the Blasius case. This result is in consistence with previous theoretical findings in [5, 6]. In those theoretical papers a rapid reduction of the receptivity amplitudes was predicted under the influence of the APG. However, no any experimental data was obtained for the vibration receptivity characteristics of the APG boundary layers. The goal of the present work is to close this gap in the receptivity research.

2. Experimental Model and Basic Flow

The experiments were conducted in the low-turbulence subsonic wind tunnel T-324 of the ITAM at the free-stream velocity $U_0 \approx 9$ m/s and turbulence level less than 0.02 %. The wind-tunnel has a 4 m long test section with a 1 m \times 1 m cross-section. A sketch of the experimental setup is shown in Fig. 1. The APG was induced over a flat plate (equipped with a flap) with the help of an adjustable wall-bump.

The measurements were carried out by means of a hot-wire anemometer. The mean flow structure was measured carefully both in the potential flow and inside the boundary layer. The experimental results were compared with the theoretical mean-flow characteristics calculated for the experimental conditions by Smorodsky in [7]. After adjustment of the wall-bump shape and

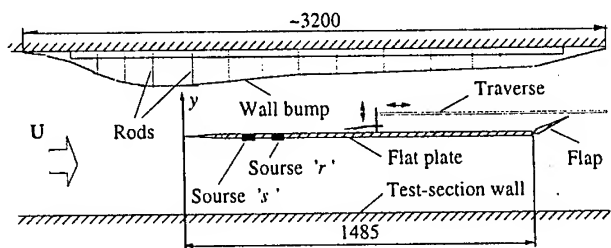


Fig. 1. Sketch of experimental model and wall bump

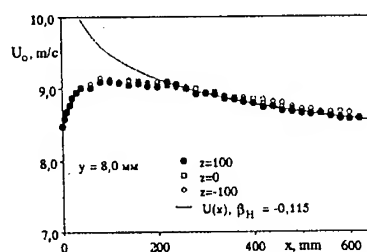


Fig. 2. Streamwise distributions of potential velocity.

the position of the flap a self-similar flow with Hartree parameter $\beta_H = -0.115$ have been obtained in a wide range of the streamwise coordinate. This fact is illustrated in Fig. 2 and 3 (see refs. [7, 8] for more detail). The results of the measurements performed outside the boundary layer (at a fixed distance $y = 8.0$ mm from the plate surface) are shown in Fig. 2 for three fixed values of the spanwise coordinate z . The dependencies show that the potential flow under study is practically two-dimensional and in the range of the streamwise coordinate x from 220 to 620 mm (i.e. up to the end of the region of measurements) corresponds to a flow with a constant Hartree parameter specified above. A mean velocity profile measured inside the boundary layer at $x = 560$ mm is presented in Fig. 3 (δ_1 is the boundary layer displacement thickness). It is seen that the experimental points are in agreement with the theoretical profile calculated by Smorodsky for the Falkner-Skan flow with $\beta_H = -0.115$. An investigation of the streamwise dependence of the boundary-layer shape factor $H = \delta_1/\delta_2$ (where δ_2 is the momentum thickness), as well as its comparison with the corresponding theoretical values, have shown that in the range $x = 420$ to 620 mm ($Re = U_e \delta_1/\nu = 901$ to 1148) the flow is self-similar and corresponds to the theoretical flow with $\beta_H = -0.115$ (see also [7]).

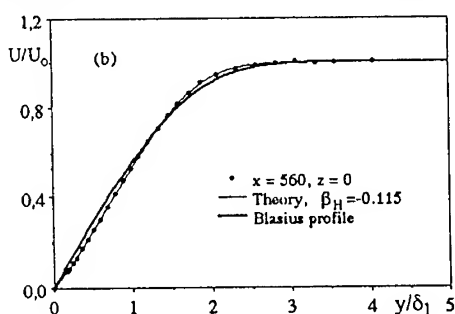


Fig. 3. Velocity profiles in boundary layer.

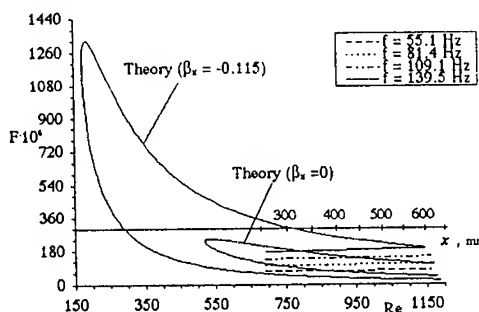


Fig. 4. Regions of main receptivity measurements.

3. Excitation of Disturbances

The experiments were conducted under controlled disturbance conditions. The 3D instability waves were excited in the APG boundary layer by means of a circular surface vibrator described in detail in [2] that played a role of the main (receptivity) source (the source 'r'). The source was mounted flush with the plate surface at a distance $x = x_r = 439$ mm from the leading edge and introduced into the boundary layer so-called wave-trains of instability modes. In order to increase the accuracy of determining the receptivity coefficients (see also introduction) an additional (stability) source was used (the source 's') that was similar to the source 'r' and situated upstream of it at $x = x_s = 287$ mm. The shape and the amplitude of the vibrations were measured with high accuracy by means of measuring system "OptoNCDT 1605".

The amplitudes of excitation were chosen small enough to provide a linearity of mechanisms of the disturbance generation and development. The receptivity was studied at four frequencies of vibrations ($f = 55.1, 81.4, 109.1, \text{ and } 139.5 \text{ Hz}$). In the center of the source 'r' ($x = x_r = 439 \text{ mm}$, $Re = 1002$) these frequencies correspond to the frequency parameters $F = 2\pi\nu f/U_c^2 = 72.1 \cdot 10^{-6}, 107.2 \cdot 10^{-6}, 142.5 \cdot 10^{-6}, \text{ and } 181.1 \cdot 10^{-6}$ respectively ($U_c \approx 8.76 \text{ m/s}$ in this point). The positions of the regions of main measurements are shown in Fig. 4 on the stability diagram for the 2D TS-waves. The stability calculations were performed in [8] by Smorodsky within the framework of a "quasi-parallel" stability theory for spatially growing 3D perturbations.

4. Procedure of Measurements and Method of Calculations

After the calibration of the source 'r' it was used for the main receptivity measurements (similar to experiment [2]) performed for all four disturbance frequencies. During these measurements four sets of spanwise distributions of the disturbance amplitudes and phases were documented for each fixed frequency at several streamwise positions downstream the vibrator (starting with $\Delta x = x - x_r = 61 \text{ mm}$). The measurements were performed at a fixed non-dimensional distance to the wall $y/\delta_1 = 0.85$ ($U/U_c = 0.455$) that was close to the amplitude maxima in the instability-wave y -profiles (see [7, 8]). After Fourier decomposition of the wave trains the information on the downstream behavior of the normal-mode amplitudes and phases was obtained for each studied value of the frequency and the spanwise wavenumber (or the wave propagation angle). The procedure of the decomposition is described in [9].

After the measurements with the source 'r' the source 's' was used. With the help of it information about the stability behavior of the normal oblique modes in the near-field of the source 'r' was obtained. The matter is that to determine the receptivity coefficients it is necessary to know the initial spectra of the TS modes at the position of the source 'r'. It is impossible to obtain this data directly from measurements with the source 'r' because of a presence of other modes in the near-field of the vibrator (like the continuous-spectrum instability modes and the bounded fluctuations produced by the surface vibrations). In previous experiment [1] (performed in the Blasius flow) the initial spectra of the TS waves were 'reconstructed' at the position of vibrator by means of an upstream extrapolation of the spectra obtained downstream from it. In the present experiment an experimental information about the downstream growth of the normal-mode amplitudes and phases in the vicinity of the source 'r' was used to improve the extrapolation procedure. This information was obtained after measurements of sets of spanwise distributions of the disturbance amplitude and phases generated by the source 's' (see section 3). The measurements were performed for each studied frequency at several streamwise positions including the positions very close to the source 'r'. Some of these positions overlapped with those used in the measurements with the source 'r'.

Receptivity coefficients were determined theoretically on the basis of linear local parallel theory. The approach used is similar to [5]. The solution of the initial problem for the disturbance field can be represented by triple Fourier integral in α , β and ω . The asymptotics of this integral in the far field from the source (which is defined by least stable eigenmode of discrete spectrum) can be evaluated by means of the residue theorem. The physical velocity field then can be expressed as a product of the magnitude of the surface perturbation, the Fourier transformation of the shape of surface perturbation, and the receptivity coefficient. The last one is proportional to the response residue and provides the amplitude of excited wave independently of the geometric shape of the vibrator. Receptivity coefficients were computed numerically for the experimental conditions. Orr-Sommerfeld equation with inhomogeneous boundary conditions at the flat plate was solved by means of orthogonalization method. The distribution of the unstable wave amplitude across the boundary layer was described by the *normalized* velocity profile $u(y)$, where $u(\omega, \beta, y^*) = 1$ and y^* was defined from the relation $U(y^*)/U_c = 0.455$.

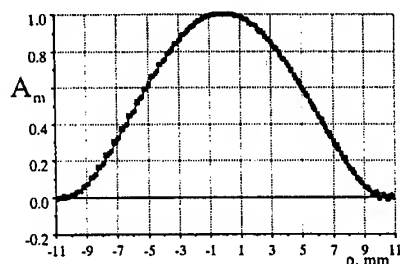


Fig. 5. Shape of vibrator oscillations.

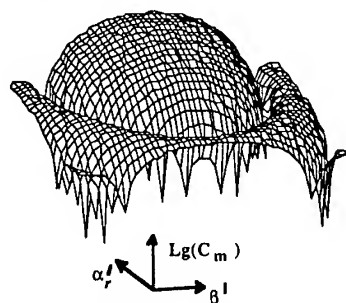


Fig. 6. Wavenumber spectrum of vibrator shape.

5. Results

5.1. Properties of surface vibrator. The measurements of the shape of oscillations of the surface vibrator (the source 'r') have shown that the non-dimensional amplitude (A_m) and phase of the oscillations are independent for this vibrator on both the frequency and the amplitude of excitation (in the range studied). The shape of oscillations of the main source is presented in Fig. 5. The shape turned out to be axisymmetric in practice. The experimentally measured distributions of the vibrational amplitude along the source radius $A_m(\rho)$ were approximated with an eight order polynomial. The coefficients of this polynomial were used for determining the 3D wavenumber spectrum of the surface vibrations the amplitude part of which is shown in Fig. 6. The spectral phase (not shown) is constant within the central cupola and the every ring but it jumps by π when crossing the circles of the amplitude minima. This spectrum is necessary for determining the vibrational receptivity coefficients.

5.2. Spanwise distributions. An example of the result of the main receptivity measurements is presented in Fig. 7 where a set of spanwise distributions of the disturbance amplitudes and phases is shown for the frequency $f = 55.1$ Hz ($F = 72.1 \cdot 10^{-6}$ at $x = x_r = 439$ mm, $Re = 1002$) for several streamwise positions. These distributions are obtained for the wave-train generated by the source 'r'. Similar spanwise distributions were measured for the other three frequencies and for the wave trains generated by the source 's'. After Fourier decomposition of these distributions the spanwise wavenumber spectra of the disturbances were obtained (not shown) for all studied regimes of excitation.

5.3. Initial disturbance spectra. As was mentioned above, a determination of the initial spectra of the disturbances generated by the vibrator represents one of the most difficult methodological problem. A solution of it used in the present experiments is illustrated in Fig. 8. Shown with filled squares in Fig. 8 is an example of the streamwise distribution of the spectral amplitude obtained for normal oblique TS mode with the frequency $f = 55.1$ Hz and the non-dimensional spanwise wavenumber $\beta \delta_{lr} = 0.177$ (where δ_{lr} is the boundary layer

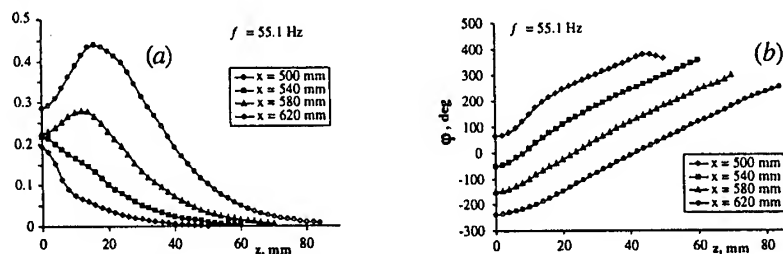


Fig. 7. Spanwise distributions of the disturbance amplitudes (a) and phases (b).

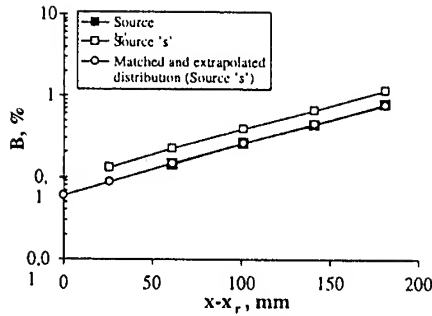


Fig. 8 Streamwise distributions of the spectral amplitudes.

the normal modes must be the same for the two sources because they are independent of the method of excitation and depend only on the stability properties of the boundary layer. Using this circumstance we rescale the amplitudes obtained for second source by means of multiplying them by coefficients $k = [\sum k_i(f, \beta, x_i)]/N$ ($k_i(f, \beta, x_i) = B_{1r}(f, \beta, x_i)/B_{1s}(f, \beta, x_i)$), where B_{1r} and B_{1s} are the amplitudes obtained in the point x_i of the range $\Delta x = x - x_r = 61$ to 181 mm for the sources 'r' and 's' respectively and N is the number of points. Such rescaling gives possibility to determine the initial spectral amplitudes generated by the vibrator in a way illustrated in Fig. 8 where the streamwise distribution of the normal-mode amplitudes obtained for the source 'r' are plotted together with rescaled distribution obtained for the source 's' (circles in Fig. 8). The initial phases of the normal oblique modes are determined in a similar way. The only difference is that the "rescaling" of the phases of the modes obtained for the source 's' is reduced to their simple shifts by $\Delta\phi = \Delta\phi(f, \beta)$ averaged for all points from range $\Delta x = 61$ to 181 mm.

5.4. Receptivity coefficients. Subsequent procedure of the experimental data analysis is similar to that used in previous study [2]. The analysis of the streamwise distributions of the normal-mode phases gives possibility to determine the dispersion curves, i.e. the dependences of the streamwise wavenumber on the spanwise wavenumber. These curves are used for selection from the spectrum of the vibrator shape (see Fig. 6) the resonance spectral modes which have the same values of the streamwise and spanwise wavenumber as the 3D TS waves. Finally, the ratio of the initial wavenumber spectrum of instability modes (see section 5.3) and the resonant spectrum of surface vibrations represent a spectrum of the receptivity coefficients that depends on the disturbance frequency and the spanwise wavenumber (or the wave propagation angle).

The obtained receptivity coefficients are shown in Fig. 9 versus the spanwise wavenumber for all four frequencies studied. A very well agreement is observed between the measured and calculated receptivity amplitudes and phases. Deviation between the experimental and theoretical

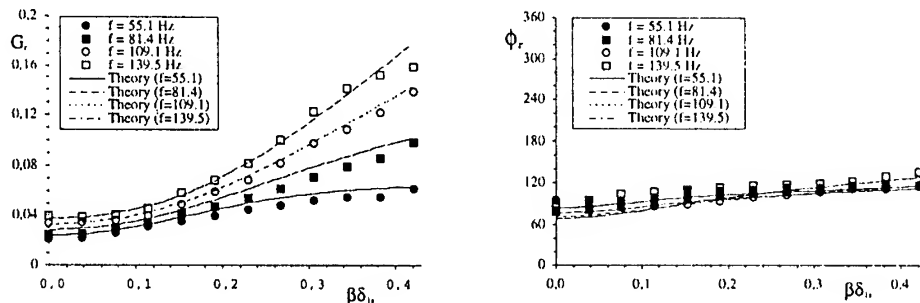


Fig. 9. Experimental and theoretical receptivity coefficients.

values of the receptivity coefficients is within an experimental accuracy. The general behavior of the receptivity coefficients with β and f is qualitatively similar to that found in [1, 2] for the Blasius flow. In particular, the receptivity amplitude increases with the wave propagation angle and frequency, while the receptivity phases are very weakly dependent on these two parameters. However, calculations performed for the same parameters but for the zero streamwise pressure gradient have shown that in the present APG case (with $\beta_H = -0.115$) the values of the receptivity amplitudes are lower, especially for 3D modes with large values of the spanwise wavenumber. Calculations have shown also that the receptivity coefficients determined in the exact position of the amplitude maximum in y -profiles for every normal mode differ negligibly small from the coefficients determined at $U/U_c = 0.455$, as in the present experiments.

6. Conclusions

The quantitative combined experimental and theoretical study of the linear 3D receptivity of an APG self-similar boundary layer is performed with the help of an advanced method of measurements and data processing. A very good agreement between the receptivity theory and experiment is found. It is shown that the APG boundary layer with Hartree parameter $\beta_H = -0.115$ is less receptive to 3D localized surface vibrations compared to the Blasius flow. The receptivity coefficients obtained in the present investigation are independent of the specific shape of vibrations and can be used for estimation of initial amplitudes of the 3D Tollmien-Schlichting waves and for verification of other theoretical approaches.

The work was supported by the Russian Foundation for Basic Research (grant 97-01-00638).

References

1. Ivanov A.V., Kachanov Y.S., Obolentseva T.G., Michalke A. Receptivity of the Blasius boundary layer to surface vibrations. Comparison of theory and experiment // International Conference on Methods of Aerophysical Research. Proceedings. Part I. - Novosibirsk: Inst. Theor. & Appl. Mech., 1998, p. 93-98.
2. Ivanov A.V., Kachanov Y.S., Obolentseva T.G. Experimental study of the Blasius boundary layer receptivity to localized surface vibrations // Thermophysics and Aeromechanics. - 1999. - V. 6. No 2. - P. 193-206.
3. Bake S., Ivanov A.V., Kachanov Y.S., Fernholz H.H. A method of experimental study of vibrational receptivity of a boundary layer on a curved wall // International Conference on Methods of Aerophysical Research. Proceedings. Part I. - Novosibirsk: Inst. Theor. & Appl. Mech., 1998, p. 17-22.
4. Ivanov A.V., Kachanov Y.S., Bake S., Neemann K., Fernholz H.H. Vibration receptivity of boundary layers. Experiment and theory // XII International Conference "Stability of Flows of Homogeneous and Heterogeneous Fluids". Abstracts / V.Y. Rudyak ed., Novosibirsk: NGASU, 2000. (Accepted for publication)
5. Michalke A., Neemann K. Excitation of instability waves in wall boundary layers with adverse pressure gradients by various types of Dirac sources // Acta Mechanica. - 1997. - V. 122. - P. 33-48.
6. Neemann K. Theoretische Untersuchungen zur Anregbarkeit instabiler Wellen in kompressiblen Wandgrenzschichten. Ph.D. Diss., Technische Universität Berlin, Berlin, 1998.
7. Kachanov Y.S., Koptsev D.B. Three-dimensional stability of self-similar boundary layer with negative Hartree parameter. 1. Wave trains // Thermophysics and Aeromechanics. - 1997. - V. 6. No 4. P. 463-477.
8. Kachanov Y.S., Koptsev D.B., Smorodskiy B.V. 3D stability and receptivity of two-dimensional self-similar boundary layer with adverse pressure gradient // Laminar-Turbulent Transition. IUTAM Symposium, Sedona, AZ/USA, 1999. / H. Fasel & W.S. Saric, eds. Berlin Heidelberg: Springer, 2000. (Accepted for publication.)
9. Kachanov Y.S., Michalke A. Three-dimensional instability of flat-plate boundary layers: Theory and experiment // Eur. J. Mech., B/Fluids. - 1994. - V. 13, No 4. - P. 401-422.

SKIN FRICTION MEASUREMENTS BY OIL FILM METHOD UTILISING DIFFUSE LIGHT SCATTERING FOR IMAGE REGISTRATION

V.I. Kornilov, S.B. Nikiforov, A.A. Pavlov

Institute of Theoretical and Applied Mechanics SB RAS
630090 Novosibirsk, Russia

INTRODUCTION

This paper describes a further development of the optical skin friction measurement technique for curved and arbitrary oriented surfaces. Fundamentals of the method formulated in [1] and [2] were further developed in [3 – 6]. The method is based on the registration changes of an oil droplet shape in time. An oil droplet placed on the surface under study is deformed under the action of a skin friction force defined as

$$\tau(\xi) = \frac{-2\rho\nu}{\Delta S(\xi) \cdot L^2(\xi)} \cdot \frac{d \int_0^\xi \Delta S(\xi) \cdot L(\xi) d\xi}{dt} \quad (1)$$

where ξ is the co-ordinate along a surface streamline, $L(\xi)$ is the oil droplet thickness, ρ and ν are oil density and kinematics viscosity, respectively, $\Delta S(\xi)$ is the stream filament width which can be presented as

$$\Delta S(\xi) = \Delta S_0 \cdot e^{\int_0^\xi \frac{d\varphi}{ds} d\xi}$$

where $d\varphi/ds$ is the derivative of the streamline inclination angle φ with respect to the co-ordinate s orthogonal to ξ .

The papers [2, 3] contain estimates of the method error of about 10 %, which is fairly acceptable for this parameter. In the previous works, the oil droplet shape was registered using specular reflection optical schemes, thus limiting the technique implementation to flat surfaces. Besides, in this case, the surface orientation must ensure the registration of the light specular reflected from the surface. In this work, a new technique based on a diffuse light interference is presented. This technique allows one to avoid the constraints of specular reflection schemes concerning surface orientation and curvature.

1. THEORETICAL JUSTIFICATION OF THE TECHNIQUE

It is well known that any incident diffuse light wave 1 (external diffuse lighting) consists of a number of plane waves spreading at different angles. In case of the infinitesimal beam limiting aperture, only one plane wave can pass through the stop. This wave will spread from the area under consideration at an angle i . Such a plane wave will form fringe patterns with an

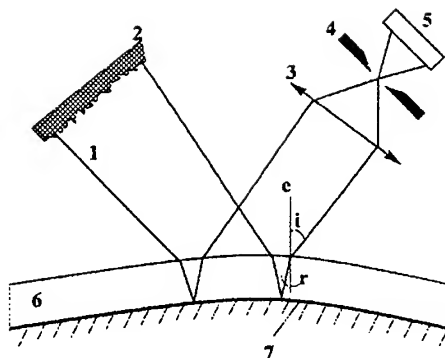


Fig. 1. Diffuse light interference scheme. 1 is incident diffuse light; 2 is diffuse light scatterer; 3 is focusing lens; 4 is diaphragm (stop); 5 is CCD array; 6 is oil film; 7 is model surface.

interference path difference $\Delta l = 2nL\cos(r)$, where L is the oil film thickness; n is the oil refractive index, r is the refraction angle [7] (Fig. 1).

For curved surfaces, the angle i corresponding to the incident beam of the specular reflection scheme is changed in accordance to surface orientation. In general, i is equal to the angle between a wave vector and a normal e to the surface under study at a corresponding point. Indeed, the beam limiting aperture is not set to zero, thus the CCD array registers a number of fringe patterns formed by plane waves, whose wave vectors lay inside a solid angle defined by the beam limiting aperture radius R and the lens focal length F . The main difference between the axial plane wave direction and any other plane wave direction is defined as: $\Delta i \gg R/F$. It is obvious that each plane wave forms its own fringe patterns, but in case of thin films and small i angle changes, all fringe patterns will agree, and fringe patterns of equal thickness will be successfully registered (in our case: $F=44$ mm, relative aperture is equal to 2).

Although the external diffuse lighting provides fringe patterns for curved surfaces, this technique requires a specular reflection of the incident light to the collecting aperture from each point of the surface thus having the constraints on the surface orientation, that common specular reflection schemes have. However, the model surface itself can be used as a diffuse light source (internal diffuse lighting). If the model surface reflects a fraction of the collimated incident light and diffuses the rest, the fringe patterns identical to the external diffuse lighting fringe patterns can be observed. The interference path difference will be the same and will depend only on the angle i . I means, that the light source and the collecting optics may rest at the same position, which does not depend on the orientation of the model surface. This simplifies the adjustment of the experimental set-up significantly.

2. EXPERIMENTAL SET-UP

The tests were conducted in T-324 subsonic wind tunnel at the Institute of Theoretical and Applied Mechanics. An airfoil with a relative thickness equal to 0.07 was investigated at the incidents of 0 and 5 degrees. Free-stream velocity was equal to 25 m/s that corresponds to the Reynolds number based on the airfoil chord equal to $4.28 \cdot 10^5$. The experimental set-up used is shown in Fig. 2.

The model was made of wood and its surface could not be prepared directly to provide the interference fringes. Therefore, small streaks of Mylar were applied to the test surface. The

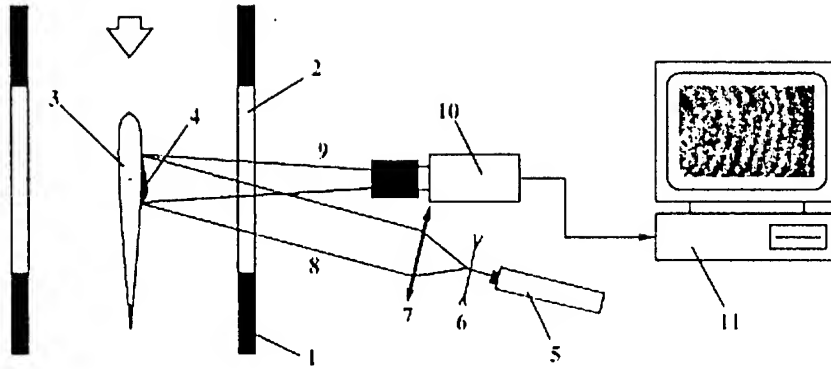


Fig. 2. Experimental set-up.

1 is wind tunnel wall; 2 is window; 3 is model; 4 is oil droplet; 5 is He-Ne laser light source; 6, 7 are lenses; 8 is incident light; 9 is scattered light; 10 is CCD camera; 11 is computer with frame grabber.

Mylar provides partially reflective and partially scattering surface thus the "internal diffuse lighting" fringe patterns can be observed. Images were captured 180 s apart by a CCD camera and stored on PS's hard disk with the resolution of 768×576 pixels. Figure 3 shows, for example, a time sequence of the fringe pattern images on the airfoil.

The oil film thickness L is determined directly from the fringe patterns. The spacing of intensity maximum or minimums (fringe spacing) can be determined. If the collected light direction is nearly perpendicular to the surface, which was provided by the adjustment of the experimental set-up, the fringe spacing corresponds to a change in the oil film thickness of $\lambda/2$, with λ being the wave length of the incident laser light. In assumption, that $\Delta S = \text{const}$, which is true in our case, the equation (1) can be simplified to

$$\tau(\xi) = \frac{-2\rho v}{L^2(\xi)} \cdot \frac{d \int_0^\xi L(\xi) d\xi}{dt}$$

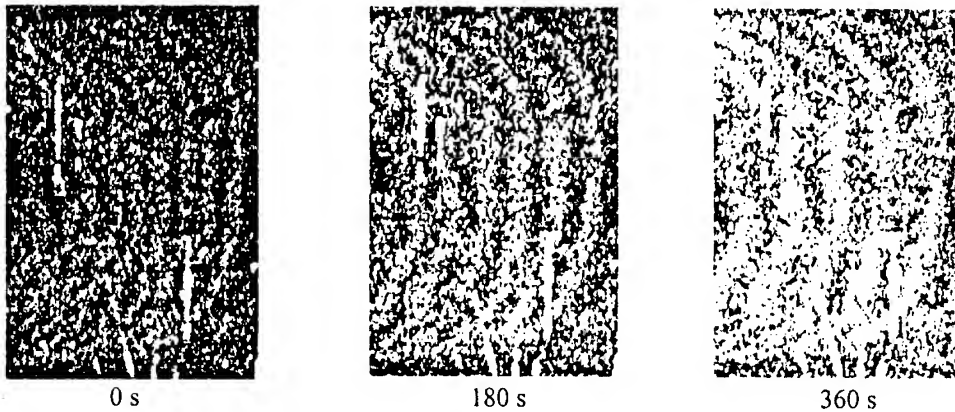


Fig. 3. Interferograms of the oil film on an airfoil. (Flow from right.)

This equation was used to calculate the skin friction. The oil used in this study was a silicon oil with a nominal viscosity $0.00049 \text{ m}^2/\text{s}$ at 25°C .

3. RESULTS AND DISCUSSION

Let us consider briefly a typical example indicating effectiveness of the mentioned approach to determine the local skin friction coefficient C_f at the flow over airfoil. The results of measurements of this value obtained by GISF method are shown in figure 4 on the leeward side of the airfoil at $\alpha = 0$ and 5 . As a comparison the averaged data derived by three geometrically similar Preston tubes are shown as well. As can be seen GISF- and Preston results are in satisfactory agreement of each other at $\alpha = 0$. The maximum discrepancy of the values C_f does not exceed 3 %.

In contrast to the case $\alpha = 0$ an essential difference in derived by two methods takes place for the airfoil at $\alpha = 5$ where the studied flow is developed under essential adverse pressure gradient effect. It is seen, that the discrepancy of the values C_f determined by the Preston- and GISF method is very large. The analysis of the boundary-layer mean velocity profiles normalised to wall variables shows an existence of logarithmic region in the velocity distribution but this one is short and can not be identified clearly. Besides, the intrusive Preston tubes cause changes in the flow especially at the initial measured stations of the wing where the boundary layer is relatively thin. These circumstances is the main reason of the pointed difference between C_f values derived by Preston tubes and those obtained directly from the GISF measurements. This means that the Preston tubes are not capable of accurate skin friction measurements in this flow.

Thus the use of diffuse light for fringe pattern registration allows measurements of skin friction on curved and free-oriented surfaces and in some cases provides more accurate results in comparison with the methods based on the similarity theory.

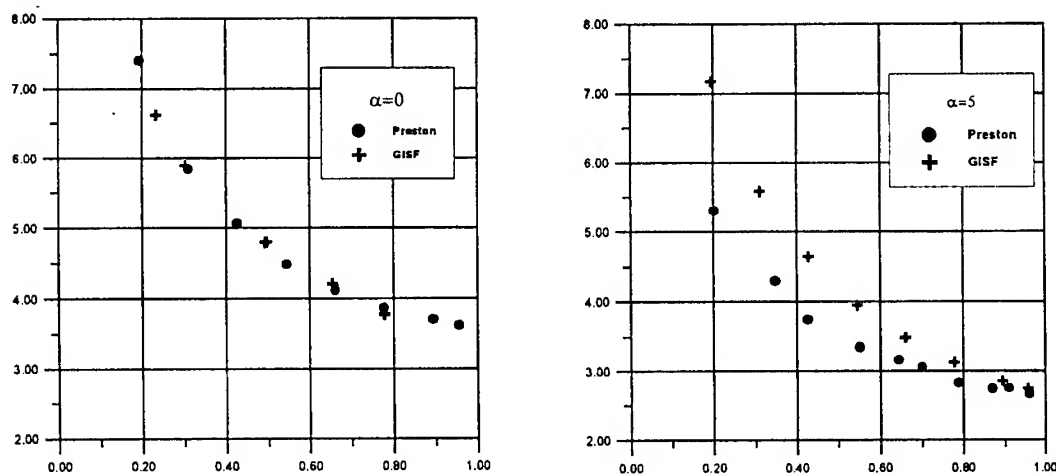


Fig. 4. Local skin friction coefficient C_f on the leeward side of the airfoil.

REFERENCES

1. Winter K.G. An outline of the techniques for the measurement of skin friction in turbulent boundary layers // *Progress in the Aerospace Sciences*. – 1977 – Vol. 18. – P. 1-57.
2. Tanner L.H., Blows L.G. A Study of the motion of oil films on surfaces in air flow with application to the measurement of skin friction // *J. of Physics E: Scientific Instruments*. – 1976. – Vol. 9. – P. 194-202.
3. Monson D.J., Driver D.M., Szodruch J. Application of a laser interferometer skin-friction meter in complex flows // *The Intern. Congress on Instrumentation in Aerospace Simulation Facilities: IEEE Publication 81CH1712-9*, 1981. P. 232-243.
4. Kornilov V.I., Pavlov A.A., Shpak S.I. On the techniques of skin friction measurement using optical method // *Intern. Conf. on the Methods of Aerophys. Research: Proc. Pt1. Novosibirsk*, 1992. P. 71 – 74.
5. Nestoulya R.V., Nikiforov S.B., Pavlov A.A. Development of the oil film method of skin friction measurement for curved and arbitrary oriented surfaces // *Intern. Conf. on the Methods of Aerophysical Research: Proc. Pt 1. Novosibirsk*, 1998. P. 167-172.
6. Garrison T.J., Ackman M. Development of a global interferometer skin-friction meter // *AIAAJ*. 1998. Vol.36, No.1. P. 62-68,
7. Franson M. *Laser speckle and application in optics*. – New York: Academic Press, 1979.

COMPARATIVE METHOD TO DETERMINE THE NOZZLE FLOW COEFFICIENT

A.A. Kuraev

Novosibirsk State Technical University, Russia

It is often required to determine the effect of the constructive parameters on the tested nozzle flow or nozzle block flow coefficient in aerophysical experiment. The accuracy of direct measurements does not exceed 1 – 3 % according to the technique [1], for example.

The method suggested is based on the comparison of the tested nozzle flow coefficient with that of the standard nozzle.

Gas flow rates through standard and tested nozzles are written down in the form

$$m_{\text{ref}} = \mu_{\text{ref}}^* \rho_{\text{ref}}^* a_{\text{ref}}^* F_{\text{ref}}^*,$$

$$m_{\text{test}} = \mu_{\text{test}}^* \rho_{\text{test}}^* a_{\text{test}}^* F_{\text{test}}^*.$$

The nozzle flow coefficient ratio:

$$\frac{\mu_{\text{test}}}{\mu_{\text{ref}}} = \frac{m_{\text{test}}}{m_{\text{ref}}} \frac{P_{0\text{ref}}}{P_{0\text{test}}} \left(\frac{T_{0\text{test}}}{T_{0\text{ref}}} \right)^{1/2} \frac{F_{\text{ref}}^*}{F_{\text{test}}^*}.$$

Making equal gas input into the pre-chambers of the standard 1 (see Figure) and tested nozzles 2 from the general chamber 3 through the nozzle grids 4, 5 we obtain the expression (1) in the form

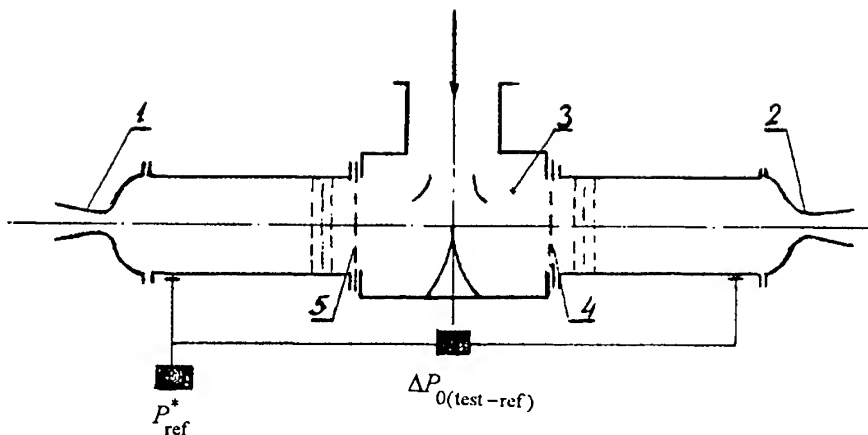
$$\frac{\mu_{\text{test}}}{\mu_{\text{ref}}} = \frac{P_{0\text{ref}}}{P_{0\text{test}}} \frac{F_{\text{ref}}^*}{F_{\text{test}}^*}.$$

The nozzle grids 4, 5 consist of a great number of diaphragms, total flow areas were selected equal with the error not less than 0.01 % and each grid sum area does not exceed half of the area F_{ref}^* . A set of the constructive measures at supercritical pressure differential on the grids provides the equality of grids diaphragm flow [2]. Taking into consideration:

$$P_{0\text{test}} = P_{0\text{ref}} - P_{0(\text{test} - \text{ref})},$$

$$P_{0\text{test}} = P_{0\text{ref}} - \Delta P_{0(\text{test} - \text{ref})},$$

$$\mu_{\text{test}} = \mu_{\text{ref}} \frac{1}{1 + \Delta \bar{P}_{0(\text{test} - \text{ref})}} \frac{F_{\text{ref}}^*}{F_{\text{test}}^*}.$$



where

$$\Delta \bar{P}_{0(test-ref)} = \frac{\Delta P_{0(test-ref)}}{P_{0ref}}.$$

Thus, the error of the method suggested is determined by the error of the measurement of the pressure differential of the standard and tested setups.

This method was approved and used for more than twenty years in gas-dynamic experiments at the Institute of Theoretical and Applied Mechanics SB RAS (Novosibirsk).

REFERENCES

1. Regulations 28-64. Measurement of fluids, gas and vapor flow by standard diaphragms and nozzles. – Moscow: Izd. Standartov, 1964.
2. Deich M.E. Technical gas-dynamics. – Moscow: Energiya, 1974. – P. 278 –301.

AN EXPERIMENTAL INVESTIGATION OF VORTEX STRUCTURES IN SRM DUCT WITH A STAR-SHAPED CHANNEL

B.M. Melamed and V.N. Zaikovskii
Institute of Theoretical and Applied Mechanics SB RAS,
630090 Novosibirsk, Russia

In mid-70s, on the basis of gas-flow visualization, it was proved [1] that a pair of vortices is formed behind a step of a star-shaped channel located in the subsonic part of the nozzle. These vortices enter the supersonic bell mouth and remain until the nozzle exit. Until now, there exists a concept that the vortex structures observed behind the step pass through the pre-nozzle volume, interact with the subsonic surface of the nozzle, and lead to heat-transfer intensification and erosion of the nozzle walls over the entire length of the nozzle. Nevertheless, the attempts to control these vortex structures to decrease their influence on the nozzle walls (for example, by smoothing the step edges) were ineffective. To suppress the adverse action of the vortex structures, it is necessary to reveal the fine features of their origin and determine the methods of vortex control on the basis of this mechanism.

Multiple experiments in star-shaped channels with different number of rays (four, six, and eight) allowed a significant refinement of the formation mechanism of these streamwise vortex structures in the ducts of the considered type. On the basis of analysis of a large number of oil-film visualizations of the subsonic portion of the nozzle, we can conclude that much more intense paired vortices, as compared to those formed at the edge of the step in a star-shaped channel, result from interaction of planar jets exhausted from the channel rays with the subsonic surface of the nozzle.

It was found that the planar jet is weakly smeared in the pre-nozzle volume and, meeting the frontal surface of the subsonic part of the nozzle, forms a singular point on the oil-film patterns, which is a node. Further downstream, the jet is smeared not only along the surface, but also in the transverse direction. Upon interaction of the neighbouring spreading jets, an intense formation of a paired system of counterrotating vortices is formed, which is evidenced by thickened convergence lines on visualization patterns of the internal surface of the subsonic part of the nozzle.

We illustrate the above by the distributions of the relative pressure in the nozzle cross-section and the oil-film visualization patterns of the subsonic and supersonic surfaces of the nozzle, which were obtained in a rocket engine with cold air passing through a six-ray simulator of the charge channel. The subsonic surface of the nozzle is shown in Fig. 1. A line of the planar jet flow is seen. The cross-flow spillage to both sides of this line is observed. This line is in the plane of the projection of the ray of the star-shaped charge channel. The bifurcated convergence line (zone) is also seen. This line is formed by the meeting of the neighbouring planar jets spreading in the transverse direction after their interaction with the subsonic portion of the nozzle. A pair of vortices corresponds to each convergence line. Thus, the number of vortices n_v is equal to the doubled number of rays n_r of the star-shaped charge: $n_v = 2n_r$.

The oil-film pattern of the internal surface of the supersonic bell is shown in Fig. 2. The rich convergence line is a continuation of the bifurcated convergence line from the subsonic portion of the nozzle. Naturally, the number of vortices in the supersonic part remains at an axisymmetric position of the nozzle, but the vortex dimensions significantly increase from the throat to the nozzle-exit cross-section occupying the entire nozzle surface in each cross-section.

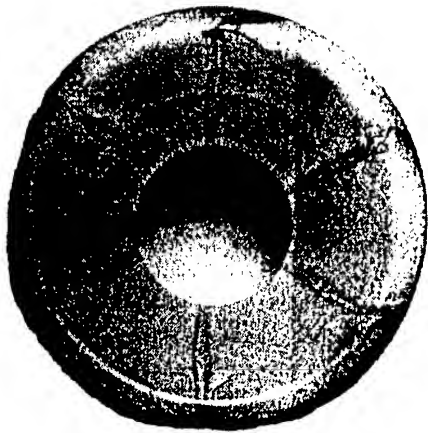


Fig.1. The subsonic surface

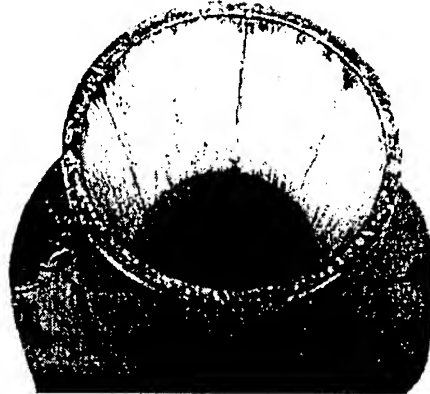


Fig.2. The internal surface of the supersonic bell

An additional verification of the observed "primacy" of the influence of planar jets exhausted from the rays of a star-shaped channel of the charge on the vortex-formation process was performed. A special experiment was conducted, in which a cylinder about 40 mm long was placed at the channel exit of the six-ray charge. The internal diameter of the cylinder was equal to the external diameter of the charge. The internal surface of the cylinder was covered by a lampblack-oil paint. The patterns of the oil-film visualization of the flow in the cylinder in Figs. 3 and 4 show the comparative degree of intensity of the vortex structures formed at the step in the charge channel and from interaction of planar jets with the cylinder surface. Both patterns were obtained in one experiment, but Fig. 3



Fig. 3. The flow pattern opposite the planar jet

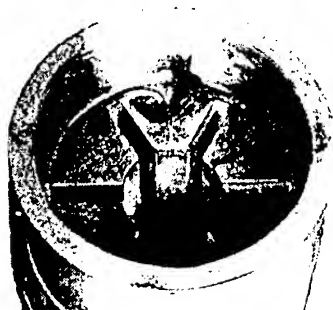


Fig. 4. The flow pattern opposite the step

shows the flow pattern opposite the planar jet and Fig. 4 opposite the step. It is seen (Fig. 3) that, leaving the ray, the planar jet interacts with the cylinder surface and also spreads in the transverse direction; vortices are formed when the flows from the neighbouring jets meet. This is also evidenced by the oil-film pattern opposite the step (Fig. 4). It is seen that the paired system of vortices formed (the dark convergence line on the cylinder behind the step) can move paint particles from the cylinder surface to the step surface (the "base region" with lower pressure) and leave a trace of the vortices there.

From the physical point of view, this means that both mechanisms of vortex formation act in reality: on the step edges and from interaction of planar jets with the cylinder surface. However, the energy content of mass fluxes forming these vortex structures are incomparably greater in the second case. This circumstance allows us to conclude that the governing mechanism of vortex formation is due to interaction of planar jets exhausted from the rays of the star-shaped channel of the charge.

Understanding of the vortex-formation mechanism in the class of flows under consideration allows one to determine methods for controlling the proceeding physical process, up to its complete suppression, to prevent adverse consequences. Such an adverse consequence in the nozzle flow of two-phase combustion products of solid propellants is additional intensification of heat transfer and erosion of the nozzle-wall material. The revealed vortex structures are rather stable. Among several methods of controlling, or, more exactly, suppressing these structures, the most effective is the method of corrugation of the internal subsonic surface of the nozzle. Figure 5 shows a scheme of vortices in the nozzle throat (marked by 2) in the absence of corrugation. Location of a given number of vortices (corresponding to the number of charge rays) on a known length of the nozzle throat circle allows one to evaluate vortex dimensions. In our case, the vortex radius r_v is about 3 mm. The geometry, dimensions, and positions of the corrugated elements on the subsonic profile of the nozzle (marked by 1) are also shown in Fig. 5. The height of the element h was chosen slightly greater than the vortex radius: $h = 4$ mm. The number of corrugated elements N_c was twice the number of vortices: $N_c = 2n_v$.

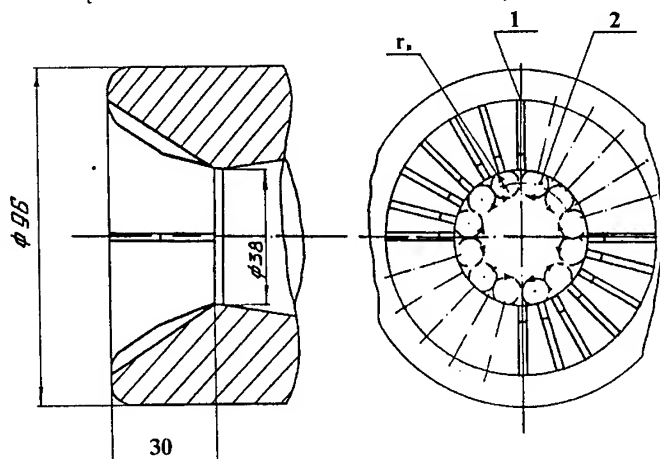


Fig. 5. The scheme of vortices in the nozzle throat and positions of the corrugated elements on the subsonic profile

Figure 6 shows the oil-film pattern of the subsonic corrugated nozzle surface for the exhaustion from the six-ray channel of the charge. Like in Fig. 1 (without surface corrugation), six convergence lines are seen on the frontal surface, which corresponds to the number of vortex pairs. Twenty four corrugation elements are identified in this figure as thin white strips. In contrast to Fig. 1 (without surface corrugation), there is no clear flow pattern in Fig. 6, which can be explained by destruction of the vortex structure by corrugated elements extended above the surface, the number of corrugated elements being twice the number of vortices. The oil-film pattern of the flow in the supersonic bell for the case of a corrugated surface in the subsonic part of the nozzle is shown in Fig. 7.

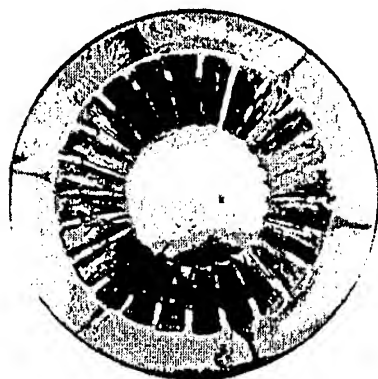


Fig. 6. The oil-film pattern of the subsonic corrugated nozzle surface

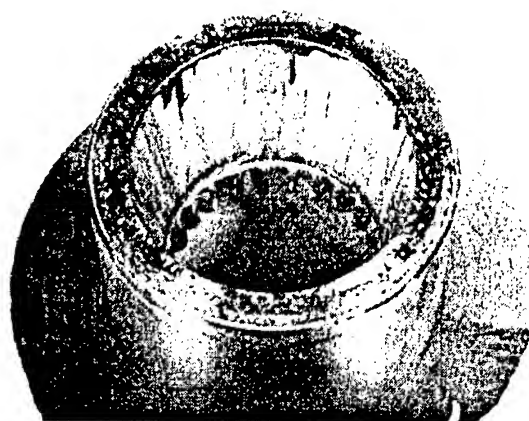


Fig. 7. The oil-film pattern of the flow in the supersonic bell

Comparing it with Fig. 2 (without surface corrugation), we can note that the primary structure of the vortices is destroyed to form ordered streamwise structures whose number is doubled (in accordance with the number of grooves between the corrugated elements) and whose size and intensity significantly decrease, which is confirmed by the character of the convergence lines. Elements of the corrugated surface are seen inside the nozzle behind the throat.

The decrease in vortex intensity is also evidenced by a comparison of the distributions of relative pressures measured in the cross-section of the supersonic part of the nozzle for identical charge channels and flow regimes with and without corrugation of the subsonic part of the nozzle. This comparison is shown in Fig. 8. The relative pressure ΔP is the ratio of the pressure deviation at a given point of the nozzle from the axisymmetric pressure distribution in the absence of vortices (for a circular channel of the charge) to the pressure for the axisymmetric distribution. The angle α is counted clockwise in the chosen cross-section of the nozzle. The open circles correspond to the absence of the corrugated surface in the subsonic part of the nozzle, and the filled circles refer to the presence of such a surface. In the absence of corrugation, the maximum values $+\Delta P$ correspond to the convergence lines of vortex pairs in the oil-film patterns. The number of these maxima coincides with the number of vortex pairs. It is seen from Fig. 8 that the

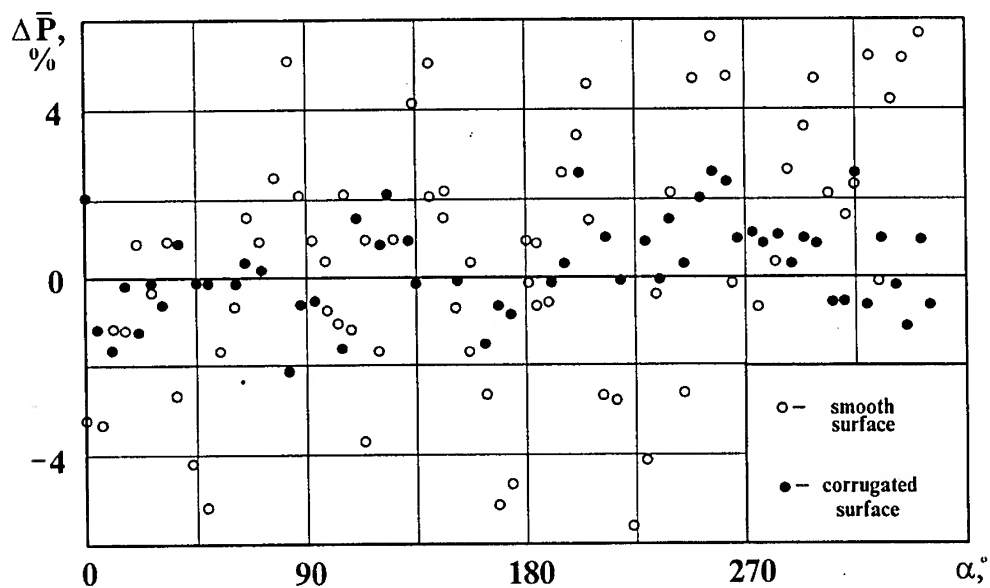


Fig. 8. The comparison of the distributions of relative pressures with and without corrugation of the subsonic part of the nozzle

presence of a corrugated surface decreases the relative pressure by more than twice, which confirms the efficiency of the chosen method for suppression of vortex structures in the class of flows under study.

1. Kuraev A.A., Kuraeva A.D., Petrova B.N. Emergence of shock waves in nozzles with vortices passing through the throat // Gas Dynamics and Physical Kinetics. — Novosibirsk, 1974. — P. 90–91.

ELECTRON-BEAM DIAGNOSTIC OF DENSITY DISTURBANCES IN HIGHLY UNDEREXPANDED LAMINAR JETS¹

S.G. Mironov

Institute of Theoretical and Applied mechanics SB RAS, Novosibirsk, 630090, Russia

Introduction.

The research of disturbance development in supersonic jets of low density is of great interest in understanding of the mechanisms of laminar-turbulent transition in shear flows. On the other hand, the study and control of instability of supersonic underexpanded jets shear layer is of applied importance. The results of these researches may be taken up in developing of methods of combustion process intensification in the channel of the hypersonic jet engine. The review of recent works on this subject is available in [1]. One of effective methods of mixing intensification in nonisobaric jets is transition of the jet stream into the regime of oscillations.

At the present time there are two alternative models of the mechanism of self-sustained oscillations: the model of unstable wave development in the shear layer on the jet boundary [2], and the model of instability of the shock wave configuration in the jet stream [3]. Previously, the author of this work made a research [4] where the co-existence of two mechanisms was shown. But the problem of the major mechanism remains unsolved. It is most probably to be found out in the laminar area of rarefied jet outflow, when shear instability is limited with viscosity, and the shock-wave structure of the jet is still in existence. Significant progress on this subject was made in [5,6]. But the results of these works are not perfect because the secondary characteristics of jet fluctuations were measured. The authors of these works had neither way nor method to measure stability of the mixing layer of low density jets. In this connection, of some interest is obtaining of experimental data of disturbance characteristics in the shear layer of supersonic laminar jets, specifically about the disturbance amplification rate. One may calculate the energetic balance of the jet as a self-oscillating system and make a conclusion about of the role a particular mechanism by amplification rate.

In the present work there is a description of measurement principles and the results of development of density disturbances in the compressed layer of a laminar strongly underexpanded nitrogen jet which outflows in submerged space of low density.

Experimental wind tunnel and measuring apparatus

The experiments are carried out in the hypersonic wind tunnel T-327A of ITAM SB RAS which is used as a vacuum jet test bench. The jet outflowed from a sonic nozzle with diameter $d = 1$ mm at room temperature. The range of ratio of pressure values $N = 2000 \div 6000$ and Reynolds numbers $Re_L = 150 \div 600$ are studied.

The calculations are made with the known method of electron-beam fluorescence [7]. The average density field and distribution of density fluctuations are reconstructed with consideration for the influence of collisional deactivation of excited molecules. Diagnostic beam scattering was not considered, for the density of molecules in submerged space did not exceed $3 \cdot 10^{21} \text{ m}^{-3}$ in the experiment, and the measurements were conducted quite far from the sonic nozzle exit. The frequency range was 2 – 40 kHz. It corresponds to Strouhal numbers $St = fd/U_{\max} = 0.1 \div 2$, and that is typical for frequencies of disturbances of the jet mixing layer. The

measuring system, apparatus and principles of signal processing described in [8] were applied in the experiments. The measuring scheme is given in Fig. 1.

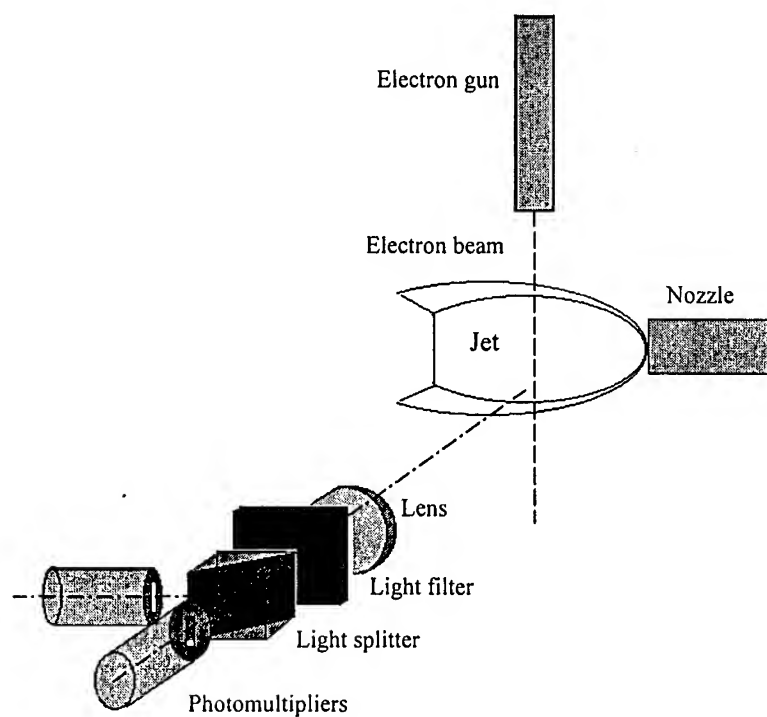


Figure 1.

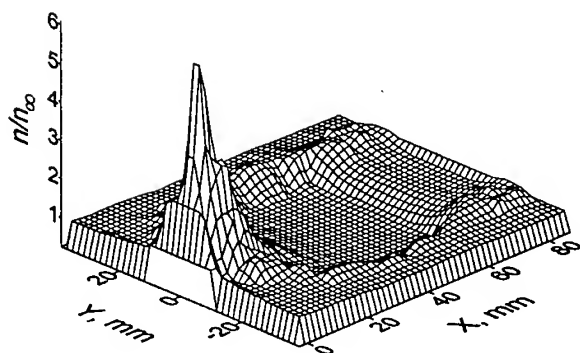


Figure 2.

The average gas density in the jet stream was reconstructed using the Stern-Volmer dependence by relation $n/n_\infty = (I/I_\infty)/(1 - K_t(I/I_\infty))$. Here K_t is a constant of quenching at intermolecular collisions, I/I_∞ is the normalized signal of the photomultiplier. The constant value was chosen by the data of [9] for the temperature of 300K. Density fluctuations were calculated by the values of cross-spectrum of the variable component of photomultiplier signals. The

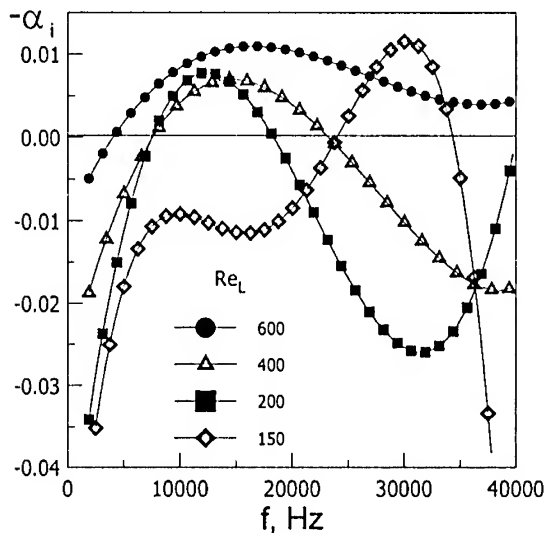


Figure 3.

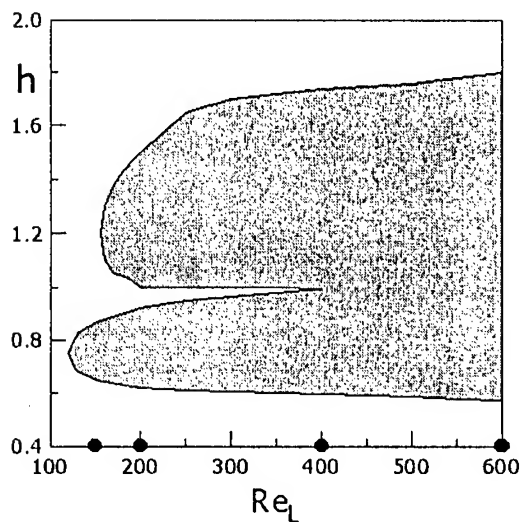


Figure 4.

Stern-Volmer dependence was also used, being transformed to determine density fluctuations $n'/n_\infty = I'/I_\infty(1+K_\tau(n'/n_\infty))^2$. Here I'/I_∞ is a normalized cross-spectrum of photomultiplier signals.

The measurement scheme allows one to measure of the streamwise and azimuth velocities of disturbance propagation. The description of the velocity measurement procedure is given in [8].

Results

The experimental data on the average density distribution in a jet are obtained (the example of distribution is in Fig. 2), as well as the spectra of disturbance amplification rate in the studied range of N and Re_L parameters (Fig. 3). The positions of Reynolds numbers whereby the measurements have been performed, are marked on the diagram of the zone of existence of self-sustained oscillations existence of the jet (the jet impinging on surface, [5,6], dark zone in Fig. 4). The values of the streamwise phase velocity of disturbances are determined. It is shown that the normalized streamwise phase velocity does not exceed 0.7 and its value falls smoothly down to the value ≈ 0.5 as the frequency rises. In measurements, there is no preferred direction of azimuth motion of density waves which is typical for weakly nonisobaric supersonic turbulent jets in the self-oscillating

regime.

The experiments on jet interaction with a target were conducted for outflow parameters whereby electron-beam measurements were realized. The presence of jet fluctuations was determined by pressure pulsations on the target. The pressure pulsations were measured by the signal of a piezoceramic pressure sensor placed in the center of circular target.

The data about the area of existence of fluctuations and their frequencies are obtained. The data were compared to the results from [5,6] and from Fig. 3,4.

1. M. Ramaswamy, E. Loth Tone excitation of a supersonic bounded shear layer // AIAA J. 1996. V. 34, № 10. P. 1997-2004.
2. V.N. Glaznev, V.S. Demin Semi-empirical theory of generation of discrete tones by supersonic underexpanded jet impinging on surface // J. Applied Mechanics and Technical Physics. 1976. № 6. P. 67-71.
3. B.G. Semiletenko, D.N. Sobkolov, V.N. Uskov A scheme of shock-wave processes at instable interaction of jet with surface // Ibid. 1973. № 13, P. 59-63.
4. S.G. Mironov The influence of parameters of external feedback loop upon self-sustained oscillations characteristics at underexpanded jet impinging on final target // Ibid. 1993. № 1. P. 94-100.
5. A.V. Savin, E.I. Sokolov, V.S. Favorskii, I.V. Shatalov The influence of rarefaction upon the process of non-stationar interaction of supersonic underexpanded jet with perpendicular target // Ibid. 1999. № 3. P. 109-116.
6. G.F. Gorshkov, V.N. Uskov Self-sustained oscillations in supersonic rarefied impact jets // Ibid. 1999. № 3. P. 109-116.
7. Experimental methods in dynamics of rarefied gases /Ed. by S.S. Kutateladze/. Novosibirsk: Institute of Thermophysics, Academy of Sciences, USSR, 1974.
8. A.A. Maslov, S.G. Mironov, A.N. Shiplyuk Wave processes in hypersonic shock layer on a plate // Izv. Rus. Acad. Nauk, 1998. № 5. P.62-168.
9. A.T. Belikov, O.V. Kusnetzov, R.G. Sharafutdinov The rate of collisional quenching of N_2O^{**} , N_2^{**} , O_2^{**} , O^{**} , O^* , Ar^* , Ar^{**} at temperature < 200 K // J. Chem. Phys. 1995. V. 102. P. 2792-2797.

CAPILLARY LOCKING EFFECTS IN PROCESSES OF IMMISCIBLE DISPLACEMENT

V.I. Penkovsky

Lavrentiev Institute of Hydrodynamics, 630090 Novosibirsk, Russia.

Introduction

The phenomenon of capillary locking plays an essential role in processes of oil production. Drilling bore wells using a clay water solution, and also displacement of petroleum by water injection wells are the main reasons "of water contamination" of oil fields. In the first case, the phenomenon of capillary locking manifests itself as the so-called end- (or skin-) effect, that causes partial plugging by water of near-well zones and drop its conductivity [1].

Macroscopic instabilities of displacement of one viscous fluid by another immiscible with it often take place in the case of waterflooding of oil fields. As experiments with transparent models show, in the course of such displacement originally connected and occupied by oil areas broken into smaller domains. The sizes of such "macroganglias" depend on local pressure gradients in a water phase, partially flowing around, and partially through these inclusions.

Experimentally and theoretically have been investigated the conditions [1, 2], at which these inclusions are in the stationary position of internal capillary locking and do not brake by the flux flow of the injected water.

Hydraulic approximation in a problem of one-dimensional partial percolation of ground waters through the closed petroleum inclusions have been investigated in the paper [1], and subject to an action of gravitation in the paper [3].

More generalized end sequential derivation of the basic equations describing process of the water filtration partially about and partially through three-dimensional petroleum inclusions is suggested here.

Three-dimensional inclusions of petroleum in a flow of ground waters.

Problem statement

Let's consider a two-dimensional forcing stream of the ground water in a bed with impermeable subsurface roof $z = F_s(x, y)$ and impermeable bottom $z = F_b(x, y)$. The axis z is directed vertically downwards, the orthogonal coordinates (x, y) placed in a horizontal plane. Let $z = F_0(x, y)$ and $z = F_1(x, y)$ are upper and the lower surface of the petroleum inclusion, respectively, and it is in the state of capillary locking in common established a steady seepage flow. It is natural, that the inequalities $F_s < F_0 < F_1 < F_b$ should be satisfied. Let's designate $D^+(x, y)$ as a projection of inclusion on a horizontal plane. It is assume, that this is the limited simply connected closed region and $D^-(x, y)$ – its exterior addition. Thus, three-dimensional region V^+ with points $(x, y, z)^+$ where $(x, y)^+ \in D^+$ and $F_0(x^+, y^+) \leq z^+ \leq F_1(x^+, y^+)$ is region of quasitwophase flow (only water are moving) , and addition V^- with points $(x, y, z)^-$, where $(x, y)^- \in D^-$ and $F_s \leq z^- \leq F_b$, or $(x, y)^+ \in D^+$, $F_s \leq z^- \leq F_0$ and $F_1 \leq z^- \leq F_b$ is region one-phase flow. Let (u, v, w) are vector components of the

petroleum velocity, (u_1, v_1, w_1) are components of water velocity. As the petroleum is stationary then $u=v=w=0$. According to the assumptions of the hydraulic theory of a filtration vertical components of vectors of a water velocity w_1^\pm in both regions V^\pm are negligibly small in comparison with horizontal components u_1^\pm, v_1^\pm depending only from coordinates x, y . It means, that pressure P (let's agree to take a pressure in head of water meters) will be hydrostatic both in water $P_1^\pm = p_1^\pm(x, y) + \rho_1 z$ and in petroleum $P^\pm = p^\pm(x, y) + \rho z / \rho_1$. Here ρ, ρ_1 are densities of petroleum and water respectively. Let's remark, that from the generalized Darcy's law

$$\vec{u} = -kf(s)\nabla p_1^+, \quad \vec{u}_1 = -k_1 f_1(s)\nabla p_1^+ \quad (1)$$

(f, f_1 is a phase permeability, k, k_1 is conductivity), being valid in the two-phase zone of flow and from condition of petroleum immobility $u^+ = v^+ = 0$ it follows, that $p^+ = p_0 = 0 = \text{const}$. Therefore the equation of pressure jump on boundary of phases $P_1^+ = P^+ - \Phi(s)$ yields a relation

$$\Phi(s) = p_0 - \varepsilon p_1^+(x, y) \quad (2)$$

Here $\Phi(s) = p_k^0 \varphi(s)$, p_k^0 is specific height of a capillary pressure, $\varphi(s)$ is known dimensionless Leveretts function. From a relation (2) it is possible to restore distribution of oil saturation in immobile inclusion, if the basic required function $p_1^+(x, y)$, will be found and while arbitrary constant p_0 also will be as necessary fixed. This function and function $p_1^-(x, y)$ should be a solution of a system of equations connected with each other by conditions on boundary Γ regions D^+ and D^- . For a derivation of a system we shall use the generalized Darcy's laws (1) for region D^+ , usual Darcy's law for region D^- and laws of mass conservation. Fluxes of water q_x and q_y through unit areas in a direction to coordinates x and y are equal respectively

$$\begin{aligned} (x, y) \in D^- : q_x^- &= -k_1(F_b - F_s) \frac{\partial p_1^-}{\partial x}; \quad q_y^- = -k_1(F_b - F_s) \frac{\partial p_1^-}{\partial y}; \\ (x, y) \in D^+ : q_x^+ &= -k_1(F_b - F_1 + F_0 - F_s) \frac{\partial p_1^-}{\partial x} - k_1 \int_{F_0}^{F_1} f_1(\Phi) dz \frac{\partial p_1^+}{\partial x}; \\ q_y^+ &= -k_1(F_b - F_1 + F_0 - F_s) \frac{\partial p_1^-}{\partial y} - k_1 \int_{F_0}^{F_1} f_1(\Phi) dz \frac{\partial p_1^+}{\partial y}. \end{aligned}$$

On a law of the mean for the integral present in the written above formulas, we draw

$$\int_{F_0}^{F_1} f_1(\Phi) dz = \int_{\Phi_0}^{\Phi_1} f_1(\Phi) \frac{dz}{d\Phi} d\Phi = -\frac{1}{\varepsilon} \int_{\Phi_0}^{\Phi_1} f_1(\Phi) d\Phi = -\frac{1}{\varepsilon} f_1(\tilde{\Phi})(\Phi_1 - \Phi_0).$$

Here $\tilde{\Phi}$ is some average value capillary pressure. Let's choose half-sum of capillary pressures on upper (F_0) and lower (F_1) surfaces of inclusion

$$\tilde{\Phi} = (\Phi_0 + \Phi_1) / 2 = p_0 - \varepsilon(F_0 + F_1) / 2 - p_1^+(x, y)$$

as a average. Thus, for an integral we shall draw approximation

$$\int_{F_0}^{F_1} f_1(\Phi) dz = f_1(\tilde{\Phi})(F_1 - F_0).$$

The functions $p_1^+(x, y)$, $p_1^-(x, y)$ do not depend on coordinate z , and at $z=F_0$ and $z=F_1$ they should coincide by virtue of pressure continuity in a water phase. Therefore for components of fluxes of water we obtain

$$q_x^+ = -k_1 [F_1 - F_s - (F_1 - F_0)(1 - f_1(\tilde{\Phi}))] \frac{\partial p_1^+}{\partial x};$$

$$q_y = -k_1 [F_1 - F_s - (F_1 - F_0)(1 - f_1(\tilde{\Phi}))] \frac{\partial p_1^+}{\partial y}.$$

Let's designate $H_t(x, y) = F_b(x, y) - F_s(x, y)$ being a topographical capacity confined aquifer, $H_g(x, y) = F_1(x, y) - F_0(x, y)$ being a capacity (on height) of petroleum inclusion. Then, requiring realization of conservation laws of a mass of water inside inclusion and outside of it, for definition desired functions $p_1^+(x, y)$ and $p_1^-(x, y)$ we shall draw the equations

$$L^+(p_1^+) = 0, (x, y) \in D^+; \quad (3)$$

$$L^-(p_1^-) = 0, (x, y) \in D^- \quad (4)$$

where L^{\pm} is elliptic operators of an aspect

$$L^+ = \text{div}[(H_t - (1 - f_1(\tilde{\Phi}))H_g) \nabla], \quad L^- = \text{div}(H_t \nabla).$$

Here operator L^+ is a quasi-linear because of $\tilde{\Phi}$ is the given function of a desired solution $p_1^+(x, y)$. The functions p_1^+ and p_1^- should be connected with each other by two conditions on a boundary Γ between the region D^+ and the region D^- . These conditions are a continuity of pressure in a water phase

$$p_1^+ = p_1^-; (x, y) \in \Gamma \quad (5)$$

and continuity of normal projections of fluxes

$$q^+_{1n} = q^-_{1n}; (x, y) \in \Gamma. \quad (6)$$

On exterior boundary Γ^- of region D^- being finite or infinite one from usual boundary conditions (the Dirichlet, Neumann or mixed) can be posed depend upon an initial physical problem. The condition, which would allow to define while a unknown constant p_0 included in relation (2) is specific to a considered problem. As it was marked in paper [2], variants of such conditions can be: 1) phases pressure aqualization in a forward lower point inclusions $p = p_0 = p_1^+ + \varepsilon_1$ that is equivalent to data of oil saturation $s = 0$; 2) a critical state of inclusion, at which small increasing of a velocity in an incident flow results in failure of the inclusion, and it means, that in a back upper point $p_0 = p_1^+ + \varepsilon_0 + p_k^0$ (i.e., $s = 1$), or 3) data of total amount of petroleum contained in region V^+ .

Conclusions

The offered system of equations allows to describe in a hydraulic approximation a distribution of oil particles in three-dimensional inclusion been under action of a field of hydrodynamic forces and field of gravitation.

References

1. **Antontsev S.N., Domansky A.V., Penkovsky V.I.** Filtration in well-by zone of a layer and problem of well discharge increasing. Novosibirsk: LIH SB USSR, 1989 (in Russian).
2. **Penkovsky V.I.** About influence of capillary forces on oil recovery by waterflooding // Mathematical Model of a Filtration and their Application. Novosibirsk: LIH SB RAS, 1999. P. 124-133 (in Russian).
3. **Penkovsky V.I.** Hydrocarbonaceous inclusion in water-saturated porous media // Dynamics of a Continuous Medium / LIH SB RAS. 1994. Vol.108. P. 27-37 (in Russian).

ABOUT CALCULATION OF A HYPERSONIC VISCOUS SHOCK LAYER ON A CONE AT ZERO INCIDENCE

T.V. Poplavskaya

Institute of Theoretical and Applied Mechanics SB RAS,
630090, Novosibirsk, Russia

This investigation is a continuation of a series of works [1-5] on theoretical and experimental study of hypersonic flow on bodies with a sharp edge.

Formulation of the problem

At high Mach numbers ($M_\infty \geq 10$) and moderate Reynolds numbers ($Re_x \sim 10^4 \div 10^5$) the boundary layer thickness is comparable with the shock wave stand-off distance. Thus, a good approximation for such flows is the full viscous shock layer (FVSL) model, which is an intermediate level of asymptotical approximation between the boundary layer equations and the full Navier – Stokes equations.

An axisymmetric hypersonic flow around a sharp cone is considered. In the coordinate system fitted to the body surface, the full viscous shock layer (FVSL) equations have the following form in dimensionless variables:

$$\begin{aligned}
 & \frac{\partial}{\partial x}(r\rho u) + \frac{\partial}{\partial y}(r\rho v) = 0, \\
 & \rho u \frac{\partial u}{\partial x} + \rho v \frac{\partial u}{\partial y} - \frac{1}{r Re_L} \frac{\partial}{\partial y} \left(r \mu \frac{\partial u}{\partial y} \right) + \frac{\partial P}{\partial x} = 0, \\
 & \rho u \frac{\partial v}{\partial x} + \rho v \frac{\partial v}{\partial y} - \frac{4}{3} \frac{1}{r Re_L} \frac{\partial}{\partial y} \left(r \mu \frac{\partial v}{\partial y} \right) + \frac{\partial P}{\partial y} = 0, \\
 & c_p \rho u \frac{\partial T}{\partial x} + c_p \rho v \frac{\partial T}{\partial y} - \frac{1}{r Re_L Pr} \frac{\partial}{\partial y} \left(r k \frac{\partial T}{\partial y} \right) - \\
 & \quad - \frac{1}{Re_L} (\gamma - 1) M_\infty^2 \mu \left(\frac{\partial u}{\partial y} \right)^2 - (\gamma - 1) M_\infty^2 \left(u \frac{\partial P}{\partial x} + v \frac{\partial P}{\partial y} \right) = 0, \\
 & P = \frac{1}{\gamma M_\infty^2} \rho T.
 \end{aligned} \tag{1}$$

In these equations, $r = r_w + y \cos \theta$. The meaning of the coordinates x and y , the radius r from the axis of symmetry, the distance r_w from the body contour to the axis of symmetry, and other dimensions is clear from Fig. 1. In Eqs. (1) P , ρ , μ , k , and T are the pressure, density, viscosity, thermal conductivity, and temperature, respectively, $Pr = \mu_\infty c_{p\infty} / k_\infty$ is the Prandtl number, $Re_L = \rho_\infty U_\infty L / \mu_\infty$ is the Reynolds number based on the free-stream parameters and model length L measured along the cone axis. The velocity components are normalized to the free-stream velocity U_∞ , the pressure to the doubled dynamic pressure $\rho_\infty U_\infty^2$, the viscosity μ , thermal conductivity k , specific heat capacity c_p , density, and temperature to their free-stream values,

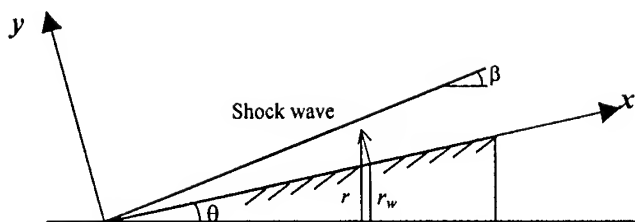


Fig. 1.

and the coordinates x and y to the model length L . The shock wave is assumed to be thin, and the generalized Rankine-Hugoniot relations are set there [6]:

$$\begin{aligned}
 u_s &= \cos(\beta - \theta) [\cos \beta + k_s \operatorname{tg}(\beta - \theta) \sin \beta] - \frac{\mu_s \cos^3(\beta - \theta) (1 - \operatorname{tg}^2(\beta - \theta))}{\operatorname{Re}_L \sin(\beta + \alpha)} \frac{\partial u}{\partial y}, \\
 v_s &= u_s \operatorname{tg}(\beta - \theta) - k_s \frac{\sin \beta}{\cos(\beta - \theta)}, \\
 P_s &= \frac{1}{\gamma M_\infty^2} + (1 - k_s) \sin^2 \beta - \frac{2\mu_s \sin(\beta - \theta) \cos(\beta - \theta)}{\operatorname{Re}_L} \frac{\partial u}{\partial y}, \\
 H_s &= 1 + \frac{\gamma - 1}{2} M_\infty^2 - \frac{\cos(\beta - \theta)}{\sigma_s \operatorname{Re}_L \sin \beta} \left[\frac{\partial H}{\partial y} - \frac{1 - \operatorname{Pr}}{2} (\gamma - 1) M_\infty^2 \frac{\partial}{\partial y} (u^2) \right], \\
 k_s &= \frac{1}{\rho_s}, \quad \sigma_s = \frac{\operatorname{Pr}}{\mu_s}.
 \end{aligned} \tag{2}$$

Here β is the shock-wave slope counted from the cone centerline, θ is the cone half-angle, γ is the ratio of specific heats, and H is the total specific enthalpy; the subscript s corresponds to flow parameters behind the shock wave. To determine the shock-wave shape y_s , we used the integral condition of conservation of the flow rate on passing through the shock wave:

$$(r + y_s \cos \theta)^2 = 2 \int_0^{y_s} \rho u r \cos \theta dy. \tag{3}$$

The slip and temperature jump conditions were used as the boundary conditions on the cone, as in [1-5].

Algorithm of solution

It is assumed that the flow in the initial cross section x_0 is described by the equations of an axisymmetric boundary layer and the shock wave has a constant slope between the cone apex and the cross section $x = x_0$. The problem of definition of the initial conditions was solved in the same manner as for a flat plate. For $x = x_0$, the FVSL system (1) reduced to ordinary differential equations using a transformation of the form $\xi = x$, $\eta = y \sqrt{\operatorname{Re}_L} / \sqrt{x}$ typical of boundary-layer flows with a uniform external flow.

Viscous shock layer equations are solved by the marching method along the coordinate x . The iteration process in each cross section is continued until the condition of conservation of the flow rate on passing through the shock wave (3) is satisfied.

In the course of solving the problem, the profiles of velocity, temperature, density, and pressure are calculated within the entire shock layer. The friction stress and the heat-transfer coefficients St (Stanton number) are calculated on the cone surface.

Results

To check the algorithm of solving FVSL equations on a cone, the flow around cones under various conditions were calculated and compared with experimental data obtained at ITAM SB RAS and available in the literature. Figure 2 shows the angle β of inclination of the shock wave arising in the flow around the cone versus the cone half-angle θ . The FVSL results are shown by the solid curve, and the data obtained using the inviscid theory [7] are shown by the dashed curve. Since the inviscid theory does not take into account the displacement effect of the boundary layer, the “inviscid” values of β are slightly lower than the FVSL results. It is shown [9] that the circular spreading on the cone leads to attenuation of the shock wave. As the cone angle increases, the shock wave is apparently attenuated to a degree at which the displacement effect practically disappears.

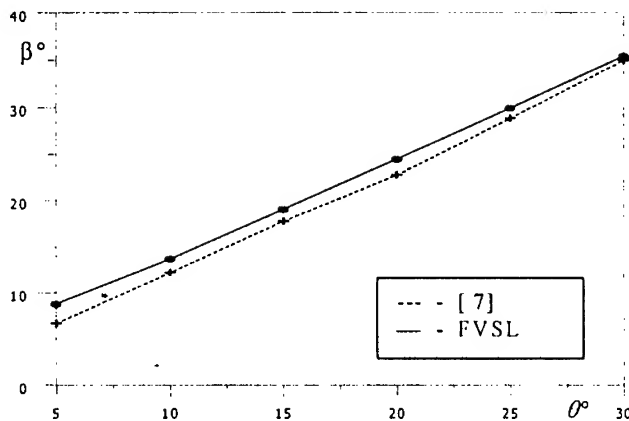


Fig. 2. Shock-wave inclination ahead of the cone versus the cone half-angle for $M_\infty=19$.

Figure 3 shows a comparison with the results of [8] on the shock-wave stand-off distance and density profile for $M_\infty=21$, $Re_l=6 \times 10^5 \text{ m}^{-1}$, $L=0.113 \text{ m}$, $T_0=1150\text{K}$, $T_w=320\text{K}$, and the angle $\theta=10^\circ$. The dashed curve shows the results of electron-beam visualization of the flow, the circles refer to the experimental data obtained by the method of electron-beam fluorescence, and the solid curves show the FVSL results. The density profile was measured in the wake behind the cone at a distance of $0.8D$ from the cone base. It should be noted that the method of electron-beam fluorescence ensures good accuracy in measurements far from the surface; therefore, these data were used for comparison. It is assumed here that, at this distance, the density profile in the wake still retains a distribution typical of the shock layer in the last cross section of the cone.

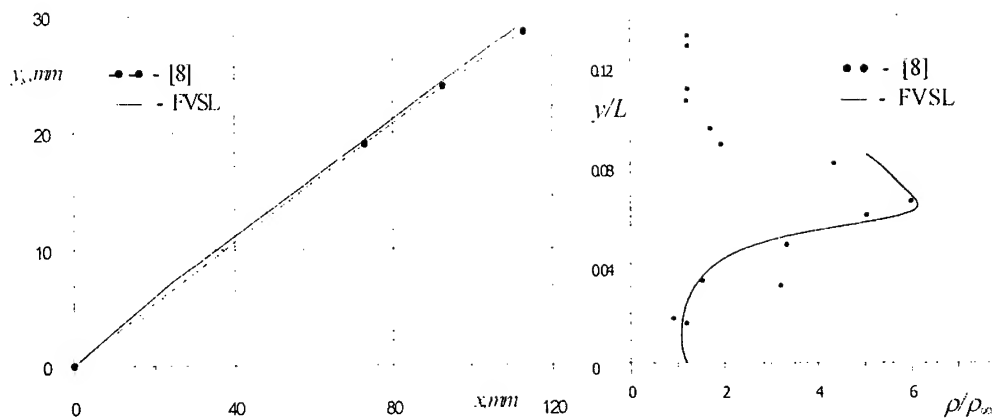


Fig. 3. Shock-wave position and density profiles on the cone for $M_\infty=21$, $Re_1=6 \times 10^5 \text{ m}^{-1}$, $L=0.113 \text{ m}$, $T_0=1150\text{K}$, $T_w=320\text{K}$, and the angle $\theta=10^\circ$.

Figure 4 is borrowed from [9]. It shows the shock-wave position on a 5° cone for different geometries of the nose part. The dashed curve here shows the FVSL results on a sharp cone under the following conditions corresponding to the experiment: $M_\infty=23.8$, $Re_1=2.76 \times 10^5 \text{ m}^{-1}$, $L=0.165 \text{ m}$, $T_0=2700\text{K}$, and $T_w=300\text{K}$.

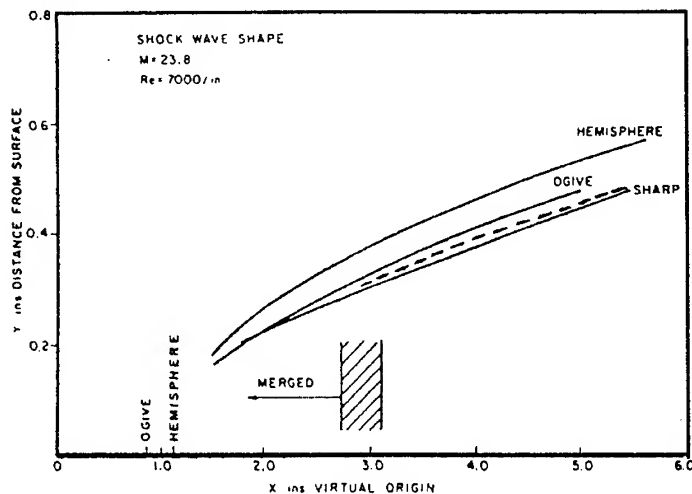


Fig. 4.

The flow field on pointed bodies in the merged layer regime was experimentally studied in [10]. The results were obtained by flow visualization with Schlieren pictures and by the discharge method, and also by local measurements of flow parameters by a Pitot tube and a hot-wire anemometer. Figure 5 shows the density profiles across the shock layer on a 10° cone in the cross section $x=0.83$, which corresponds to the region of strong interaction. The solid curve shows the density profiles calculated using FVSL equations as a function of the dimensionless coordinate y normalized to its value on the shock wave, and the crosses refer to the data of [10].

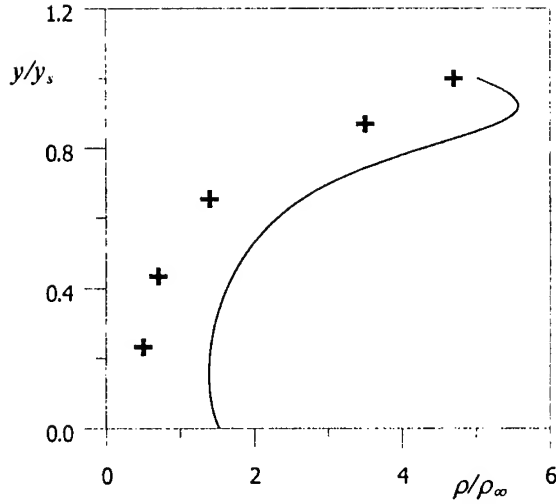


Fig. 5. Density profiles on a 10° cone for $M_\infty=24.5$, $Re_l=3.94 \times 10^5 \text{ m}^{-1}$, $L=0.091 \text{ m}$, $T_0=2000\text{K}$, and $T_w=294\text{K}$.

Experimental measurements of density by the method of electron-beam fluorescence were performed in [11]. The velocity in [11] was found from the measured density and pressure behind the shock wave, which was measured by a Pitot tube. These parameters (crosses) are compared in Fig. 6 to the results of the present study (solid curves). The velocity profiles are in good agreement, and the discrepancy in density is of the same order as with the results of [10]. This can be explained, on one hand, by the fact that the cross sections are in the region of transition from the merged flow regime to the regime of strong viscous interaction, i.e., in the region of flow reconstruction, and on the other hand, by imperfection of the density-measurement techniques applied to an axisymmetric flow (these techniques have been justified only for planar flows).

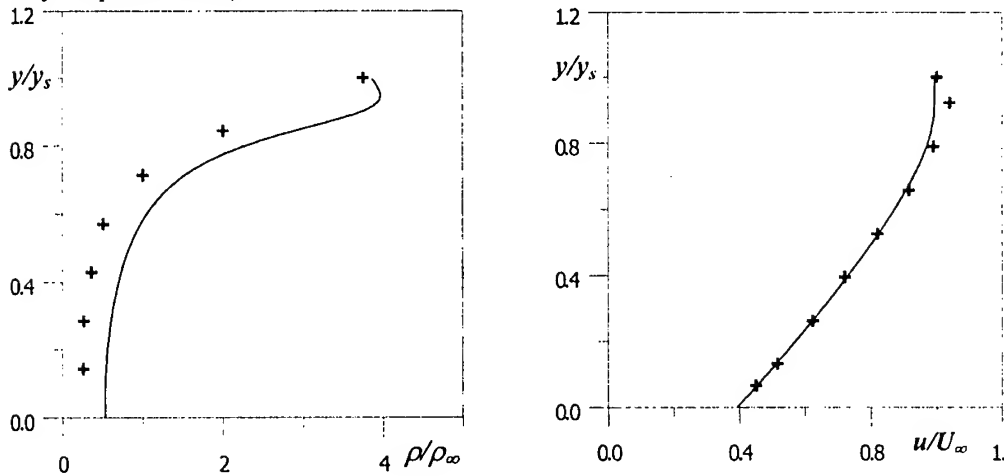


Fig. 6. Density and velocity profiles on a 5° cone for $M_\infty=25$, $Re_l=4.33 \times 10^5 \text{ m}^{-1}$, $L=0.242 \text{ m}$, $T_0=1850\text{K}$, $T_w=300\text{K}$, and $x = 0.533$.

Thus, an algorithm for calculation of a viscous shock layer on a cone at zero incidence has been developed. All flow characteristics have been calculated for various mach and Reynolds numbers. The agreement of numerical and experimental results is a solid argument in favor of the applicability of the flow model chosen and the algorithm developed.

This work was supported by the Russian Foundation for basic Research (grant No. 98-01-00735).

References

1. Vetlutsky V.N., Maslov A.A., Mironov S.G., Poplavskaya T.V. and A.N.Shiplyuk A.N. Hypersonic flow on a flat plate. Experimental results and numerical simulation // J. Appl. Mech. Tech. Phys. – 1995. – Vol. 36, No. 6. – P. 60-67.
2. Poplavskaya T.V. and Vetlutsky V.N. Calculation of viscous shock layer on a plate // Ibid. – 1997. – Vol. 38, No. 2. – P. 91-100.
3. Maslov A.A., Mironov S.G., Poplavskaya T.V. and Vetlutskiy V.N. On the incidence angle effect on the flow over a plate // High Temperature. – 1998. – Vol. 36, No. 5. – P. 730-736.
4. Maslov A.A., Mironov S.G., Poplavskaya T.V., Shiplyuk A.N., Vetlutsky V.N. // Study of aerodynamic heating on a plate in viscous hypersonic flow // High Temperature. – 1999. – Vol. 37, No. 3. – P. 415-419.
5. Maslov A.A., Mironov S.G., Poplavskaya T.V., Shiplyuk A.N., Vetlutsky V.N. // Viscous shock layer on a plate in hypersonic flow // Eur. J. Mech. B/Fluids. 1999. – 18, No. 2. – P. 213-226.
6. Tirskey G.A. On the theory of the viscous chemically reacting gas flow over plane and axisymmetric blunt bodies with injection // Scientific Papers of the Institute of Mechanics, No. 39 – Moscow State University, 1975. – P. 5-38.
7. Krasnov N.F. Aerodynamics of Bodies of Revolution. – Moscow: Mashinostroenie, 1964.
8. Aniskin V.M., Mironov S.G. Experimental investigation of density fluctuations in a hypersonic laminar wake of a cone // J. Appl. Mech. Tech. Phys. – 2000. – No. 5 (in press).
9. Feik R.A., Genchi A., Vas I.E. A study of merging on cones // Rarefied Gas Dynamics / Eds. L. Trilling and H. Y. Wachman. – Vol. 1. – 1969. – P. 493-500.
10. McCroskey W.J., Bogdonoff S.M., Genchi A.P. Leading edge flow studies of sharp bodies in rarefied hypersonic flow // Ibid. / Ed. C.L. Brundin, 1967. – Vol. 2. – P. 1047-1066.
11. Vas I.E., Sierchio J.G. Downstream effects of bluntness in the merged flow regime // Ibid. / Ed. by K. Karamcheti, 1974. – P. 307-315.

INFLUENCE OF ENERGY SUPPLY IN FREE STREAM ON STABILITY OF HYPERSONIC BOUNDARY LAYER ON CONE-CYLINDER

T.V. Poplavskaya

Institute of Theoretical and Applied Mechanics SB RAS,
630090, Novosibirsk, Russia

The study of the flow with external energy supply is important to solve the following actual problems: decrease of drag and heat flux, efficient control of aerodynamic characteristics at flight with high speed, stabilization of disturbances, and control of laminar-turbulent transition.

The present paper considers a flow around a cone-cylinder with a local energy source in the form of a thin cylinder on the axis of symmetry in front of the body. The cone half-angle is 30° , and the cylinder diameter is $D = 40$ mm. A free stream passes around the body at zero incidence at the Mach number $M_\infty = 6$. The source of energy produces a zone of heated gas whose temperature changes in a radial direction according to the Gaussian law.

To calculate axisymmetric boundary layer on the cone-cylinder a code of calculation of three-dimensional boundary layer on a pointed body developed earlier and described in detail in [1] is used. Formulations of the problems of boundary layer on the cone with the cylinder with an energy source in front of the body and without it are similar.

In Fig. 1, the distribution of parameters $P_e = P_e^* / \rho_\infty U_\infty^2$, $U_e = U_e^* / U_\infty$ and $T_e = T_e^* / T_\infty$ at the boundary layer edge for flows with an energy source and without it (index $*$ corresponds to dimensional values and ∞ to parameters of the free stream) are given. These parameters are taken from the solution for inviscid flow around the body obtained by codes of the Euler equations elaborated in ITAM SB RAS [2].

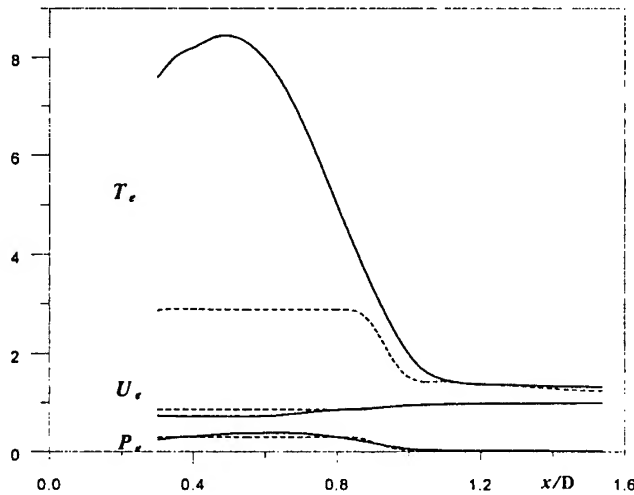


Fig. 1. Data at the outer edge of the boundary layer.

--- a flow without an energy source, — a flow with an energy source in front of the body.

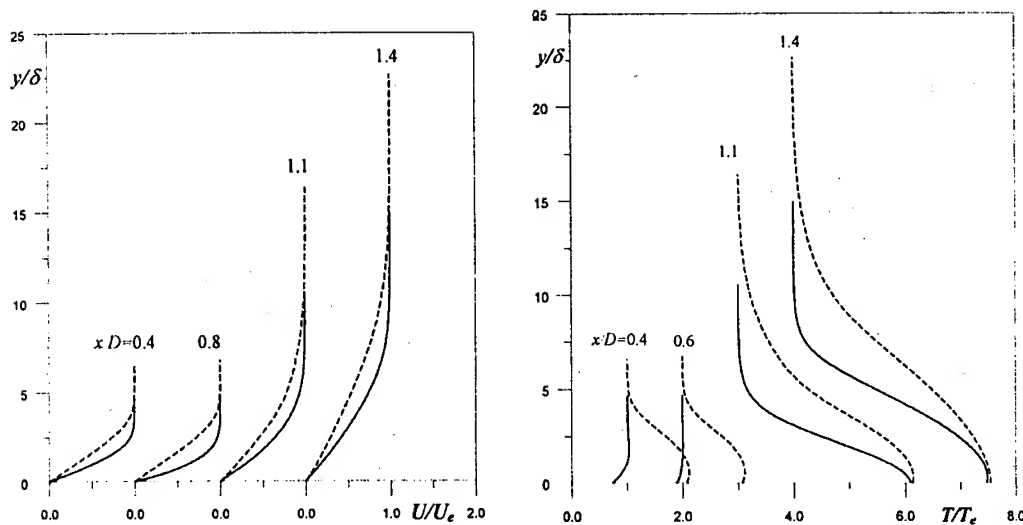


Fig. 2. Velocity and temperature profiles on the cone ($x/D = 0.4, 0.7$) and on the cylinder ($x/D = 1.1, 1.4$):

--- flow without a source of energy
 — flow with a source of energy in front of the body.

The calculation of the boundary layer on a cone-cylinder model with an energy source in front of the body and without it was performed for the free-stream Mach number $M_\infty = 6$, angle of attack $\alpha = 0$, temperature factor $T_w/T_\infty = 6$ (T_w is the surface temperature) and Reynolds number $Re_D = Re_{\infty} D = 5 \times 10^6$, calculated by the parameters of the free stream and cylinder diameter D .

In Fig. 2 the velocity and temperature profiles in various cross sections of a cone-cylinder body in a flow without energy supply (dashed lines) are shown. They depend on the normal coordinate y normalized to $\delta = \sqrt{\nu_e x / U_e}$. It is seen that all profiles on the cone in the flow without energy supply are similar, i. e. the flow is self-similar. After turning to the cylinder ($x/D > 0.8$) the flow accelerates, and velocity profiles become less filled from one cross-section to another. The flow is essentially non-self-similar.

In the same figures, the velocity and temperature profiles are presented for the flow with a source of energy by solid lines. The influence of the energy source results in a greater filling of velocity profiles and a strong change of temperature profiles near the body surface.

The stability of the velocity and temperature profiles represented are investigated with regard to small disturbances. The analysis of stability was performed within a local-parallel approximation. The interest in stability of the boundary layer on a body in the presence of a local energy source is connected with the effects of

- (1) acceleration of a supersonic flow near a convex surface
- (2) the source of energy.

A stabilizing effect of the negative pressure gradient in the plane case has been known for a long time [3]. The effect of energy supply on the characteristics of the supersonic boundary layer and its stability on the cone-cylinder model for the Mach number $M_\infty = 2$ was studied in the paper [4]. A similar problem for the hypersonic boundary layer for $M_\infty = 6$ is solved in the present paper.

As a result of solution, a neutral stability curve for two-dimensional disturbances on the cone without the energy source in front of it (dashed line in Fig. 3) calculated in the approximation of a self-similar flow in the boundary layer on a cone with a profile corresponding to the section $x/D = 0.4$ was plotted.

Then the stability of profiles of an axisymmetric boundary layer on the cone-cylinder model without the energy source in front of the body (symbols + in Fig. 3) was calculated. Like in a plane case [3] strong stabilization of the flow in the zone of flow turning ($0.8 < x/D < 1.0$) was found. Calculation of amplification rates in the mentioned zone showed that disturbances decay for all frequencies. This leads to a discontinuity of the neutral stability curve with the formation of a closed curve in the region of moderate Reynolds numbers (see Fig. 3). For $x/D > 1.1$, the curve of neutral stability marked by symbols (crosses) corresponds to a boundary layer on the cylinder. A similar picture was observed for the Mach number $M_\infty = 2$ [4].

The neutral curve calculations on the cone and the cylinder were carried for the angle of inclination of the wave vector χ corresponding to the most unsteady disturbances (on the cone $\chi = 72.5^\circ$ and on the cylinder $\chi = 74^\circ$). In Fig. 3, the neutral curve for a flow with a source of energy (points Δ) is given. The influence of the energy source results in complete stabilization of the flow on the conical part of the body. On the cylindrical part of the body, the energy supply increases both the region of instability and the amplification rates. It is connected to the growth of the temperature gradient near the body in the flow with energy supply.

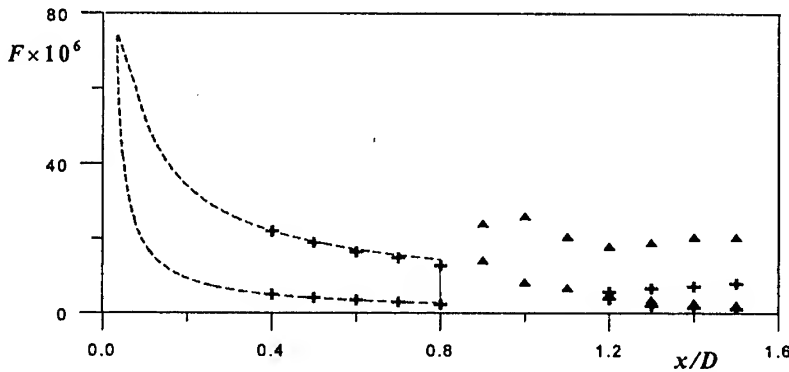


Fig. 3. Neutral stability curves on a cone-cylinder model for $M_\infty = 6.0$, $T_0 = 400K$, $T_w/T_\infty = 6.0$, $\chi = 72.5^\circ$ on the cone and $\chi = 74^\circ$ on the cylinder:

- calculation in the self-similar approximation of the boundary layer flow on a cone,
- + -- flow without a source of energy,
- Δ -- flow with a source of energy in front of the body.

The Mach number on the outer edge of the boundary layer M_e , the Reynolds numbers $R_\delta = \frac{U_e}{\nu_e} \delta = \sqrt{Re_e x}$ and the temperature factor $T_w = T_w^*/T_e$ used for stability calculations in

different cross-sections x/D are presented in the table. It is seen that the Mach numbers on the cylinder are greater than 5 and Reynolds numbers are greater than 2000. It is known that the second mode of disturbances exists on a flat plate for those Mach and Reynolds numbers (see curve 1 in Fig. 4).

However, the second mode is not found in the present calculations. The amplification rate dependence on the dimensionless frequency parameter F on the plate and on the cylinder in

the cross-section $x/D=1.5$ are shown in Fig.4. It is seen that the second mode in present calculations (curves 2 and 3) is stable in contrast to a heat-insulated plate (curve 1). It is connected with the fact that velocity and temperature profiles on the cylinder are different from the same profiles on the flat plate.

The flow without an energy source				The flow with an energy source		
x/D	M_e	R_δ	T_w	M_e	R_δ	T_w
0.4	3.03	2010.4	2.07	1.51	752.7	0.73
0.5	3.03	2248.1	2.07	1.48	886.7	0.71
0.6	3.03	2464	2.08	1.54	1053.3	0.75
0.7	3.03	2664	2.08	1.81	1351.4	0.89
0.8	3.02	2849.3	2.08	2.26	1730.7	1.2
0.9	3.26	2732.3	2.36	2.92	2057.6	1.8
1.0	4.67	1971.8	3.89	3.99	2082.8	3.01
1.1	4.82	1978.2	4.13	4.82	1990.9	4.1
1.2	4.95	2010.3	4.3	5.02	1996.8	4.35
1.3	5.0	2076.9	4.37	5.08	2039.8	4.40
1.4	5.11	2103.8	4.54	5.15	2091.3	4.47
1.5	5.18	2158.9	4.63	5.19	2149.9	4.53

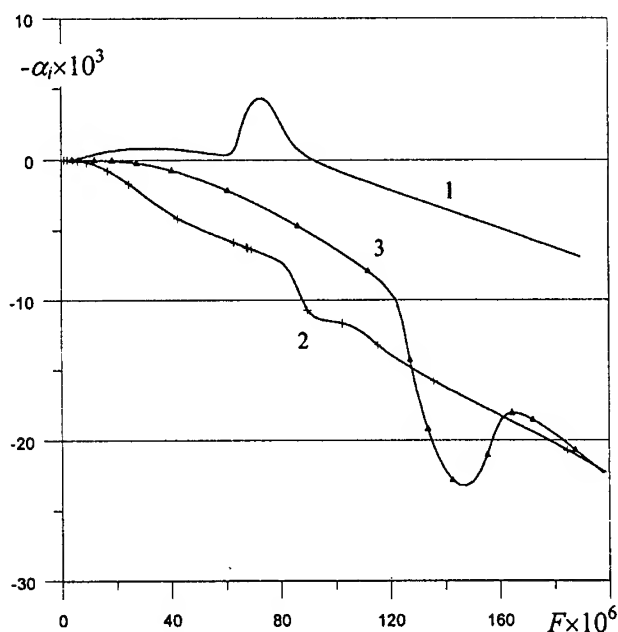


Fig. 4. Amplification rates of disturbances: 1 – on the heat-insulated plate for $R_\delta = 2159$, $M_e = 5.18$, $\chi = 0^\circ$,
2 – on the cone-cylinder model without the energy source for $x/D = 1.5$
3 – on the cone-cylinder model with the energy source for $x/D = 1.5$.

Thus obtained data showed that the energy source in front of the body stabilizes disturbances in the boundary layer on the conic section of the model. The region of instability corresponding to the first mode increases on the cylinder part. The unstable disturbances corresponding to the second mode have not been found both in the flow without the energy source and with it.

This work was performed under financial support of Boeing, Rockwell company (Contract No. B8X413840) and the Russian Foundation for Basic Research (Grant No. 98-01-00735).

REFERENCES

1. L.M. Vetlutskaya and V.N. Vetlutsky, On calculation of a spatial compressed boundary layer on the pointed body // Numerical Methods of Mechanics of Continuous Medium. Novosibirsk, ITAM SB AS USSR, 1986, Vol. 17, No. 5. P. 25 – 42.
2. T.A. Korotaeva, V.M. Fomin and A.P. Shashkin, Spatial supersonic flow around of a pointed body with power source in front of it // J. Appl. Mech. and Tech. Phys., 1998, No. 5. P. 116 – 121.
3. S.A. Gaponov and G.V. Petrov, Stability of supersonic boundary layer at a flow turn. // Izv. SO AN SSSR, Ser. tech. Nauk. 1987, No. 18. Iss 5. P. 25 – 29.
4. T.V. Poplavskaya, A.A. Maslov and V.N. Vetlutsky, Supersonic boundary layer and its stability on a cone-cylinder body with an energy source. // Thermophysics and Aeromechanics. 1999. Vol. 6. No. 4. P. 575-578.

HYSTERISES OF THE ACOUSTIC AND THRUST CHARACTERISTICS OF THE RAMJET COMBUSTION CHAMBER AT VIBRATION REGIMES OF FUEL COMBUSTION

A.V. Potapkin, D.Yu. Moskvichev, A.I. Trubitsin

Institute of Theoretical and Applied Mechanics SB RAS
630090, Novosibirsk, Russia

Studies of vibrational combustion of hydrogen in a ramjet combustion chamber of the ejector type [1] showed that, at developed vibrational combustion, thrust appears at the chamber inlet, and the value of this thrust is determined by the shape of the chamber inlet, fuel consumption, and injector position. The value of this thrust can be controlled by variation of these parameters. Besides, it depends on geometry and resonator positions on the combustion chamber [2]. In paper [3], an acoustic hysteresis was described (according to the data of Rogers, Marble and Kloch). At this hysteresis, the disappearance of vibrations was observed for a poorer fuel-air mixture in comparison to their appearing at mixture enrichment. The acoustic hysteresis for various fuels was studied in [4]. Since in papers [1, 2] the correlation between the acoustic and thrust characteristics of the ramjet combustion chamber at vibrational combustion was established, it was assumed that the hysteresis effect will be observed in thrust characteristics too. The results of the experimental test of this assumption are presented in this paper.

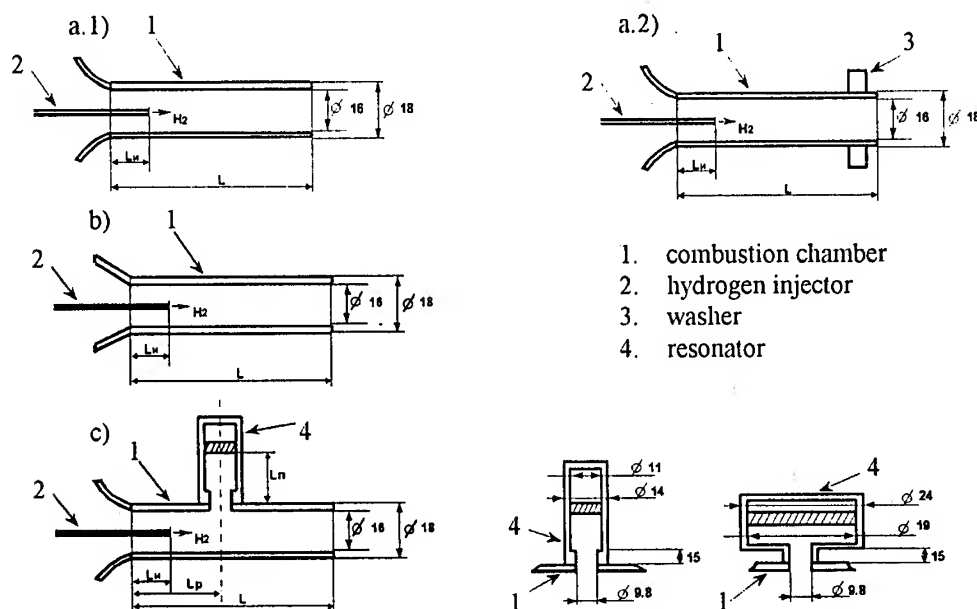


Fig. 1

The combustion chambers of various geometrical configurations are shown in Fig. 1. L is the length of the cylindrical combustion chamber 146.5 – 150 mm. Lu is the position of the spike of hydrogen injector relative to the chamber section $Lu/2L = 0.169$ (in fractions of the sound wave $\lambda = 2L$). The injector is not connected mechanically with the combustion chamber. In figure, the combustion chamber with a confusor whose inner surface had the shape of a torus with the largest diameter of 35 mm and the length of 17 mm is shown. The chamber in Fig. 1.a.2) differed from the chamber in Fig. 1.a.1) by the large washer at the outlet which changed the total weight of the combustion chamber. In Fig. b) the combustion chamber with the head at the inlet in the shape of a truncated cone is shown. The angle between the cone wall and the symmetry axis is $\sim 14^\circ$. In Fig c) the combustion chamber with the torus-like inlet and

$d=11\text{ mm}$ $Ln/2L$	$d=19\text{ mm}$ $Ln/2L$	Vp, mm^3
	0.051	1130.9
	0.0642	2207.8
0.153	0.0865	4050.5
0.194	0.0984	5000.3
0.225	0.1102	5950.2
0.256	0.1215	6900.0
0.297	0.1335	7849.9
0.327	0.1455	8799.7
0.368	0.1575	9749.6
0.4	0.1675	10699.4
0.43		11649.3

Table 1.

resonator is shown. Two changeable resonators which are cylindrical tubes of different diameter are shown. A piston was located in each resonator. The piston location was varied at tests. The resonators were connected with the combustion chamber by a cylindrical adapter of height 15 mm. The power position of the piston corresponded to a distance $Ln = 15$ mm. The linear dimension of the resonator at $d = 19$ mm was chosen proceeding from the equality of the volumes of both resonators. The linear dimensions of the resonators $Ln/2L$ corresponding to the piston location at equal volumes are shown in Table 1 (where d is the inner diameter of the resonator, Vp is the resonator volume and the volume of the cylindrical adapter). The axis of the resonator is normal to the axis of the combustion chamber. The resonators were connected to the combustion chamber at the point $Lp/2L = 0.251$. In tests, the combustion chamber was fixed on the pantograph so that only a streamwise displacement was possible. The streamwise force (thrust or drag) F was registered by a strain-gage balance. The amplitude of sound vibrations A was measured by a condenser microphone. The flow rate of hydrogen Q was determined by the pressure differential on a hydroresistance. All readings of the devices were displayed and registered on a mirror-galvanometer oscillograph.

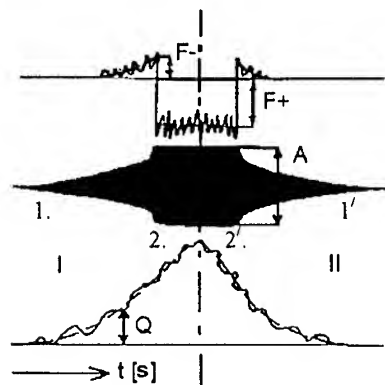


Fig. 2

II). Points 1., 2., 2', 1' are the points of the change of combustion regimes at transition from

zone I to zone II. Points 1. and 2. correspond to the points of transition to the regimes of vibrational and developed vibrational combustion, points 2' and 1' correspond to the points of outcome from the regimes of the developed vibrational and vibrational combustion.

Generalization of the measurements of flow rate Q at which the regimes change is shown in Fig. 3. Here q is the derivative dQ/dt , regions I and II correspond to zones I, II in Fig. 2, i.e. regions of Q increasing and decreasing, the arrows show the direction of tracing around by Q .

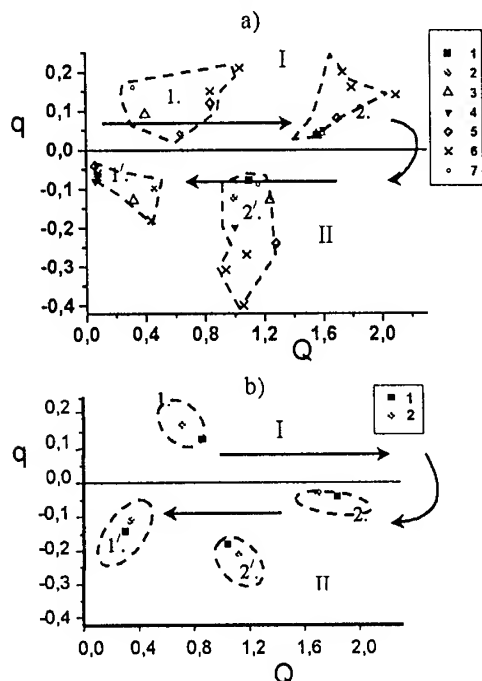


Fig. 3

The points shown in the figure are the data processing according to the recordings in different series of the experiments. The points were connected by the dashed line and the obtained regions 1., 2., 2', 1' correspond to the points of the change of combustion regimes 1., 2., 2', 1' in Fig. 2. Fig. 3.a) shows the data for the configuration of the combustion chamber shown in Fig. 1.a); the data on the configuration of the combustion chamber with a cone probe at the inlet (Fig. 1.b)) are given in Fig. 3.b). Inter-displacement of regions 1. and 1' showed that the development of vibrational combustion at Q increase and the ceasing of the regime of vibrational combustion at Q decrease take place at various values of hydrogen flow rate irrespective of the shape of the inlet into the combustion chamber. A similar hysteresis was observed for the regime of developed vibrational combustion. Relative-location of regions 2. and 2' made it possible to conclude that the appearing and disappearing of the regime of developed vibrational combustion

take place at different Q values depending on the sign of q . A comparison of Fig. 3.a) and 3.b) showed that the change of the shape of the inlet into the combustion chamber leads to the change of the values of Q and q at which the regime of developed vibrational combustion takes place. For the chamber with a conical inlet, the regime of developed vibrational combustion was realized only for $q < 0$ (zone II), this fact and the noted location of regions 1., 1', 2., 2' manifests the stability of the realized regime of combustion to Q change, it shows the dependence of the coefficient of the air ejection on the amplitude-frequency characteristics of sound.

A hysteresis in the thrust and acoustic characteristics of the combustion chamber is shown in Fig. 4. The dimensions of the thrust force F is force gram, specific impulse $I = F/Q'$ is second where Q' is weight of flow rate hydrogen, the amplitude of the sound vibrations A is given in dB. Figure a) has three curves – the data on three experiments for the combustion chamber with the inlet in the shape of a torus, Fig. b) shows the results of the measurements for the chamber with a conic inlet. Location of the curves shows good replication of the experiments. The arrows show the direction of tracing at Q change. Numbers 2. and 2', as in the previous figure, show the points of inlet into the regime of vibrational combustion and the outlet. The following results are distinguished: at the regime of developed vibrational combustion A and F reach the "threshold" values depending on the inlet shape and a Q increase does not lead to an increase in

A and F , a decrease in Q makes the A and F values be the same with their further synchronic decrease, the specific impulse increases because of the F consistency and Q decrease, it shows a

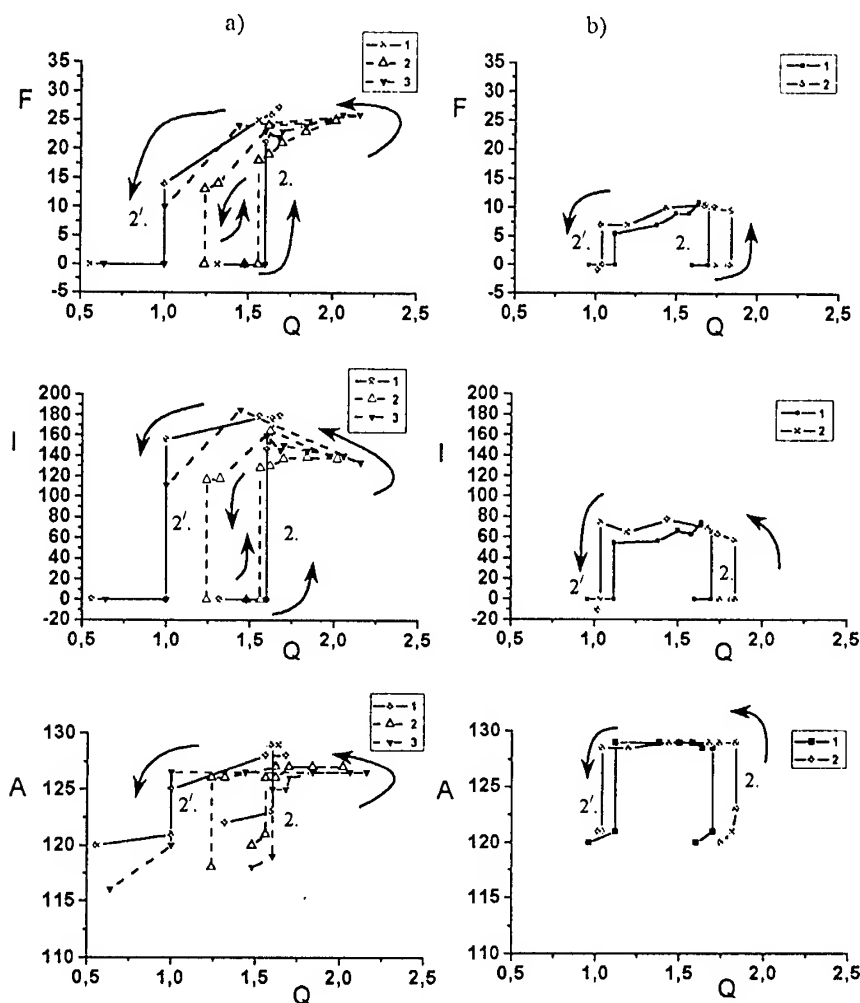


Fig. 4

more complete use of fuel in the thrust formation. This behavior of the curves shows the transmission ability of the inlet head at air ejection under the condition of sound vibrations in the flow and stability of the ejection coefficient to Q change. The integral characteristics of F and I are significantly determined by the shape of the inlet into the combustion chamber as it is seen from this figure.

The dependences of F , impulse I and amplitude of the sound vibrations A on the flow rate Q for the combustion chamber with a resonator (see Fig. 1.c) at $Lu/2L = 0.169$ are shown in Fig. 5. The dependences for the resonator at $d = 11$ mm are shown in Fig. 5.a). Here curve 1 corresponds to the value $Ln/2L = 0.368$ and curve 2 to $Ln/2L = 0.153$. Curve 1 corresponds to $Ln/2L = 0.051$ for the resonator at $d = 19$ mm, curve 2 to value $Ln/2L = 0.0642$ in Fig. 5.b). Points 2. and 2' correspond to the points of inlet and outlet regimes of developed vibrational combustion (see Fig. 2). These results show that the value of the thrust force correlates with the

amplitude of the sound vibrations. The behavior of the function $F(Q)$ is similar to that of $A(Q)$. The acoustic hysteresis was displayed in preserving the amplitude of the sound vibrations at

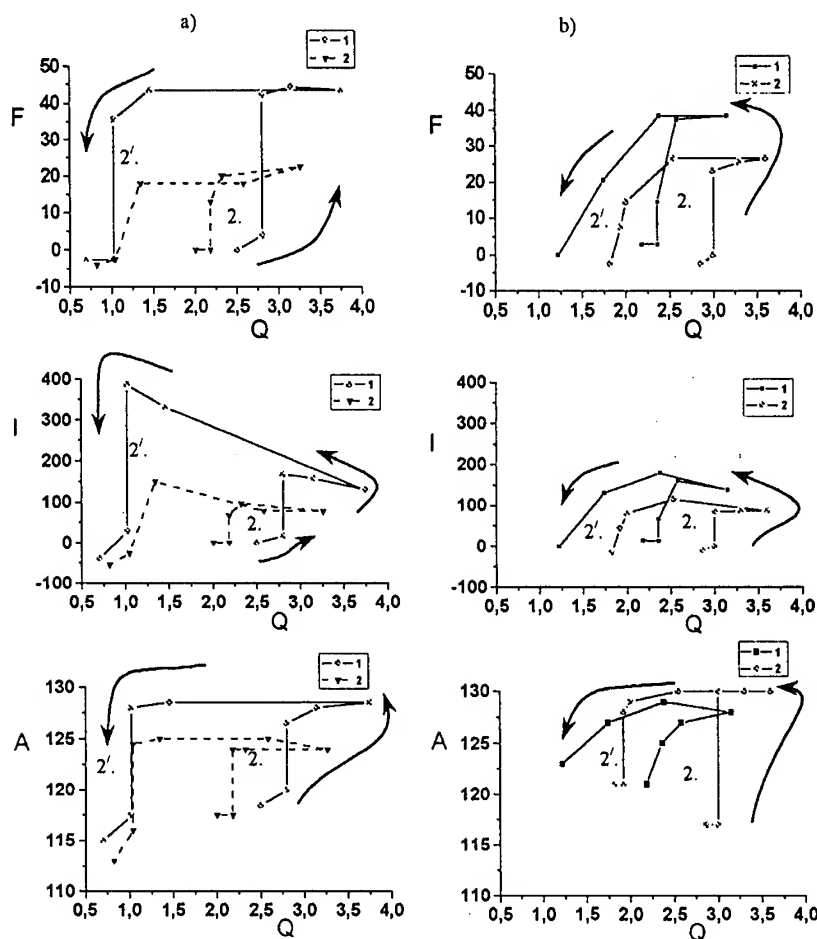


Fig. 5

decreasing fuel consumption when developed vibrational combustion was realized. $F(Q)$ preserved its constant value and the relative quantity $I = F/Q$ increased at the expense of Q decrease. Due to this effect, a considerable growth of the specific impulse I can be obtained in zone II in comparison to the impulse in zone I at some optimal dimensions of the resonator. For $Ln/2L = 0.368$, the maximum value of the impulse in zone I was $I \sim 160$ s at $Q \sim 3.75$ 1/s, whereas the maximum impulse in zone II reached the value $I \sim 380$ s at $Q \sim 1$ 1/s. Correlation of the acoustic and force characteristics of the combustion chamber and a hysteresis were observed for the resonator with $d = 19$ mm (Fig. 5.b)). The differences between the dependences in Fig. 5.a) and 5.b) were in the maximum values of the force F and impulse I and in earlier and smoother transition from developed vibrational combustion to the vibrational combustion. The force and impulse reached the values $F \sim 46$ G and $I \sim 380$ s (for $Ln/2L = 0.368$) in Fig. 5.a) and $F \sim 38$ G and $I \sim 180$ s (for $Ln/2L = 0.051$) in Fig. 5.b). An increase in the diameter of the resonator cavity leads to a small increase of the impulse at transition from zone I to zone II, $I \sim$

160 s at $Q \sim 2.6$ l/s and $I \sim 180$ s at $Q \sim 2.3$ l/s. The data presented in Fig. 5 show that the effect of hysteresis of the acoustic and thrust characteristics of the combustion chamber with a resonator is observed irrespective of the resonator shape at various linear dimensions of the resonator. The hysteresis at the realized regime of developed vibrational combustion allows one to increase the greatest specific impulse of the combustion chamber with the resonator approximately by two times.

Thus, the hysteresis in thrust characteristics can be used to increase the efficiency of the ramjet combustion chamber at developed vibrational combustion of fuel.

REFERENCES

1. Baev V.K., Potapkin A.V., Chusov D.V. Effect of heat-acoustic processes on thrust characteristics of the combustion chamber // *Matem. model., aerodin. i fizich. gasodin.* / Ed. Fomin V.M.. Novosibirsk, 1995. P. 187 – 188.
2. Baev V.K., Moskvichev D.Yu., Potapkin A.V.. The influence of acoustic resonator on the air-breathing combustor operation under pulsation burning of hydrogen // *Intern. Conf. on the Method of Aerophysical Research: Proc. Pt. III.* Novosibirsk, 1998. P. 55 – 59.
3. **Non-stationary flame propagation** / Ed. Markshtein G.G.. Moscow: Mir, 1968. 437 p.
4. Bardakhanov S.P. and Potapkin A.V. Hysteresis regimes in fuel burning processing. *Proc. 3d Russian-Korean Intern. Symp. on Science and Technology, Korus-99. Vol. I.* Novosibirsk, 1999. P. 46 – 49.

NUMERICAL ANALYSIS OF FLOWS OVER SPACE TRANSPORTATION SYSTEMS

W. Schröder, A. Henze
Aerodynamisches Institut, RWTH Aachen
D-52062 Aachen, Germany

Introduction

The further development of space activities, especially those of commercial nature, will heavily depend on more economic space transportation systems. Currently spaceflight is based primarily on conventional vertically launched transportation systems that are not or only partially reusable. Although these systems represent reliable means of space transportation, the cost of delivering payloads into Earth orbits are still too high. They are in the order of 100 Mio US Dollars and as such are not acceptable for future space activities of larger scale. The European launch market in the period 2006 to 2025 has been assessed to app. 200 launches. In case of a new, more economic launch vehicle with only 10 – 30 % of today's cost per launch the total launch cost within 20 years could be significantly reduced.

Consequently, worldwide efforts aim to develop concepts for completely reusable space transportation systems that are capable of taking off and landing like aeroplanes. Apart from the economic and safety aspects, new airbreathing engines that reduce the atmospheric pollution are also of interest. In 1988 the Federal Ministry of Research and Technology (BMFT) initiated a hypersonic technology program to develop a well-founded technological basis for the next generation of space transportation systems. As a reference concept a two-stage space transportation system, based on an idea of E. Sänger, was used. Since 1990 the German Research Association (DFG) supports three collaborative research centers (SFB) on hypersonic research at the universities in Aachen, Munich and Stuttgart. The emphasis of the work at the University of Aachen is on fundamentals of space plane design. In accordance with the technology program a Sänger-type two-stage vehicle serves as a reference configuration. The lower (ELAC) and the upper stage (EOS), both designed as high lift over drag vehicles, take off as a pickaback system, speed up to a Mach number of $M=7$, and ascend to an altitude of approximately 30 km. Subsequently, a separation maneuver is carried out. Thereafter the lower stage returns to the launch site for horizontal landing and the completely reusable upper stage flies into orbit. After its mission is completed it returns Shuttle-like to earth.

The purpose of the paper is a general presentation of the numerical analysis of the flow field over such a two-stage-to-orbit system. First we succinctly describe the geometry of the lower and upper stage, second the flow field over ELAC and EOS is discussed after the separation has taken place, and subsequently the flow in the vicinity of the single-expansion ramp nozzle is analyzed. Finally we turn to the numerical investigation of the staging maneuver. Since different methods were employed to compute the laminar flow fields we briefly describe the numerical method in the beginning of each section, in which the various flow problems are discussed. Unless otherwise stated the computations were performed for the semispan.

Geometry of the Two-Stage System

The lower stage looks like a slender delta wing with an aspect ratio of 1.1, lateral stabilizers with rudders at the wing tips, trailing edge flaps for pitch and roll control, and an airbreathing engine. The cross section consists of two semi ellipses with equal major and

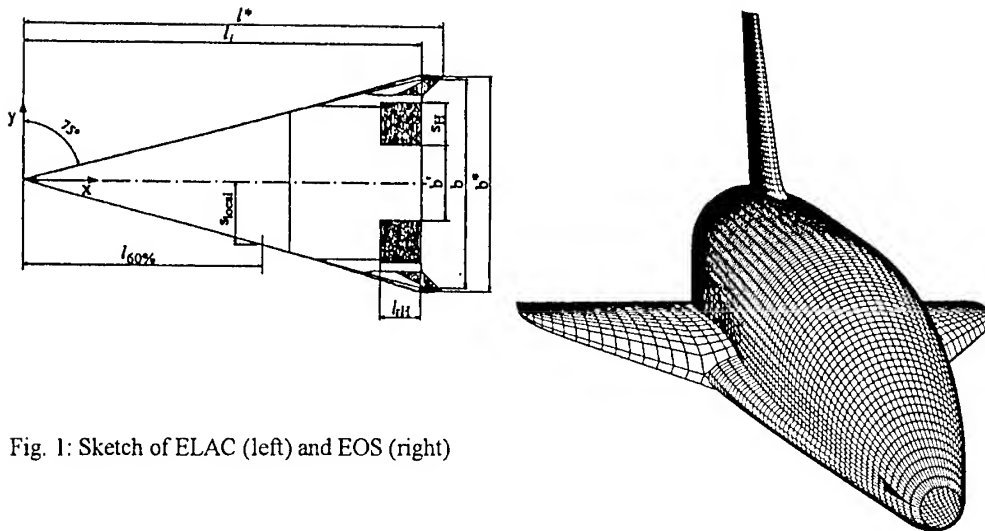


Fig. 1: Sketch of ELAC (left) and EOS (right)

different minor axes. For the upper side the ratio of the semi axes is 1:4, and for the lower side 1:6. The sweep angle is 75 deg. Downstream of the rounded nose the minor semi axes increase linearly to $x/l = 0.63$, where the maximum thickness of ELAC occurs, and then they decrease linearly to the trailing edge. The engine is located on the lower side of the first stage whose forebody serves as compression device. The rear part of ELAC's lower surface is formed as an expansion ramp. The fins have a NACA 0010 profile, and their dehidral angle is 65 deg (Fig. 1).

At first side the upper stage possesses a Shuttle-like shape. Conic sections such as ellipse, circle, parabola etc. are used to define the geometry of EOS. For example, the nose is part of an ellipsoid and the adjoined fuselage consists on the upper side of a half cylinder that is connected with the ellipse of the lower side by vertical surfaces. The front part of the delta wing, that is defined by a parabola in the horizontal plane, extends from $x/l=0.125$ to $x/l=0.50$. Downstream of $x/l=0.52$ the delta wing possesses a straight leading edge with a sweep angle of 65 deg. Using a third-order polynomial the maximum span is reached at $x/l=0.94$. The profile of the wing is given by the NACA 0009 profile. The angle of the fin's leading edge is 45 deg and that of the trailing edge 65 deg. The shape of the fin is defined by the NACA 0010 profile (see Fig. 1). More details on the geometry of ELAC and EOS can be found in [1].

Supersonic Flow past ELAC

Assuming spanwise and no streamwise separation the parabolized Navier — Stokes equations are an efficient means to describe the three-dimensional laminar supersonic flow field over ELAC. The equations were solved using a space-marching technique [2]. A 5-stage Runge — Kutta method was used for the integration in time. The coefficients of the Runge-Kutta scheme were optimized for upwind discretizations and local time steps were applied to speed up the rate of convergence. The inviscid fluxes were computed using the reformulated flux-vector splitting of Schwane et al. [3]. To achieve a higher-order scheme linear extrapolation was used in the normal and spanwise directions whereas in the streamwise direction a second-order extrapolation was necessary. The van Albada limiter [4] was implemented to avoid oscillations in the vicinity of discontinuities. The viscous fluxes were computed using central differences. The initial conditions were based either on conical solutions or on Navier-Stokes solutions for subsonic region downstream of the bow shock. At

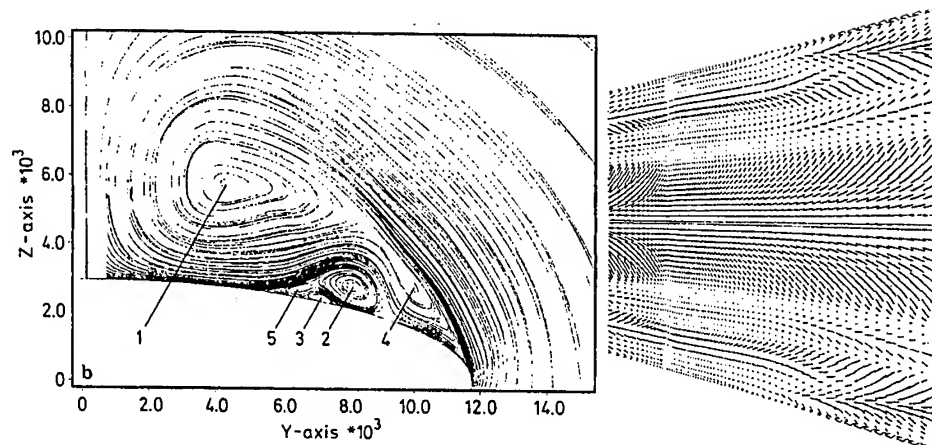


Fig. 2: Cross flow pattern (left) and numerical oil flow pattern of the rear part (right)

the wall the no-slip condition was imposed, the normal pressure gradient was set zero, and the adiabatic condition was assumed.

The flow parameters of the flow field depicted in Fig. 2 are $M_\infty=2$, $Re_\infty=4 \cdot 10^6$, and $\alpha=24$ deg. Primary (1), secondary (2), and tertiary (3) vortices are clearly visible. Additionally, another two vortices (4,5) are evidenced between the secondary vortex and the free shear layer, and between the primary and the tertiary vortex. The numerical oil flow pattern on the leeside of ELAC shows the impact of the main vortices on the flow field. The secondary and tertiary separation, and the primary, secondary, and tertiary reattachment can be observed. This well-organized flow pattern is dramatically perturbed by the lateral stabilizers that generate a new vortex and thereby strongly influence the location of the secondary reattachment line. More findings are discussed in [2, 5].

Supersonic Flow past EOS

The full Navier — Stokes equations were approximately integrated using the aforementioned Runge — Kutta method. A modified formulation of the advective upstream splitting method (AUSM) [6] was applied to discretize the inviscid terms. To obtain a robust higher-order approximation the MUSCL approach for the primitive variables in conjunction with the von Albada limiter [4] was used. The discretization of the viscous terms, and the formulation of the boundary conditions were identical with the ELAC computations.

The flow over EOS was investigated under various supersonic flow conditions. To give an impression of the findings we show the results at a Mach number $M_\infty=2.0$, a Reynolds number $Re_\infty=2 \cdot 10^6$ and at an angle of attack $\alpha=10$ deg. The bow shock interacts neither with the delta wing nor with the fin. The streamlines in Fig. 3 evidence the shift of the stagnation line from the leading to the windward side when α is increased. The flow separates above the delta wing and above the fuselage close to the symmetry plane.

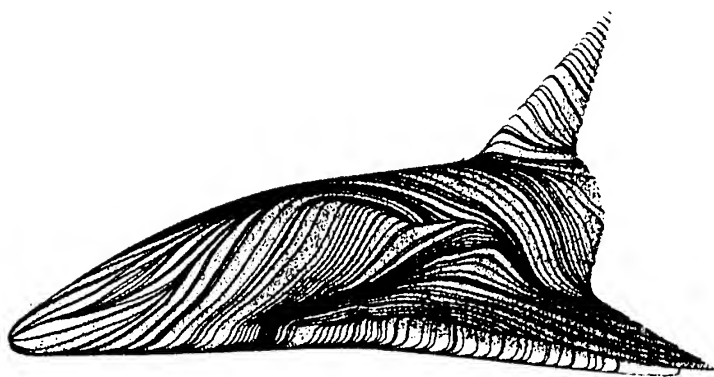


Fig. 3: Wall streamlines on EOS

Thrust Control in Supersonic Flow

To analyze the impact of the external burning of a hydrogen jet on the thrust vector angle the Navier-Stokes equations plus one additional species equation were solved. The reduction to a single species equation was possible since chemical equilibrium and only one diffusion coefficient were assumed for the two-feed (air /H₂) system. Without production or destruction of chemical elements the source terms disappear yielding only one equation for the mixture fraction. The spatial discretization agreed with that of the EOS computations. However, an implicit method based on a line relaxation was used to propagate the solution in time. The boundary conditions of the ELAC computations were completed by a vanishing normal gradient of the mass fractions.

Nose-to-tail computations in the symmetry plane of ELAC were performed at a freestream Mach number $M_\infty = 3.8$, a Reynolds number $Re_\infty = 2.4 \cdot 10^6$, a temperature $T_\infty = 220$ K, and an angle of attack $\alpha = 3.4$ deg. To juxtapose the flow field without and with ejected hydrogen jet the Mach numbers below the engine and in the region of the ramp nozzle are depicted in Fig. 4. The total pressure of the H₂-jet was 5 bar, and the total temperature 1000 K. Due to the supersonic flow it goes without saying that the compression wave emanating from

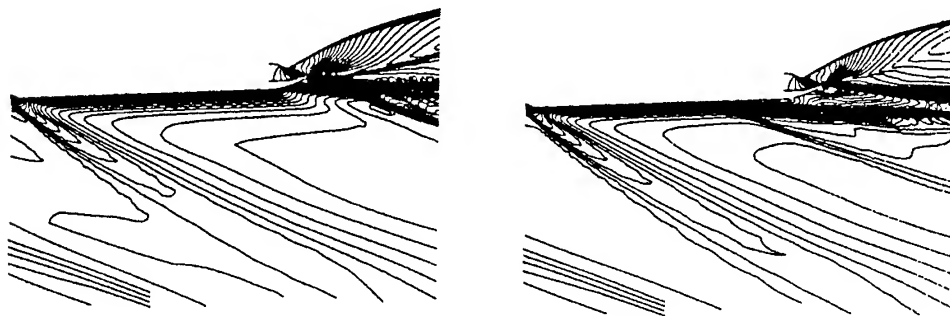


Fig. 4: Mach number contours without (left) and with external burning (right)

the entrance of the engine is not affected by the jet. However, downstream of the injection location the flow pattern changes significantly. Upstream of the jet a shock is generated and downstream of the injection a separation bubble develops. The expansion of the flow at the convex corner is less pronounced compared to the no-jet case. For this reason the shock emerging at the trailing edge is almost aligned with the flow past the lower side of ELAC. The external burning of the jet increases the lift and the thrust vector angle of the aircraft [7].

Stage Separation at Supersonic Flow

The numerical scheme to solve the full Navier — Stokes equations was implicit in time and employed Newton's method to compute the solution at each new time step. To discretize the spatial differentials a cell-centered approach was adopted. The viscous terms were expressed by central differences, in which second derivatives were treated as differences across the cell faces of first-derivative terms. The derivatives of the inviscid fluxes of the explicit part were approximated by a symmetric TVD scheme with a four-argument minmod limiter applied to the difference of the Riemann invariants. The implicit operator was discretized first-order accurate. The resulting block-heptadiagonal system of equations was solved by a symmetric point Gauss — Seidel relaxation scheme with red-black ordering. In the iteration the boundary conditions were treated explicitly. That is, the solution vector had all its components at the same order of accuracy only when the iterations were converged [8]. The body surfaces were assumed adiabatic, the no-slip condition was applied, and a vanishing normal pressure gradient was prescribed. Otherwise freestream conditions and non-reflecting boundary conditions were imposed.

Fig. 5 shows the flow over a simplified Sanger space system. The Mach number was $M_\infty = 6$, the Reynolds number per meter $Re_\infty/m = 1.13 \cdot 10^6$, the temperature $T_\infty = 242$ K, the angle of attack of the lower stage $\alpha = 0$ deg, and the relative angle of attack between upper and lower stage $\Delta\alpha = 2$ deg. The bow shocks of the aircraft and the space vehicle interact in the symmetry plane in the vicinity of the nose of the upper stage. Further downstream this interaction occurs further away from the symmetry plane and from the space vehicle. The flow pattern within the gap is characterized by strong expansions and shock reflections. The first impingement of the compression wave upon the surface of the aircraft occurs in the symmetry plane. Further downstream the shock impingement location moves in the spanwise direction such that its trace within the trough has a c-like shape. The reflected compression, that looks

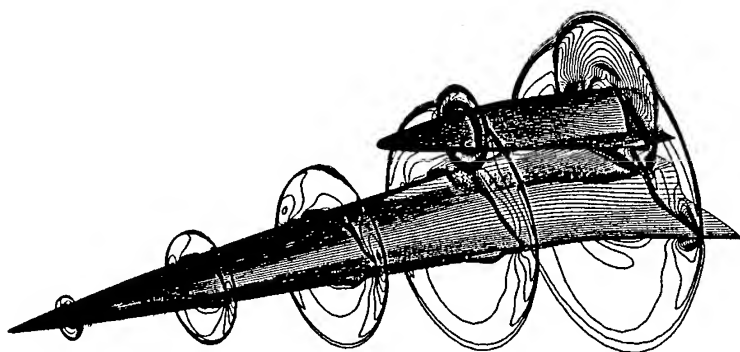


Fig. 5: Density contours at several cross sections

like a bow, interferes with expansion waves and, depending on $\Delta\alpha$, it interacts with the lower side of the space vehicle, the impingement points again form a c-like trace, and an adverse pressure gradient occurs near the tail of the upper stage.

Conclusion

This brief survey and outlook shows the intricacy and the beauty of the flow fields encountered in space design. Future investigations will deal with the transonic flow over ELAC, the reentry phase of EOS, a closer look into the staging maneuver, and the impact of heated surfaces on various flow phenomena.

References

1. Krause E. German university research in hypersonics. Fourth International Aerospace Planes Conference, 1-4 December 1992, Orlando, Florida.
2. Henze A., Houtman E. M., Jacobs M., Vetlitsky V. N. Comparison between experimental and numerical heat flux data for supersonic flow around ELAC 1. *Z.Flugwiss.Weltraumforsch.* 1996, 20, P. 61-71.
3. Schwane R., Hänel D. An implicit flux vector scheme for the computation of viscous hypersonic flows. AIAA Paper 89-0274, 1989.
4. Van Albada G., van Leer B., Roberts R. A comparative study of computational methods in cosmic gas dynamic. *Astron. Astrophysics*, 1982. 108, P.76-84.
5. Krause E., Limberg W., Kharitonov A. M., Brodetsky M. D., Henze A. An experimental investigation of the ELAC 1 configuration at supersonic speeds. *Exp. in Fluids*, 1999, 26, P. 423-436.
6. Liou, M. S., Steffen, C. J. A new flux splitting scheme. *J.Comp.Phys.* 1993, 107, P. 23-39.
7. Kropp M. Reagierende Über- und Hyperschallströmung eines Raumtransportsystems mit Außenverbrennung. PhD Thesis, RWTH Aachen, 1998.
8. Schröder W., Hartmann G. Detailed numerical analysis of hypersonic flows over a two-stage spacecraft. *Comp.Fluid.Dyn.J.* 1993, 4, P.375-404.

ON DEFINITION OF A RECEPTIVITY FACTORS OF SUPERSONIC BOUNDARY LAYER FROM EXPERIMENTAL DATA

N.V. Semionov

Institute of Theoretical and Applied Mechanics SB RAS,
630090, Novosibirsk, Russia

Theoretical studies of leading edge receptivity at supersonic speeds to the external sound waves has been performed by several groups [1-7]. An excitation of the first and the second modes by longitudinal sound waves in the vicinity of a sharp leading edge of flat plate was analyzed by Fedorov & Khohlov [1]. An excitation was caused by sound diffraction at the displacement effect of boundary layer. These results were generalized for any falling angle of an external wave in [2]. Two mechanisms of excitation were defined there. First mechanism was connected with diffraction of the sound waves and the second - with occurrence of sound field sources due to wave interference on the leading edge. From this point of view it may be obtained, that the generation of unstable waves in the boundary layer depends on the inclination angle of the acoustic wave and on the direction from where the sound waves falls, i.e. from above or below. The excitation of the oscillations by longitudinal sound field in boundary layer was investigated by Gaponov [4]. Strong dependence of disturbance intensity inside boundary layer from spatial orientation of the forced sound wave was obtained in this work. In [5] was found, that the ratio of amplitudes of mass flux perturbations inside boundary layer and at its outer edge can reach significant values. Conclusions about existence of critical values of Reynolds number and an angle of orientation of acoustic wave, at which efficiency of excitation is highest, is confirmed. The receptivity of supersonic boundary layer to time periodic Mach waves at $M=2.2$ were examined numerically in [6]. It was obtained that when the Mach waves is coming from below the plate, the Tollmien-Schlichting waves excited at the leading edge are dominant. In the lower side the forced field governs the excited fluctuations. Study of blunted edge receptivity appeared most recently [7]. The excited disturbances in the boundary layer by the free stream forcing waves maintain relatively the same wave number α , corresponding to that of the forcing waves [4, 5, 7]. Note, that theoretical results of [1-7] need experimental verification.

Very few experimental investigations of supersonic receptivity phenomena have been fulfilled up to date. First experiments were made by Kendall [8] who tested the development of natural disturbances in the boundary layer and also measured the correlation factor between fluctuations in the free stream and boundary layer oscillations. The measurements have shown that correlation coefficients increased with increasing Mach number M . Creation of the source of controlled disturbances at supersonic speeds allowed for us to begin experimental study of this problem. Overview of the results earlier obtained by us is presented in [9]. The experimental results of unstable disturbances excitation in a supersonic boundary layer on a plate leading edge by external controlled disturbances are presented in [9-14]. The controlled disturbances fell on the leading edge of the plate from below. In this case generation of disturbances in the boundary layer by the external controlled acoustic field takes place only near the leading edge of the plate. Experimental investigations of the supersonic boundary layer receptivity on sharp leading edge of the plate to the external controlled disturbances were carried out at Mach number $M=2$ in [9-12], at $M=3.5$ in [9, 13] and on blunted leading edge in [14]. In this paper some questions of definition of receptivity factor are considered.

1. Experimental Conditions

The experiments were performed in the supersonic wind tunnel ITAM T-325 with the test section dimensions $600 \times 200 \times 200$ mm at Mach numbers $M=2$. A model consists of two flat plates placed at zero angle to the flow. A generator of periodic disturbances, based on electrical discharge, was mounted on the plate 1 [10-12]. The controlled disturbances of frequency $f=20$ kHz were generated by electric discharge in chamber. This process was accompanied by the sound radiation into the free stream. More precisely this radiation was used as external controlled disturbances. The controllable disturbances fell on the leading edge of the plate 2 from below. In this case generation of disturbances in the boundary layer by the external controlled acoustic field takes place only near the leading edge of the plate 2. The sizes of plate 2 are 280 mm length, 160 mm width at top and 80 mm at basis, 7 mm thickness. The radius of the leading edge bluntness was equal $r < 0.01$ mm. Disturbances were registered by using a hot-wire anemometer. A probe with $5 \mu\text{m}$ tungsten wire was used. The technique of experiment and procedure of data processing was described in [12] in details. Factors of transformation of acoustic disturbances into the eigen fluctuations of the supersonic boundary layer were obtained from the ratio of the amplitude of disturbances generated in the boundary layer to the amplitude of acoustic waves falling onto the leading edge [11, 12].

2. Results

The initial field of controlled fluctuation in free stream was measured in a plane of the plate 2 (plate 2 was established further downstream). At the analysis of the experimental data in [11, 12] simplified physical model of disturbances generation near to the source was used. The artificial disturbances penetrate through the aperture of the plate 1 into the boundary layer. Hence, it is conceivable that vortices with different directions of rotation in yx -plane were formed as the result of deceleration of the flow in the near up and downstream field of discharge. Further downstream, the generated disturbances became the origin of Tollmien-Schlichting (TS) waves in the boundary layer of plate 1. This process was accompanied by radiation of controlled disturbances into the free stream. The acoustic nature of the radiation was obtained in [12]. The radiation was separated on several zones. The first zone corresponded to acoustic waves, radiated by disturbances from the source, propagated upstream in the boundary layer of the plate 1 where phase reduction with increasing of the coordinate x was observed. The second zone corresponded to radiation from the vortex behind of the aperture. The third zone was observed as radiation from TS waves.

For the definition of initial disturbance field in the free stream the measurements of spanwise distribution of amplitude and phase $A(z)$, $\Phi(z)$ of controlled disturbance in streamwise positions where distribution $A(x)$ has maximum in all zones of radiation were carried out. To study the disturbance field in the boundary layer, excited by external controlled fluctuations, the plate 2 was mounted in such way that the leading edge was placed consequently in positions where initial disturbances were studied. The distributions $A(z)$ and $\Phi(z)$ were measured for two values x^* in boundary layer of the plate 2 ($x^*=40$ and 50 mm, where x^* is the distance from the leading edge of the plate 2). Using discrete Fourier-transformation the wave spectra in β for the mentioned above zones were obtained. After that quantitative comparison of levels of initial acoustic disturbances in free stream and fluctuations of the supersonic boundary layer, caused by them was made.

The transformation coefficients of acoustic disturbances into oscillations of the supersonic boundary layer were obtained. It was found, that the excitation of disturbances in the boundary layer by external disturbances at the sharp leading edge grow with Mach number increasing and the transformation coefficients for the oblique waves in the boundary layer are more, than for the plane wave at $\beta \approx 0$. The excitation of disturbances in the boundary layer by external disturbances at the blunted leading edge occurs considerably more heavily than at the sharp leading edge. The experimental data for the sharp leading edge are in the quality correspondence with the theoretical results [4, 5].

The main problem at comparison of theoretical and experimental receptivity factors is caused by indeterminacy in experiments of controlled disturbances α_r -spectra in free stream. Note, that using of the new automatized system of data gathering has allowed to study in more detail the radiation structure in free stream at $M=2$ [14, 15]. Using these data and distributions $A(x)$ and $\Phi(x)$ it is possible to estimation a wave number α_r for each radiation zone. The approximate values of wave number α_r are presented in a table 1. Note, that the radiation have complex structure, but this value of α_r obtained for the disturbances at inclination angle $\chi=0^\circ$.

Table 1

Mach number	First zone	Second zone	Third zone	Theory (TS wave)
M=2	≈ 1.7	≈ 0	≈ 0.68	0.48
M=3.5	≈ 0.38	≈ 0	≈ 0.35	0.35

The dependencies of transformation coefficients $K(\beta)$ over wave number β were obtained in [9-15]. But on this experimental data it is possible also be defined mean receptivity factors K . The total (integrated and dimensionless) controlled pulsation of mass flux was defined by:

$$m_{tot} = \int m_r(\beta) d\beta.$$

Mean transfer factors K were defined using values of m_{tot} by:

$$K = m_b / m_{fs},$$

where m_b and m_{fs} are mass flux pulsations in free stream and in boundary layer, respectively. Values of mean receptivity factors for the sharp leading edge are presented in table 2.

Table 2

	Mach number	First zone	Second zone	Third zone
$x^*=40$ mm	M=2	0.46	0.99	1.88
$x^*=50$ mm	M=2	0.49	1.02	1.47
$x^*=40$ mm	M=3.5	1.357	2.042	2.564
$x^*=50$ mm	M=3.5		2.070	2.573

As was obtained in [6] when radiation fell on the plate leading edge from below, T-S waves is observed to develop at about two wavelengths from the leading edge. Their intensity is proportional to that of T-S wavenumber spectrum contained in the external

disturbances. Note that the radiation has complex structure [15]. The obtained values correspond to disturbances having a maximum long in radiation. The disturbances with others α , also presented at the radiation. Let's compare the data, presented in the tables 1 and 2. It is possible to make a conclusion that the more the wavenumber value in the radiation is closer to the value α , relevant to the T-S waves, the more transformation coefficient K is greater. It is in a good agreement with theoretical results [4-6]

To illustrate what kind of disturbances is excited in the boundary layer by external controlled pulsations, we consider phase velocity of the waves. The data are shown in fig.1 ($M=2.0$) and in fig.2 ($M=3.5$). Here the dash line separates the waves of discrete and continuous spectra. This line corresponds to the critical phase velocity $C^*=1-1/(M\cos\chi)$. Experimental data are compared with linear stability calculations performed by I.I.Maslennikova (solid line). Obtained, that excited in the boundary layer disturbances correspond TS waves, when external disturbances correspond to the radiation from second or third zone. This experimental data are in agreement with numerical results of [6], where obtained that external disturbances from below excite in the boundary layer TS waves. It is shown in fig.1 that for the first zone of radiation excited disturbances correspond to the acoustic oscillation. This experimental data are in contradiction with numerical results of [6]. Probably, this contradiction is caused by that the receptivity is more complex process, than is described by the theory. Apparently, the interaction of external radiation with a shock wave reduces in creation of an additional source of external controlled disturbances. The similar additional disturbance source was detected at interaction of external controlled disturbances with bow shock wave on the plate with blunted leading edge [14]. It has reduced to increasing of receptivity factors $K(\beta)$ in some times in comparison with the case of sharp leading edge [9, 14].

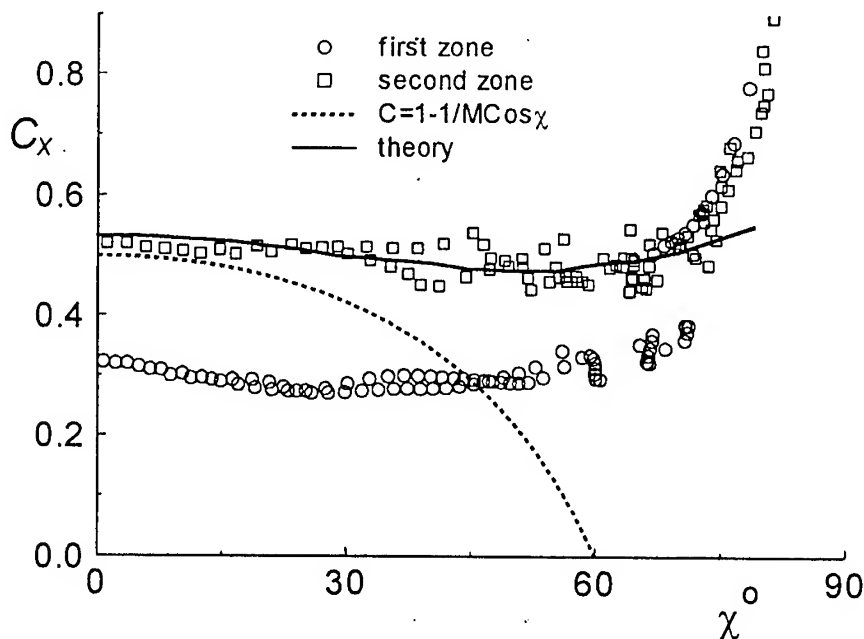


Fig.1. Wave structure of excited in the boundary layer disturbances at $M=2$.

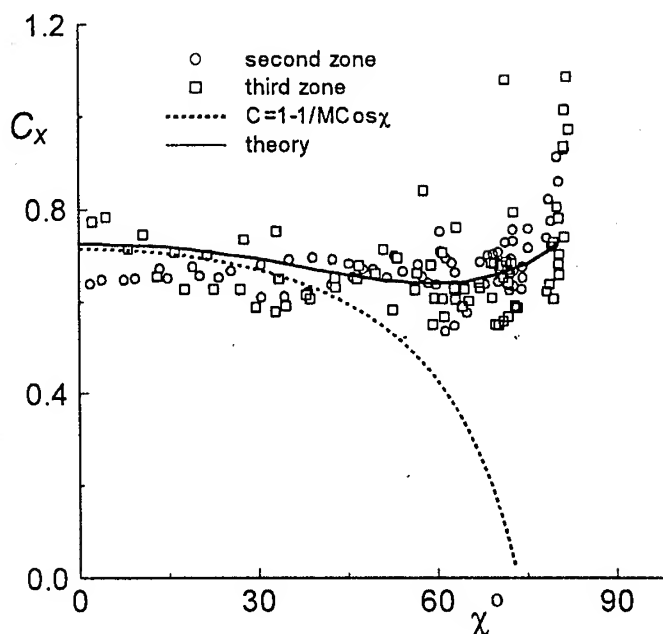


Fig.2. Wave structure of excited in the boundary layer disturbances at $M=3.5$.

The work was supported by the Russian Foundation for Basic Research (grant №99-01-00623).

References

1. Fedorov A.V., Khohlov A.P. Excitation of unstable modes in a supersonic boundary layer by acoustic waves// *Izv. Akad. Sci. USSR. Zh. Mech. Zhid. G.* - 1991. - V.1. - P.67-74 (in Russian).
2. Fedorov A.V., Khohlov A.P. Supersonic boundary layer receptivity to the acoustic disturbances// *Izv. Akad. Sci. USSR. Zh. Mech. Zhid. G.* - 1992. - V.1. - P.40-47 (in Russian).
3. Duck P.W. The response of a laminar boundary layer in supersonic flow to small amplitude progressive waves// *J. Fluid Mech.* - 1990. - V.219. - P.423-448.
4. Gaponov S.A. On the interaction of a supersonic boundary layer with acoustic waves// *J. Thermophysics & Aeromechanics.* - 1995. - V.3. - P.181-189.
5. Gaponov, B.V. Smorodsky. Disturbance excitation in supersonic boundary layer by acoustics// *Proc. International Conference on the Methods of Aerophysical Research.* - Novosibirsk, 1998. - Pt.3. - P.103-108.
6. Sakaue S., Asai M., Nishioka M. On the receptivity process of supersonic laminar boundary layer// *Laminar-Turbulent Transition* (eds. W.Saric, H.Fasel). - Heidelberg: Springer-Verlag, 2000.
7. Zhong X. Direct numerical simulation of hypersonic boundary layer transition over blunt leading edge, part II: receptivity to sound// *AIAA Paper.* - 1997. - N 97-0756.
8. Kendall J.M. Wind tunnel experiments relating to supersonic and hypersonic boundary-layer transition// *AIAA J.* -1975. - V.13. - N 3. - P.290-299.

-
9. Semionov N.V., Kosinov A.D., Maslov A.A. Experiments on supersonic leading edge receptivity to acoustic waves// Proc. Third International Conference on Fluid Mechanics. – Beijing: Beijing Institute of Technology Press, 1998. - P.225-230.
 10. Kosinov A.D., Maslov A.A., Semionov N.V. Methods of controlled disturbances generation for experimental investigation of supersonic boundary layer receptivity// Proc. International Conference on the Methods of Aerophysical Research. - Novosibirsk, 1994. - Pt.1. - P.138-144.
 11. Semionov N.V., Kosinov A.D., Maslov A.A. Experimental investigation of supersonic boundary layer receptivity// Transitional Boundary Layers in Aeronautics (eds. R.A.W.M.Henkes, J.L. van Ingen). - Amsterdam, 1996. - P.413-420.
 12. Kosinov A.D., Maslov A.A., Semionov N.V. Modified method of experimental study of supersonic boundary layer receptivity// Proc. International Conference on the Methods of Aerophysical Research. - Novosibirsk, 1996. - Pt.3. - P.161-166.
 13. Semionov N.V., Kosinov A.D., Maslov A.A. Experimental study of boundary-layer receptivity at $M=3.5$ // Stability and Transition of Boundary-Layer Flows (Collection of Abstracts), EUROMECH Colloquium 359. - Stuttgart, 1997. - N 18.
 14. Semionov N.V., Kosinov A.D., Maslov A.A. An experimental study of instability disturbances excitation by external source in supersonic boundary layer of a blunted plate// Proc. International Conference on the Methods of Aerophysical Research. - Novosibirsk, 1998. - Pt.2. - P.192-197.
 15. Semionov N.V. Structure of external controlled disturbances at studying of supersonic boundary layer receptivity// Proc. V Intern. Conference on Stability and Turbulence of Homogeneous and Heterogeneous Flows. - Novosibirsk: NSAB. - 1998. – Pt.2. - P.213-218.

DEVELOPMENT OF NATURAL DISTURBANCES IN THE SUPERSONIC BOUNDARY LAYER ON THE SWEEPED WING

N.V.Semionov, G.I.Klinkova, A.D.Kosinov, V.Ya.Levchenko
Institute of Theoretical and Applied Mechanics SBAS
630090, Novosibirsk, Russia

Introduction

Laminar-turbulent transition in 3-D boundary layers is heavily investigated. It is caused by practical application. Such boundary layers take place, in particular, in flows on a swept wings of a airplanes. The main theoretical and experimental results on stability of a three-dimensional boundary layer were obtained for subsonic speeds. The role of stationary vortexes and traveling waves of instability of secondary flow was investigated during transition at a different turbulence degree of flow, the periodic changing of traveling waves amplitude in span direction was detected. But there are some qualitative difference between numerical and experimental data. It is connected with the complexity of the problem: along with the well-known Tollmien-Schlichting waves, which development results to the turbulent transition in the 2-D boundary layers, stationary vortexes with axes directed along the outer streamlines and some travelling waves (not T-S waves) in a 3-D case exist. Development of all instability disturbances and their relative role in transition strongly depend on the environmental conditions.

However very few theoretical and experimental investigations of supersonic 3-D boundary layer stability have been fulfilled up to date. Malik et al. [1] chose the Mach 3.5 flow over a swept 76° cylinder as a test problem. The secondary instability analysis yields three unstable modes with the peak growth rate at frequencies about 100 kHz, 1.05 kHz, 970 kHz. The most unstable traveling crossflow disturbance has a peak frequency of about 50 kHz; therefore, the unstable frequency for secondary instability is an order of magnitude higher than that of the travelling crossflow disturbance. This result is in agreement with the findings in low-speed flows. Mielke and Kleiser [2], using the linear stability theory, have shown dominance of crossflow instability. The secondary instability analysis reveals a broad band of secondary unstable modes travelling in streamwise direction. Catafesta et al. [3] using the envelope e^N method for linear stability calculation, obtained the N -factor and compared results with the observed transition locations. Travelling disturbances with $N=13$ provide a good correlation with the transition data over a range of unit Reynolds numbers and angles of attack.

The experimental results on the laminar turbulent transition in 3-D boundary layers for $M>1$ were conducted in [3-5]. It was obtained in [3] for the swept wing, that the surface flow visualization results demonstrate that a clean model surface shows faint evidence of stationary disturbances and a fairly smooth transition front, in which case the travelling crossflow disturbances likely play a major role in the transition. King [4] observed a similar phenomenon on the side surface of a sharp cone at an angle of attack of 4° for $M=3.5$. King [4] concluded that crossflow vortexes are less susceptible to acoustic disturbances than the fundamental mode disturbances or Tollmien-Schlichting waves. Creel et al. [5] registered

steady vortices on the side surface of cylinder model installed at an angle of 45° to the incoming flow using the method of flow visualization for $M=3.5$. The first experimental studies of a 3-D boundary layer instability at supersonic velocities were conducted in [6, 7]. Evolution of natural fluctuation in the boundary layer on a swept wing was studied. It was shown that the character of distribution of the mean and fluctuating characteristics of the boundary layer is similar to the case of subsonic velocities.

The objective of present work is to study evolution of natural disturbances in a boundary layer on a swept wing model for $M=2$ and 3.5 .

Experiments and methods

The experiments were conducted in supersonic wind tunnel T-325 of the Institute of Theoretical and Applied Mechanics SB RAS with the test section sizes $200 \times 200 \times 600$ mm³ for Mach numbers 2 and 3.5 and range of Reynolds numbers from $Re=589$ up to $Re=1048$. In experiments the model of a swept wing with lens profile and 40° swept angle of the leading edge was used. The model was mounted horizontally under zero angle of attack in the test section of the wind tunnel. The model was 260 mm length, 200 mm width, 20 mm maximum thickness. The disturbances in a flow were registered by constant temperature hot-wire anemometer with a 1:10 ratio of the bridge arms and frequency range up to 500 kHz. The probes were made from a tungsten wire with 5 microns in diameter. For measurement of the mass flux fluctuations (m'), the overheat ratio of wire probes was established to be 0.8. The measurements were carried out over coordinate z' that was parallel to the leading edge, in the maximum of fluctuations across the boundary layer at $y=\text{const}$, where y is coordinate normal to the model surface. The scheme of the model is shown in fig. 1. For convenience the value of coordinate $z \neq 0$ was put to coincided with $z=0$. The fluctuating and mean flow characteristics were measured by automated data acquisition system [6]. The fluctuations signal from the hot-wire anemometer was measured by a 12-bit 750 kHz A/D converter, and the output mean voltage of CTA was measured by digital voltmeter. Length of oscillograms was 16384 points. The frequency spectra of disturbances were determined by the discrete Fourier transform.

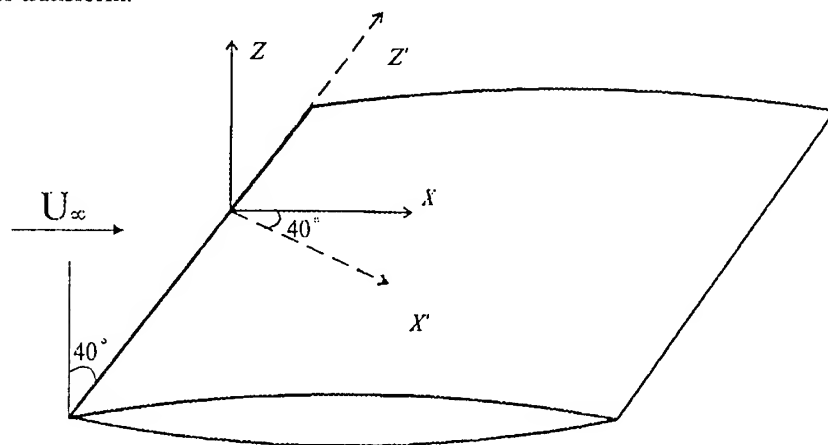


Fig. 1. The model of the swept wing.

Results of measurements

The data presented on disturbances development for the Mach number 3.5 were obtained in two series of experiments. In the first series the measurements were conducted from transversal coordinate $z' = -22$ mm to $z' = -6$ mm, and in the second— from $z' = -10$ mm to $z' = 3$ mm. The results of measurements of the root mean square fluctuations $\langle m \rangle$ and mass flux ρu inside a boundary layer at Mach number 3.5 are shown in fig.2. The value ρu was calculated from a ratio [8]:

$$\rho \cdot u = \left(\frac{E^2}{N} \right)^{\frac{1}{0.56}}, \quad N=3.05$$

and was normalized on the free stream value of ρu_∞ . The measurements were performed in the section $x=50$ mm from the leading edge in a spanwise direction. The periodicity of fluctuation velocity was detected. It may be resulted from appropriate periodic change of mean velocity in the spanwise direction at $y=\text{const}$. Scattering of amplitudes and periodicity scales takes place due to an accident of external turbulent disturbances. The similar picture was observed in experiments at $M=2$ [6], and also in subsonic experiments performed in "natural" conditions [9]. In addition to the smallscale periodicity of the mean mass flux, the highscale disturbances component is observed. This highscale disturbances have an unknown nature, that is probably resulted from the 3-D roughness on the back side of the model.

Disturbances development in the boundary layer was studied at $M=3.5$. The measurements were performed at one position and unit Reynolds number was changed from $Re_1 = 8 \cdot 10^6 \text{ m}^{-1}$ up to $Re_1 = 15.7 \cdot 10^6 \text{ m}^{-1}$. Pulsations oscillograms were fixed simultaneously. Dependence of pulsation amplitude over the Reynolds number is shown in fig.3 for two positions ($x=50$ mm, $z'=-6$ mm) and ($x=70$ mm, $z' \approx 3.1$ mm), where x is a distance from the leading edge and $Re = (Re_1 \cdot x)^{\frac{1}{2}}$. The disturbances growth is observed for all the measurements range except last point in the distribution for second position. We can say that transition took the place at $x=70$ mm on the basis of the distribution and pulsation oscillograms [10]. The measurements were started when the single "picks" appeared in the oscillogram, that

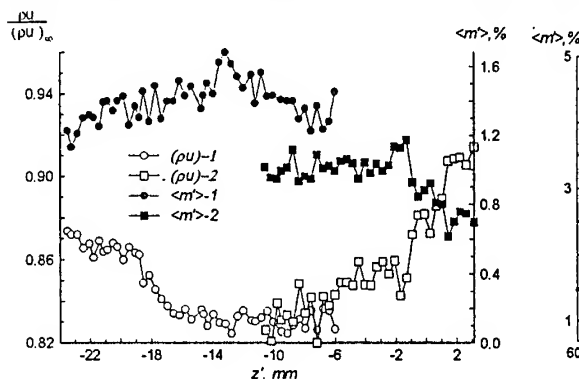


Fig.2. The root mean square fluctuations $\langle m \rangle$ and mass flux ρu inside a boundary layer in a spanwise direction z' , $x=50$ mm, $M=3.5$, $Re \sim 687$. 1-first series, 2-second series of measurements.

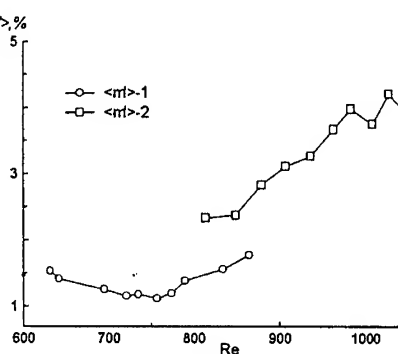


Fig.3. The root mean square fluctuations $\langle m \rangle$ depending on Reynolds number, 1-first series at $x=50$ mm, $z' \approx -6$ mm. 2-second series at $x=70$ mm, $z' \approx 3.1$ mm

corresponded to the beginning of transition to a turbulence. Pulsations passed the maximum and the form of oscillograms was as for a turbulent case at the last points in fig.3. The experimental study of natural disturbances development at $M=2$ was made in [6] and the similar results were obtained.

An additional information about disturbances development can be obtained from disturbances spectra. Measurements of the frequency spectra were performed at $M=2$ and $M=3.5$. The spectra of disturbances obtained in experiments on the swept wing at $M=2$ are shown in fig.4. The comparison with the spectra on the flat plate [11] shows, that the disturbances growth in three-dimensional boundary layer occurs much faster, than in the flat plate case. Note that the range of amplifying disturbances in swept wing boundary layer is similar to the flat plat case. The degree of disturbances growth on the swept wing is greater by an order.

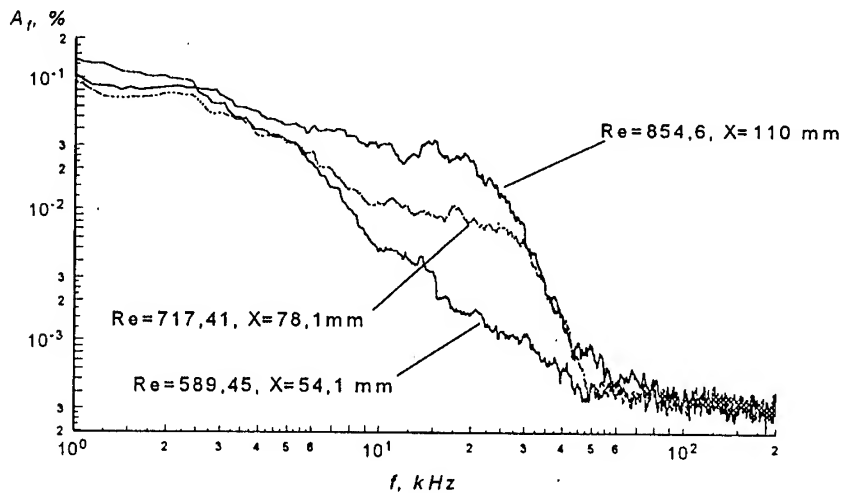


Fig.4. Disturbances spectra on the swept wing at $M=2$

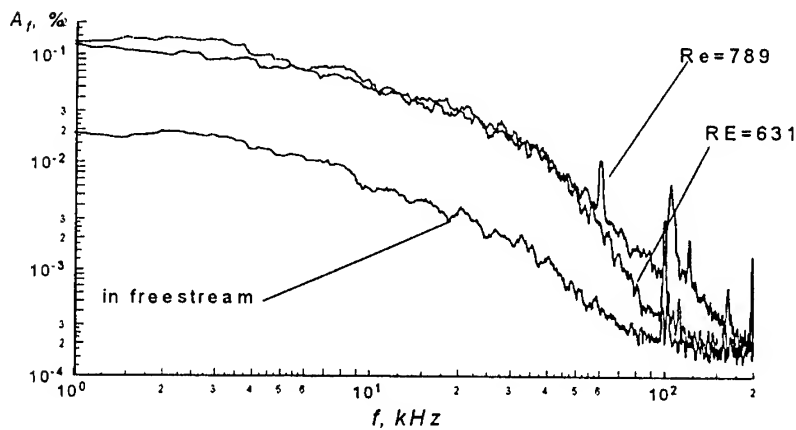


Fig.5. Disturbances spectra on the swept wing at $M=3.5$, first series of measurements, $x=50$ mm, $z'=-6$ mm

Evolution of spectra obtained at $M=3.5$ on a swept wing is shown in fig.5,6. It is obtained, that the frequency band of the amplifying disturbances is extended and fills practically all range of the measured frequencies with increasing of Mach number. The spectra become turbulent at lesser Reynolds number for the case $M=3.5$, than for the case $M=2$. Besides, the high-frequency modes for frequencies about 60 kHz, 115 kHz and 250 kHz were detected. It is shown that this high-frequency disturbances exist in the free stream spectra and boundary layer only amplify them. These frequencies correlate with calculated ones obtained in [1].

The spectra also were obtained in transversal measurements (see fig.2). The spectra corresponded to the points of middle and right side of the low-frequency stationary structure are shown in fig.7. Note that disturbances amplification was observed only at right side of the stationary structure. Spectra corresponded to the points of middle and left side of the stationary structure are the same.

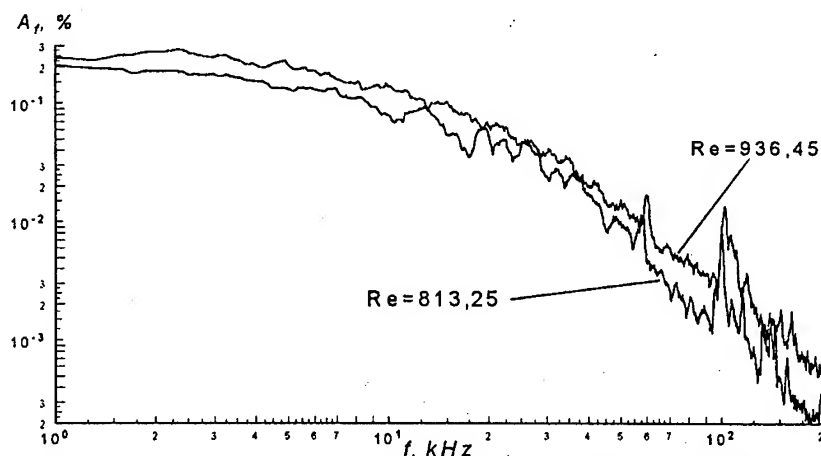


Fig.6. Disturbances spectra on the swept wing at $M=3.5$, second series of measurements.. $x=70$ mm, $z'=3.1$ mm

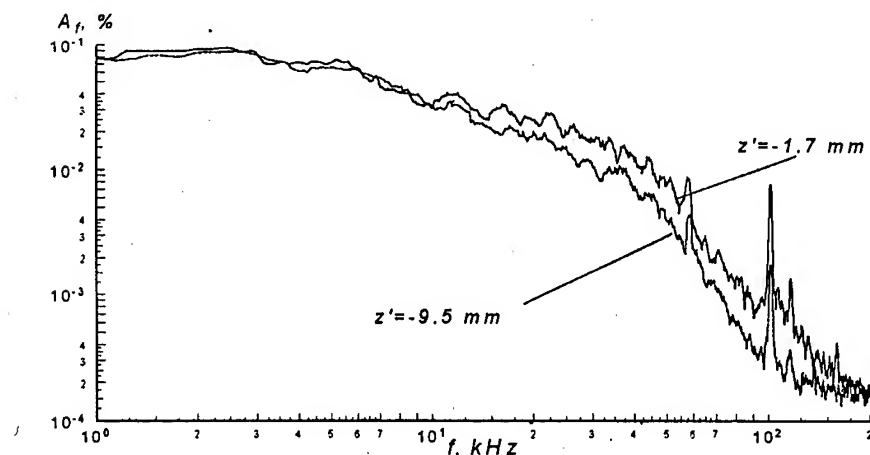


Fig.7. Disturbances spectra on the swept wing at $M=3.5$, $Re \sim 687$

Conclusion

The development of the natural disturbances in supersonic boundary layer on the swept wing model was studied. It was obtained at $M=2$, that the disturbances growth in three-dimensional boundary layer occurs much faster, than in the flat plate case. The increase of the Mach number up to 3.5 extends frequency band of amplifying disturbances and leads to earlier turbulent transition.

The work was supported by the Russian Foundation for Basic Research (grant №99-01-00558).

References

1. Malik M.R., Li F., Chang C.-L. Nonlinear crossflow disturbances and secondary instabilities in swept-wing boundary layers// Nonlinear instability and transition in three-dimensional boundary layers.- Dordrecht etc.: Kluwer Academic Publishers. - 1996. - P.257-266.
2. Mielke Ch., Kleiser L. Investigation of transition to turbulence in a 3D supersonic boundary layer// Laminar-Turbulent Transition (eds. W.Saric, H.Fasel). - Heidelberg: Springer-Verlag. - 2000.
3. Cattafesta L.N. III, Iyer V., Masad J.A., King R.A., Dagenhart J.R. Three-dimensional boundary-layer transition on a swept wing at Mach 3.5// AIAA J. - 1995. - V.33. - N11. - P.2032-2037.
4. Creel T.R.Jr., Beckwith I.E., Chen F.J. Transition on swept leading edge at Mach 3.5// J. Aircraft. - 1987. - V.24. - № 10. - P.710-717.
5. King R.A. Three-dimensional boundary-layer transition on a cone at Mach 3.5// J.Exp. Fluids. - 1992. - №13. - P.305-314.
6. Ermolaev Yu.G., Kosinov A.D., Levchenko V.Ya., and Semionov N.V. Instability of a three-dimensional supersonic boundary layer// Prikl. Mekh. Tekh. Fis., 1995. - 36, № 6. - P.50-54.
7. Levchenko V.Ya., Kosinov A.D., Semionov N.V., Ermolaev Yu.G. Instability of a three-dimensional supersonic boundary layer// Nonlinear instability and transition in three-dimensional boundary layers. Dordrecht etc.: Kluwer Acad. Publ. - 1996. - P.361-368.
8. Kosinov A.D., Semionov N.V., Yermolaev Yu.G. Disturbances in test section of T-325 supersonic wind tunnel. - Novosibirsk. - 1999. - 24 p. (Preprint/ SB RAS. Institute of Theoretical and Applied Mechanics, No 6-99).
9. Müller B. Experimental study of the travelling waves in a three-dimensional boundary layer// Laminar-turbulent Transition. Berlin: Springer-Verl. - 1990. - P.489-498.
10. Stainbeck P.C., Wagner R.D. Comparison of Wind Tunnel Transition and Freestream Disturbances Measurements // AIAA J. - 1975. - V.13. - N.3. - P.266-269.
11. Ermolaev Yu.G., Kosinov A.D., Semionov N.V. Experimental study of the natural laminar-turbulent transition in supersonic boundary layer// Proc. V Int. Conf. On stability and turbulence of homogeneous and heterogeneous flows. Novosibirsk. - 1998. - Part II. - P.184-190.(in Russian).

COMPUTATION OF CROSSING-SHOCK-WAVE/BOUNDARY-LAYER INTERACTIONS WITH REALIZABLE TWO-EQUATION TURBULENCE MODELS

Frédéric Thivet,* Doyle D. Knight† and Alexander A. Zheltovodov‡

*ONERA, Centre de Toulouse, 31055 Toulouse, France

†Rutgers University, Piscataway, New Jersey 08854

‡Institute of Theoretical and Applied Mechanics, Novosibirsk 630090, Russia

1 INTRODUCTION

Understanding and modeling Crossing-Shock-Wave/Turbulent-Boundary-Layer Interactions (SWBLI) is of critical importance for predicting the performance of supersonic inlets. The complex three-dimensional interactions occurring in such devices can be experimentally reproduced in very simple geometrical configurations, named the Single Sharp Fin Plate (SSFP) and the Double Sharp Fin Plate (DSFP), the latter being either symmetrical or asymmetrical: one or two fins with sharp leading edge are mounted on a flat plate with different combinations of deflection angles. In the last decade, a large number of experimental and computational studies have been carried out on those configurations. The features of these flows were thoroughly reviewed by Settles in 1993¹ for SSFP and by Zheltovodov *et al.*^{2,3} in 1998 for DSFP. From a computational and modeling point of view, reviews by Knight and Degrez^{4,5} emphasize the fact that, in strong SWBLI, the skin-friction and heat-transfer coefficients are systematically overestimated by numerical simulations based on either algebraic, two-equation or full Reynolds-Stress Equation turbulence models. The error can be as large as 150 % in strong SWBLI. In this paper are reported the results of an investigation about the impact on SWBLI of the three corrections which are now usual for compressible boundary layers, namely the realizability, the turbulent length scale limit and the compressibility corrections.

2 EXPERIMENTAL AND NUMERICAL DATA

2.1 CONFIGURATIONS

The configurations correspond to the experiments conducted at ITAM by Zheltovodov *et al.*^{2,3} The model is a plate with two symmetrical or asymmetrical mounted fins with sharp leading edges, located at a distance of 210 mm from the plate leading edge. Chamfered fins of length 192 mm and height 100 mm are employed, separated by a minimum distance of 32 mm in the constant-width section (the throat). The Throat Middle Line (TML) forms the x axis. Three of the six experimental configurations have been computed: the $7^\circ \times 7^\circ$ (weak interaction), $15^\circ \times 15^\circ$ (strong symmetrical interaction) and $7^\circ \times 11^\circ$ (strong asymmetrical interaction) configurations; due to space constraints, only the $7^\circ \times 11^\circ$ case is used to illustrate the present analysis. The flow Mach number is 3.92 (± 0.03), the total pressure 1485 ($-5/+13$) kPa, the total temperature 260 (± 4) K, yielding a Reynolds number of 88 ($-3/+5$) $10^6/\text{m}$. The measurements consist in surface flow visualization by an oil film technique, pressures and adiabatic temperatures at the bottom wall in adiabatic conditions, heat fluxes and temperatures at the heated bottom wall, so that heat transfer coefficients can be derived with a ± 15 % accuracy.

2.2 NUMERICAL SOLVER

The computations are performed with the code *GASPex*,⁶ which solves the Reynolds-Averaged three-dimensional compressible time dependent Navier-Stokes equations (RANS). The convective fluxes are computed to third-order accuracy using the Roe scheme and a MUSCL reconstruction method with the Min-Mod limiter. The viscous terms are evaluated by second order central differencing. The steady solution is obtained by applying a time-marching method based on the hybrid AF/Relaxation algorithm. Special attention is paid to obtain mesh-converged results so that the conclusions drawn from the comparison to measurements are reliable. The inflow conditions are the mean experimental values (§2.1) supplemented with a computed boundary layer matching the measured 0.128 mm momentum thickness, 14 mm upstream of the fin leading edges. Turbulence is represented using the Wilcox' $k-\omega$ model,⁷ implemented with the smooth wall boundary condition.⁸ The choice of the model in the two-equation class is not very important at this point, since it has been demonstrated earlier that the SWBLI heat-flux issue is common to all two-equation turbulence models that have been tested in these cases so far.⁵

2.3 RESULTS WITH THE STANDARD MODEL

The results obtained with the standard $k-\omega$ model (W1) are primarily discussed in Ref. 9. Our conclusion is that these results are at least comparable to and, at some points, slightly better than given by $k-\epsilon$ models and shown in the literature.⁵ Fig. 1 provides a view of the skin-friction lines and heat-transfer coefficient on the bottom wall, compared to the topological scheme derived from the oil-flow visualization obtained in the experiments.³ The high heat fluxes are associated with the attachment of the Entrainment Flow to the bottom wall along the divergence line R_2 . The Entrainment Flow comes from an essentially inviscid part of the incoming flow, impinges the bottom wall along R_2 and then spreads out from this line.⁹

3 REALIZABILITY CORRECTIONS

The basis of this analysis is the mathematical concept of realizability.^{10,11} the variances of the fluctuating velocity components must be positive and the cross-correlations bounded by the Schwartz inequality. The goal here is to determine if the SWBLI heat-flux issue is related to some violation of the realizability constraints. Indeed, the solutions obtained with the Wilcox's $k-\omega$ model (and very likely any usual two-equation turbulence model) are not realizable in the outer part of the boundary layer and above.⁹ The size of the unrealizable zones increases with the interaction strength and they are clearly related to the largest values of the dimensionless strain rate invariant in the flow, mainly across the shocks.

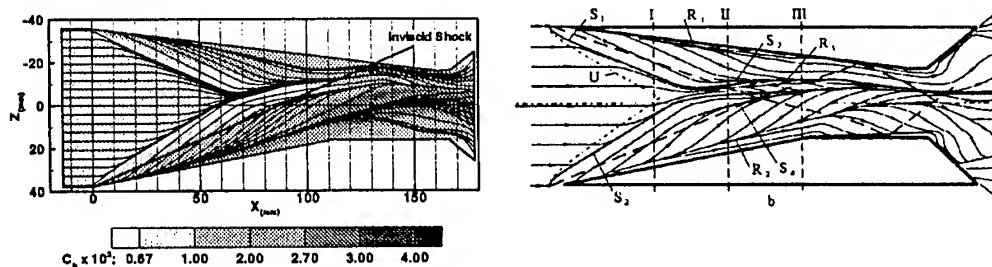


Figure 1: $7^\circ \times 11^\circ$ configuration · Left: Skin-friction lines and heat-transfer coefficient on the bottom wall (W1) · Right: Topological scheme derived from the oil-flow visualization

A recent review of the realizability corrections to two-equation turbulence models¹² recalls that the idea is to enforce the realizability constraints by limiting the value of the constant in the definition of the eddy viscosity $\mu_t = \alpha_\nu c_\mu \rho k / \omega$ (where $\omega = \epsilon / k$) with:

$$\alpha_\nu = \min \{1, \bar{\alpha}_\nu\} \quad \text{and} \quad \frac{1}{\bar{\alpha}_\nu c_\mu} = A_o + A_s (s^2 + A_r \varpi^2)^{1/2}, \quad (1)$$

where c_μ is the usual constant 0.09, s is the dimensionless mean strain rate S/ω with $S^2 = 2S_{ij}S_{ji} - \frac{2}{3}S_{kk}^2$, and ϖ is the dimensionless vorticity invariant $\sqrt{2\Omega_{ij}\Omega_{ij}}/\omega$ where:

$$S_{ij} = \frac{1}{2} \left(\frac{\partial U_i}{\partial x_j} + \frac{\partial U_j}{\partial x_i} \right) \quad \text{and} \quad \Omega_{ij} = \frac{1}{2} \left(\frac{\partial U_i}{\partial x_j} - \frac{\partial U_j}{\partial x_i} \right). \quad (2)$$

Moore and Moore¹² propose a set of coefficients derived from an Algebraic Reynolds Stress Model ($A_o = 2.85$, $A_s = 1.77$) and assuming, in a first approximation, that the strain rate and rotation have symmetrical effects ($A_r = 1$). They show that, in the case of flows near leading edges where the inviscid strain field is very large ($s = 100 - 400$), the modification ends up with a much better prediction of the Turbulent Kinetic Energy (TKE) level. This kind of correction has also been shown to contribute significantly to cure the stagnation point anomaly as encountered in supersonic impinging jets. For instance, Durbin propose a correction of the form (1) with $A_o = A_r = 0$ and $1/A_s = c/\sqrt{3}$, where $c \leq 1$ ensures the realizability,¹³ while $c = 1/2$ is needed to get good results in the jet impingement problem.¹⁴ Note that with this last value, the Durbin proposal $1/A_s = 0.29$ leads to values of α_ν smaller than the Moore and Moore expression and is virtually identical to the one by Coakley^{15,16} or by Menter¹⁷ in the SST model, where $1/A_s = \sqrt{c_\mu} = 0.3$.

One question remains about what should be done to the transport equation for the dissipation. A first group of researchers^{12,16} keeps the formal equation in its usual form, while the second group^{9,13} recommends maintaining the incompressible part of the production term at its unmodified level by dividing it by α_ν :

$$P_\omega = \alpha \frac{\omega}{k} \left(\frac{P_{ki}}{\alpha_\nu} + P_{kc} \right) \quad \text{with} \quad P_{ki} = \mu_t S^2 \quad \text{and} \quad P_{kc} = -\frac{2}{3} \rho k S_{kk}, \quad (3)$$

where P_{ki} and P_{kc} are the incompressible and compressible part of the TKE production. In order to determine the impact of the realizability enforcement on SWBLI, four models are tested: the so-called Wilcox-Moore (WM) and Wilcox-Durbin (WD) models, where the realizability factor (1) is used to compute the eddy viscosity with the Moore and Moore¹² and Durbin¹³ (with $c = 1/2$) coefficients respectively, and the WM⁺ and WD⁺ models where, in addition, the production term in the specific dissipation equation is modified according to Eq. (3). The tests are mainly conducted on the intermediate grid of the $7^\circ \times 11^\circ$ configuration ($96 \times 40 \times 80$, first cell height of 0.8 wall unit in the incoming boundary layer), which is sufficient to obtain the pressure within 5 % of the mesh-converged solution and the skin-friction and heat-transfer coefficients within 10 % of the mesh-converged values on the bottom wall.⁹ The WI and WM⁺ models are also run on the fine grid ($96 \times 80 \times 160$, first cell height between 0.35-1.5 wall units) to confirm that the trends shown below are correctly caught on the intermediate grid. This is illustrated by Fig. 2, which compares the TKE profiles and skin-friction coefficient along the cross-section $x = 46$ mm as obtained with the Wilcox's model on the intermediate and fine grids. The transverse reduced location z_r is 0 at the fin and 1 at the location of the inviscid shock generated by the 11° fin as indicated in Fig. 1.

In the logarithmic region of the flat plate boundary layer, the TKE level given by the $k - \omega$ model is⁸ $\rho k = \Gamma \rho_w U_\tau^2$, with $\Gamma = 1/\sqrt{c_\mu} - M_\tau^2$, and $M_\tau = U_\tau/a_w$. In the $7^\circ \times 11^\circ$ configuration, Γ is below its “incompressible” limit by less than 0.4 % on the whole bottom plate. Then, the quantity $\sqrt{c_\mu} \rho k / (\rho_w U_\tau^2)$, plotted in Fig. 2, should be 1 in the logarithmic layer. This is verified indeed by the first profile, which is taken at the TML ($z = 0$) in the cross-section $x = 46$ mm and corresponds to the flat plate boundary layer (Fig. 1). The other profiles exceed this limit, more than twofold near the location of the inviscid shock. The corresponding fourfold increase in the skin-friction coefficient is significantly shifted in space with regard to the TKE increase.

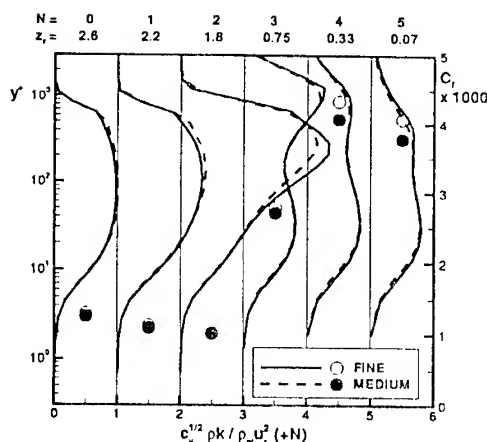


Figure 2: TKE profiles (lines) and skin-friction coefficient (big dots) in the cross-section $x = 46$ mm

The effect of the different realizability corrections on the pressure is negligible everywhere but in the very region where the primary shocks intersect (Fig. 3). In this region, the pressure plateau observed in the experiment, and not in the WI solution, appears with the corrections, but at an underestimated level. As expected, the WM solution is closer to the reference solution (WI) than WD. It has also to be noticed that the WM⁺ solution is almost not distinguishable from the WD solution (only the first one is reported on Figs. 3, 4); it means that exactly the same effect is achieved either by reducing directly μ_t via α_ν , or by increasing indirectly the TKE dissipation via the modification of the dissipation production term. The WD⁺ model is the one leading to the most important modification of the solution. The heat-transfer coefficient is decreased by 20 % along the TML (Fig. 3) and around the attachment line R_2 (Fig. 4). At best (WD⁺), the computed heat-transfer coefficient exceeds the experimental value by about 100 %, which represents even so a significative improvement with regards to the initial overprediction of 150 % (WI).

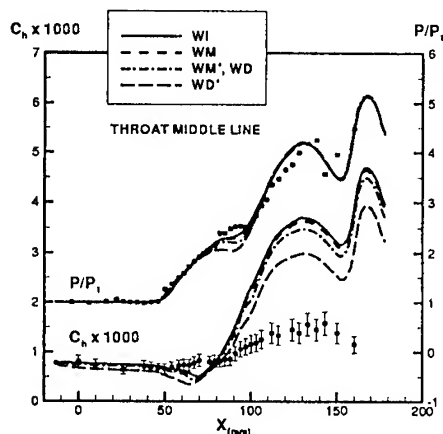


Figure 3: Pressure and heat-transfer coefficient along the TML

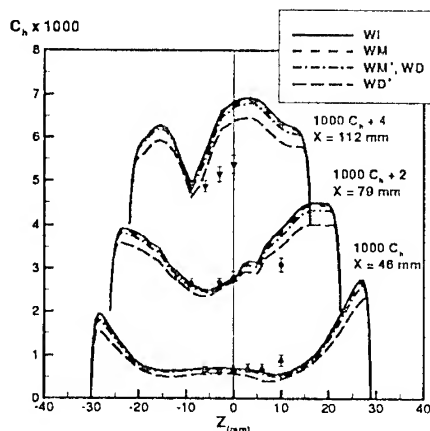


Figure 4: Heat-transfer coefficient in three cross-sections

In order to determine if it is possible to obtain further improvement with a correction based on the strain rate/vorticity invariant, Fig. 5 is drawn. It represents the profiles of s ($\simeq \varpi$ in the boundary layer) in cross-section $x = 46$ mm at the same stations as in Fig. 2. Since the value of s in the logarithmic layer of an incompressible boundary layer is $1/\sqrt{c_\mu}$, the quantity $\sqrt{c_\mu}s$ is plotted. Fig. 5 demonstrates that the large increase of ρk through the shock is not linked to a large increase of s . The largest values in the flow are around 10, which is at least one order of magnitude less than in the cases in which the realizability corrections have been shown to be beneficial.^{12,13}

4 THE TURBULENT LENGTH SCALE LIMIT

In hypersonic flows, Coakley and co-workers¹⁶ propose to limit the turbulent length scale ℓ to its value in the logarithmic part of an incompressible boundary layer:

$$\mu_t = \rho c_\mu k^{1/2} \ell \quad \text{with} \quad \ell = \min \left\{ \ell_{\log}, \frac{k^{1/2}}{\omega} \right\} \quad \text{and} \quad \ell_{\log} = \frac{\kappa}{c_\mu^{3/4}} d, \quad (4)$$

where d is the distance to the wall and κ is the von Kármán constant ($\kappa/c_\mu^{3/4} = 2.5$); then the value of the dissipation term in the TKE transport equation is recomputed according to $\omega = k^{1/2}/\ell$. In order to determine whether or not this correction could help in the SWBLI cases considered here, the ratio of the computed turbulent length scale ℓ to the logarithmic expression ℓ_{\log} is examined in the solutions obtained with the different models. Fig. 6 shows that this limit is violated indeed in the WI solution, but only slightly and in the upper part of the logarithmic layer. The realizability corrections, and more exactly the modification of the production of ω , give solutions where this limit is strictly respected almost everywhere. It can be concluded that the turbulent length scale limit would not be of great help in this case and that a similar effect may be achieved in a more natural way by avoiding the reduction of the production of dissipation.

5 THE COMPRESSIBILITY CORRECTIONS

The primary manifestation of compressible turbulence is the appearance of the dilatation dissipation in the TKE and dissipation equations. This occurs at high turbulent Mach

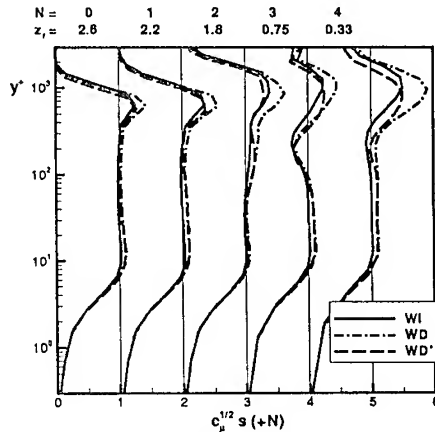


Figure 5: Profiles of the dimensionless strain rate invariant s at $x = 46$ mm

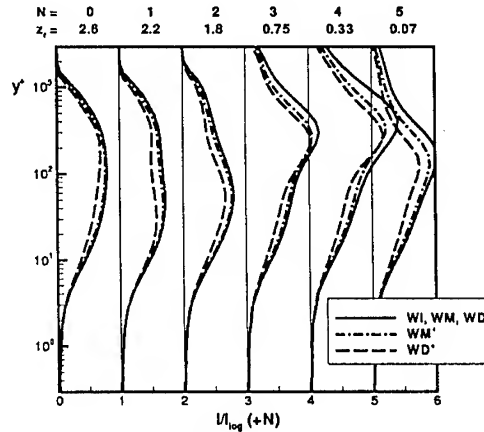


Figure 6: Profiles of the ratio of the turbulent length scale ℓ to its value in the logarithmic layer at $x = 46$ mm

numbers $M_t = \sqrt{2k}/a$, where a is the local speed of sound. The most popular corrections are due to Sarkar *et al.*¹⁸ and Zeman,¹⁹ and have been primarily derived for compressible mixing layers. However, they have been shown to lead to undesirably lowered skin-friction coefficients in turbulent boundary layers.^{16,20} In this case, the so-called compressibility corrections are not active at least when the turbulent Mach number is under the threshold $M_{to} = 0.25$.⁸ The maximum turbulent Mach number in the WI solution is 0.3. For this value, the increase of the dissipation term is only 4 % according to the Wilcox compressibility correction.⁸ The WM⁺, WD and WD⁺ solutions give values of M_t below the compressible threshold all over the computational domain. It can be concluded that this kind of correction would be of no help in the considered case.

6 CONCLUSIONS

The SWBLI heat-flux prediction has been shown to be sensitive to the realizability corrections, even though the largest value of the dimensionless strain invariant is at least one order of magnitude smaller than in the cases for which the corrections have been designed. The modification consisting in decreasing the TKE production but not the dissipation production has been shown to lead to effects similar to what could be achieved with the turbulent length scale limit. The compressibility effects, due to a large turbulent Mach number, have been shown to be negligible in the considered case. At best, the overprediction of the heat-transfer coefficient is reduced from 150 % to 100 %. The investigation is now oriented towards the effect of the density increase across the shocks on the eddy viscosity.

ACKNOWLEDGMENTS

The work was done while the first author was Visiting Research Scholar at Rutgers University, as recipient of a research fellowship awarded by DGA/DSP (Délégation Générale pour l'Armement/Direction des Systèmes de Forces et de la Prospective). The computational resources were provided by the National Science Foundation at NCSA, University of Urbana-Champaign, Illinois (grant no. MSS990001N). The third author was also supported by the Russian Foundation of Basic Research (grant no. 97-01-00885) and EOARD (contract no. F61708-97-W0136).

REFERENCES

- ¹Settles, G. S., "Swept Shock/Boundary-Layer Interactions – Scaling Laws, Flowfield Structure, and Experimental Methods," in AGARD R 792, AGARD FDP / VKI Special Course on *Shock-Wave/Boundary-Layer Interactions in Supersonic and Hypersonic Flows*, AGARD, Rhode-Saint-Genèse, Belgium, Aug. 1993, pp. 1-1-1-40.
- ²Zhelotovodov, A. A., Maksimov, A. I., and Shevchenko, A. M., "Topology of Three-Dimensional Separation Under the Conditions of Symmetric Interaction of Crossing Shocks and Expansion Waves with Turbulent Boundary Layer," *Therm. AeroMech.*, Vol. 5, No. 3, 1998, pp. 293-312.
- ³Zhelotovodov, A. A., Maksimov, A. I., Shevchenko, A. M., and Knight, D. D., "Topology of Three-Dimensional Separation Under the Conditions of Asymmetrical Interaction of Crossing Shocks and Expansion Waves with Turbulent Boundary Layer," *Therm. AeroMech.*, Vol. 5, No. 4, 1998, pp. 483-503.
- ⁴Knight, D. D., "Numerical Simulation of 3-D Shock Wave Turbulent Boundary Layer Interactions," in AGARD R 792, AGARD FDP / VKI Special Course on *Shock-Wave/*

Boundary-Layer Interactions in Supersonic and Hypersonic Flows, AGARD, Rhode-Saint-Genèse, Belgium, Aug. 1993, pp. 3-1-3-32.

⁵Knight, D. D. and Degrez, G., "Shock Wave Boundary Layer Interactions in High Mach Number Flows – A Critical Survey of Current CFD Prediction Capabilities," in AGARD AR 319, Vol. II, *Hypersonic Experimental and Computational Capability, Improvement and Validation*, AGARD, Neuilly Sur Seine, France, Dec. 1998.

⁶AeroSoft, Inc., "GASP, General Aerodynamic Simulation Program Version 3," User's manual, May 1996.

⁷Wilcox, D. C., "Reassessment of the Scale-Determining Equation for Advanced Turbulence Models," *AIAA J.*, Vol. 26, No. 11, Nov. 1988, pp. 1299-1310, also AIAA Paper 84-0176.

⁸Wilcox, D. C., *Turbulence Modeling for CFD*, 2nd ed., DCW Industries, Inc., La Cañada, California, July 1998.

⁹Thivet, F., Knight, D. D., Zheltovodov, A. A., and Maksimov, A. I. "Some Insights in Turbulence Modeling for Crossing-Shock-Wave/Boundary-Layer Interactions," AIAA Paper 2000-0131, AIAA 38th Aerospace Sciences Meeting & Exhibit, Reno, Nevada, 10-13 Jan. 2000.

¹⁰Schumann, U., "Realisability of Reynolds Stress Turbulence Models," *Phys. Fluids*, Vol. 20, 1977, pp. 721-725.

¹¹Lumley, J. L., "Computational Modeling of Turbulent Flows," *Advances in Applied Mechanics*, Vol. 18, Academic Press, 1978, pp. 123-176.

¹²Moore, J. G. and Moore, J. "Realizability in Two-Equation Turbulence Models," AIAA Paper 99-3779, AIAA 30th Fluid Dynamics Conference, Norfolk, Virginia, 28 June - 1 July 1999.

¹³Durbin, P. A., "On the $k - \epsilon$ Stagnation Point Anomaly," *Int. J. Heat & Fluid Flow*, Vol. 17, No. 1, 1996, pp. 89-90.

¹⁴Behnia, M., Parneix, S., and Durbin, P. A., "Simulation of Jet Impingement Heat Transfer with the $k - \epsilon - v^2$ Model," *Annual Research Briefs 1996*, Center for Turbulence Research, California, Dec. 1996, pp. 3-16, also <http://www-fpc.stanford.edu/CTR/ResBriefs96/behnia.ps.Z>.

¹⁵Coakley, T. J. "Turbulence Modeling Methods for the Compressible Navier-Stokes Equations," AIAA Paper 83-1693, Danvers, Massachusetts, June 1983.

¹⁶Coakley, T. J. and Huang, P. G. "Turbulence Modeling for High Speed Flows," AIAA Paper 92-0436, AIAA 30th Aerospace Sciences Meeting & Exhibit, Reno, Nevada, 6-9 Jan. 1992.

¹⁷Menter, F. R., "Two-Equation Eddy-Viscosity Turbulence Models for Engineering Applications," *AIAA J.*, Vol. 32, No. 8, Aug. 1994, pp. 1598-1605, also AIAA Paper 93-2906.

¹⁸Sarkar, S., Erlebacher, G., Y, Hussaini, M. Y., and Kreiss, H. O., "The Analysis and Modelling of Dilatational Terms in Compressible Turbulence," *J. Fluid Mech.*, Vol. 227, June 1991, pp. 473-493.

¹⁹Zeman, O., "Dilatation Dissipation: The Concept and Application in Modeling Compressible Mixing Layers," *Phys. Fluids*, Vol. 2, No. 2, Feb. 1990, pp. 178-188.

²⁰Aupoix, B., Desmet, E., and Viala, S., "Hypersonic Turbulent Boundary Layer Modelling," Symposium on Transitionnal and Turbulent Compressible Flows, ASME Fluids Engineering Conference, Washington, D. C., 20-23 June 1993.

USE OF MODERN OPTICAL METHODS FOR SUPERSONIC DIFFUSION FLAME STRUCTURE RESEARCH

S.S. Vorontsov, V.A. Zabaikin, P.K. Tretyakov, V.V. Pickalov,
A.V. Postnov, N.V. Chugunova, C. Bruno*, M. Filippi*

Institute of Theoretical and Applied Mechanics SB RAS,
630090, Novosibirsk, Russia
*Roma University, Italy

The results of investigation of the H_2 plume structure in the case of diffusion combustion in a cocurrent supersonic high-temperature off-design air jet are presented. The complexity of the object of investigation (high temperature, velocity up to 1500 m/s, significant density changes in shocks, interaction of the combustion process with the gasdynamical structure) does not allow one to apply conventional contact measurement methods and makes urgent the use of only contactless (first of all, optical) methods of research.

The process of combustion H_2 under conditions of a complicated wave flow structure is affected by both dynamics of the process of mixing, and correlation of combustion intensity with the gasdynamical structure. Defined by radiation of excited OH-radicals, the intensity of combustion can be increased by several times in zones behind shock waves in comparison with zones of reduced pressure (I_{OH} drop). Changes in temperature and pressure along the off-design jet (in "barrels") [1] have a significant effect on the overall time of the delays of ignition and hydrogen combustion and also makes difficult the direct application of calculation methods. For example, in Fig. 1 the change of hydrogen-air mixture temperature depending on time is shown, where the beginning of the temperature increase corresponds to the moment of ignition. It is visible that for the stream parameters ($T = 2000$ K; $\alpha = 3.3$, $T_{H_2} = 300$ K), corresponding to experiment conditions, the time of ignition delay corresponds to the beginning of combustion only in the 4-th barrel of an air jet – 280–290 mm from the nozzle exit (1, *a*), and the ignition really observed in the first barrel (30–120 mm) in calculations can be reached only by increasing the air stream temperature up to 2500 K (Fig. 1, *b*), which at the total temperature of air 2000 K is achieved only in shock waves.

Thus, the flow structure significantly influences the process of combustion. However, in a hot air stream (T up to 2000 K) the application of many optical methods is difficult. The matter is that on the boundary of an air jet there arises a high-power turbulent thermal mixing layer, which, more and more increasing in length, highly distorts the path of optical rays on small-scale structures on the jet periphery and makes impossible registration of its inner structure. For example (photo No. 9 in work [2]), it is possible to see that even at heating up to 700 K, already from second barrel the jet structure at shadow methods of research becomes indistinguishable. Application of interferometrical methods of research is more perspective, but since it also allows one to see only the jet boundary with an indistinguishable inner structure, the work in this direction will be continued.

As a result, the most informative method of research has turned out to be the registration of hydrogen flame radiations by the optical-mechanical scanner at wavelengths connected with ultraviolet radiation of OH-radicals immediately from zones of heat release [3, 4]. However, in earlier measurements, radiation was registered only along the axes of a flame with integration in

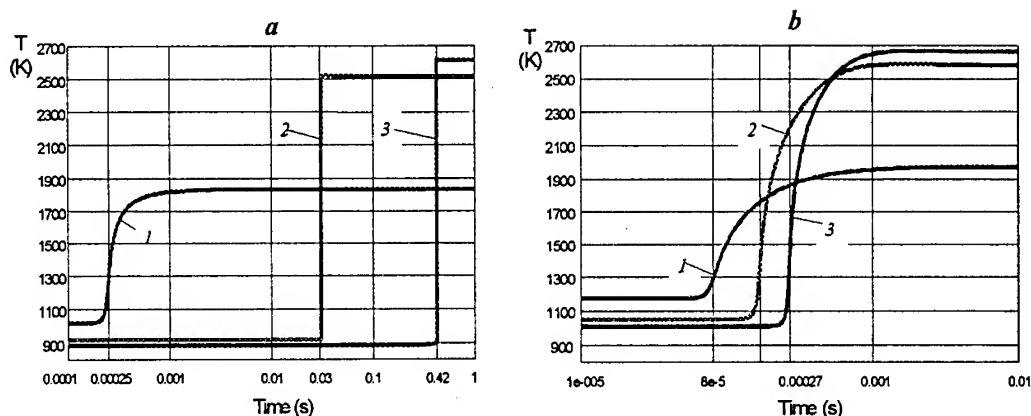


Fig. 1. A change of hydrogen-air mixture temperature at various α .
Initial parameters: $T_{H_2} = 300$ K; $P = 0.6359$; $T_0 = 2000$ K (a); 2500 K (b).
 $\alpha = 3.3$ (1); 1.25 (2); 1 (3).

a plane perpendicular to the stream direction (Fig. 2, a), which limited possibilities of studies of the flame structure in the radial direction. In the given work we applied a new optical-mechanical scanner EFA-360UF, which allows registration of two-dimensional images.

Intrinsic radiation of a flame in the ultra-violet range at the wavelengths of 260–380 nm was registered, which corresponds to radiation of an excited OH-molecule. The optical-mechanical scanner EFA-360UF was connected to the ISA bus of a personal computer IBM PC through the input register. The input parameters are as follows: transformation capacity 8 digit, image dimension 128×128 points, time of frame scanning 0.3 s, interval between the frames 2 s, and time of line scanning 3 ms. The information was preliminarily processed using the TVGS 2.0 program package [5] and standard graphical tools of the WINDOWS system. To exclude random noise, the raw information was smoothed by an adapted median filter.

The experiments were conducted on a facility described in [3], with an arc heater of air. The Mach number at the contoured nozzle exit was 2.2, and the nozzle diameter was 50 mm. The total temperature was equal to 2000 K in all the regimes, the total pressure was $6.8 \cdot 10^5$ N/m², which corresponds to the jet pressure ratio $n = 0.64$. At such parameters in the air jet, a series of periodic structures (barrels) will be formed of length approximately up to 90 mm, which in a cold stream are well visible at shadow visualization. The area of observation (from the nozzle up to an exhaust device) was 450–500 mm. The hydrogen was injected along the axis of the air nozzle through an injector with a diameter of 10 mm. The parameters of the air stream and, accordingly, the initial gasdynamical flow structure in all experiments remained constant, the hydrogen exhaustion velocity did not exceed the speed of sound, the flow rate of hydrogen G_{H_2} varied within the limits from 1.5 up to 5 g/s ($\alpha = 3.3$ –11.5).

In Fig. 2, the outcomes of different modes of registration, analysis and information representations for one combustion regime of hydrogen are shown. Figure 2, a shows integrated on a line-of-sight and in transversal direction distribution of radiation intensity along the plume, and (d) – the same one-dimensional distribution, but taken only along the axial line (1), and also on the plume edge (2). Except for the basic maxima, a great number of peaks of low intensity are observed, whose frequency of appearance is higher than the frequency of "barrel-type" structures of a supersonic off-design jet. These local maxima were also observed in previous experiments, however, because of the lack of data, the radial distribution of combustion

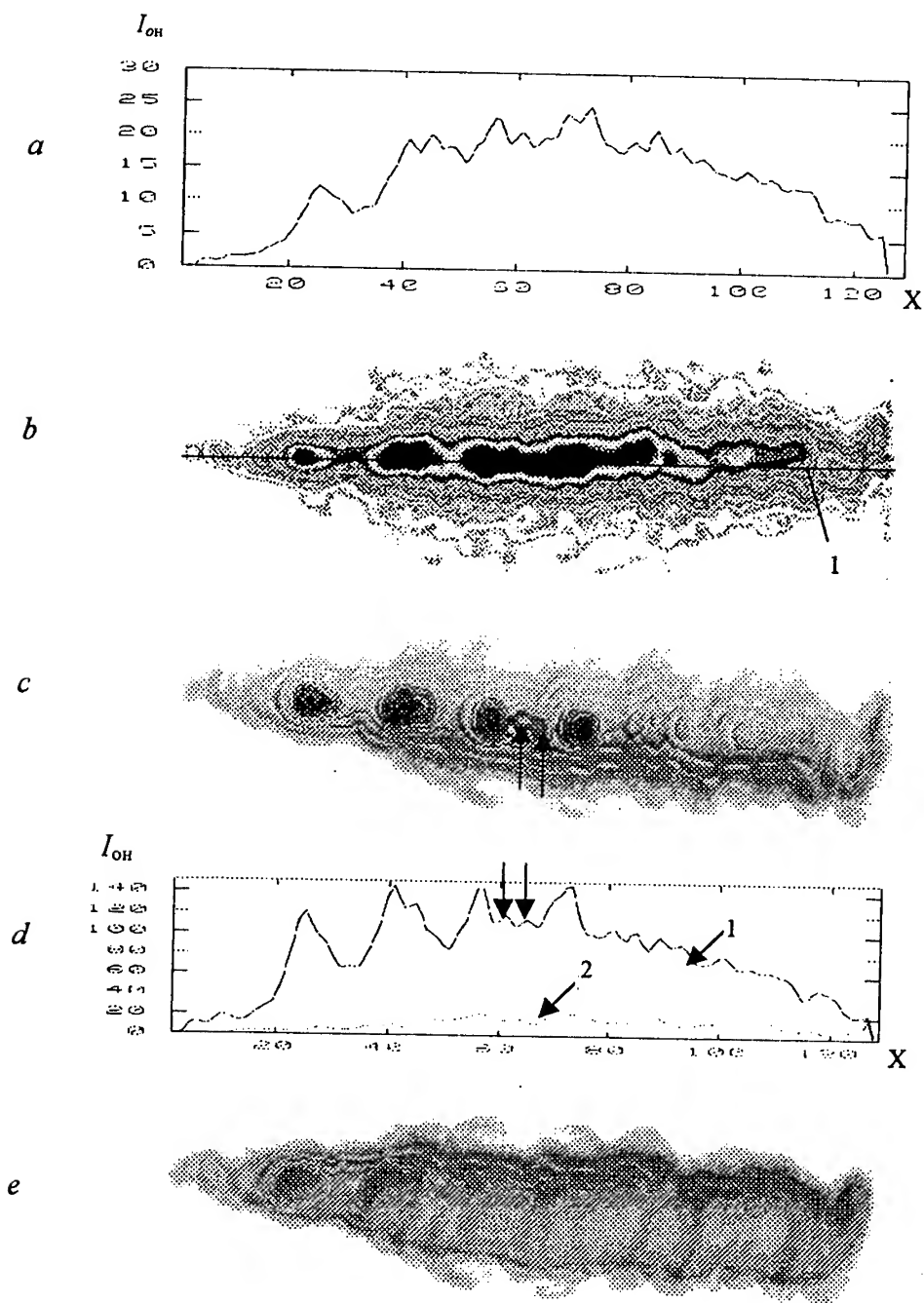


Fig. 2. Intensity of flame radiation distributions and results of three-dimensional reconstruction for the regime $G_H = 4.6$ g/s.
a – integrated distribution of intensity by length; *b* – two-dimensional distribution of intensity;
c – reconstruction of inner plume areas; *d* – axial (1) and peripheral (2) distributions of radiation intensity;
e – reconstruction of exterior plume areas.

intensity could not be correlated with any parts of gasdynamical flow structure, or qualified as hardware distortions.

Panoramic registration of radiation of the whole plume (Fig. 2, *b*) carried out with the help of the optical-mechanical scanner EFA-360UF has immediately shown the complexity of the spatial structure of the combustion zone. To obtain more detailed information, a three-dimensional image of the plume was reconstructed. The experimental data were interpreted as a set of integral radiations, and local distributions were assumed to be axisymmetric in each vertical cross section of a three-dimensional emission object. Abel's transformation formed the basis of the algorithm of three-dimensional reconstruction [5]. It is known that this transformation can be used only for axisymmetric input projections. To obtain symmetric projections from the data registered, a special method of symmetrization was developed. Two approaches are used in this method for choosing the point relative to which the right and left wings of the distribution are averaged. The first approach includes symmetrization of a projection relative to its maximum. In the second approach, the point of symmetrization coincided with the center of mass of the middle part of the wings of the one-dimensional projection. One of these approaches is chosen automatically by minimizing the norm of deviation of the right wing of the projection from the left one; the reliability of reconstruction was tested by model numerical experiments.

The results of three-dimensional tomographic reconstruction are represented in Fig. 2, *c* and *e*, in (*c*) the inner part is distinguished, and in (*e*) the exterior zones of plume radiation are better shown. The dark areas correspond to higher radiation intensity. In Fig. 2, *c* the areas of the increased luminosity (connected with intensity of heat release) are well seen, localized immediately after shocks of the gasdynamical structure of a supersonic off-design air jet, which confirms the correlation of combustions zones with the gasdynamical structure. Comparison of figures (*c*) and (*d*) shows that in the central part of the stream there can also arise additional small zones of increased heat release (shown by arrows), whose nature can be understood by increasing the resolving capability of the measuring instrument.

Of the utmost interest, however, is an exterior part of the plume. In figures, ring-shaped zones of combustion are visible, whose emergence is apparently related to the above noted local maxima in the distribution of intensity along the plume.

It should be noted that the technology of obtaining raw information did not allow us to register the temporal evolution of peripheral combustion zones; therefore, we cannot draw any conclusions about the reason of their origin and stability of existence. They can be steady or unsteady structures, and also helical vortex structures, which yield annular combustion zones after axisymmetric processing.

Thus, panoramic registration by an optical-mechanical scanner with subsequent special analysis of a signal is up to the present one of the most informative methods of obtaining data about three-dimensional distribution of combustion intensities under conditions of a high-speed and high-temperature jet. The performed measurements show that the structure of the H_2 plume under conditions of its interaction with a periodic wave structure of a supersonic off-design jet is multiplane and also includes basic steady zones of heat release along the flame axes and a great number of local zones of heat release of low intensity both inside the plume and on its edges.

Panoramic registration and three-dimensional processing of the plume images fully confirmed the interrelation between the gas-dynamic structure and the combustion intensity and for the first time revealed the presence of structures of the type of annular (vortex) or, possibly, helical combustion zones at the periphery of the main plume.

This work was partially supported by the Russian Foundation for Basic Research (grant No. 00-01-00834).

REFERENCES

1. Zabaikin V.A., Lazarev A.M. Experimental studies of combustion of a gaseous fuel under different conditions of fuel injection into a supersonic high-enthalpy air flow // Modeling of Gas-dynamic and Energy Processes: Proc. All-Union Conf. Novosibirsk: Inst. Theor. Appl. Mech., Sib. Branch, Acad. of Sci. of the USSR, 1985. P.260–264.
2. Zabaikin V.A., Tretyakov P.K. Geometry of an initial part of supersonic non-calculable jets which are flowing out in open area // Gasdynamics of Flows in Nozzles and Diffusers. Novosibirsk: Inst. Theor. Appl. Mech., Sib. Branch, Acad. of Sci. of the USSR, 1982. P.156–163.
3. Zabaikin V.A., Lazarev A.M. Influence of different injection methods on hydrogen combustion in supersonic air flow // Izvestiya Sibirskogo Otdeleniya AN SSSR, Ser. Tech. Nauk. 1986. Iss. 1, No. 4. P.44–49.
4. Bayev V.K., Vorontsov S.S., Soloukhin R.I., Tretyakov P.K. Application of an opticommechanical system in a complex with a computer for studying flame structures // Structure of Gas-Phase Flames: Proc. All-Union Workshop on the Structure of Gas-Phase Flames. Pt 2. Inst. Theor. Appl. Mech., Sib. Branch, Acad. of Sci. of the USSR. 1984. P.112–122.
5. Borisov A.V., Vorontsov S.S., Zheltovodov A.A., et al. Development of experimental and numerical methods of studying supersonic separated flows: Preprint No. 9–93. Novosibirsk: Inst. Theor. Appl. Mech., Sib. Branch, Russ. Acad. of Sci. 1993.
6. Pickalov V.V., Melnikova T.S. Tomography of plasma. Low-temperature plasma. Iss. 13. Novosibirsk: Nauka, 1995 (in Russian).

METHOD OF INVESTIGATION OF IONIZATION RELAXATION IN SHOCK WAVES

V.I. Yakovlev and P.V. Grigor'ev

Institute of Theoretical and Applied Mechanics SB RAS,
630090, Novosibirsk, Russia

Introduction. The available notions of ionization relaxation in monatomic gases behind shock wave (SW) front have some aspects that do not allow one to consider these notions as fully completed. On one hand, a collisional-radiative model of ionization kinetics has been founded [1, 2]. It is noted, however, that the calculated values of the relaxation zone in inert gases, in contrast to molecular ones, are greater than the measured values [2]. On the other hand, anomalous effects or instability of shock waves are observed in certain ranges of Mach numbers [3 – 15]. Consideration of an enlarged number of elementary reactions with participation of metastable particles and molecular ions [6] and of the change in the relative role of collisional and radiative processes [7] associates instability effects with the formation of additional channels of energy exchange between the particles, which alter the temperature of atoms and electrons. However, there is no direct evidence of manifestation of these mechanisms (apart from the fact of instability itself). In [16, 17], the authors report an elevated temperature of electrons (close to the gas temperature behind the SW front) in the electron-cascade front of argon. In [18] the activation energy determined at the initial stage of the cascade turned out to be much lower than the expected excitation energy, which could not be explained within the framework of the generally accepted model. Thus, the available model does not offer an exhaustive description of ionization kinetics behind the shock wave front in monatomic gases. New, more effective approaches and research methods are needed.

A new method for studying ionization relaxation of monatomic gases is proposed in this paper. This method allows one to reveal manifestation of additional mechanisms of energy exchange of the particles within an electron-cascade front of relaxation zone. In contrast to the commonly accepted comparison between the measured and calculated (with some parameters varied) distributions of electron density (degree of ionization), the method proposed is based on comparison between the measurement results and the calculation of another parameter – the electron density production rate in the flow region where the collisional electron-atomic mechanism of ionization (electron-cascade front) dominates. The measured values are found from the registered dynamics of electron density $n_e(t)$, and the calculated data are obtained from the known temperature dependence of the forward and reverse rate coefficients with determination of the electron temperature from the energy equation at a local steady-state approximation. The measured results for the electron (and atomic) density are also used in the calculation. Experiments are performed under conditions close to the boundary of the region wherein instability is manifested so that the changes in the flow parameters were still regular to obtain rather exact quantitative characteristics of the process under study.

Numerical relations. In a shock-fitted coordinate system, the flow of a partially ionized gas in the shock tube channel is described by one-dimensional equations and their integrals:

$$d\rho u/dx = 0, \quad \rho u = \rho_1 u_1, \quad (1)$$

$$(1/\rho)dP/dx + udu/dx = 0, \quad P + \rho u^2 = P_1 + \rho_1 u_1^2, \quad (2)$$

$$d\varepsilon/dx + Pd(1/\rho)/dx = 0, \quad h + u^2/2 = h_1 + u_1^2/2 \quad (3)$$

where the subscript "1" refers to the parameters ahead of the front, u and ρ are the flow velocity and density, $h = \varepsilon + P/\rho$ is the specific enthalpy of the gas, $P = (\rho k/m_a)(T_a + \alpha T_e)$ is the pressure, $\varepsilon = (1,5k/m_a)(T_a + \alpha T_e) + \alpha E_I/m_a + w$ is the specific internal energy, the subscripts a and e refer to the atomic and electron components, E_I is the ionization energy, k is the Boltzmann constant, m_a is the atomic mass, and α is the degree of ionization equal to $\alpha = n_e/(n_e + n_a)$, where n is the density of electrons or atoms. Shock waves of moderate strength are considered in the present study (the SW Mach number M is less than 12 – 15 depending on the gas), the degree of ionization behind SW fronts is less than several percent, and the specific energy w of excited atoms and ions can be ignored. In the range of interest here the radiative processes are considered to be insignificant, because they may be substantial at the initial stage only at a very high M and low gas densities [2].

The integrals of system (1)-(3) yield relations for unknown values of the parameters [20]:

$$u/u_1 = \rho_1/\rho = (1/8)\{5 + 3/M^2 - [9(1 - 1/M^2) + 96\alpha E_I/5M^2 k T_1]^{1/2}\} \equiv f(\alpha, M), \quad (4)$$

$$(T_a + \alpha T_e)/T_1 = 1 - 2\alpha E_I/5k T_1 + (1/3)M^2[1 - (\rho_1/\rho)^2] \equiv T_{a0}. \quad (5)$$

Taking into account that $n_e = \alpha\rho/m_a$, we obtain the required equation for the dynamics of the degree of ionization: $\alpha(t)\rho_1/m_a n_e(t) = f(\alpha, M)$. Thus, to determine the distribution of α , u , and ρ , and also approximate values (with accuracy to $\alpha T_e/T_1$) of the pressure P and T_a behind SW front, it is sufficient to measure the electron density distribution $n_e(t)$ only.

The equations of ionization kinetics and electron energy balance (using the terminology and notation of [2]) have the form:

$$dn_e u/dx = S_e \quad (6)$$

$$d(1,5n_e u k T_e)/dx + n_e k T_e du/dx = Q_{el} - Q_{in} \quad (7)$$

where S_e is the source of electrons (net electron density production rate caused by the totality of elementary electron-catalyzed processes), Q_{in} is the rate of electron's energy losses by inelastic collisions (excitation, ionization), and Q_{el} is the heating rate by elastic collisions with atoms (a) and ions (i).

To determine S_e in a gas flow behind SW front, Eq. (6) is transformed to $S_e = dn_e u/u_1 dt = (u/u_1)dn_e/dt + (n_e/u_1)du/dt$, where du/dt is found from the system of differential equations (1) – (3) and their integrals. It is taken into account that, since the flow velocity behind the front u (in the SW front-fitted coordinate system) differs from the propagation velocity of the shock wave front u_1 , the registration time interval dt is related to the intrinsic interval dt_c of residence of the particle in the flow by the relation $u_1 dt = u dt_c = dx$. As a result, we obtain the necessary formula relating the value of the experimentally measured rate of variation of the electron density dn_e/dt behind the SW front and the magnitude of the source of electrons:

$$S_e = \{1 - 2\alpha E_I/[5k T_1 + m_a u_1^2 (1 - 4(u/u_1)^2)]\} (u/u_1) (dn_e/dt). \quad (8)$$

For moderate shock waves it is possible to ignore the convective term $n_e k T_e du/dx$ (except for the region near the shock wave front) and to take into account the local steady-state approximation to atomic excited states and electron temperature [2, 20], i.e., $dT_e/dx = 0$. In this case, the temperature T_e is determined by the local energy balance [2]:

$$1,5k T_e S_e = Q_{el} - Q_{in}. \quad (9)$$

In the region of electron-cascade ionization (where the role of inter-atomic collisions is insignificant), the energy losses are presented as $Q_{in} = E_i S_e + Q_R + Q_{st}$ (ionization, radiation, and excitation). The heating rate is determined by the expression [19, 20]:

$$Q_{ei} = 1,5k(T_a - T_e)n_e 2(m_e/m_a)(v_{ea} + v_{ei}) = 3n_e(m_e/m_a)(v_{ea} + v_{ei})k(T_a - T_e)$$

where the frequencies of elastic ea - and ei - collisions are determined by the corresponding cross sections σ : $v_{ea} = n_a(8\pi m_e/kT_e)^{1/2}\sigma_a(T_e)$, $v_{ei} = n_i(8\pi m_e/kT_e)^{1/2} \times \sigma_i(T_e)$. The temperature dependence $\sigma_a(T_e)$ is known (e.g., [3, 4]), and $v_{ei}(T_e) = n_i(4/3)(2\pi)^{1/2}(m_e/kT_e)^{3/2}(e^2/m_e)^2 \ln A$, where $\ln A$ is the Coulomb logarithm equal to $\ln(9/4\pi)(kT_e)^3/e^6 n_e^{1/2}$ [20]. Using the energy equation (9) and the integral of the energy conservation law in the form of (5), we obtain the equation to determine the electron temperature T_e :

$$(1 + \alpha)T_e + [(1,5T_e + E_i)S_e + Q_R + Q_{st}]T_e^{3/2} / (An_e^2 \ln A + Bn_e n_a \sigma_a(T_e)T_e^2) = T_{a0} \quad (10)$$

where A and B are constants depending on the type of the gas. Within electron-cascade front (where degree of ionization higher than 10^{-3}) the electron-atomic mechanism of ionization dominates, therefore:

$$S_e = \beta n_e n_a - \alpha n_e^3 \quad \text{or} \quad S_e = \beta n_e n_a [1 - n_e^2/n_a K(T_e)] \quad (11)$$

where $\beta(T_e)$, $\alpha(T_e)$ and $K(T_e)$ are the ionization, recombination coefficients (or forward, reverse rate coefficients [3, 4]) and the constant of ionization equilibrium, respectively. In addition, in inert gases, because of the special feature of atomic energy level's structure (excitation energy is close to ionization one), we can assume that $Q_{st} = 0$ [2]. For the test conditions used, we can also assume the approximation $Q_R = 0$.

Results of experiments. The experiments were conducted with argon and krypton in a shock tube [8, 16] with internal diameter of 76 mm and 4.2 m length of the low-pressure section. Heated helium was used as a driver gas. The electron density was measured by interference method with photoelectric registration of the signal. Laser radiation with the wavelength of 10600 nm was used for argon measurements. In krypton the wavelength was 630 and 1150 nm simultaneously. Apart from the dynamics of electron density, this allowed us also to determine the changes in atomic density. Typical results of $n_e(t)$ measurement in argon obtained by the authors are presented in [16], and the dynamics of electron and atomic density in krypton is described in [21].

The results of experiments, which show measured distribution of S_e associated with (8) behind shock-wave front in argon ($M = 11.3$, $P_1 = 5$ Torr) and krypton ($M = 11.4$, $P_1 = 14$ Torr), are plotted by curves 1 in Fig. 1. The calculated results are shown by curves 2. The temperature dependence $\beta(T_e)$ was taken from the data of [3, 4] (approximation of instantaneous ionization). For comparison, curves 3 show the electron production rate in inter-atomic collisions (calculated using the known atomic temperature from energy integral (5)), which is insignificant in the electron-cascade region. With account of this allowance, the measured value of S_e (curve 1) corresponds to the electron-atomic mechanism of ionization. The uncertainty of the calculated values of this parameter is close to the error of S_e determined from experimental data and does not exceed 15–20 %.

The result obtained shows a significant (severalfold for argon and more than twofold for krypton) increase in the measured rate of electron-cascade ionization as compared to the calculated value corresponding to the commonly accepted model of electron energy balance. This disagreement cannot be caused by the assumptions used ($Q_{st} = 0$, $Q_R = 0$, and also $w = 0$), since it is only amplified otherwise. An analysis of the role of other factors in the results

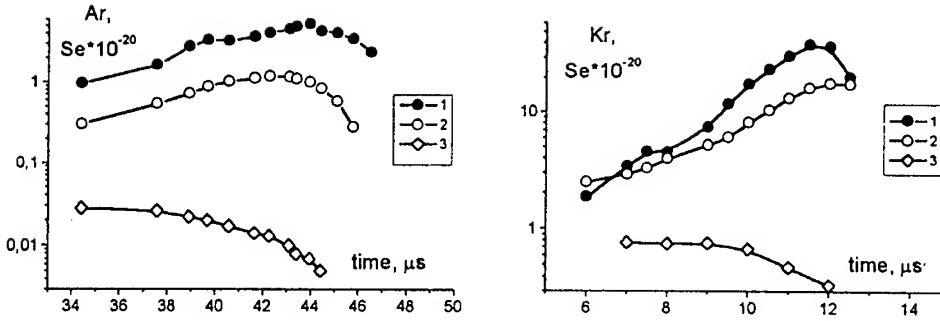


Fig 1. S_i in Argon ($M=11.3$, $P_i=5$ Torr) and Krypton ($M=11.4$, $P_i=14$ Torr) behind shock wave. Curves 1 are results of experiments; curves 2 are results of calculations. In addition, curves 3 show the electron production rate by interatomic collisions.

obtained did not allow us to eliminate the considerable difference between the measured and calculated results either. The uncertainty of the value of $\beta(T_e)$ (for example, the data of [2] are lower than those of [3, 4] by a factor of 1.8) leads to an increase in the discrepancy found by 25–36% over the relaxation region length in the zone of measurements. The allowance for refinement of the Coulomb logarithm for small Λ [19] also increases this difference (though only slightly, by 5–7 %).

Since the reliability of the results obtained in a shock tube is known to depend significantly on the flow imperfection due to the development of a boundary layer on the channel walls, a grounded estimate of the boundary layer effect on the results obtained is required. In the next section, we consider the problems of taking into account the effect of flow imperfection within the framework of this research method.

Effect of the boundary layer. A quasi-one-dimensional model of the flow is used. The development of the boundary layer in this model is equivalent to the change of the channel cross section $A(x)$ according to a certain law [22, 23]: $A(x)=A(0)/[1 - (x/l_m)^N]^{1/N}$, where $A(0)$ is the cross section of the shock-tube channel and l_m is a parameters fixed for certain test conditions ($N = 0.5$ or 0.8 for a laminar or a turbulent boundary layer). As a result, system (1)-(3) acquires the form:

$$d\rho A(x)/dx = 0, \quad (12)$$

$$(1/\rho)dP/dx + udu/dx = 0, \quad (13)$$

$$d\varepsilon/dx + Pd(1/\rho)/dx = 0. \quad (14)$$

In this system, the equations (12), (14) are integrated in a finite form. However, taking into account the “conservatism” of pressure, which is manifested in a weak change of this parameter upon gas ionization behind the shock wave, we can use an approximate solution in the form of a calculated value of $P(x)$ in a perfect gas ($\alpha = 0$). The deviation of both values is small, whereas even low ionization of the gas leads to a noticeable decrease in temperature and to an increase in the gas density. In a variable cross-section channel, we have $P(x)/P_1 = \pi(x)P_s/P_1$, where P_s/P_1 is the pressure jump across SW front and $\pi(x)$ is calculated using the method proposed in [23]. Thus, system (12) – (14) is approximately integrated in the form:

$$\rho u A(x) = \rho u A(0), \quad (12^*)$$

$$\pi(x) P_s / P_1 = \rho k (T_a + \alpha T_e) / m_a P_1, \quad (13^*)$$

$$\varepsilon + P/\rho + u^2/2 = 5kT_e/2m_a + u_1^2/2. \quad (14^*)$$

Using these solutions, we transform previously obtained relations (4), (5) (for $A = \text{Const}$) in a similar manner to:

$$u/u_1 = (15\pi/8a) \{ -1 + [1 + (8a/15\pi)^2 (1 + 3/M^2) - (2a/15\pi)^2 96 \alpha E_i / 5kT_e M^2]^{1/2} \}, \quad (4^*)$$

$$T_{e0}^* \equiv (\pi/a) (P_s/P_1) f^*(\alpha, M) \quad (5^*)$$

where $u/u_1 = f^*(\alpha, M)$, $a(x) = A(0)/A(x) = 1 - (x/l_m)^N$. Relations (4*) and (5*) determine the approximate dependence of the flow parameters on the electron density: $a(x) \rho_1 \alpha / n_e m_a = f^*(\alpha, M)$. The new relation for S_e is exact within the framework of the model accepted, since the approximate solution (13*) was not used:

$$S_e = \{1 - 2\alpha E_i / [5kT_e + m_a V^2 (1 - 4(u/u_1)^2)]\} (u/u_1) (dn_e/dt) - S_e^*, \quad (8^*)$$

$$S_e^* = f^*(\alpha, M) u_1 n_e (dA/dx/A) [5kT_e + m_a u_1^2 (1 - (u/u_1)^2)] / [5kT_e + m_a u_1^2 (1 - 4(u/u_1)^2)].$$

The effect of the boundary layer is manifested both by changing of the effective cross section of the channel ($dA/dx/A \neq 0$) and by changing of the flow velocity. The relative velocity u/u_1 decreases, which leads to an increase in the residence time of an elementary particle in the flow. Correspondingly, the experimental value of S_e determined from the measured electron density distribution also decreases. The change in the calculated value of S_e (11) depends on the relative variations of the integrals of density (4) and (4*) and energy (5) and (5*), which determine the change in the atomic density and electron temperature.

For argon test conditions, the parameter l_m is almost independent of the Mach number and amounts to 350 cm for $P_1 = 5$ Torr [22]. Under these conditions, the most important parameter is the variation of the flow velocity u , since another parameters determined from integrals (4*) and (5*) vary insignificantly, by 2–3 % in the final stage of the relaxation zone. A noticeable (up to 20 %) relative change in velocity, associated with boundary layer effect leads to a decrease in the value of S_e determined from the measured dn_e/dt by no more than 25 %. For an almost constant calculated value of S_e , this allowance does not eliminate the noticeable difference between the numerical and experimental results. In krypton, the measured distribution of the gas density corresponds to the calculated value (obtained using (4)) within the measurement error, which indicates a weak manifestation of the boundary layer effect due to the smaller length of the relaxation region and the higher initial pressure.

Scheme of the method. The method developed to study ionization relaxation in shock waves is clearly illustrated in Fig. 2 *a, b* and compared with the traditional approach. In both cases, the parameters used are the measured dynamics of electron density $n_e(t)$ ($\text{Ne}(t)$ in Fig. 2) and the system of differential equations of a multi-species two-temperature medium and their integrals (1) – (5), which express the conservation laws at the shock wave front (block A in Fig. 2). In the traditional approach (Fig. 1 *a*), the system of equations of block A is solved by numerical methods for the initial conditions with determination of the dynamics of the governing parameters, including the electron density $n_e(t)$. Then the measurement results are compared with the calculated value of this parameter. The drawback of this approach is the necessity to have a full set of data on the elementary processes over the entire relaxation region

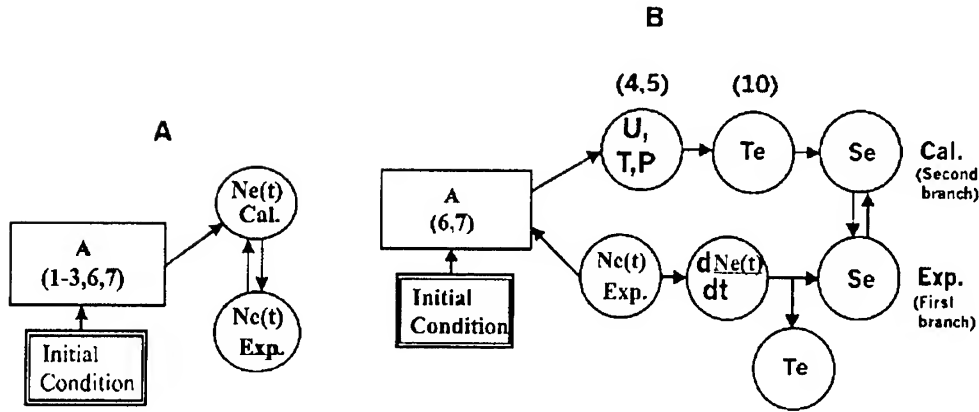


Fig. 2. Basic diagram showing the different in methods for investigation of ionizing relaxation phenomena behind the shock wave. A is traditional concept; B is new concept.

– from the SW front to the equilibrium region. The advantage of the method is the possibility of considering the whole complex of collisional-radiative processes in an ionized gas by using the corresponding equations. However, these advantages are often not implemented because of indefinite values of many parameters, for example, the kinetic coefficients of the elementary processes (associated with metastable atoms, molecular ions).

The method proposed (Fig. 2 b) is also based on the use of the measured dynamics of electron density $n_e(t)$ with an accuracy that allows one to determine additionally the rate of variation of this parameter (i.e. derivative) dn_e/dt ($dNe(t)/dt$ in Fig. 2 b). Moreover, to determine the effect of flow imperfection (if it is considerable), the density distribution of the gas (atoms) is measured using two-wavelength interferometry. As a result, using (8), we determine the net electron production rate (source of electrons) S_e (Se in Fig. 2) proportional to the determined dn_e/dt . The proportionality factor includes the measured quantities, since $\alpha = n_e/(n_e + n_a)$, $\rho = (n_e + n_a)m_a = n_e m_a / \alpha$ and $\rho_I = n_I m_a$. Under the condition $\alpha \ll 1$ (SW of moderate intensity and the Mach numbers less than 12–15 depending on the type of the gas), the first term in (8) is close to unity, and the second term $-u/u_I$ – to density jump ρ_I/ρ across SW front. As a result, to determine S_e without noticeable loss in accuracy we can confine ourselves only by registration of the dynamics of electron density, verifying the data for gas density and degree of ionization from the integral relation (4) and $\rho = n_e m_a / \alpha$ (under a weak effect of the boundary layer). In the case of noticeable imperfection of the flow, we use relation (4*). Thus, we determine the distribution of experimental values of S_e behind the shock wave (the first branch in Fig. 2) based completely on the measured density of electrons (and atoms).

In the second branch of this scheme, the measured density of electrons and atoms (determined also from (4) or (4*)) are used in the electron energy balance equation of the form (10) (determined at steady-state approximation from the system of equations of block A). The known dependence (11) of the electron-cascade ionization rate is used to determine the calculated values of the electron temperature and, hence, the rate of this process. Such a calculation is unambiguous for a region where a single electron-atomic mechanism of ionization dominates due to the high density of electrons (relative to admixtures to certain limits, metastable particles, molecular ions, etc.). Since the parameter S_e to be determined depends significantly on T_e , a comparison of the measured and calculated values of this parameter yield direct information about the electron temperature and, hence, it shows whether the numerical

model of electron energy balance used is adequate to the real process. The results of this comparison make it also possible to determine (under certain assumptions) additional mechanisms of energy exchange with participation of electrons in the case of different data.

Conclusions. A method for studying ionization relaxation in shock waves is developed, which is based on comparison of the measured and calculated results for the electron density production rate in electron-cascade front of relaxation zone. It is shown that the measured rate for monatomic gases is greater than calculated using the commonly accepted model within the range of parameters close to the development of flow instability in argon and krypton. Since there is no alternative to an ionization mechanism by electron-atomic collisions, the observed effect of a high electron production rate is explained by the presence of an additional channel of energy exchange of the particles, which increases the electron temperature. Determination of particular mechanisms of energy transfer and their relation to the development of flow instability requires correction of the electron energy balance equation with account of experimental results in an enlarged range of test conditions.

This work was partly supported by the Russian Foundation for Basic Research (Grants No. 97-01-00772 and 00-01-00829).

References

1. Oettinger P.E. and Bershader D.A. A Unified treatment of the relaxation phenomenon in radiating argon plasma flow // *AIAA J.* 1967. Vol. 5, 9. P. 1625-1632.
2. Biberman L.M., Mnatsakanyan A.Kh., Yakubov I.T. Ionising relaxation behind strong shock waves in gases // *Usp. Fiz. Nauk.* 1970. Vol. 102, № 2. P. 431-462.
3. Glass I.I. and Liu W.S. Effects of hydrogen impurities on shock structure and stability in ionizing monatomic gases. Part 1. Argon // *J. Fluid Mech.* 1978. Vol. 84. Pt 1. P. 55-77.
4. Glass I.I., Liu W.S. and Tang F.C. Effects of hydrogen impurities on shock structure and stability in ionizing monatomic gases. Part 2. Krypton // *Can. J. Phys.* 1977. Vol. 55. P. 1269-1279.
5. Mishin G.I., Bedin A.P., Yushchenkova N.I. et al. Anomalous relaxation and stability shock waves in gases // *Zhurn. Tekh. Fiz.* 1981. Vol. 51, № 11. P. 2315-2324.
6. Yushchenkova N.I., Mishin G.I., Roshchin O.R. The mechanism of anomalous relaxation in shock waves of inert gases // *Pisma v Zh. Tekh. Fiz.* 1985. Vol. 11, № 9. P. 517-524.
7. Tumakaev G.K. Systematization of anomalous phenomena in shock heated monatomic gases // *High-Temperature Gas-Dynamics, Shock Tubes, and Shock Waves* / Ed. R.I. Soloukhin. Minsk, 1983. P. 154-160. (in Russian).
8. Grigor'ev P.V., Makarov Yu.P., Pozdniakov G.A. The second kind instability of shock heated krypton plasma in experiment on shock tube // *CD Rom Proc. 8th Int. Symp. of Flow Visualization*. Torino: Levrotto and Bella, 1998. P. 53.1.-53.4.
9. Tumakaev G.K., Stepanova Z.A. About the threshold character of suppresses of plasma intensity fluctuations of shock heated monatomic gases // *Zhurn. Tekh. Fiz.* 1982. Vol. 52, № 11. P. 2305-2307.
10. Grigor'ev P.V. The 1st kind of instability of shock heated argon and xenon in experiment on shock tube // *Proc. 2nd Intern. Conf. on Experimental Fluid Mechanics*. Torino: Levrotto and Bella, 1994. P. 772-778.
11. Tumakaev G.K., Stepanova Z.A., Grigor'ev P.V. The interferometric study of shock heated xenon plasma in the regime of existing of the second kind instability // *Zhurn. Tekh. Fiz.* 1994. Vol. 64, № 4. P. 46-50.
12. Tumakaev G.K., Stepanova Z.A., D'yakov B.B. About xenon atom induced radiation of the hyper-radiative transition $5d[7/2]_3-6p[5/2]_2$ in the relaxation zone behind the shock front // *Ibid.* 1992. V. 62, № 11. P. 25-31.
13. Tumakaev G.K., Stepanova Z.A., Grigor'ev P.V. Variation of plasma parameters behind shock waves at first kind instability development // *Ibid.* 1991. Vol. 61, № 9. P. 149-153.

-
14. Tumakaev G.K., Stepanova Z.A., Grigor'ev P.V. An experimental investigation of the second kind of instability of xenon plasma heated in a shock tube // *Sov. Phys. Tech. Phys.* 1991. Vol.36. P. 516-522.
 15. Tumakaev G.K., Stepanova Z.A., Grigor'ev P.V. Experimental study of the second kind of instability of a shock-heated xenon plasma in a shock tube: dynamics of the relaxation zone in the flux behind the shock-wave front // *Ibid.* 1992. Vol. 37. №1. P. 37-41.
 16. Soloukhin R.I., Yacobi Yu.A. and Yakovlev V.I. Studying ionizing shock waves by IR-diagnostic technique // *Archives of Mechanics.* 1974. V.26. P. 637-646.
 17. Weiss C.O. and Kotzan B. A Multiple-Pass Interferometer for Electron and atom density measurements in shock tube plasmas // *Appl. Phys.* 1975. Vol. 7, No. 3. P.203-207.
 18. Shneider K.-P. and Park C. Effect of shock tube cleanliness on the initial ionization rate in argon plasma // *Phys. Fluids.* 1975. Vol. 18. No.8. P. 969-981.
 19. Mitchner M., Kruger C. Partially ionized gases. New York et al.: Wiley, 1973.
 20. Hoffert M.I. and Lien H. Quasy-one-dimentional nonequilibrium gasdynamics of partially ionized two-temperature argon // *Phys. Fluids.* 1967. Vol. 10., No. 8. P.1769-1782.
 21. Grigor'ev P.V., Makarov Yu.P. Observation of transition from the second harmonic to the fundamental mode in one experiment upon evolution of the second type instability shock heated krypton // *CD Rom Proc. 9th Intern. Symp. of Flow Visualization*, 2000. P.112.1 – 112.4.
 22. Mirels H. Test time in low-pressure shock tubes // *Phys. Fluids.* 1963. Vol. 6, №9. P.1201-1214.
 23. Mirels H. Flow nonuniformity in shock tubes operating at maximum test time // *Ibid.* 1966. Vol. 10, No. 9. P.1907-1912.

COMPRESSIBLE LARGE EDDY SIMULATION USING UNSTRUCTURED GRID: SUPERSONIC BOUNDARY LAYER AND COMPRESSION RAMPS

*Hong Yan,¹ Gerald Urbin,² Doyle Knight

Rutgers University, Piscataway, New Jersey 08854

and Alexander A. Zheltovodov

Institute of Theoretical and Applied Mechanics, Novosibirsk 630090, Russia

A Mach 3 adiabatic flat plate turbulent boundary layer at $Re_\delta = 2 \times 10^4$ is studied using the Monotone Integrated Large Eddy Simulation (MILES) method. The Favre-filtered compressible Navier-Stokes equations are solved on a three-dimensional unstructured grid of tetrahedral cells. A variable limiter denoted the extremum limiter is developed to control the overshoots caused by high order interpolation. The statistical predictions computed with and without the limiter are compared with experimental data and Direct Numerical Simulation (DNS). Results for 8° and 25° compression corners at Mach 3 and $Re_\delta = 2 \times 10^4$ are compared with experimental data.

1 Introduction

High order Total Variation Diminishing (TVD) schemes have been developed in one dimension into reliable tools for numerical prediction of the solution of hyperbolic systems of equations. However, in higher dimensions it has proved difficult to obtain the same degree of robustness and accuracy with extensions of these one dimensional techniques or using a one dimensional scheme in each coordinate direction, particularly on unstructured grids. As a consequence, a significant amount of research has been carried out into the creation of genuinely multidimensional high order TVD schemes.

One of the strategies is to develop a multidimensional limiter for modifying high order finite volume schemes in such a way that the resulting method is monotonic, thus avoiding the creation of unphysical oscillations in the numerical solution and so improving the robustness of the algorithm. One commonly used approach is the slope limiting (MUSCL) technique of van Leer [1], in which the limiter is applied in a geometric manner to the gradients of a piecewise linear reconstruction of the solution to create a monotonic scheme. Some progress has been made in extending one dimensional limiters to multidimensional cell-centered finite volume scheme for unstructured triangular meshes by Barth and Jespersen [2], Durlofsky et al. [3], Liu [4], Batten [5] and Hubbard [6]. Each of these schemes involves the construction of an appropriate linear representation of the solution within a triangular cell which is limited in a manner which enforces a positivity constraint on the scheme.

The compression corner is a classical problem of the interaction of shock wave with a turbulent boundary layer. When the ramp angle exceeds a certain critical value, a

shock wave of sufficient strength is formed to cause a separation near the corner. The relationship between the shock motion, the separation bubble and the incoming turbulence is not fully understood despite numerous experimental and theoretical studies [7, 8, 9, 10, 11, 12, 13, 14, 15, 16, 17]. Conventional RANS methods fail to provide an accurate prediction of the mean wall pressure and skin friction [18]. Direct Numerical Simulation (DNS) of isotropic turbulence interacting with a shock wave has been achieved [19, 20]; however, little work has been done in the practical case of a boundary layer interacting with a shock wave.

This paper consists of two parts. In the first part, we develop a variable limiter denoted the extremum limiter to avoid the overshoots near the discontinuities. The motivation for developing the limiter is to compute shock wave turbulent boundary layer interactions and the flat plate boundary layer is used as a necessary test to evaluate its validity. The effect of the extremum limiter on the statistical quantities is investigated. The second part presents some previous results of the 8° compression corner without a limiter and 25° compression corner with a slope limiter proposed by Urbin and Knight [17]. Additional details are presented in Urbin and Knight [16, 17].

Future research will focus on the application of the extremum limiter to the 25° compression corner and the construction of Essentially Non-oscillatory (ENO) schemes in an unstructured grid system and its numerical implementation in the 25° compression corner.

2 Governing Equations

A 3-D compressible turbulent flow is governed by the conservative Favre-filtered Navier-Stokes equations (here written using the Einstein summation notation where repeated indices denote summation) [21].

$$\frac{\partial \bar{\rho}}{\partial t} + \frac{\partial \bar{\rho} \tilde{u}_k}{\partial x_k} = 0 \quad (1)$$

$$\frac{\partial \bar{\rho} \tilde{u}_i}{\partial t} + \frac{\partial \bar{\rho} \tilde{u}_i \tilde{u}_k}{\partial x_k} = -\frac{\partial \bar{p}}{\partial x_i} + \frac{\partial \mathcal{T}_{ik}}{\partial x_k} \quad (2)$$

$$\frac{\partial \bar{\rho} \tilde{e}}{\partial t} + \frac{\partial}{\partial x_k} (\bar{\rho} \tilde{e} + \bar{p}) \tilde{u}_k = \frac{\partial}{\partial x_k} (Q_k + \mathcal{T}_{ik} \tilde{u}_i) \quad (3)$$

$$\bar{p} = \bar{\rho} R \tilde{T} \quad (4)$$

where

$$\begin{aligned} \mathcal{T}_{ik} &= \tau_{ik} + \bar{\sigma}_{ik} & Q_k &= Q_k + \bar{q}_k \\ \tau_{ik} &= -\bar{\rho}(\tilde{u}_i \tilde{u}_k - \tilde{u}_i \tilde{u}_k) & Q_k &= -\bar{\rho} c_p (\tilde{T} \tilde{u}_k - \tilde{T} \tilde{u}_k) \\ \bar{\sigma}_{ik} &= \mu(\tilde{T}) \left(-\frac{2}{3} \frac{\partial \tilde{u}_j}{\partial \tilde{x}_j} \delta_{ik} + \frac{\partial \tilde{u}_i}{\partial x_k} + \frac{\partial \tilde{u}_k}{\partial x_i} \right) & \bar{q}_k &= k(\tilde{T}) \frac{\partial \tilde{T}}{\partial x_k} \\ \bar{\rho} \tilde{k} &= \frac{1}{2} (\overline{\rho u_i u_i} - \bar{\rho} \tilde{u}_i \tilde{u}_i) = -\frac{1}{2} \tau_{ii} & \bar{\rho} \tilde{e} &= \bar{\rho} c_v \tilde{T} + \frac{1}{2} \bar{\rho} \tilde{u}_i \tilde{u}_i + \bar{\rho} \tilde{k} \end{aligned}$$

For a function f , its filtered form \bar{f} and its Favre-averaged form \tilde{f} are

$$\bar{f} \equiv \frac{1}{V} \int_V G f dV \quad \tilde{f} \equiv \frac{\overline{\rho f}}{\bar{\rho}}$$

where G is the filtering function and ρ is the density. All the flow variables are nondimensionalized using the reference density ρ_∞ , velocity U_∞ , static temperature T_∞ and length scale L . The reference Mach number $M_\infty = U_\infty / \sqrt{\gamma R T_\infty}$. Moreover, the governing equations may be written in finite volume form for a control volume V with surface ∂V (additional details are presented in Knight *et al.* [21])

$$\frac{d}{dt} \int_V Q dV + \int_{\partial V} (F\hat{i} + G\hat{j} + H\hat{k}) \cdot \hat{n} dA = 0 \quad (5)$$

3 Numerical Method

The numerical computation is implemented on an unstructured grid of tetrahedra with a cell-centered storage structure. The cell-averaged values, stored at the centroid of each cell of volume V_i are

$$Q_i = \frac{1}{V_i} \int_{V_i} Q dV \quad (6)$$

The MILES model [22] takes the numerical dissipation as the SGS model (*i.e.*, $\tau_{ik} = 0$, $Q_k = 0$). An exact Riemann solver (second order Godunov scheme [23]) is applied to the inviscid fluxes normal to each face, using a second-order reconstruction by the Least Squares method [24] to obtain the values of each variable on either side of the cell faces. The viscous fluxes and heat transfer are obtained by the second order accurate scheme [25] in which Gauss' Theorem is applied to each face. A second order accurate Runge-Kutta scheme is implemented for temporal integration. A rescaling-reintroducing method extended to compressible flows by Urbin *et al.* [17] is used to generate a realistic turbulent inflow condition. The primitive variables are averaged both in time and in the spanwise direction. The notation for the combined temporal and spanwise average of a function $f(x, y, z)$ is

$$\ll f \gg \equiv \frac{1}{L_z} \frac{1}{t_f - t_i} \int_0^{L_z} \int_{t_i}^{t_f} f dt dz$$

4 Limiter Implementation

The second order Godunov scheme in semi-discretized form can be written as

$$\frac{dQ_i}{dt} = -\frac{1}{V_i} \sum_{\text{face}} \Gamma^{-1} M^G dA \quad (7)$$

where Γ^{-1} is the transformation matrix [21] and M^G is the second order Godunov numerical flux

$$M^G = M(\hat{Q}_R, \hat{Q}_L) \quad (8)$$

where M is the physical flux and \hat{Q} is the cell averaged value of flow variables defined in the transformed coordinates. The quantities \hat{Q}_R and \hat{Q}_L evaluated on the right side and left side of the face k of a cell i are used to obtain the numerical flux by an exact Riemann solver. The second order approximation to \hat{Q}_L (for example) by the MUSCL method is

$$\hat{Q}_L = \hat{Q}_i + \vec{r}_i \cdot \nabla \hat{Q}_i \quad (9)$$

where \vec{r}_i is the vector from the centroid of cell i to the centroid of the face k and $\nabla \hat{Q}_i$ is the gradient of flow variables at the centroid of cell i and is obtained by the Least Squares

method. The piecewise linear interpolation within each cell yields second order accuracy, but it doesn't prohibit overshoots and undershoots and therefore non-linear correction factors called limiters have to be introduced. Following the principle of constructing limiters discussed above, an extremum limiter Φ is proposed and formulated as

$$\hat{Q}_L^{(m)} = \hat{Q}_L + \Phi \quad (10)$$

where

$$\Phi = \begin{cases} 0 & \text{if } \min(\hat{Q}_i, \hat{Q}_j) \leq \hat{Q}_L \leq \max(\hat{Q}_i, \hat{Q}_j) \\ \max(\hat{Q}_i, \hat{Q}_j) - \hat{Q}_L & \text{if } \hat{Q}_L > \max(\hat{Q}_i, \hat{Q}_j) \\ \min(\hat{Q}_i, \hat{Q}_j) - \hat{Q}_L & \text{if } \hat{Q}_L < \min(\hat{Q}_i, \hat{Q}_j) \end{cases}$$

where \hat{Q}_j is the cell-averaged value for the adjacent cell. The extremum limiter gets its name from that fact that it does not limit the gradients, but directly limits the values of the variables on both sides of the face.

5 Results

5.1 Flat Plate Boundary Layer

Two separate computations of a Mach 3 supersonic flat plate boundary layer at $Re_\delta = 2 \times 10^4$ were performed, where δ is the incoming turbulent boundary layer thickness. The two cases, one with the extremum limiter and another without a limiter, are presented to compare with the empirical formula, the experimental data [8, 26, 27, 28, 29] and DNS results [30]. Allowing x, y and z to denote the streamwise, transverse and spanwise directions, respectively, the computational domain for the no limiter case is $L_x = 14.8\delta$, $L_x = 3.4\delta$, $L_z = 1.1\delta$. For the limiter case, the spanwise width is $L_z = 2.2\delta$. The streamwise length L_x is approximately three times the mean experimental streamwise streak size. The height L_y is based on the requirement that acoustic disturbances originating at the upper boundary do not interact with the boundary layer on the lower wall. The details of the grid are listed in Table 1, where $\Delta y^+ = \Delta y u_\tau / \nu_w$ (ν_w is the kinematic viscosity at the wall, u_τ is the friction velocity). The time averaging period $t_f - t_i$ is $138\delta/U_\infty$ and $150\delta/U_\infty$ for the no limiter and limiter cases, respectively.

Table 1: Details of Grids

Name	Δx^+	Δy^+ at the wall	Δz^+	$\Delta x/\delta$	$\Delta y/\delta$ at $y = \delta$	$\Delta z/\delta$	Tetras
No limiter	11	1.1	3.1	0.09	0.105	0.069	1,688,960
With limiter	20	1.6	6.8	0.10	0.187	0.034	1,632,000

We will discuss the effect of the extremum limiter on the flowfield from two points of view. First we present the mean flow variables. The Van Driest transformed velocity for an adiabatic flat plate flow is

$$U_{VD} = \frac{U_\infty}{A} \sin^{-1} \left(A \frac{U}{U_\infty} \right) \quad \text{with} \quad A = \sqrt{\frac{\frac{\gamma-1}{2} M_\infty^2 Pr_{tm}}{1 + \frac{\gamma-1}{2} M_\infty^2 Pr_{tm}}}$$

where $Pr_{tm} = 0.89$ is the mean turbulent Prandtl number. The mean Van Driest stream-wise velocity profile is shown in Fig. 1. The computed friction velocity u_τ/U_∞ is 0.056 and 0.0506 for the cases with and without the extremum limiter, respectively. According to the combined Law of the Wall and Wake, the theoretical value of u_τ/U_∞ is 0.054 with $\Pi = 0.12$ which is obtained by an extrapolation of the available experimental data [31] at $Re_\delta = 2 \times 10^4$. The mean velocity with the extremum limiter overestimates the Law of the Wall by approximately 10% due to the underprediction of the friction velocity. The mean density (Fig. 2), mean streamwise velocity (Fig. 3) and the mean temperature (Fig. 4) with and without the limiter show good agreement with the experimental data of Zheltovodov and Yakovlev [8, 29].

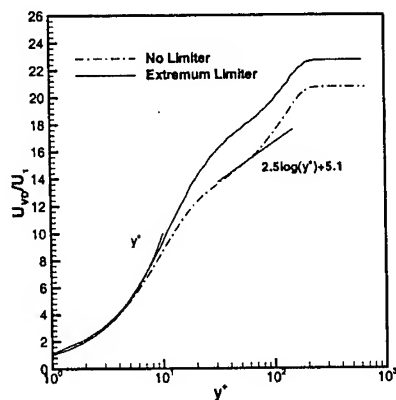


Figure 1: Van Driest velocity

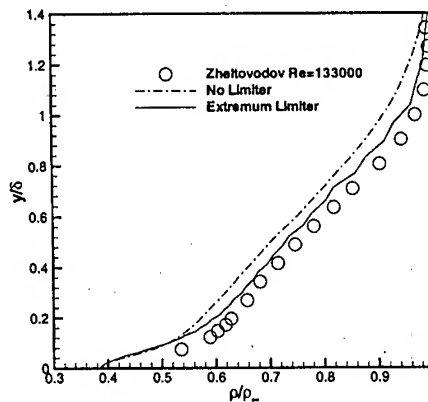


Figure 2: Mean density

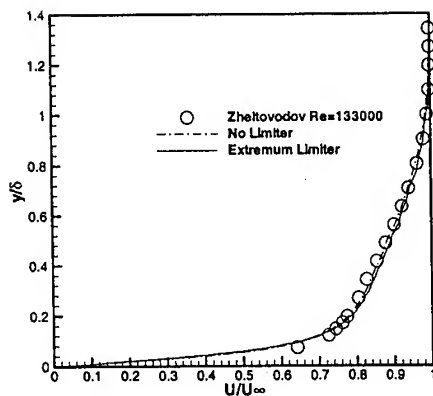


Figure 3: Mean streamwise velocity

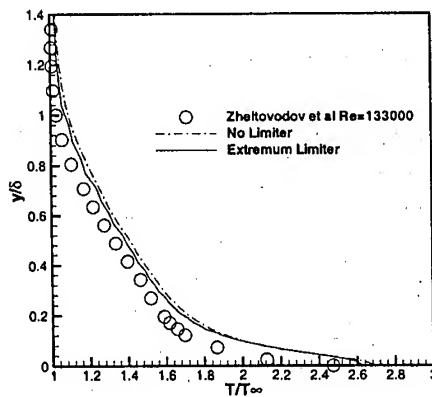


Figure 4: Mean temperature

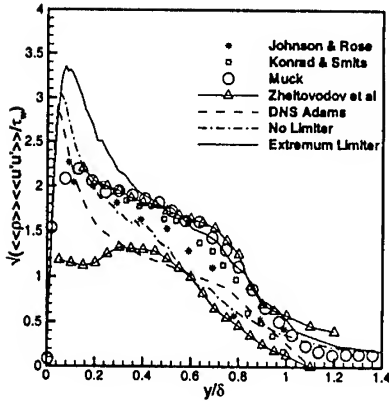


Figure 5: Streamwise Reynolds stress

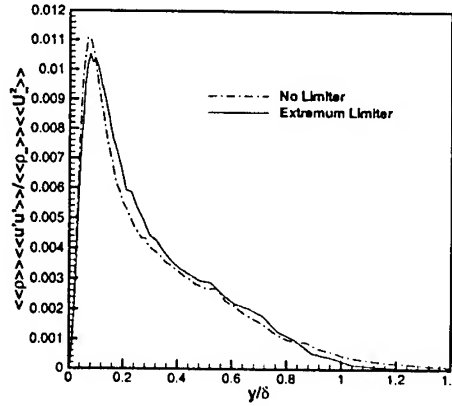


Figure 6: Streamwise Reynolds stress

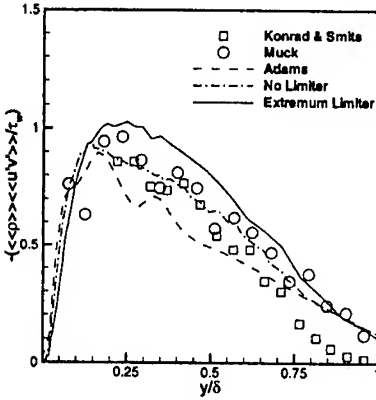


Figure 7: Reynolds shear stress

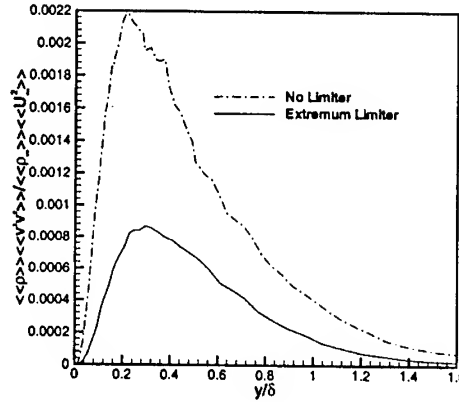


Figure 8: Normal Reynolds stress

Second, we focus on the analysis of the statistical predictions of the Reynolds stresses. The streamwise Reynolds stress, normalized by the wall shear stress τ_w , is presented in Fig. 5. The no limiter results are within the range of experimental data except close to the wall where the uncertainty in the measurements is large. The extremum limiter results are at or above the upper limit of the range of experimental data. The higher value of the extremum limiter profile, compared to the no limiter case, is due to the lower value of u_τ for the extremum limiter case. The profiles of the streamwise Reynolds stress, normalized by $\rho_\infty U_\infty^2$ and shown in Fig. 6, are virtually identical for the extremum limiter and no limiter cases. Thus, the extremum limiter has negligible effect on the streamwise Reynolds stress. The Reynolds shear stress, normalized by the wall shear stress, is shown in Fig. 7. The extremum limiter and no limiter profiles are in reasonable agreement with the range of experimental data. Since the near wall region of the turbulent boundary layer is approximately a constant stress layer, the Reynolds shear stress must achieve

a maximum value of τ_w within the logarithmic region irrespective of the details of the limiter. The normal Reynolds stress, normalized by $\rho_\infty U_\infty^2$, is displayed in Fig. 8. The extremum limiter profile shows a significant reduction in the level of the normal Reynolds stress compared to the no limiter case. This reduction in normal velocity fluctuations reflects the reduced turbulent shear stress predicted by the extremum limiter.

5.2 Compression Corners

In this section, we present results of the 8° and 25° compression corners at Mach 3.0 and $Re_\delta = 2 \times 10^4$ previously presented in [16] and [17]. No limiter is applied to the 8° compression corner, while a slope limiter proposed by Urbin [17] is used in the computation of the 25° compression corner. The inflow data are extracted from the flat plate boundary layer which keeps the same inflow grid configuration and time step size as the compression corner. The 8° compression corner simulation employed the Smagorinsky subgrid-scale model.

First, the results of the 8° compression corner are presented. Fig. 9 shows surface pressure along the wall as a function of x/δ . After the shock system, the value of the surface pressure reaches the level predicted by the experiments [8, 29] and inviscid theory. The slope of the pressure rise is correctly predicted.

Comparisons of mean streamwise velocity profiles (Fig. 10) and temperature profiles (Fig. 11) are performed upstream and downstream of the corner against the $Re_\delta = 1.1 \times 10^5$ data of Zheltovodov *et al* [29]. Except near the wall where the effect of the difference in computed and experimental Reynolds number is evident, the decrease in velocity due to the shock is well reproduced. The mean streamwise resolved turbulent kinematic normal stress $\ll u''u'' \gg$, normalized using the local mean density $\ll \rho \gg$ and upstream wall shear stress τ_{ref} , is shown in Fig. 12. The reference wall shear stress is constant and measured at $x = -2\delta$ which is close to the experimental value $x = -1.95\delta$. Comparisons are presently shown with Muck *et al* [28] data ($\alpha = 8^\circ$, $M = 3$, $Re_\delta = 1.6 \times 10^6$). In Fig. 13 the Reynolds shear stress distributions are shown for the same experiment. The deformation of these quantities associated with the adverse pressure gradient is evident in the vicinity of the corner. Their evolution shows a qualitative agreement. The Reynolds normal stress is amplified by a factor as high as 2^2 . This maximum increase appears at $y/\delta = 0.3$, which is consistent with experiment. The collapse of the experimental fluctuations between $0.6 < y/\delta < 1.0$ is also evident in the LES. Similar tendencies and qualitative agreement with the computations are found with the Reynolds normal stress data of Zheltovodov *et al* [8, 29, 32].

A preliminary study of the 25° compression corner has been carried out. The strong shock generated by the corner requires incorporation of a limiter to ensure numerical stability. An inhomogeneous limiter [17] has been developed. The incident shock causes the expected boundary layer separation upstream of the point of impingement of the primary shock with a secondary shock forming near the separation. An instantaneous image of the shock (specifically, the isosurfaces $p/p_\infty = 1.4$ and $p/p_\infty = 2.0$) and streamwise cut of the velocity (at $y^+ = 20$) are shown in Fig. 14. The rippling of the shock wave by the large scale structures in the incoming boundary condition is evident. Approximately five ripples are evident indicating a mean wavelength approximately equal to δ . This is consistent with VLES prediction from Hunt [13] and Marshall [33]. The instantaneous regions of negative streamwise velocity are also evident. This separated flow structure is in qualitative agreement with the experiments of Zheltovodov *et al* [7, 8, 29].

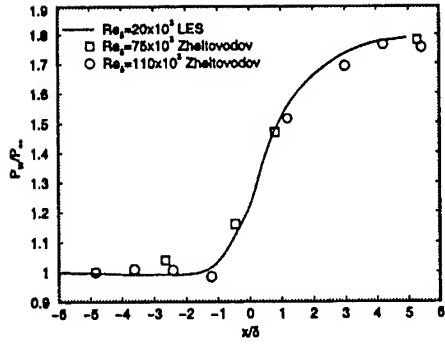


Figure 9: Wall surface pressure

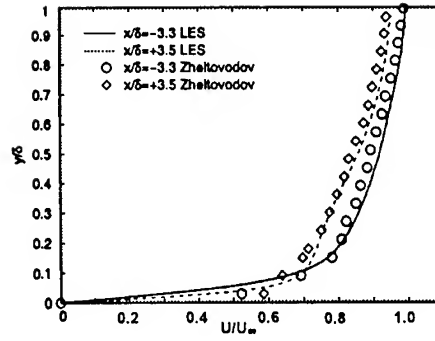


Figure 10: Mean streamwise velocity

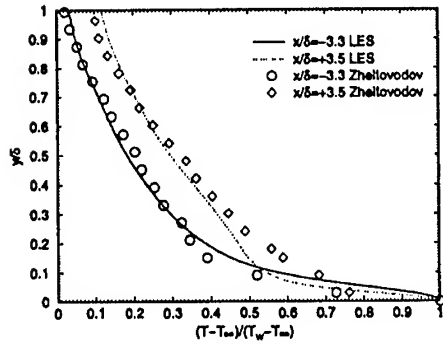


Figure 11: Mean temperature

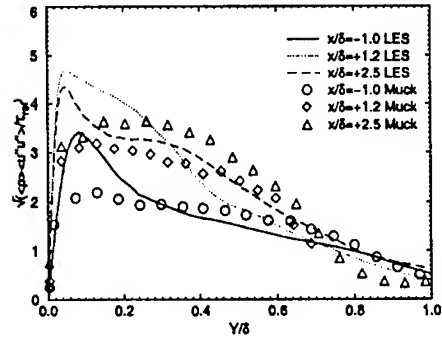


Figure 12: Streamwise Reynolds stress

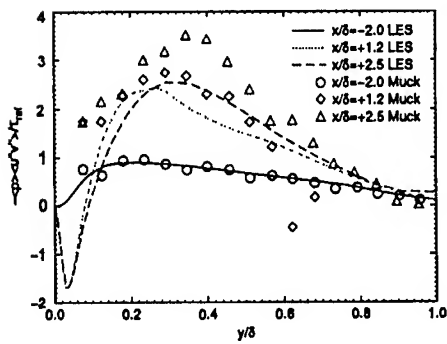


Figure 13: Reynolds shear stress



Figure 14: Shocks and streamwise velocity

6 Conclusions

A new limiter denoted the extremum limiter is proposed and its effectiveness is assessed by comparison with results without a limiter in the Monotone Integrated Large Eddy Simulation of a compressible supersonic flat plate boundary layer. Comparison of the statistical quantities with experimental data and DNS results shows that the extremum limiter affects only the normal Reynolds stress and reduces the predicted friction velocity by 8% compared to the no limiter case. Results of the 8° and 25° compression corners at Mach 3 are presented. The 8° compression corner shows good agreement with experiment and the preliminary results for 25° compression corner exhibit qualitative agreement with experimental data.

Acknowledgments

This research is supported by AFOSR under Grant Number F49620-99-1-0008 monitored by Dr. L. Sakell. The computations were performed at Rutgers University and the National Center for Supercomputing Applications and the Scientific Computing Facility Boston University under Grant CTS980016N. The fourth author was also supported by the Russian Foundation of Basic Research (grant No. 97-01-00885).

References

- ¹Van Leer, B., "Towards the Ultimate Conservative Difference Scheme V. A Second Order Sequel to Godunov's Method," *J. Comput. Phys.*, Vol. 32, 1979, pp. 101.
- ²Barth, T. J. and Jespersen, D. C., "The Design and Application of Upwind Schemes on Unstructured Meshes," *AIAA Paper 89-0366*, 1989.
- ³Durlofsky, L. J., Engquist, B., and Osher, S., "Triangle Based Adaptive Stencils for the Solution of Hyperbolic Conservation Laws," *J. Comput. Phys.*, Vol. 98, 1992, pp. 64.
- ⁴Liu, X. D., "A Maximum Principle Satisfying Modification of Triangle Based Adaptive Stencils for the Solution of Scalar Hyperbolic Conservation Laws," *SIAM J. Numer. Anal.*, Vol. 30, 1993, pp. 701.
- ⁵Batten, P., Lambert, C., and Causon, D. M., "Positively Conservative High-Resolution Convection Schemes for Unstructured Elements," *Int. J. Numer. Methods Eng.*, Vol. 39, 1996, pp. 1821.
- ⁶Hubbard, M. E., "Multidimensional Slope Limiters for MUSCL-Type Finite Volume Schemes on Unstructured Grids," *J. Comput. Phys.*, Vol. 155, 1999, pp. 54.
- ⁷Zhel'tovodov, A. A., Schuelein, E., and Yakovlev, V., "Turbulent Boundary Layer Development Under Conditions of Mixed Interaction with Shocks and Expansion Waves," *Rep No 28-83, Institute of Theoretical and Applied Mechanics*, USSR Academy of Sciences, 1983, in Russian.
- ⁸Zhel'tovodov, A. A. and Yakovlev, V., "Stages of Development, Gas Dynamic Structure and Turbulence Characteristics of Turbulent Compressible Separated Flows in the Vicinity of 2-D Obstacles," *Rep No 27-86, Institute of Theoretical and Applied Mechanics*, USSR Academy of Sciences, 1986, in Russian.
- ⁹Ong, C. and Knight, D., "Hybrid MacCormack and Implicit Beam-Warming Algorithms for a Supersonic Compression Corner," *AIAA Journal*, Vol. 25, 1987, pp. 401.
- ¹⁰Wilcox, D. C., "Supersonic Compression Corner Applications of a Multiscale Model for Turbulent Flows," *AIAA Journal*, Vol. 28, 1990, pp. 1194.
- ¹¹Dolling, D. S., "Fluctuating Loads in Shock Wave/Turbulent Boundary Layer Interaction: Tutorial and Update," *AIAA Paper 93-0284*, 1993.

- ¹²Unalms, O. H. and Dolling, D. S., "Decay of Wall Pressure Field and Structure of a Mach 5 Adiabatic Turbulent Boundary Layer," *AIAA Paper 94-2363*, 1994.
- ¹³Hunt, D. and Nixon, D., "A Very Large Eddy Simulation of an Unsteady Shock Wave/Turbulent Boundary Layer Interaction," *AIAA Paper 95-2212*, 1995.
- ¹⁴Cassel, K., Ruban, A., and Walker, D., "An Instability in Supersonic Boundary Layer Flow Over a Compression Ramp," *Journal of Fluid Mechanics*, Vol. 300, 1995, pp. 265.
- ¹⁵Zheltovodov, A. A., "Shock Waves / Turbulent Boundary Layer Interaction - Fundamental Studies and Applications," *AIAA Paper 98-1977*, 1996.
- ¹⁶Urbain, G., Knight, D., and Zheltovodov, A. A., "Compressible Large Eddy Simulation using Unstructured Grid: Supersonic Turbulent Boundary Layer and Compression Corner," *AIAA Paper 99-0427*, 1999.
- ¹⁷Urbain, G., Knight, D., and Zheltovodov, A. A., "Large Eddy Simulation of a Supersonic Compression Corner Part I," *AIAA Paper 2000-0398*, 2000.
- ¹⁸Dolling, D. S., "Considerations in the Comparison of Experimental Data with Simulation-Consistency of Math Models and Flow Physics," *AIAA Paper 96-2030*, 1996.
- ¹⁹Sarkar, S., "The Stabilizing Effect of Compressibility in Turbulent Shear Flow," *Journal of Fluid Mechanics*, Vol. 282, 1995, pp. 163.
- ²⁰Lee, S., Lele, S., and Moin, P., "Interaction of Isotropic Turbulence with Shock Waves: Effect of Shock Strength," *Journal of Fluid Mechanics*, Vol. 300, 1997, pp. 383.
- ²¹Knight, D., Zhou, G., Okong'o, N., and Shukla, V., "Compressible Large Eddy Simulation Using Unstructured Grids," *AIAA Paper 98-0535*, 1998.
- ²²Boris, J., Grinstein, F., Oran, E., and Kolbe, R., "New Insights into Large Eddy Simulation," *Fluid Dynamics Research*, Vol. 10, 1992, pp. 199.
- ²³Gottlieb, J. and Groth, C., "Assessment of Riemann Solvers for Unsteady One Dimensional Inviscid Flows of Perfect Gases," *J. Comput. Phys.*, Vol. 78, 1988, pp. 437.
- ²⁴Ollivier-Gooch, C., "High Order ENO Schemes for Unstructured Meshes Based on Least Squares Reconstruction," *AIAA Paper 97-0540*, 1997.
- ²⁵Knight, D., "A Fully Implicit Navier-Stokes Algorithm Using an Unstructured Grid and Flux Difference Splitting," *Applied Numerical Mathematics*, Vol. 16, 1994, pp. 101.
- ²⁶Johnson, D. and Rose, W., "Laser Velocimeter and Hot Wire Anemometer Comparison in a Supersonic Boundary Layer," *AIAA J.*, Vol. 13, 1975, pp. 512.
- ²⁷Konrad, W. and Smits, W., "Turbulence Measurement in a Three Dimensional Boundary Layer in Supersonic Flow," *J. Fluid Mech.*, Vol. 372, 1998, pp. 1.
- ²⁸Muck, K., Spina, E., and Smits, A., "Compilation of Turbulence Data for an 8 Degree Compression Corner at Mach 2.9," *Tech. Rep. Report MAE-1642*, Princeton University, 1984.
- ²⁹Zheltovodov, A. A., Trofimov, V. M., and Yakovlev, V. N., "An Experimental Documentation of Supersonic Turbulent Flows in the Vicinity of Forward- and Backward-Facing Ramps," *Rep No 2030, Institute of Theoretical and Applied Mechanics*, USSR Academy of Sciences, 1990.
- ³⁰Adams, N., "Direct Numerical Simulation of Turbulent Supersonic Boundary Layer Flow," *Advances in DNS/LES*, Greyden Press, 1997, p. 29.
- ³¹Fernholz, H. and Finley, P., "A Critical Commentary on Mean Flow Data for Two Dimensional Compressible Turbulent Boundary Layers," *Tech. Rep. 253*, AGARD, 1980.
- ³²Zheltovodov, A. A. and Yakovlev, V., "Turbulent Study in Compressible Unseparated and Separated Flows," *Rep No 1418, Institute of Theoretical and Applied Mechanics*, USSR Academy of Sciences, 1984, in Russian.
- ³³Marshall, T. and Dolling, D., "Computation of Turbulent Separated Unswept Compression Ramp Interaction," *AIAA Journal*, Vol. 30, 1992, pp. 2056.

CALCULATION OF THE STRUCTURE OF UNSTEADY SUPERSONIC FLOW IN A PLANE CHANNEL WITH INSTANTANEOUS LOCAL ENERGY RELEASE

V.P. Zamuraev

Institute of Theoretical and Applied Mechanics SB RAS, Novosibirsk, Russia

The effectiveness of combustion in a supersonic flow and chemical reactions in reactors depends significantly on the degree of mixing of the substances participating in the processes [1]. The mixing is largely determined by flow vorticity. One of the methods of organization of the combustion process is an electric discharge or another mechanism of initial addition of energy. Shock waves and other phenomena arise in the ignition zone, flow vorticity increases, and the temperature of the mixture becomes higher than the free-stream static temperature, whereas the added energy is rather small.

In the present paper, we study the effect of one-time local addition of low energy on the structure of a supersonic flow in a plane channel. Special attention is paid to the effect of this energy supply on the flow vorticity, on the dimensions of the zone wherein this vorticity is significant, and on the delay of this zone in the channel. We confine our consideration to the Euler equations. In contrast to [2], the energy release occurs inside the channel rather than near the wall. The varied parameters are the free-stream velocity (Mach number $M = 2 - 5$), the magnitude of the supplied energy (the corresponding pressure increases by a factor of 10 – 50 as compared to the undisturbed value), the dimensions and position of the energy-release zone. It is assumed that the size of this zone is much smaller than the channel length. A previously developed technique [3] is used to solve the problem.

PROBLEM FORMULATION

A supersonic flow in a plane constant-section channel with a local source of energy is simulated. The Euler equations in a conservative form are solved for a gas with a constant ratio of specific heats γ :

$$\partial U / \partial t + \partial F / \partial x + \partial G / \partial y = 0,$$

$$U = (\rho, \rho u, \rho v, e), F = (\rho u, p + \rho u^2, \rho uv, u(p + e)), G = (\rho v, \rho uv, p + \rho v^2, v(p + e)).$$

Here the x and y coordinates are directed along and across the channel, respectively, and normalized to the channel width d ; the time t is normalized to d/a_0 , the components of the gas velocity u and v and the velocity of sound a to a_0 , the density ρ to ρ_0 ; the pressure p and the total energy per unit volume of the gas e are normalized to $\rho_0 a_0^2$; p_0 and a_0 are the dimensional pressure and velocity of sound at the channel entrance (the corresponding density of the gas equals $\gamma \rho_0$). For the gas model under consideration, we have

$$p = (\gamma - 1) \cdot (e - \rho(u^2 + v^2)/2), \quad a^2 = \gamma p / \rho.$$

To solve these equations, the parameters of an undisturbed flow are set at the channel entrance ($x = 0$). Extrapolation is applied at the exit ($x = l$) for supersonic velocities. The no-slip conditions $v = 0$ are posed at the channel walls ($y = 0$ and 1). Initially, all the gas parameters in the entire flow region, except for a small energy-release zone, are the same as at the channel entrance. The energy-release zone is located inside the channel and has a rectangular shape

($l_1 \leq x \leq l_2$, $d_1 \leq y \leq d_2$). It is assumed that the energy is released very fast, and the gas density is not changed during the corresponding period of time, only the local pressure and temperature are changed. A higher initial pressure (and temperature) is set in this zone. The other parameters (ρ , u , and v) are the same as in the remaining part of the flow.

NUMERICAL METHOD

The posed problem is solved using the MacCormack method [4, 5] combined with a certain grid procedure. Overlapping grids are widely used in the literature to solve steady problems [6,7]. Unsteady problems are solved using two- and three-level adaptive grids with a two- to fourfold refinement of the step [8-10], and also using the method of unstructured grids [11] in which the number of connections of a given node with the neighboring ones is at most doubled. However, all these approaches require large memory resources for solving the problem considered here. In the present work, we use the technique [3], which allows one to introduce grids with a smaller (by an order of magnitude) step in some subdomains. The above approaches do not allow this because of the appearance of substantial oscillations or nonphysical waves.

In brief, the essence of this technique is as follows. The entire domain of the flow wherein the gas-dynamic equations are solved is divided into several nested subdomains. Each subdomain has its own rectangular grid with identical alignment of the cell sides. The coarsest grid is used in the external subdomain. The grids are refined in the direction from the external subdomain to the internal one. The finest grid is in the very internal subdomain, which includes the energy-release zone. These grids do not overlap.

When passing from a coarse grid to a finer one, the step can be significantly reduced, for example, by an order of magnitude. The step of integration in time decreases correspondingly. Thus, the Courant number has the same value for all subdomains, and the solution in all of them can be found using the same difference scheme.

To merge the solutions, the subdomains are extended to the neighboring ones. Two layers of the coarse grid nodes are introduced in a subdomain with the refined grid near the boundary with the subdomain with the coarse grid. The values of the flow parameters in these layers at the previous time layer are found from the values of these parameters in the nodes of the refined grid for the same time instant. This is done by linear interpolation. Because of the small step, the interpolation error is also small. The resultant parameters are used as boundary conditions for finding a solution in the coarse grid subdomain at a new time layer.

In turn, the refined grid is extended to the coarse grid subdomain for one coarse step (with refinement ratio r for r small steps). The flow parameters in additional nodes of the refined grid are also calculated by linear interpolation of their values in the coarse grid nodes. The resultant parameters are used as boundary conditions for finding a solution in the refined grid subdomain. The use of linear interpolation induces a certain error in the mass, momentum, and energy fluxes at the grid boundaries. However, as shown in [3], the appearance of this error in a second-order difference scheme does not reduce the order of its approximation and almost does not violate the conservation laws.

Using the same difference scheme (an arbitrary scheme using hydrodynamic fluxes), the calculation at a new time step is performed in each subdomain independently. Only one time step Δt is made in the subdomain of the coarse grid, whereas r steps are made in the subdomain of the refined grid, each of them being equal to $\Delta t/r$. The number of nodes in each extended subdomain, where the new parameters are calculated, is reduced on the side of the other

subdomain. As a result, the flow parameters at the new time step are known in all nodes of non-extended subdomains. This procedure does not induce oscillations and nonphysical waves.

The MacCormack scheme [4] with spatial splitting was used as a difference scheme. The order of integration with respect to coordinate axes was alternated. To improve the difference scheme properties, artificial viscosity of the fourth order was applied [5]. It is modified here, taking into account that the grid is refined in a certain subdomain.

The test computations [3] confirmed the efficiency of this numerical technique. Other types of artificial viscosity were also used in the test computations [12].

NUMERICAL RESULTS

The influence of local energy release on the structure of supersonic flow in the channel was calculated for various values of parameters of both the flow itself and the energy release. The main results presented here refer to the following case. At the channel entrance $p = 1$, $\rho = 1.4$, $u = 5$, and $v = 0$. The channel length is $l = 10$. The energy-release zone is determined by $l_1 = 4.725$, $l_2 = 4.975$, $d_1 = 0.11$, and $d_2 = 0.135$. The initial pressure in it equals $p = 50$. In this variant, the added energy is $\sim 0.38\%$ of the total energy of the gas in the channel. Figures 1 - 5 show the influence of the local energy release on the flow structure at an early stage of disturbance development ($t = 0.03$). These figures show the fields of pressure, density, Mach numbers, gas velocity, and flow vorticity, respectively (only a part of the flow domain is shown). The isobars in Fig. 1 are separated by the pressure interval equal to 0.01; in addition, an isobar equal to 0.057 is also plotted. The external isobar, which covers the disturbed flow region, is determined as $p = 0.02$ (the pressure is normalized to the initial value in the energy-release zone). The dashed lines in the figure represent the coarse grid. The refined grid is only partly shown along the external edge of an appropriate subdomain (the refinement ratio is $r = 5$). The dashed line in this subdomain shows the energy-release zone. The arrow indicates the main flow direction in the channel.

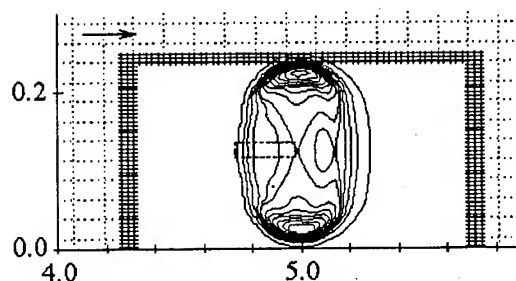


Fig. 1

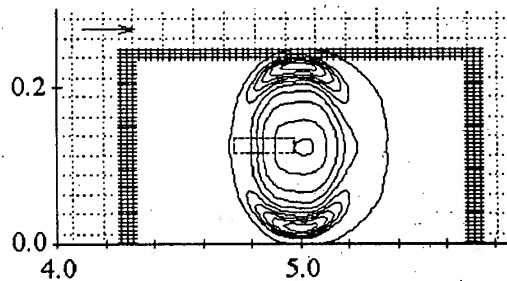


Fig. 2

The decay of an arbitrary discontinuity set at the initial time ($t = 0$) results in formation of a shock wave. At first, it is straight at some sections. The shock wave is rather strong at the sections corresponding to wave propagation across the channel. The appropriate isobars in Fig. 1 lie close to each other, and the crossflow size of the disturbed region increases rapidly. The shock wave strength decreases rapidly at the sections corresponding to the shock wave propagation upstream and downstream. This character of shock wave propagation is related to the energy source geometry ($d_2 - d_1 = 0.025 \ll l_2 - l_1 = 0.25$).

Rarefaction waves propagate inside the disturbed flow region. The interaction of rarefaction waves propagating upstream and downstream toward each other is shown in Fig. 1. Significant removal of the mass from the central part of the disturbed region leads to a drastic decrease in the gas density. This is seen from Fig. 2, which shows the density levels 0.003, 0.005, and then up to 0.045 with an interval of 0.005 (the comments to Fig. 1 given above refer also to Figs. 2, 3, and 5, in particular, the density is normalized to its initial value in the energy-release zone).

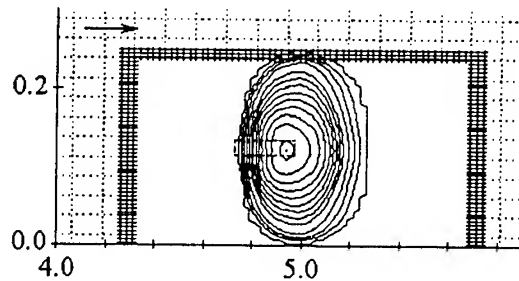


Fig. 3

The flow velocity in the central part of the disturbed region decreases. For a certain value of energy, the flow even becomes subsonic. Figure 3 shows the Mach contours with a step of 0.25 from 1.00 to 3.00, and then to 5.00 with a step of 0.50. The point in the figure corresponds to the local value of the Mach number $M = 0.954$. The arrows in Fig. 4 show the direction of the gas velocity and its magnitude in a certain scale. In the refined grid, the velocities are not given in all nodes.

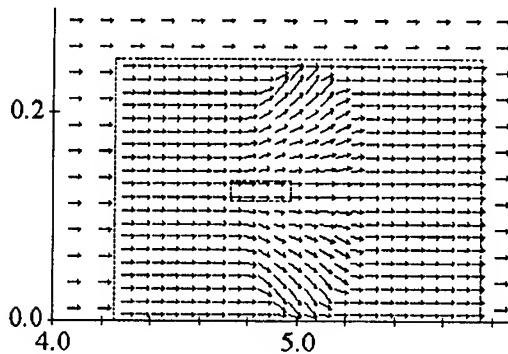


Fig. 4

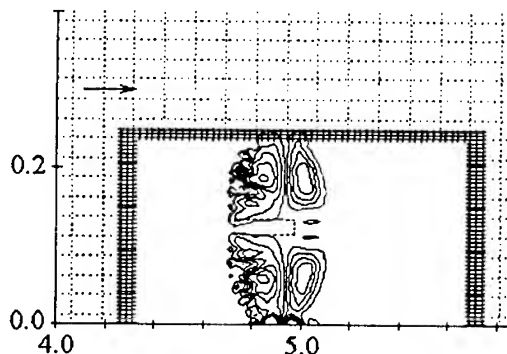


Fig. 5

Figure 5 shows the lines of constant vorticity from -18 to $+18$ with an interval 4 . Above the source of energy, it has negative values upstream of the energy-release zone and positive values downstream (in the right part of the domain); vice versa, below the source of energy, positive values are observed on the left (upstream) and negative values on the right. Thus, significant vorticity is developed in the disturbed flow region.

The further evolution of the disturbance is illustrated in Figs. 6 – 10. Figure 6 shows the pressure distribution at the time $t = 0.07$: the pressure levels from 0.02 to 0.09 are plotted with an interval 0.01. The shock wave propagating to the upper wall of the channel has passed in the coarse grid subdomain. The pressure in the shock wave reaches ~ 0.06 . The shock wave propagating downward is reflected from the lower wall. The reflected wave is curved. The greatest intensity of this wave is observed at those sections of the wave front where the shock wave propagating toward the upper wall of the channel simultaneously propagates upstream and downstream. At these sections of the wave front, the pressure behind the shock wave equals ~ 0.08 and ~ 0.09 , respectively. A rarefaction wave reflected from the channel wall propagates between them. The minimum pressure in the rarefaction wave is less than 0.05 and it is lower than its value directly on the wall. An effect similar to that observed in the case of reflection of a

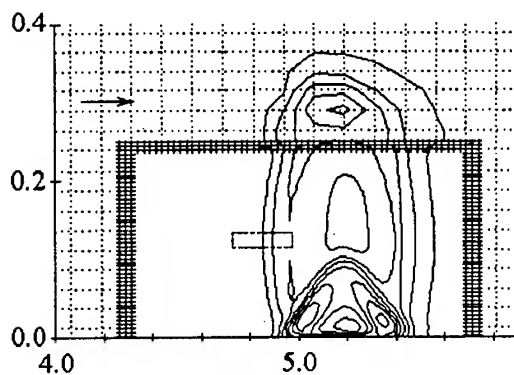


Fig. 6

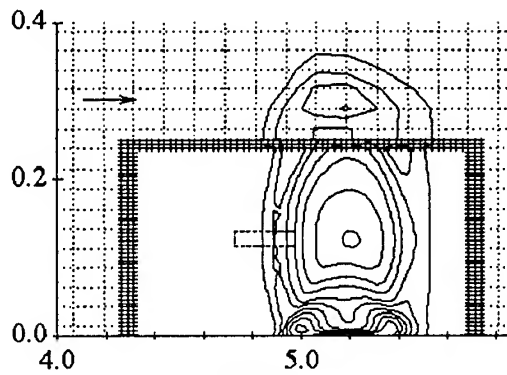


Fig. 7

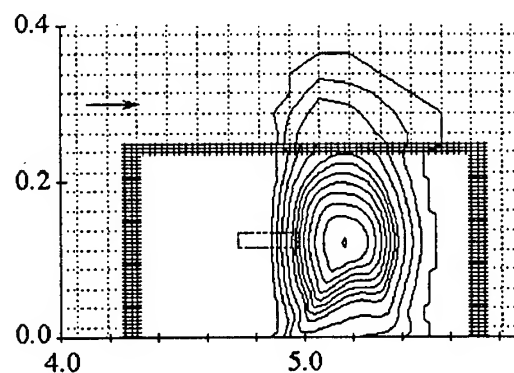


Fig. 8

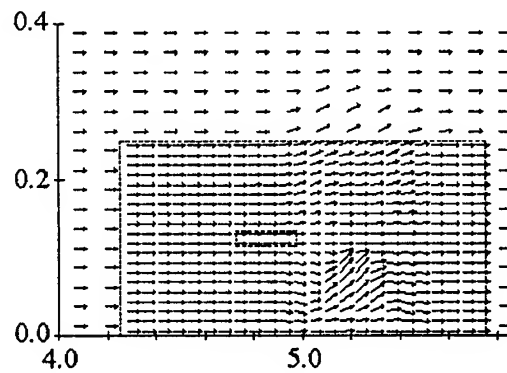


Fig. 9

centered rarefaction wave from the wall in the plane one-dimensional unsteady case [13]. When a simple reflected rarefaction wave is formed, the pressure in it becomes lower than that on the wall. This effect is complicated here by the two-dimensionality of the problem; it is related to the finite size of the energy-release zone.

The pressure in the central part of the disturbed region is also comparatively small (less than 0.03). This is associated with gas spreading. As a whole, the pressure gradients along the line passing through this part of the disturbed region along the channel are small. The gas density, as is seen from Fig. 7 (which shows the density levels for the values of ρ from 0.005 to 0.045 with an interval 0.005 and for $\rho = 0.002$), has dramatically decreased here to ~ 0.002 (more than ten times as compared to the undisturbed value). Some analogy with a strong explosion is observed [14].

It is of interest that, for the given energy release, the pressure distribution relatively weakly depends on the gas velocity u_0 at the channel entrance. This is illustrated in Fig. 11, which shows isobars for the values of p from 0.02 to 0.09 with an interval 0.01 for the time $t = 0.07$ for $u_0 = 2$ (the other parameters are the same as in the basic variant).

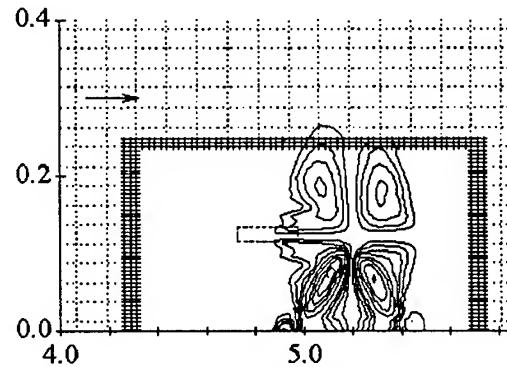


Fig. 10

The level of the Mach numbers in the disturbed flow region has already increased at the time under consideration ($t = 0.07$). The flow is supersonic everywhere. The minimum value of the Mach number is about 1.25. Figure 8 shows the Mach contours from 1.25 to 3.00 with an interval 0.25 and up to 5.0 with an interval 0.5.

The flow vorticity in the lower part of the channel has even increased. Figure 10 shows the curves of constant vorticity for the values $-24, -20, \pm 16, \pm 12, \pm 8, \pm 6, \pm 4, \pm 2$.

Upon further evolution of the disturbance, the shock wave approaching the upper wall becomes rather weak. The shock waves propagating upstream and downstream are even weaker. The local Mach number in the disturbed flow region increases but it still noticeably smaller than its undisturbed value. At the same time, the gas density in the disturbed region at a distance from the wall approximately determined by the position of the energy-release zone is several times smaller than the initial value. The dimensions of the disturbed region significantly increase. The level of flow vorticity decreases. The periodic character of energy supply seems to sustain a significant level of vorticity [2].

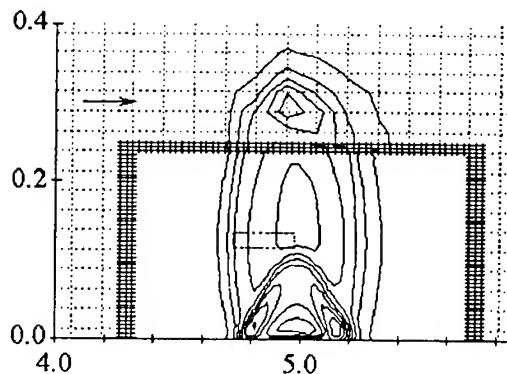


Fig. 11

REFERENCES

1. Baev V.K., Golovichev V.I., Tret'yakov P.K., et al., Combustion in Supersonic Flow. — Novosibirsk: Nauka, 1984. — 304 p.
2. Zamuraev V.P. Numerical modeling of supersonic flow in plane channel with the local source of energy // Intern. Conf. on the Methods of Aerophys. Research: Proc. Pt. 1. — Novosibirsk, 1998. — P. 239 — 244.
3. Zamuraev V.P. The influence of the local energy release on the supersonic flow in a plane duct // Thermophysics and Aeromechanics — 1999. — Vol. 6, No. 3. — P. 331 — 340.
4. MacCormack R.W. Numerical solution of the interaction of a shock wave with a laminar boundary layer // Lecture Notes in Physics. — Berlin et al.: Springer - Verlag, 1971. — Vol. 8. — P. 151 — 163.
5. Hung C.M., MacCormack R.W. Numerical solutions of supersonic and hypersonic laminar compression corner flows // AIAA J. — 1976. — Vol. 14, No. 4. — P. 475 — 481.
6. Kao K.H., Liou M.S., Chow C.Y. Grid adaptation using Chimera composite overlapping meshes // AIAA J. — 1994. — Vol. 32, No. 5. — P. 942 — 949.
7. Wang Z.J. A fully conservative interface algorithm for overlapped grids // J. Comput. Phys. — 1995. — Vol. 122, No. 1. — P. 96 — 106.
8. Berger M.J., Colella P. Local adaptive mesh refinement for shock hydrodynamics // J. Comput. Phys. — 1989. — Vol. 82, No. 1. — P. 64 — 84.
9. Quirk J.J. A Cartesian grid approach with hierarchical refinement for compressible flows // Proc. of the 2th European Computational Fluid Dynamics Conf., Stuttgart, Germany. — 1994. — P. 200 — 209.
10. Ton V.T. Improved shock-capturing methods for multicomponent and reacting flows // J. Comput. Phys. — 1996. — Vol. 128, No. 1. — P. 237 — 253.
11. Fursenko A., Sharov D. Efficient algorithms for non-stationary Euler equations // Proc. of the 2th European Computational Fluid Dynamics Conf., Stuttgart, Germany. — 1994. — P. 24 — 32.
12. Schmidt W., Jameson A. Euler solvers as an analysis tool for aircraft aerodynamics // Recent Advances in Numerical Methods in Fluids. — 1985. — Vol. 4. — P. 371 — 404.
13. Landau L.D., Lifshits E.M. Mechanics of Continuous Media. — Moscow: Gos. Izd-vo tekhniko-teoretich. lit., 1953. — 788 p.
14. Sedov L.I. Methods of Similarity and Dimension in Mechanics. — Moscow: Gos. Izd-vo tekhniko-teoretich. lit., 1957. — 376 p.

VERIFICATION OF CROSSING-SHOCK-WAVE/BOUNDARY LAYER INTERACTION COMPUTATIONS WITH THE $k-\varepsilon$ TURBULENCE MODEL

A.A. Zheltovodov, A.I. Maksimov
Institute of Theoretical and Applied Mechanics SB RAS,
Novosibirsk 630090, Russia

E. Schülein
German Aerospace Center DLR, Institute of Fluid Mechanics,
37073 Goettingen, Germany

Datta V. Gaitonde, J.D. Schmisser
Computational Sciences Branch Air Vehicles Directorate,
Air Force Research Laboratory Wright-Patterson AFB, OH 45433-7521, USA

Introduction

Experimental study and numerical modeling of crossing-shock-wave/turbulent boundary layer interactions (CSWTBLI) are of critical importance for development of efficient air-breathing propulsion systems for high speed flight. For example, this phenomenon generally degrades the flowfield quality in proposed promising scramjet designs. Development of advanced numerical methods require a comprehensive understanding of the physics of such interactions by examples of simplified canonical configurations. Among these configurations actively studied the last time there are two vertical fins mounted on a flat plate (Fig. 1). The features of these flows as well as the possibilities of their numerical modeling were reviewed in [1–4]. The surveys emphasize the fact that with increasing of CSWTBLI strength the skin-friction and heat-transfer coefficients are systematically overestimated by numerical simulations based on different turbulence models parallel with the appearance of some discrepancies in the surface flow pattern topology. To clarify possible reasons for these discrepancies, it is necessary to perform a more careful analysis of the flow structure obtained numerically for the cases with widely varied strength of the shock waves and a systematic comparison of the results with experiment.

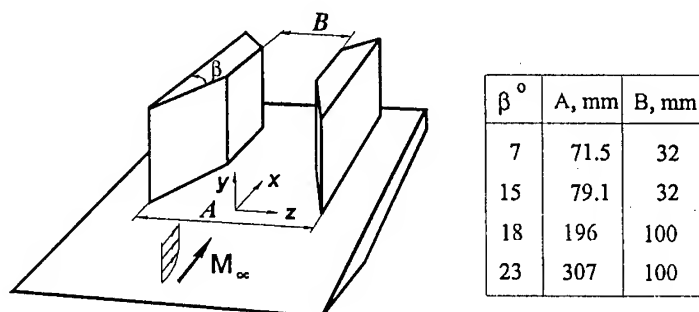


Fig. 1. Double-fin geometry

This paper is the next stage of collaborative studies [5–8] on the validation of computations with the $k-\varepsilon$ turbulence model by comparison with available experimental data.

© A.A. Zheltovodov, A.I. Maksimov, E. Schülein, D.V. Gaitonde, J.D. Schmisser, 2000

The recent publication by Zheltovodov and Schülein [9] of experimental evidence of new surface flow pattern topology for CSWTBLI with strengths far greater than those employed before has stimulated new computations by Gaitonde and Schmisser [10] as well as some additional experimental study of the crossing-shock-wave (CSW) structures. All these previous and additional new studies are used here as a background for conclusion regarding the adequacy of performed numerical computations at high range of the CSW strength.

Theoretical Model

The numerical model consists of the full three-dimensional mean compressible Navier-Stokes equations in strong conservation form and mass-averaged variables. Details may be found in [5–7, 10] and are not repeated here. Briefly, the inviscid fluxes are evaluated to nominal third-order accuracy with Roe's flux-difference split scheme together with a limiter to enforce monotonicity. Viscous terms are differenced to second-order accuracy in a centered manner. An implicit time-integration scheme, based on the Beam-Warming approach [11], is employed to march the solution to steady state. The effects of turbulence are incorporated through the eddy viscosity μ_t assumption and the turbulent Prandtl number $Pr_t = 0.90$. The turbulence model used to determine μ_t is based on the $k - \varepsilon$ equations [12, 13] with low Reynolds number terms and a compressibility correction. The computations were performed at the U.S. Air Force Research Laboratory (formerly Wright Laboratory).

Flow Conditions and Grid Geometry

To facilitate validation, the interactions examined experimentally at the Institute of Theoretical and Applied Mechanics (ITAM) SB RAS, Novosibirsk [1, 2, 14] at the Mach number $M_\infty = 4$ as well as at the German Aerospace Center DLR, Institute of Fluid Mechanics, Goettingen [9] at the Mach number $M_\infty = 5$ are used for numerical simulation. Some additional description of the experimental results [9] with tabulated surface pressure data is presented in [15]. A comparison of numerical calculations with the data obtained at ITAM is performed below for symmetric double-fin configurations with deflection angles $\beta = 7^\circ$ and 15° (Fig. 1) and the adiabatic wall conditions. The flowfield stagnation conditions are $P_0 = 1.492$ MPa, $T_0 = 260.4$ K, respectively resulting a freestream unit Reynolds number of 87.5 million per meter. The boundary layer and momentum thickness at a distance of 4δ upstream of the fin leading edge were, respectively $\delta = 3.5$ mm and $\theta = 0.13$ mm. Two symmetric double-fin configurations are examined, one with $\beta = 18^\circ$ and the other with 23° in accordance with the studies performed at DLR [9]. The stagnation conditions $P_0 = 2.2$ MPa and $T_0 = 427$ K, resulting in a freestream unit Reynolds number of 36.5 million per meter. The wall temperature is $T_w = 295$ K. The boundary layer and momentum thickness are $\delta = 3.8$ mm and $\theta = 0.157$ mm at a distance of 6δ upstream of the fin leading edge.

Due to the configuration symmetry, only half the domain is computed [5, 6, 8, 10]. On the symmetry plane, all gradients are set to zero with the exception of the normal velocity which is itself set to zero instead. On the solid surfaces the no-slip boundary condition is invoked, with k , ε and the normal pressure gradient specified to be zero. The incoming boundary-layer profile is specified at the indicated positions upstream of the fin leading edges by matching the momentum thickness with two-dimensional calculations. At the outflow and top boundaries, zero-gradient extrapolation boundary conditions are applied.

The grid employed for each simulation is composed of sequential non-uniform Cartesian planes oriented normal to the freestream direction. Gridpoints are clustered to resolve the secondary features of the interior vortical flowfield, with the location of the clustered regions determined from previous experience. For the $7^\circ \times 7^\circ$ weak interaction and $15^\circ \times 15^\circ$ mild interaction cases the solutions were computed on the meshes with 9.9×10^5 and 1.9×10^6 points [5, 6]. Based on these studies, 123 and 88 points were employed in the streamwise ($X = x/\delta$) and normal to the plate directions ($Y = y/\delta$), respectively. The spanwise ($Z = z/\delta$) direction was resolved with 109 points.

For the strongest, $23^\circ \times 23^\circ$ interaction, the solution was computed on several meshes with various grid spacings to yield some indication of the degree of mesh independence [10]. A summary of the parameters for each mesh is presented in Table 1 where IL, JL and KL represent the number of grid points in the streamwise, plate-normal and spanwise directions respectively. The finest mesh, Mesh 3, has about twice as many points as Mesh 2 and consists of 5.3×10^6 mesh points. Convergence of the solution is determined from monitoring the global norm, surface pressure and skin friction coefficients.

Table I. Grid configurations

Fin Angle / Resolution	IL \times JL \times KL
18 deg.	153 \times 143 \times 103
23 deg. Mesh 1	91 \times 72 \times 52
23 deg. Mesh 2	181 \times 143 \times 103
23 deg. Mesh 3	229 \times 179 \times 129

Comparison of Computations with Experiment

As it follows from experimentally registered oil-flow visualization on a bottom plate for the $7^\circ \times 7^\circ$ configuration (Fig. 2, a), a local (singular) separation appears immediately ahead of the vertices of the fins, and the separation lines S_1 and S_2 emanating from saddle points [1] rather rapidly degenerate to finite-width convergence regions slightly higher than the traces of the shock waves (dashed lines) corresponding to the inviscid part of the flow. The limiting streamlines in these regions begin to curve in the region of the upstream influence lines (indicated by the dash-dotted lines and marked U) and asymptotically approach each other to form a narrow region of parallel flow in the direction toward the channel axis. Some streamlines penetrating downstream in the vicinity of the symmetry axis converge to form a characteristic throat. The

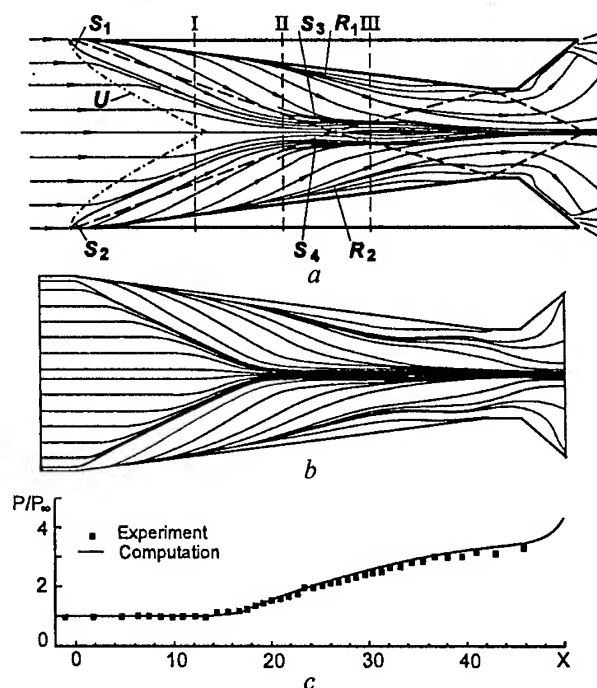


Fig.2. Surface flow patterns (a, b) and pressure distribution (c) for $7^\circ \times 7^\circ$ interaction

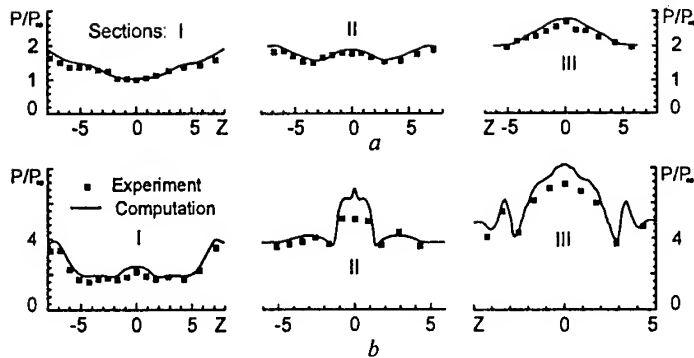


Fig. 3. Surface pressure in cross sections for $7^\circ \times 7^\circ$ (a) and $15^\circ \times 15^\circ$ (b) interactions

flow penetrates through this fluidic throat without any signs of separation. The interaction of intense secondary flows propagating from the divergence lines R_1 and R_2 and the flow passing through the throat results in the formation of secondary convergence lines S_3 and S_4 which may be considered as indication of incipient secondary separation. In the computations, the same main features in the skin-friction line pattern are evidenced in such weak interaction case (Fig. 2, b). Nevertheless, we should note a smaller width of the flow penetrating through the throat near the channel centerline and the absence of the secondary convergence lines S_3 and S_4 .

The computed surface pressure distributions along the channel centerline (Fig. 2, c) and in three cross-sections I, II and III (Fig. 3, a) respectively at $X = 13.14$, 22.57 and 32.0 (the sections are indicated also in Fig. 2, a) are in good agreement with the experimental data.

In the $15^\circ \times 15^\circ$ case, the experiment shows (Fig. 4, a) that the convergence regions transform to the separation lines S_1 and S_2 , and the attachment lines R_1 and R_2 which become more definite. The secondary separation lines S_3 and S_4 become more clearly distinct under

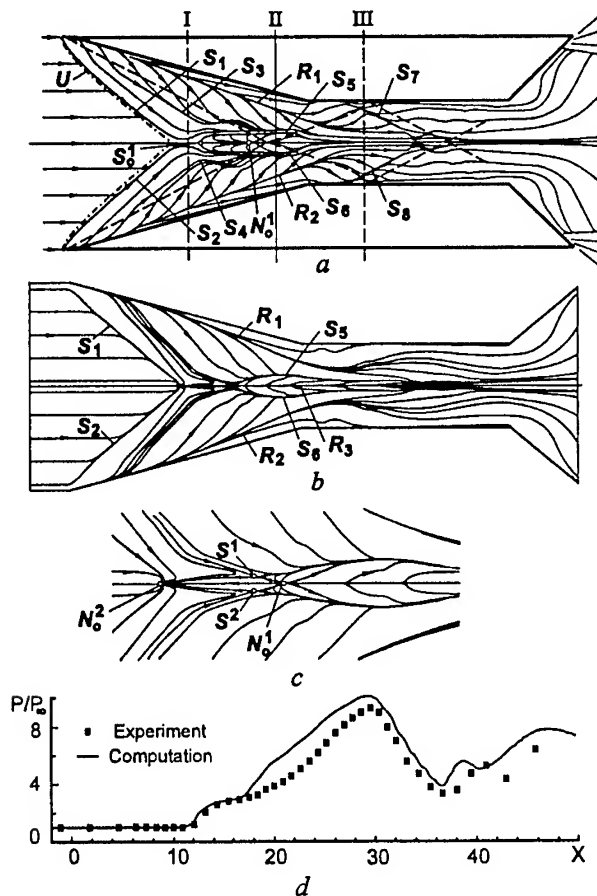


Fig. 4. Surface flow patterns (a, b) and pressure distribution (c) for $7^\circ \times 7^\circ$ interaction

the secondary flow propagating from the lines R_1 and R_2 in such mild interaction case. A large-scale separation region is formed in the throat behind the centerline singular saddle point S_0^1 and bounded by the separation lines S_5 and S_6 . The centerline node point N_0^1 was observed further downstream. The line S_3 is very close to merge with S_5 (and so is S_4 with S_6 on the opposite side) approximately in the middle of the central separated zone. The computed topology is somewhat different: the primary separation lines intersect at the centerline node N_0^2 and therefore, no fluidic throat but as in experiment, another centerline node N_0^1 is observed (Fig. 4, *b, c*). This is more clearly shown in an enlarged fragment in Fig. 4, *c*. Unsteady intermittent nature of the real flow upstream of the singular separation point S_0^1 [1, 8, 17] (Fig. 4, *a*) not predicted by computations may be by a reason of such discrepancy. Additional features, which were not registered in experiment, are two saddle points S^1 and S^2 located symmetrically about the centerline (Fig. 4, *c*).

The calculations do not reveal the signs of the secondary separation lines S_3 and S_4 and the central separated zone is more compressed by the flows propagating from the fins and noticeable smaller in width comparing with experiment (Figs. 4, *a, b*). As result, the computed surface pressure is noticeably overestimated in the vicinity of the channel centerline for $X > 17$ (Fig. 4, *d; 3, b*). This discrepancy may be related to a difference in the turbulence level in the near-wall region of the secondary flows between experiment and computation. Such a statement is supported by previous experiments [16] with sand-grain roughness mounted in the secondary flow region, between the divergence and convergence lines of one-fin configurations. By such way, the experiments demonstrated that the secondary separation could be suppressed for weak and some mild interactions by amplifying turbulence in the secondary flow. In accordance with experiments [16] and recent computations [18] the turbulence suppressing stimulated the appearance of the secondary separation lines.

Figures 5 and 6 depict both the experimentally inferred and computed surface streamlines for much stronger the $18^\circ \times 18^\circ$ and $23^\circ \times 23^\circ$ interactions at the Mach number $M_\infty = 5$. As shown in [9], the increasing of fins angles in the range $\beta = 16^\circ - 18^\circ$ stimulates complex surface flow topology transformation. The primary separation lines S_1, S_2 merged in the $17^\circ \times 17^\circ$ case and only small central separation zone appeared in this place. This local zone with two symmetric node/foci N_1 and N_2 off the centerline was limited upstream and downstream by two centerline saddle points S_0^1 and S_0^2 . Two symmetric secondary coalescence lines S_3 and S_4 and centerline divergence line R_3 existed downstream after this separated zone. In the $18^\circ \times 18^\circ$ and $23^\circ \times 23^\circ$ cases the reversed flow appeared and penetrated from the downstream located node N_0^1 (in the apex of the centerline divergence line R_3) to the first separation saddle

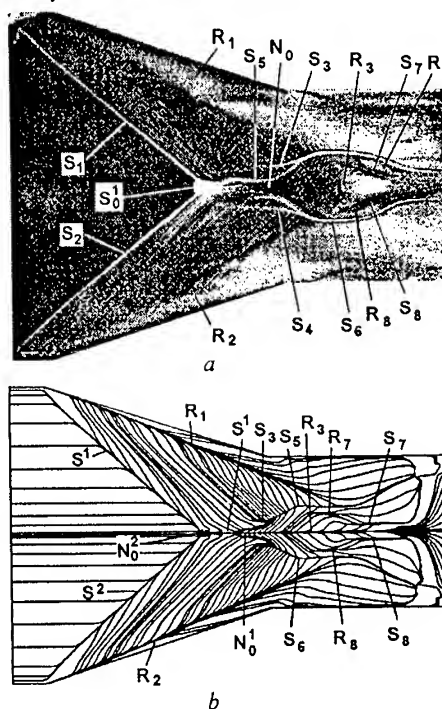


Fig.5. Surface flow patterns for $18^\circ \times 18^\circ$ interaction

point S_0^1 . The rear centerline saddle point S_0^2 may be considered to have bifurcated into the two saddles S^1 and S^2 off centerline on either side. These features are shown in an enlarged fragment in Fig. 6, *b* for the $23^\circ \times 23^\circ$ case. Two symmetric foci N^1 and N^2 exist in the points where the central separation line intersects the primary separation lines S_1 and S_2 [9]. The oil-paint mixture that used for the visualization converged and penetrated to the region in the vicinity of central separation line limited by dotted line. So, the interpretation of surface flow pattern in this region is difficult as well as in two regions located downstream the saddles S^1 , S^2 and limited by dotted lines. Nevertheless, an existence of the divergence lines can be supposed in these two regions. Similar features exist also in the $18^\circ \times 18^\circ$ case but not indicated in the Fig. 5, *a*.

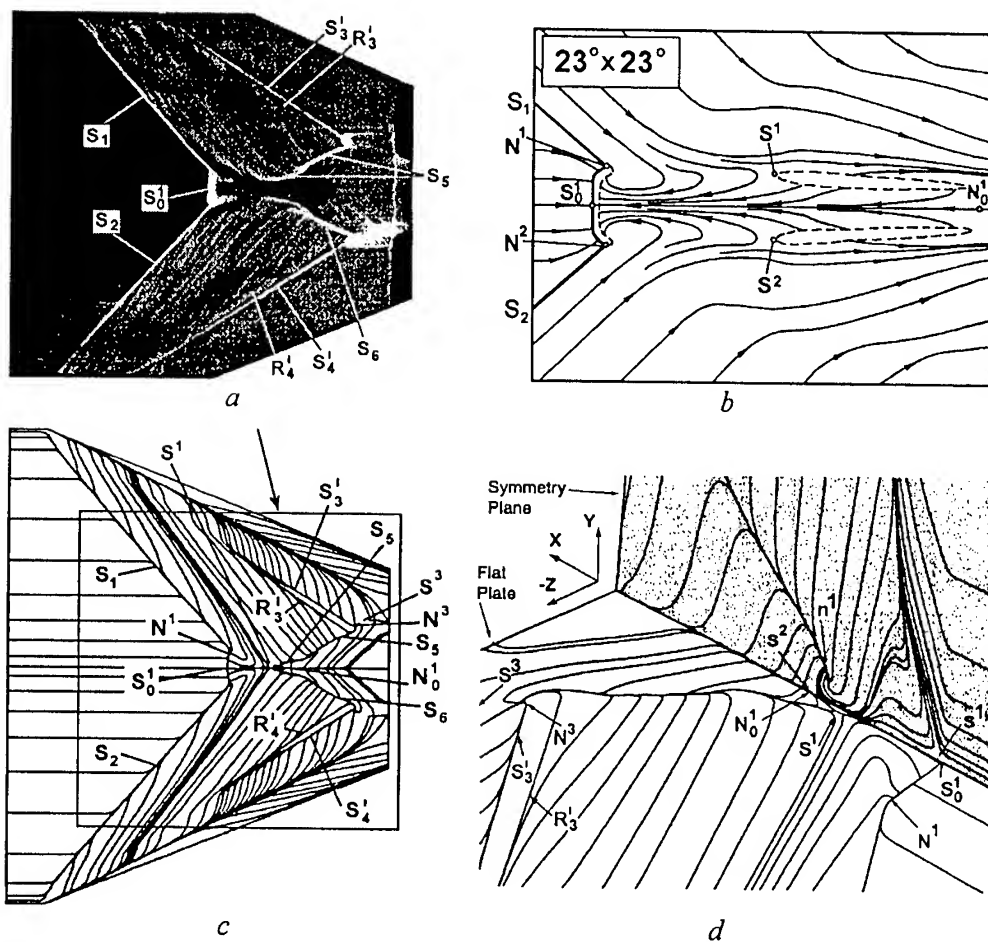


Fig. 6. Surface flow patterns for $23^\circ \times 23^\circ$ interaction

The computed "surface streamlines" for the $18^\circ \times 18^\circ$ case (Fig. 5, *b*) is identical to the Mach 4 $15^\circ \times 15^\circ$ case (Fig. 4, *b*, *c*) from the standpoint of number and types of critical points and again demonstrate some discrepancy with the experiment where the saddle point S_0^1 but not the node N_0^2 exists on the centerline (Fig. 5, *a*). Nevertheless, the appearance of additional saddle point S^1 and its mirror counterpart S^2 off the centerline is supported by experiment [9].

All other features are evident for this more stronger interaction, marked in the experimental oil flow as separation lines (S_1, S_3, S_5, S_7), attachment lines (R_1, R_3, R_7) and their counterparts on the opposite side ($S_2, S_4, S_6, S_8, R_2, R_3, R_8$). Figure 7 depicts the spanwise pressure at several planes for the $18^\circ \times 18^\circ$ interaction. In this case the computations show overall good agreement with the experimental data in the major portion of the domain. Near the symmetry plane however, while the trends are reproduced, significant quantitative discrepancies are evident. Although both experiment and computations exhibit a rapid rise in pressure on approaching $Z \sim 0$, the computational values are substantially higher.

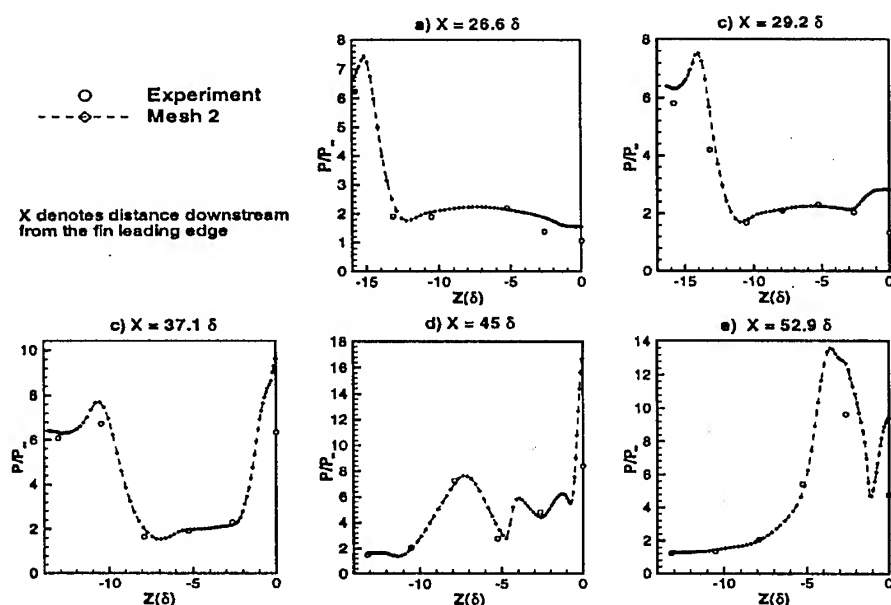


Fig. 7. Surface flow distributions for $18^\circ \times 18^\circ$ interaction

The computations for the strongest $23^\circ \times 23^\circ$ interaction (Figs. 6, c, d) reproduce accurately main topological features revealed by the experiments (Figs. 6, a, b). To specify details of the flowfield topology an enlarged fragment of the kinematic structure is shown in Fig. 6, d in accordance with the computations [10]. Also shown are select streamlines in the symmetry plane normal to the plate. These streamlines may be interpreted as intersections of streamsurfaces with the symmetry plane. Critical points on the symmetry plane are designated by lower case letters. The streamline structure on the symmetry plane exhibits the presence of two half-saddles at the surface (s^1 and s^2) and a focus/node above the surface (n^1). On the plate surface the two primary lines of coalescence each terminate into off-centerline foci (N^1 and its mirror counterpart N^2). A new saddle-point S_0^1 is observed on the centerline as in the experiment and is linked to each of the foci (N^1) through lines of coalescence. Although there is a clear distinction between these lines on the one hand and the primary lines of separation (S^1 and S^2) on the other – they are separated by a node (N^1) – at present separate designators are not employed. In accordance with the computations the upstream separated boundary layer and vortex interaction regions separate on either side of the primary separation line, but near the interaction centerline the two regions intertwine to form two vortex filaments that leave the surface at the two foci on either side of the interaction centerline. (The vortex interaction region contains the fluid that attaches near the fin

and sweeps spanwise from the fin to separate on the downstream side of the primary separation line [10]). In a simplistic sense, the separated boundary layer sheet forms kinks due to the vortex filaments associated with the node N^1 and its mirror image. Such features are in good agreement with the experimental maps (Fig. 6, *a, b*).

The next aspect examined is that of secondary separation S_3-R_3 pair and its counterpart (S_4-R_4 , Figs. 6, *a, c, d*). Although commonly observed in delta wing flows, the phenomenon is relatively rare in shock/turbulent boundary layer interactions. It has previously been reported in experimental observations of the single fin configuration in strong interactions [16, 19, 20]. In accordance with computations (Fig. 6, *c, d*) the secondary separation line S_3 as well as S_5 downstream, terminate in a node-saddle (N^3-S^3) combination. Such conclusion is in agreement with the experiment. Additional local shock wave appeared above the secondary separation lines S_3 and S_4 in the computations as was predicted by experiments [16, 19, 20]. It is important to note that the secondary separation line (S_3) appearance between the lines S_1 and R_1 in the vicinity of fins (Fig. 4, *a*), disappearance in some mild interaction case (Fig. 5, *a*) and reappearance in the strongest interaction case, but in different position (S_3 , Fig. 6, *a*), are in agreement with previous experimental studies [16, 19] of one-fin interaction. As it was concluded in the papers, such complex phenomena stimulated by the change of the secondary flow in the interaction region from laminar to turbulent state parallel with its acceleration to supersonic speeds. So, the numerical modeling of such phenomena is very important but rather difficult.

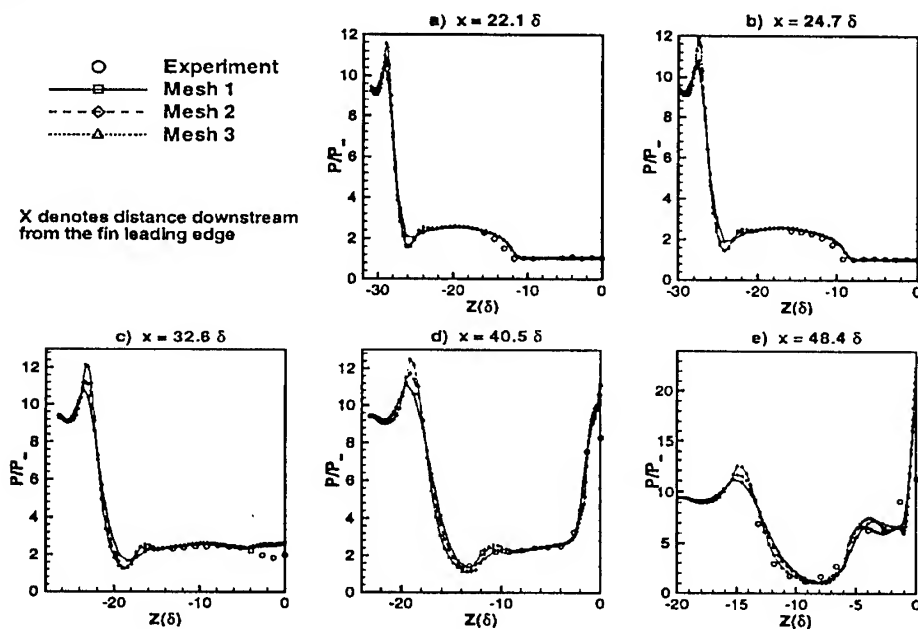


Fig. 8. Surface pressure distributions for $23^\circ \times 23^\circ$ interaction

In Fig. 8, the spanwise surface pressure distributions for the $23^\circ \times 23^\circ$ interaction are compared at several streamwise stations with the experimental data. At the anterior stations, $X = 22.1$ and 24.7δ , the pressure profile is similar to that of the well-documented single-fin interaction and results from all three meshes exhibit close agreement with available experimental data. Further downstream, $X = 32.6\delta$, the pressure profile exhibits the impact of

the shock system due to the opposing fin. With the exception of regions near the location of the peak pressure – shown subsequently to correspond to flow attachment near the fin plate corner – the solutions are relatively well-resolved. Nevertheless, near the symmetry plane, while the trends are reproduced, significant quantitative discrepancies are evident as in the $18^\circ \times 18^\circ$ case.

A final comment is made regarding the shock structure in the external inviscid flow. Figures 9, *a*, *b* show the computed shock structure, plotted again with the magnitude of the three-dimensional pressure gradient, at the top boundary plane. It is evident that the primary shocks cross each other in a regular fashion for the $18^\circ \times 18^\circ$ interaction (Fig. 9, *a*) but form a Mach stem or irregular crossing in the $23^\circ \times 23^\circ$ case (Fig. 9, *b*). The regular reflection for the $18^\circ \times 18^\circ$ case is supported by the optical visualization on a basis of the surface reflective visualization technique (SRV) [9] as well as by additional visualization which has been performed on a basis of the high-speed shadowgraphy. In the second case the glass plate in the region of the crossing shock waves has been applied. To obtain the instantaneous shock waves images the CCD camera (with 30 frames/s) synchronized with the 30 ns spark that was used as a light source. The shock waves photography for the $23^\circ \times 23^\circ$ interaction has detected the regular reflection with high level of unsteadiness but not the Mach reflection predicted by the numerical simulation (Fig. 9, *c*). For the comparison in the figure together with the crossing-shock-waves image a variation of their position with a time is

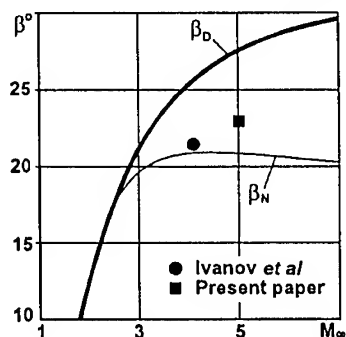


Fig. 10. The boundaries of regular and Mach reflection regions

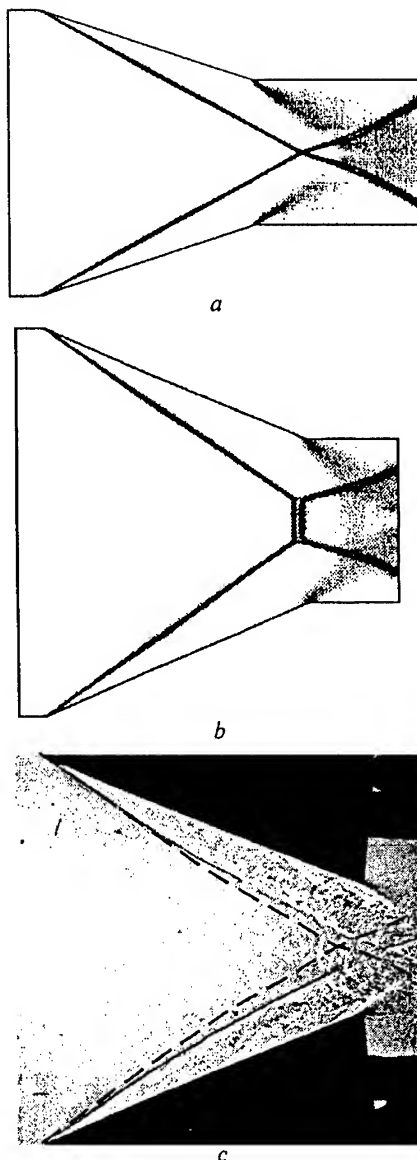


Fig. 9. Shock-wave structure in the $18^\circ \times 18^\circ$ (*a*) and $23^\circ \times 23^\circ$ (*b*, *c*) interactions

drawn by dotted lines. The oscillation period can be estimated as fraction of a second. It is necessary to note that similar features have been detected in the vicinity of the isolated double-wedge configuration (without the plate) at the Mach number $M_\infty = 4$ in [21].

In accordance with Fig. 10 such unsteady regular reflection regime exists between the boundaries that are determined by so called von Neumann (β_N) and detachment

(β_D) criteria. These additional experimental studies specify preliminary conclusions [10] concerning the crossing-shock-wave structure for the $23^\circ \times 23^\circ$ case. For this case the possibility of hysteresis cannot be discounted since such irregular crossings are known to be susceptible to hysteresis phenomena [21, 22]. A coupled effect concerns three-dimensionality: small perturbations even if introduced in the initial transients can influence the final observed shock-crossing pattern particularly if the flow parameters lie near a bifurcation boundary.

Conclusions

A systematic comparison of experimental and CFD results has been considered in the cases of weak ($7^\circ \times 7^\circ$) and mild ($15^\circ \times 15^\circ$) CSWTBLI at the Mach number $M_\infty = 4$ as well as strong ($18^\circ \times 18^\circ$) and very strong ($23^\circ \times 23^\circ$) interactions at $M_\infty = 5$. The topological features of such flows, surface pressure distributions in the interaction regions and the crossing-shock-wave structures have been examined in great detail. Experiment and CFD agree on a lot of main features at various stages of the flows development. The topological features, as well as pressure distribution, are in close agreement in the weak interaction case. Moderate to significant discrepancies occur in the mild and strong interactions in topology predicting on the stages of the central separated zone and secondary separation appearance and development. Nevertheless, they are successfully predicted for very strong interaction case. The pressure is always correctly predicted, except the centerline region, where it is significantly over-estimated in the mild, strong and very strong interaction cases. The primary origin of the discrepancies between experiments and computations may be the turbulence level in the secondary flow: it seems to be much lower in the experiments than in computations. The unsteady nature of turbulent separation might also explain some discrepancies evidenced in the vicinity of singular separation points and the secondary separation lines. The discrepancy between the computations and experiment in the crossing-shock-wave structure on a stage of the Mach stem appearance in very strong interaction is detected.

Acknowledgments

The authors affiliated with ITAM were supported by the Russian Foundation for Basic Research (project code 97-01-00885) and the European Office of Aerospace Research and Development (EOARD contracts No. F61708-97-W0136 and F61775-98-WE091 monitored by C. Raffoul). Some of experimental investigations were performed at the DLR Institute of Fluid Mechanics during a visit of the first author as Visiting Scientist and supported by the German Research Association (DFG grant No. 436 RUS 17/29/97). The authors affiliated with Air Force Research Laboratory Wright-Patterson AFB are grateful for AFOSR sponsorship under tasks monitored by R. Canfield and S. Walker. This work was also supported in part by a grant of HPC time from the DoD HPC Shared Resource Centers at CEWES and NAVO. The authors acknowledge several insightful communications with J. Shang, M. Visbal and A.E. Medvedev.

References

1. Zheltovodov A.A., Maksimov A.I., Shevchenko A.M. Topology of three-dimensional separation under the conditions of symmetric interaction of crossing shocks and expansion waves with turbulent boundary layer // *Thermophys. and Aeromech.* 1998. Vol. 5, No. 3. P. 293-312.
2. Zheltovodov A.A., Maksimov A.I., Shevchenko A.M., Knight D.D. Topology of three-dimensional separation under the conditions of asymmetrical interaction of crossing shocks and expansion waves with turbulent boundary layer // *Thermophys. and Aeromech.* 1998. Vol. 5, No. 4. P. 483-503.

3. Knight D.D. Numerical simulation of compressible turbulent flows using the Reynolds-averaged Navier – Stokes Equations // *Turbulence in Compressible Flows*, Advisory Group for Aerospace Research and Development, June 1997, AGARD Report, No. 819, p. 5-1 – 5-52.
4. Knight D.D., Degrez G. Shock wave boundary layer interaction in high Mach number flows. A critical survey of Current CFD prediction capabilities // *Hypersonic Experimental and Computational Capability, Improvement and Validation*, Advisory Group for Aerospace Research and Development, AGARD Report. December 1998. No. 319. Vol. II. P. 1-1 – 1-35.
5. Gaitonde D., Shang J.S., Garrison T.J., Zheltovodov A.A., Maksimov A.I. Evolution of the separated flowfield in a 3-D shock wave/turbulent boundary layer interaction. AIAA 97-1837, June 1997.
6. Gaitonde D., Shang J.S., Garrison T.J., Zheltovodov A.A., Maksimov A.I. Three-dimensional turbulent interactions caused by asymmetric crossing-shock configurations // AIAA J. 1999. Vol. 37, No.12. P.1602-1608.
7. Gaitonde D.V., Visbal M.R., Shang J.S., Zheltovodov A.A., Maksimov A.I. Parametric study of flowfield structure and validation issues in 3-D crossing- shock wave/turbulent boundary layer interactions // *Int. Conf. on the Methods of Aerophys. Research: Proc. Pt. 1. Novosibirsk, Russia 29 June – 3 July 1998. Novosibirsk, 1998. P. 67–80.*
8. Zheltovodov A.A., Maksimov A.I., Gaitonde D.V., Visbal M.R., Shang J.S. Experimental and numerical studies of symmetric crossing-shock-wave/turbulent boundary layer interaction // *Thermoph. and Aeromech.* 2000. Vol. 7, No 2.
9. Schüle E., Zheltovodov A.A. Development of experimental methods for the hypersonic flows studies in Ludwig tube // *Intern. Conf. on the Methods of Aerophys. Research: Proc. Pt. I. Novosibirsk, Russia 29 June – 3 July, 1998. Novosibirsk, 1998. P. 191–199.*
10. Schmisser J.D., Gaitonde D.V. Numerical investigation of new topologies in strong crossing shock-wave/turbulent boundary layer interactions. AIAA 2000–0931, 2000, 13 p.
11. Beam R., Warming R. An implicit factored scheme for the compressible Navier – Stokes equations // AIAA J. 1978. Vol.16, No. 4. P. 393–402.
12. Jones W.P., Launder B.E. The prediction of laminarization with a two-equation model of turbulence. *Int. J. of Heat and Mass Transf.* 1972. No.15. P. 301–314.
13. Launder B.E., Sharma A.I. Application of the energy dissipation model of turbulence to the calculation of flows near a spinning disk // *Letters in Heat and Mass Transfer.* 1974. No. 1. P.131–138.
14. Zheltovodov A.A., Maksimov A.I. Symmetric and asymmetric crossing-shock-waves/turbulent boundary layer interactions: EOARD Rep. F61708-97-W0136. Novosibirsk: ITAM SB RAS, 1998. 76 p.
15. Zheltovodov A.A., Maksimov A.I. Hypersonic crossing-shock-waves/turbulent boundary layer interactions: EOARD Rep. F61775-98-WE091. Novosibirsk, ITAM SB RAS, 1999. 78 p.
16. Zheltovodov A.A., Maksimov A.I., Schüle E. Development of turbulent separated flows in the vicinity of swept shock waves // *The Interactions of Complex 3-D Flows. Novosibirsk: ITAM USSR Acad. Sci., Siberian Branch, 1987. P. 67-91.*
17. Dolling D.S. Unsteady phenomena in shock wave-turbulent boundary layer interactions // *Turbulent Boundary-Layer Interactions in Supersonic and Hypersonic Flows*, Advisory Group for Aerospace Research and Development, August 1993. AGARD Report. 1993. No. 792. P. 4-1 – 4-46.
18. Panaras A. G. Algebraic turbulence modeling for swept shock-wave/turbulent boundary-layer interactions // AIAA J. 1997. Vol. 35, No.3. P. 456–463.
19. Zheltovodov A.A. Regimes and properties of 3D separated flows initiated by swept shock waves // *J. Appl. Mech. Techn. Phys.* 1982. No. 3. P. 116–123.
20. Knight D.D., Horstman C.C., Settles G.S., Zheltovodov A.A. Three-dimensional shock wave/ turbulent boundary layer interactions generated by a single fin // *Thermophys. and Aeromech.* 1998. Vol. 5, No. 2. P. 131–140.
21. Ivanov M.S., Klemenkov G.P., Nikiforov S.B., Pavlov A.A., Kharitonov A.M., Fomin V.M. Wind tunnel experiments on shock wave reflection transition and hysteresis. 22nd Intern. Symp. on Shock Waves: Paper 1121. Imperial College, London, UK, July 18–23, 1999. London, 1999. 6 p.
22. Hornung H. Regular and Mach reflection of shock waves // *J. Fluid Mech.* 1986. Vol. 18. P. 33–58.

Contents

1. A.R. Ablav, A.V. Dovgal, G.R. Grek, M.M. Katasonov, and V.V. Kozlov. Experimental investigation of localized disturbances in a separation bubble	5
2. N.P. Adamov, M.D. Brodetsky, V.M. Gilyov, M.S. Ivanov, A.E. Medvedev, and O.N. Mosseichuk. Shareable database of aerodynamic experiments and computations	10
3. N.P. Adamov, M.D. Brodetsky, A.M. Kharitonov, A.V. Zabrodin, and A.E. Lutsky. Numerical and physical modeling of supersonic flow around separating winged bodies	16
4. S.M. Aulchenko, A.F. Latypov, and Yu.V. Nikulichev. The study of influence of airfoils contour approximation on its rating characteristics	22
5. V.K. Baev and V.V. Shumskii. Effect of fuel type on the thrust characteristics of ramjet engines	27
6. V.K. Baev, G.V. Klimchik, A.D. Frolov, and D.V. Chusov. A method for calculation of hydraulic and thermal characteristics of the disk rotor machines with tangential input and output of the working body	33
7. W.H. Beck. Aerothermodynamics at the DLR Göttingen. Experimental and numerical tools	40
8. V.I. Borodulin, Y.S. Kachanov, and D.B. Koptsev. Study of resonant instability wave interaction in self-similar boundary layer with adverse pressure gradient.	47
9. M.D. Brodetsky, A.M. Kharitonov, E. Krause, A.A. Pavlov, S.B. Nikiforov, and A.M. Shevchenko. Experimental investigation of the supersonic flow on the lee side of a delta wing: experimental techniques and results	53
10. D.A. Buntin, A.A. Sidorenko, and A.N. Shiplyuk. The development of natural disturbances in hypersonic boundary layer on a sharp cone.	59
11. V.G. Chernoray, A.A. Bakchinov, V.V. Kozlov, and L. Lofdahl, Experimental study of K-regime of breakdown in STRAIGHT and swept wing boundary layers	65
12. N.N. Fedorova, I.A. Fedorchenko, and E. Schülein. Impinging shock wave/flat plate turbulent boundary layer interaction at $M = 5$ (experiments and computations)	71
13. V.M. Fomin, Th. Alziary de Roquefort, A.V. Lebedev, and A.I. Ivanchenko. Gasdynamic and electric phenomena on glow discharge in supersonic air flow	79
14. V.M. Fomin, Th. Alziary de Roquefort, A.V. Lebedev, and A.I. Ivanchenko. Influence of a hypersonic air flow on electric characteristics of the self-sustaining glow discharge	85
15. V.M. Fomin, Th. Alziary de Roquefort, A.V. Lebedev, and A.I. Ivanchenko. Influence of near-electrode region on the effect of interaction of the glow discharge and supersonic air flow	89

16. A.F. Garanin and A.I. Glagolev. Pressure variation on the face section of the body of revolution with a spike at its length variation, geometry and blowing out inert gas from the spike	94
17. Yu.P. Goonko and I.I. Mazhul. Some hypersonic inlet/airplane interactions	98
18. Yu.P. Goonko, A.N. Kudryavtsev, I.I. Mazhul, and R.D. Rakhimov. Some comparison of flows around hypersonic aircraft whose forebodies are integrated with two-dimensional and three-dimensional-convergent inlets	104
19. Yu.P. Goonko, A.M. Kharitonov, A.N. Kudryavtsev, I.I. Mazhul, and R.D. Rakhimov. Aerodynamics of a convergent inlet integrated with a forebody convergent-compression surface	110
20. M. Habermann, H. Olivier. Upgrade of the Aachen shock tunnel with a detonation driver	116
21. M.S. Ivanov, A.N. Kudryavtsev, D.V. Khotyanovsky, and G.N. Markelov. Numerical study of 3D regular and Mach reflections of steady shock waves	122
22. M.S. Ivanov, G.P. Klemenkov, A.N. Kudryavtsev, S.B. Nikiforov, A.A. Pavlov, A.M. Kharitonov, and V.M. Fomin. Experimental investigation of 3d steady shock wave interaction	128
23. Y.S. Kachanov, D.B. Koptsev, and B.V. Smorodsky. Suppression of 3D vibration receptivity of boundary layer by an adverse pressure gradient	134
24. V.I. Kornilov, S.B. Nikiforov, and A.A. Pavlov. Skin friction measurements by oil film method utilising diffuse light scattering for image registration	140
25. A.A. Kuraev. Comparative method to determine the nozzle flow coefficient	145
26. B.M. Melamed and V.N. Zaikovskii. An experimental investigation of vortex structures in srm duct with a star-shaped channel	147
27. S.G. Mironov. Electron-beam diagnostic of density disturbances in highly underexpanded laminar jets	152
28. V.I. Penkovsky. Capillary locking effects in processes of immiscible displacement	156
29. T.V. Poplavskaya. About calculation of a hypersonic viscous shock layer on a cone at zero incidence	160
30. T.V. Poplavskaya. Influence of energy supply in free stream on stability of hypersonic boundary layer on cone-cylinder	166
31. A.V. Potapkin, D.Yu. Moskvichev, and A.I. Trubitsin. Hysterises of the acoustic and thrust characteristics of the ramjet combustion chamber at vibration regimes of fuel combustion	171
32. W. Schröder and A. Henze. Numerical analysis of flows over space transportation systems	177
33. N.V. Semionov. Definition of a receptivity factors of supersonic boundary layer from experimental data	183

34. N.V. Semionov, G.I. Klinkova, A.D. Kosinov, V.Ya. Levchenko. Development of natural disturbances in the supersonic boundary layer on a swept wing	189
35. F. Thivet, D.D. Knight, and A.A. Zheltovodov. Computation of crossing-shock-wave/boundary-layer interactions with realizable two-equation turbulence models	195
36. S.S. Vorontsov, V.A. Zabaikin, P.K. Tretyakov, V.V. Pickalov, A.V. Postnov, N.V. Chugunova, C. Bruno, M. Filippi. Use of modern optical methods for supersonic diffusion flame structure research	202
37. V.I. Yakovlev, P.V. Grigoryev. Method of investigation of relaxation in shock waves	207
38. H. Yan, G. Urbin, D. Knight, and A. Zheltovodov. Compressible large eddy simulation using unstructured grid: supersonic boundary layer and compression ramps	215
39. V.P. Zamuraev. Calculation of the structure of unsteady supersonic flow in a plane channel with instantaneous local energy release	225
40. A.A. Zheltovodov, A.I. Maksimov, E. Schülein, D. V. Gaitonde, and J.D. Schmisser. Verification of crossing-shock-wave/boundary layer interaction computations with the $k - \varepsilon$ turbulence model	231
C o n t e n t s	242

International Conference on the Methods of Aerophysical Research:
Proc. Pt I /Ed. by A.M. Kharitonov. — Novosibirsk: Publishing House
of Siberian Branch of RAS, 2000. — 244 p.

Ответственный за выпуск А.М. Аульченко
Технический редактор Т.В. Ветровская
ЛР № 020909 от 01.09.99

Формат бумаги 70 × 100 / 16, Усл. п. л. 18.5
Уч.-изд. л. 19.7, Тираж 200 экз., Заказ № 208

Издательство СО РАН
630090, Новосибирск-90, Морской проспект, 2